Bis(benzoxazol-2-yl)methanides in main group organometallic syntheses and enquiry-based education

Dissertation

zur Erlangung des mathematisch-naturwissenschaftlichen Doktorgrades

"Doctor rerum naturalium"

der Georg-August-Universität Göttingen

im Promotionsstudiengang Chemie

der Georg–August University School of Science (GAUSS)

vorgelegt von

Nico Graw

aus Göttingen

Göttingen, 2022

Betreuungsausschuss

Prof. Dr. Dietmar Stalke, Fakultät für Chemie, Institut für Anorganische Chemie, Georg-August-Universität Göttingen

Jun.-Prof. Dr. Anna Krawczuk, Fakultät für Chemie, Institut für Anorganische Chemie, Georg-August-Universität Göttingen

Prof. Dr. Manuel Alcarazo, Fakultät für Chemie, Institut für Organische und Biomolekulare Chemie, Georg-August-Universität Göttingen

Mitglieder der Prüfungskommission

Referent: Prof. Dr. Dietmar Stalke, Fakultät für Chemie, Institut für Anorganische Chemie, Georg-August-Universität Göttingen

Korreferentin: Jun.-Prof. Dr. Anna Krawczuk, Fakultät für Chemie, Institut für Anorganische Chemie, Georg-August-Universität Göttingen

Weitere Mitglieder der Prüfungskommission:

Prof. Dr. Manuel Alcarazo, Fakultät für Chemie, Institut für Organische und Biomolekulare Chemie, Georg-August-Universität Göttingen

Prof. Dr. Thomas Waitz, Fakultät für Chemie, Institut für Anorganische Chemie, Georg-August-Universität Göttingen

Dr. Lisa Vondung, Fakultät für Chemie, Institut für Anorganische Chemie, Georg-August-Universität Göttingen

Dr. Alessandro Bismuto, Fakultät für Chemie, Institut für Organische und Biomolekulare Chemie, Georg-August-Universität Göttingen

Date of the oral examination: 29.09.2022

"I simply respect the chemistry. The chemistry must be respected."

– Walter White

Parts of the present work have already been published or are under peer-review in scientific journals. The present dissertation constitutes a part of the PhD work that is inseparable from these articles, as listed below.

I. *Introducing NacNac-Like Bis(4,6-isopropylbenzoxazol-2-yl)methanide in s-Block Metal Coorindation* by Ingo Koehne, **Nico Graw**, Thorsten Teuteberg, Regine Herbst-Irmer, Dietmar Stalke,* *Inorg. Chem.* **2017**, *56*, 14968-14978, DOI: 10.1021/acs.inorgchem.7b02276

II. *$HAlCl_2$ and H_2AlCl as Precursors for the Preparation of Compounds with Four- and Five Coordinate Aluminum* by Mingdong Zhong, Yashuai Liu, Subrata Kundu, **Nico Graw**, Regine Herbst-Irmer, Dietmar Stalke,* Herbert W. Roesky,* *Inorg. Chem.* **2019**, *58*, 10625-10628, DOI: 10.1021/acs.inorgchem.9b02001

III. *Amidinate based indium(III) monohalides and β-diketiminate stabilized In(II) -In(II) bond: synthesis, crystal structure and computational study* by Samya Banerjee, Sayan Dutta, Samir Kumar Sarkar, **Nico Graw**, Regine Herbst-Irmer, Debasis Koley,* Dietmar Stalke,* Herbert W. Roesky,* *Dalton Trans.* **2020**, *49*, 14231-14236, DOI: 10.1039/d0dt03161e

IV. *Cyclic (Alkyl)(Amino)Carbene Stabylized Aluminum and Gallium Radicals Based on Amidinate Scaffolds* by Mujahuddin M. Siddiqui, Samya Banerjee, Sanjoy Bose, Samir Kumar Sarkar, Sandeep K. Gupta, Johannes Kretsch, **Nico Graw**, Regine Herbst-Irmer, Dietmar Stalke,* Sayan Dutta, Debasis Koley,* Herbert W. Roesky,* *Inorg. Chem.* **2020**, *59*, 11253-11258, DOI: 10.1021/acs.inorgchem.0c01913

V. *Preperation and Reactivity Studies of Four and Five coordinate Amidinate Aluminum Compounds* by Samya Banerjee,* Chowan Ashok Kumar, Sanjoy Bose, Samir Kumar Sarkar, Sandeep K. Gupta, **Nico Graw**, Christian Köhler, Regine Herbst-Irmer, Dietmar Stalke,* Sayan Dutta, Debasis Koley,* Herbert W. Roesky,* *Z. Anorg. Allg. Chem.* **2021**, *647*, 1735-1743, DOI: 10.1002/zaac.202100125

VI. *Ducks in space groups! Students grasping 3D arrangement of symmetry elements with hands-on models* by **Nico Graw**, Dietmar Stalke, *Acta Cryst.* **2021**, *77A*, C765, DOI: 10.1107/S0108767321089327

VII. *Tangible Symmetry Elements and Space Group Models to Guide from Molecular to Solid-State Composition* by **Nico Graw**, Dietmar Stalke,* *J. Appl. Cryst.* **2021**, *55*, 144-148, DOI: 10.1107/S1600576721012218

VIII. *Fluorescent organo-antimony compounds as precursors for syntheses of redox-active trimeric and dimeric alkali metal antimonides: an insight into electron transfer reduction processes* by Ekta Nag, Aditya Kulkarni, Sai Manoj N. V. T. Gorantla, **Nico Graw**, Maria Francis, Regine Herbst-Irmer, Dietmar Stalke,* Herbert W. Roesky,* Kartik Chandra Mondal,* Sudipta Roy,* *Dalton Trans.* **2022**, *51*, 1791-1805, DOI: 10.1039/D1DT03398K (featured as inside front cover, DOI: 10.1039/D2DT90019J)

IX. *Synthesis and computational aspects of Al(II)-Al(II) and Ga(II)-Ga(II) dihalides based on an amidinate scaffold* by Arun Kumar, Samja Banerjee,* Nishant Sharma, Mohd

Nazish, **Nico Graw**, Regine Herbst-Irmer, Dietmar Stalke,* Upakarasamy Louderaj,* Herbert W. Roesky,* *Dalton Trans.* **2022**, *51*, 4898-4902, DOI: 10.1039/D2DT00317A

X. *Excellent yield of a variety of silicon-boron-radicals and their reactivity* by Mohd Nazish, Yi Ding, Christina M. Legendre, Arun Kumar, **Nico Graw**, Brigitte Schwedereski, Regine Herbst-Irmer, Parameswaran Parvathy, Pattiyil Parameswaran, Dietmar Stalke,* Wolfgang Kaim,* Herbert W. Roesky,* *Dalton Trans.* **2022**, *51*, 11040-11047, DOI: 10.1039/D2DT01318E

XI. *Compounds with Alternating Single and Double bonds of Antimony and Silicon; Isoelectronic to Ethane-1,2-Diimine* by Mohd Nazish, Christina M. Legendre, **Nico Graw**, Regine Herbst-Irmer, Shahila Muhammed, Pattiyil Parameswaran,* Dietmar Stalke,* Herbert W. Roesky,* *Inorg. Chem.* 2023, DOI: 10.1021/acs.inorgchem.2c03695.

XII. *Coordination and stabilization of a lithium ion with a silylene* by Mohd Nazish, Christina M. Legendre, **Nico Graw**, Regine Herbst-Irmer, Dietmar Stalke,* Siddharth Sankar Dutta, Upakarasamy Lourderaj, Herbert W. Roesky,* *Chem. Eur. J.* 2023, DOI: 10.1002/chem.202203528

XIII. *[2+4]-Cycloadditon Product of an Amidinate Substituted Dialumene with Toluene* by Arun Kumar, Komal Yadav, **Nico Graw**, Mohd Asif Ansari, Regine Herbst-Irmer, Upakarasamy Lourderaj,* Dietmar Stalke,* Herbert Roesky,* *Chem. Eur. J.* **2023**, submitted.

XIV. *Investigation of Solid-State Emission of Halogenated Diphenyl Phosphanyl Anthracenes* by Tim Patten, **Nico Graw**, Sebastian Friedl, Dietmar Stalke, Anna Krawczuk,* *Adv. Opt. Mater.* **2023**, 2202753, DOI: 10.1002/adom.202202753

XV. *Indium K_a radiation from a MetalJet X-ray source: The long way to a successful charge density investigation* by **Nico Graw**, Paul Niklas Ruth, Tobias Ernemann, Regine Herbst-Irmer, Dietmar Stalke,* *IUCrJ*, **2023**, submitted.

XVI. *Indium K_a radiation from a MetalJet X-ray source: Comparison of the Eiger 2 CdTe and Photon III detectors* by Paul Niklas Ruth, **Nico Graw**, Tobias Ernemann, Regine Herbst-Irmer, Dietmar Stalke,* *IUCrJ*, **2023**, submitted.

Table of contents

Abbreviations

ADP	anisotropic displacement parameter
ATR	attenuated total reflection
BASF	batch scale factor
^{Bzh}Box	bis(4-benzhydrylbenzoxazol-2-yl)methanide
^{Me}Box	bis(4-methylbenzoxazol-2-yl)methanide
^{Me}BoxH	bis(4-methylbenzoxazol-2-yl)methane
^{n}Bu	butyl
^{t}Bu	*tert*-butyl
CAD	computer-aided design
$CDCl_3$	deuterated chloroform, chloroform-*d*
cif	crystallographic information file
COD	1,5-cyclooctadiene
Cp	cyclopentadienide
CSD	Cambridge Structural Database
Cy	cyclohexyl
DAT	dynamic adaption technology
dcm	dichloromethane
Dip	2,6-diisopropylphenyl
EDX	energy dispersive X-ray spectroscopy
et al.	*et alii* (lat.) “and others”
e.g.	*exempli gratia* (lat.) “for example”
Fc	ferrocenyl
FTIR	Fourier-transform infrared spectroscopy
FWHM	full width at half maximum
HMDS	bis(trimethylsilyl)amide
HSAB	Hard and Soft Acids and Bases
i.e.	*id est* (lat.) “that is to say”
IAM	independent atom model

ICSD	Inorganic Crystal Structure Database
LIFDI	Liquid Injection Field Desorption Ionisation
Mes	mesityl, 2,4,6-trimethylphenyl
NacNac	*β*-diketiminate
NHC	*N*-heterocyclic carbene
NHGe	*N*-heterocyclic germylene
NMR	nuclear magnetic resonance
ORTEP	Oak Ridge Thermal Ellipsoid Plot
OTf	triflate, trifluoromethanesulfonate
PLA	poly lactic acid
^{c}Pr	*cyclo*-Propyl
^{i}Pr	*iso*-Propyl
Py	pyridyl
rpm	rotations per minute
SC-XRD	single crystal X-ray diffraction
SHG	second harmonic generation
thf	tetrahydrofuran
TMS	trimethylsilyl
VSEPR	valence shell electron pair repulsion
ylide	2-dimethylsulfuranylidene-1,3-indanedione

Compound Index

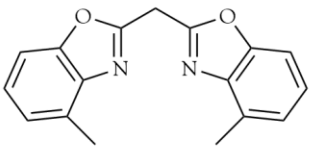

I

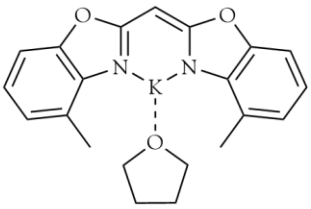

II

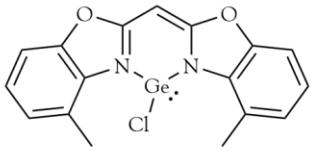

III

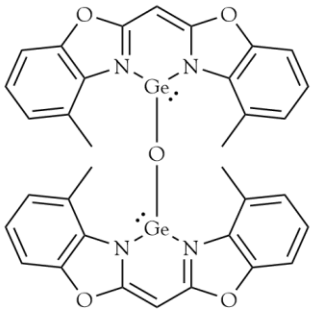

IV

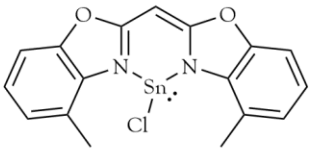

V

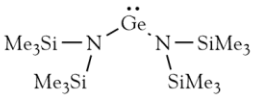

VI

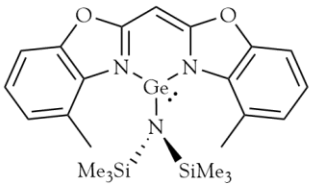

VII

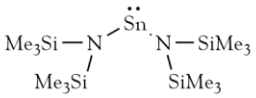

VIII

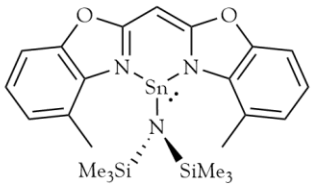

IX

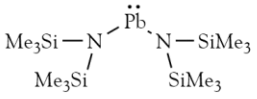

X

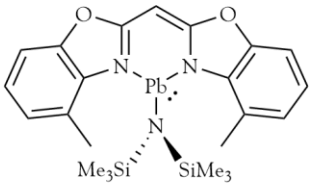

XI

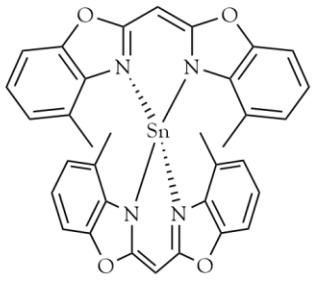

XII

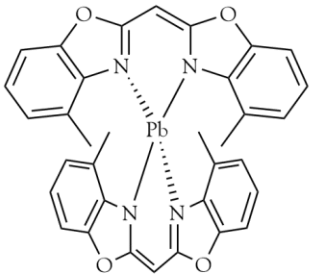

XIII

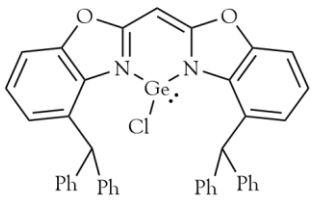

XIV

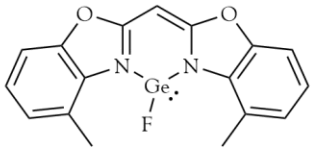

XV

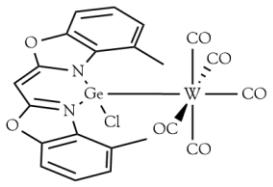

XVI

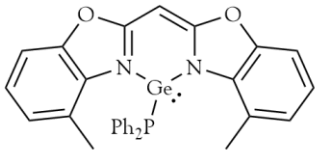

XVII

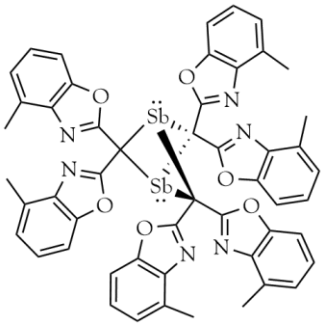

XVIII

Foreword

Serendipity always played a major role in natural sciences.

When Hennig Brand conducted alchemical experiments with urine with the intention to obtain the philosopher's stone, he instead isolated white phosphorus and thus discovered the first element, which had not been known since antiquity. In 1856, William Henry Perkin synthesised mauveine, the first synthetic dye, although he actually was aiming to make quinine, a drug used to treat malaria. With his accidental discovery, he sparked the emergence of an entire dye industry. X-rays were noticed by Wilhelm C. Röntgen only by chance because fluorescent screens were scattered around his laboratory, which had nothing to do with the actual experiment. The advances and possibilities his observation has brought to modern medicine and structural sciences are immeasurable. Uncountable lives have been saved by penicillin and antibiotics based on it and all of that started thanks to a petri dish, which accidently got contaminated with fungal spores. 1938 Teflon was created because Roy Plunkett forgot to put his chemicals back in a fridge. From its initial use in uranium enrichment and space crafts, this material has found its way in our everyday lives, be it frying pans or outdoor clothing.

These are just a few of the more popular examples, which show how research and scientific progress over centuries have been impacted by serendipity. And while I do not want to put myself in a row with the aforementioned scientists, I have the feeling that the path, which led to this thesis, also had some fortuitous moments.

When I learned about chemistry in school and for the first time started to understand (or at least believed to do so) the treasure trove that is the periodic table of elements, I set myself a very clear goal: My name will be on that table. It did not take too long for me to realise that this would most probably never happen.

Nevertheless, the fascination for chemistry remained unshaken. Over the course of my studies, it quickly became apparent that inorganic chemistry is my cup of tea. I wanted to specialise in main group metal organics and chose a PhD position accordingly. A topic was chosen, and a plan laid out, when it just so happened that at the start of my PhD a new X-ray diffractometer arrived. There was a chance to work with a one-of-a-kind machine and I took it.

I don't know what my reasoning was to do so, especially since my prior experiences with crystallography weren't exactly what one would call motivating but following my gut instinct was

a terrific choice. Not only because I got the chance to work with the first real revolution in X-ray technology since Röntgens times, but also because taking care of diffractometers from micrometre adjustments to gentle tapping with a hammer offered a completely different access to crystallography. With the University of Gottingen's strong tradition in solid-state chemistry and the company of Prof. Dr. Dietmar Stalke and Dr. Regine Herbst-Irmer, both scholars of Georg M. Sheldrick, there probably aren't many places better suited to learn about chemical crystallography.

With my work on the MetalJet diffractometer finished, I was back on track to do synthesis and promptly another opportunity arose: A project funded by the state of lower saxony, which allowed me to combine my newly won affection for crystallography with the passion for teaching – an offer I could not possibly refuse. And just like that, synthesis was postponed again to instead develop three-dimensional models for crystallography education.

After working on these two projects, which were completely unforeseen at the beginning of my PhD, I finally focussed on synthesis and used bis(benoxazol-2-yl)methanides to create novel tetrylenes. Of course serendipity stroke again and besides the sought after compounds, unintentionally also unexpected new structural motif was discovered.

This explains why the present thesis constitutes three main chapters, which are thematically largely independent of each other. Was all that serendipity? The fate of natural sciences? Chaos? I will not judge on that myself. One thing I do know for certain, however, is that this thesis and the work that lead to it conclude the most arduous, but also gratifying stage of my adventures in chemistry so far. Still, I did not manage to add a new element to the periodic table. Instead, I believe I did better. Because rather than adding something, I learned how to take something away from it. And I made use of this ability to teach others and to create this thesis, which – at least I hope – forms a small and modest contribution to our shared body of knowledge.

Chapter I:
MetalJet X-ray source

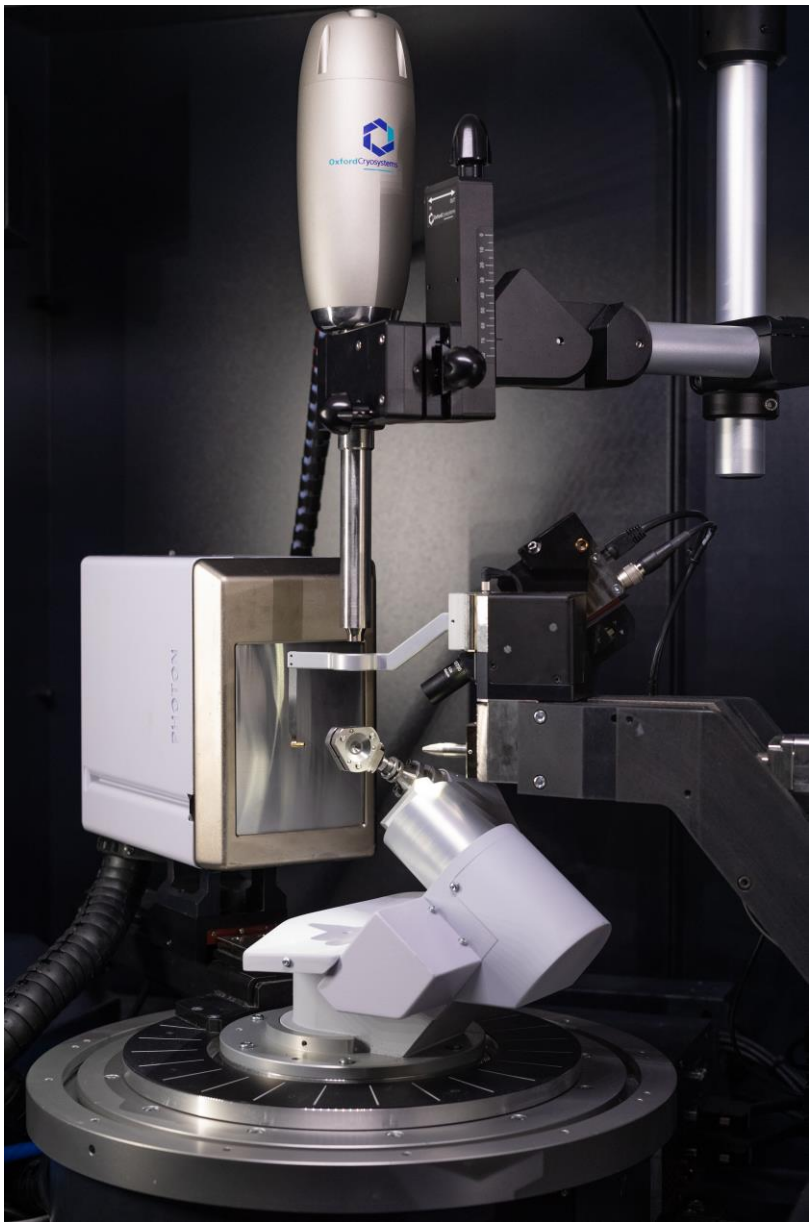

The work presented in chapters 1.2.2, 1.2.3 and 1.2.4 was done in collaboration with Paul Niklas Ruth and cannot be separated from his contributions.

1.1 Introduction

1.1.1 Historical background

As with many other great scientific discoveries, coincidence also played an important role in the first description of X-rays. Wilhelm Conrad Röntgen was experimenting with gas discharge tubes during December 1895 when he noticed fluorescence on sheets of paper which were priorly treated with a solution of *bariumplatincyanür* (barium tetracyanoplatinate(II), $Ba[Pt(CN)_4]\cdot xH_2O$) and by chance positioned close enough to the discharge tubes so that fluorescence could be observed.[1] His initial findings on the properties and characteristics of X-rays were first published in the proceedings of the Physical-Medical Society in Würzburg where Röntgen was professor of physics at that time.[1–3] It should be noted that Röntgens discovery right away caught public attention. Transcripts of his first report alongside the infamous X-ray photography of his wife's hand were quickly distributed by the press across Europe and the United States.[4,5] In this way, the discovery of X-rays became known and recognized by the general public as well as the scientific community within less than a month. Remarkably, this has led to Röntgen becoming a published author in *Nature* even though he never submitted to that journal himself.[6] Finally, Röntgens combined notes on X-rays were republished in 1898.[7–9]

The discharge tubes utilized by Röntgen were constructed according to the ones described by William Crookes.[10] These Crookes tubes consisted of a pair of electrodes embedded in a sealed glass body filled with different gases at low pressures like the one shown in Figure 1-1. They were used at the time for the study of so-called cathode rays (later identified to be free electrons in the gas phase by Emil Wiechert[11] and Joseph John Thomson[12] in 1897). It should be noted, however, that a similar experimental setup had already been used by Julius Plücker since 1857.[13] After that, the fundamental working principle of laboratory X-ray sources has not changed much in over a century. Instead, the individual components of the source have been optimised to meet the requirements of increasingly demanding scientific and medicinal questions and applications. Some landmark improvements – not taking into account large scale facilities like synchrotrons – will be briefly discussed in the following.

Figure 1-1: Cathode ray tube produced by *Greiner & Friedrichs* around 1896, similar to the ones W. C. Röntgen had at his hands. On the right side of the tube a disc cathode is embedded, on the bottom left the anode is connected. Photograph kindly provided by the Deutsche Röntgen-Museum Remscheid, Photographer: Christina Falkenberg.

The original Crookes tube required residual gas to be present at a certain pressure. Due to for example photoionization processes or natural radioactivity some free electrons and cations are always present in a gas. These charged particles are then accelerated by the high voltage applied to the electrodes generating more free electrons in a so called Townsend avalanche *via* collision ionisation with other particles or liberation of electrons from the cathode material upon impact.[14] Because of this, the current of free electrons in the tube and therefore also the resulting X-ray intensities were a function of the gas pressure and depending on the operation mode (completely sealed or attached to a vacuum pump) subject to significant changes. To circumvent this problem William Coolidge, employee at General Electrics Co., replaced the cathode with a tungsten filament.[15,16] This filament can be heated if a sufficient electrical current is applied and generates free electrons *via* thermionic emission.[17,18] Therefore, they are also called hot cathode tubes in contrast to Crookes' cold cathode tube. Having the source of free electrons independent of the residual gas from then on allowed for more precise control of the intensity of generated X-rays as it is directly correlated to the heating current of the filament.[19] For the same reasons, the pressure in the tube no longer had to be controlled in terms of its absolute value but should be as low as possible to avoid collisions between electrons and gas particles.

Systematic studies were performed to assess the efficiency at which the electrical power supplied to the tube is converted into X-rays. For this purpose, the X-ray intensities were measured

indirectly by means of calorimetry. Early estimates of the efficiency gave values between 0.06 and 0.19 %.[20] Those could be raised to be about 0.56 % after optimisations and careful consideration of absorption effects. However, it was already recognized that these values were systematically too small, since the soft X-rays that are completely absorbed by the glass of the tube could not be taken into account.[21] In fact, todays estimate for the efficiencies of hot cathode tubes is around 1 %.[22] Increasing the intensity of the X-rays produced by increasing the filament current would be straightforward, but on one hand for any given acceleration voltage the current of free electrons is limited by space charge effects[19] and on the other hand the maximum power input has to be capped to prevent melting of the anode material. These limits have been investigated depending on the geometry and material of the anode,[23] the movement of the focal spot,[24,25] and the shape of the focal spot on the anode surface.[26] The idea of moving the focal point on the anode target came about as early as 1897, however, the first working X-ray tube with a rotating anode was not presented until 1928.[27] Moving mechanical parts in a high vacuum surrounding of course created new problems. In the following years solutions for the continuous supply with a cooling medium,[28] new types of low pressure lubricants[29] and motion resistant high vacuum seals[30] were developed.

In addition to pushing the limits in terms of anode power input, another major leap to higher usable X-ray intensities was achieved through the introduction of exit windows into the tubes. The original glass tubes had their limitations with respect to wall thickness and elemental composition. Therefore, solid metal tubes were designed with dedicated exit windows, which were covered by thin metal foils to minimise X-ray absorption. Due to its easy machinability and robustness even with thin foils, aluminium became the standard material for exit windows.[31] However, because of the low melting point it is impossible to form a sturdy seal between the aluminium and the metal body of the X-ray tube. Creative solutions were employed to overcome this problem, for example application of wool fat as a sealing agent,[32] before beryllium was recognized to be a promising material.[33] After methods had been developed to produce thin films of beryllium[31] these exit windows proved themselves to be superior to aluminium in every aspect[34] and are still used today.

Strictly speaking, optics are not part of the X-ray source. However, they are of great importance to single crystal X-ray diffraction setups and will therefore be included in this discussion as well. X-ray sources naturally produce a spectrum of characteristic radiation and bremsstrahlung. But to be employed in a single crystal X-ray diffraction experiment the X-ray beam needs to be monochromatic as diffraction is dependent on the wavelength. Ideally, it should also be focussed

so that the diameter of the beam at the focal spot is about the size of the single crystal. This makes sure that most of the X-ray photons can interact with the crystal lattice and therefore contribute to the intensity of the diffraction image. Because the refractive index of X-rays is very close to unity, they cannot be shaped by conventional lenses.[35] Instead, different designs for focussing X-ray optics were proposed,[36–40] and graded multilayer mirrors became well established.[41–43] Moreover, they cannot only focus the beam but also monochromatise it at the same time.[44] The combination of focusing optics with a microfocus X-ray source, i.e. a source in which the electron beam is concentrated on a small spot on the anode, to achieve a high brilliance X-ray beam for diffraction experiments was pioneered by Arndt.[45]

However, all those improvements did not change the fact, that the maximum X-ray flux of a source is limited by the tolerable heat load of the anode target before melting. It was not until 2003 that this principle limitation was overcome when Hemberg, Otendal and Hertz demonstrated an X-ray source with a liquid metal anode.[46]

In summary, since the discovery of X-rays by Röntgen in 1895, the basic operating principle of laboratory X-ray sources, namely the bombardment of solid metal targets with accelerated electrons, has not changed fundamentally in more than 100 years. Instead, individual components such as cathodes, anodes, exit windows and optics were improved and optimised for certain applications to maximise the usable X-ray flux. Only recently the MetalJet X-ray source with a liquid metal anode was developed.

1.1.2 MetalJet X-ray source

The MetalJet X-ray source utilises a jet formed out of a liquid metal as the anode, hence its name. Using an already molten anode of course eliminates the power load restriction due to melting on conventional anodes. In a conceptual experiment Hertz *et al.* have shown that such an X-ray source is functional and can potentially achieve a brightness two orders of magnitude higher than solid anode sources.[46,47] Their original setup used a tin-lead alloy, which was ejected from a heated reservoir into a vacuum chamber, yielding a laminar jet with 75 µm diameter and a speed of about 60 m/s. A 50 keV electron beam was focussed on this jet producing continuous bremsstrahlung as well as the expected characteristic X-ray radiation of lead and tin. The potential for significantly higher brightness with such an X-ray source lies not only in the superior thermal properties and the higher heat loads tolerable, but also in the high speed of the jet, as it transports

heat away from the electron impact area faster than in rotary anodes and continuously renews the anode as long as laminar flow is maintained. Further development tested the borders of the power density the jet anode can tolerate,[48] the influence of the jet diameter on performance and debris emission as well as source stability in terms of X-ray spot size and position.[49] Four years after the report of the first proof-of-concept experiments, the application of a MetalJet source operated with a pure tin jet was shown for phase-contrast X-ray imaging performed on a spider.[50] Using material with a high atomic mass for the anode produces relatively hard characteristic X-rays. To extend the portfolio of usable wavelengths, operation of the MetalJet technology with a gallium jet was demonstrated producing an emission of characteristic radiation at the 9.3 keV Ga K_α line.[51] With peak spectral brightness of about 10^{10} photons/(s·mm²·mrad²·0.1% BW) and an energy close to well established copper radiation (8.04 keV)[52] the MetalJet source was deemed suitable for lab-scale X-ray crystallography. Going one step further, it was even demonstrated that the source can be run on methanol as anode material, claiming that the jet anode concept allows for potentially all liquid materials to be used for X-ray generation and hence gives access to a broad range of wavelengths for different applications.[53]

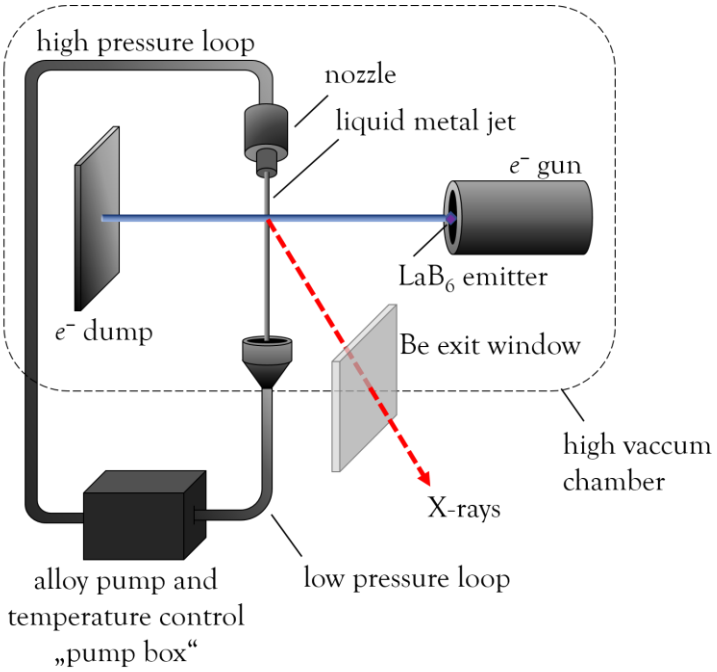

Figure 1-2: Schematics of the commercially available MetalJet X-ray source.

In 2007 EXCILLUM AB was founded and made the MetalJet X-ray source commercially available. They presented the first system, which allowed for continuous operation, the schematics of which are shown in Figure 1-2. The alloy is pumped in a closed cycle instead of ejection from a finite

reservoir. The used alloy consisted of gallium (68.5 %), indium (21.5 %) and tin (10 %) because it has a melting point of −19°C and therefore does not require additional heating.

The source was intended to make use of the Ga K_α line. However, the characteristic indium radiation has a higher energy of 24.2 keV, which is rather close to the silver K_α line (22.2 keV),[52] making it interesting for X-ray diffraction studies of highly absorbing compounds and imaging of thicker samples. Therefore, experiments were performed with alloy enriched in indium (35 % Ga, 65 % In, meting point 70°C) to also increase the brightness of the indium K_α line in the emitted spectrum.[54]

Apart from the anode also the cathode represents a small novelty for sources used in single crystal X-ray diffraction. While conventional X-ray sources use tungsten wire for the emission of free electrons, the MetalJet system employs a crystalline lanthanum hexaboride (LaB_6) emitter. Hexaborides are long known to be excellent electron emitters[55] and have been used as cathodes in electron microscopes[56,57] successfully for many years. Tungsten wires have limited bending radii whereas crystalline lanthanum hexaboride can provide a sharp crystal corner as emission source if mounted accordingly. Limiting the emission to a small point allows for the electron beam to be focussed more easily by magnetic optics. While this is mandatory in electron microscopes to achieve high resolution, it was counterproductive for solid target X-ray sources as the power density needed to be limited to prevent melting. Removing this restriction in the MetalJet system allows the electron beam to be focused on smaller X-ray spots. This in turn leads to emission of X-rays from a more confined area and therefore a higher brightness of the X-ray beam.

The commercial MetalJet source was further developed by EXCILLUM AB towards specialisations for different applications. Alloys with different weight percentages of gallium, indium and tin as well as high voltage generators capable of 70 kV or 160 kV acceleration voltage are currently available. Introduction of the dynamic adaption technology (DAT) compensates for the slow evaporation of the LaB_6 cathode by continuously adapting the electron optics to the changing emission angles and therefore prolonging the cathode lifetime. A high accuracy determination of the photon flux was performed on the latest model D2 MetalJet source using the ExAlloy I1 (68.5 % Ga, 21.5 % In, 10 % Sn).[58] Running the source with 200 W electron beam power (70 keV, 2.857 mA) a brightness of roughly $5 \cdot 10^{10}$ photons/(s·mm²·mrad²·0.1% BW) for the Ga K_α line and $2 \cdot 10^{9}$ photons/(s·mm²·mrad²·0.1% BW) for the In K_α line was obtained. Albeit being impressive, it falls somewhat short of the original claim that the MetalJet source could become

an “in-house synchrotron” entering the regime of bending-magnet synchrotrons with brightnesses on the order of 10^{14} to 10^{15} photons/(s·mm²·mrad²·0.1% BW).[51]

Since its introduction, the MetalJet X-ray source has been used in single crystal X-ray diffraction studies involving all kinds of different compounds. From small organic molecules[59–64] to proteins,[65–68] polymers[69,70] and metal organic frameworks.[71] Furthermore inorganic compounds containing p-block elements[72,73] as well as d-metal complexes[74–80] have been investigated. All of these studies have been performed using the gallium K_α radiation even on highly absorbing gold compounds.[81] While this is reasonable for organic compounds with low absorption, it can become a problem if heavier atoms are present. The In K_α line is less intense due to the lower indium content in all available alloys but it also has some advantages. Besides the lower absorption coefficient, the smaller wavelength allows for higher (theoretical) resolution as the maximum resolution is limited to half of the employed wavelength. A highly intense X-ray source that potentially permits data collection up to a resolution of at least 0.45 Å would be perfectly fitted to perform experimental charge density studies. Additionally, due to the inverse relationship between resolution and wavelength the diffraction pattern becomes more narrow when harder X-rays are used. In other words, a given resolution can be obtained under smaller diffraction angles if shorter wavelength X-rays are used. This is especially important if the observable Θ-range is limited by the experimental setup, for example in a diamond anvil cell. Therefore, the use of a MetalJet system as a source not for gallium but for indium K_α radiation for single crystal X-ray diffraction seems promising as it provides an X-ray beam with higher intensity and smaller wavelength than with the previously available laboratory sources.

1.1.3 Experimental setup at the University of Göttingen

In September 2017 a complete diffractometer was installed in Göttingen, which at that time was the only single crystal X-ray diffractometer using indium K_α radiation in the world. The MetalJet X-ray source (model D2) was integrated in a BRUKER D8 Venture safety enclosure together with a four-circle kappa goniometer, a Photon II detector from BRUKER and exchangeable Montel multilayer optics from INCOATEC optimised for Ga K_α or In K_α radiation. However, all experiments performed within this work utilised In Kα radiation and the respective optics, focussing the X-rays into a beam with a diameter of roughly 50 µm (FWHM) at the beam centre. ExAlloy I1 (68.5 % Ga, 21.5 % In, 10 % Sn) was used for the anode at a default pressure of

190 bar. The source was equipped with a 70 kV high voltage generator delivering 200 W of electron beam power. Additionally, a 160 kV generator was purchased to be able to increase the electron beam power at a later stage.
When issues with the tin content in ExAlloy I1 became apparent, the decision was made to use ExAlloy I3 (75 % Ga, 25 % In) instead. This alloy was not available when the system was installed, so the whole pump system, which is cycling the alloy and controlling the operating parameters connected to the anode, needed to be exchanged in January 2019.
When the dynamic adaptation technology became available in January 2020 the system was upgraded. Due to the improved cathode performance after DAT installation, the electron beam power was permanently increased from 200 W to 250 W, which corresponds to a nominal electron current of 3.57 mA.

1.2 Employing In K_α radiation from a MetalJet X-ray source for SC-XRD

1.2.1 Determination of spectral contamination by Ga K_α radiation

The goal was to utilise In K_α radiation from the MetalJet source for single crystal X-ray diffraction experiments. However, due to its design the X-ray source of course still emits characteristic gallium radiation. Although the X-ray optics are designed to filter and focus one wavelength with a very small bandwidth from the source spectrum, contamination with scattered radiation from the very intense Ga K_α line cannot be avoided. Because every wavelength in principle will cause its own diffraction pattern, this contamination must be suppressed. The most straightforward way to do so would be to place an attenuator in the beam path between the crystal and the X-ray optics. Ideally, this attenuator blocks the contamination without significant absorption of the desired wavelength. The linear absorption coefficient of the attenuator depends on the atomic number and the density of the material. Additionally, it is also a function of the X-ray wavelength. In general, absorption becomes stronger for low energy X-rays and high-density absorbers composed of heavy elements. This trend does not hold, if the absorber material exhibits absorption edges at specific energies, which are characteristic of the used material and caused by electronic transitions. Because the Ga K_α line has a relatively low energy of 9.3 keV, it is in general absorbed more strongly than the In K_α line. A suitable material to be used as attenuator is aluminium. The linear absorption coefficients form a ratio of μ_{Al} (9 keV) / μ_{Al} (24 keV) ≈ 15, indeed showing that Ga K_α is absorbed more strongly than In K_α radiation (see Figure 1-3).

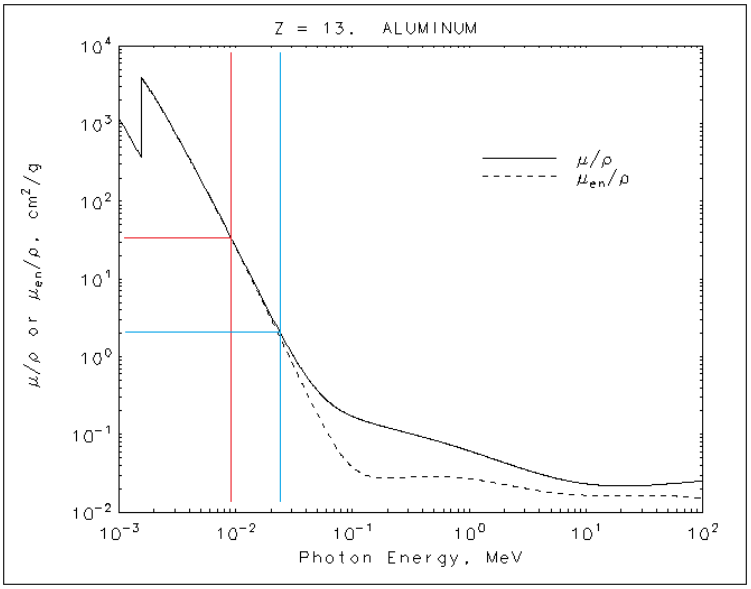

Figure 1-3: Mass attenuation coefficient as a function of photon energy plotted for the element aluminium. Red line: 9 keV. Blue line: 24 keV. Adapted from reference.[82]

The thickness of the attenuator should be optimised to make sure that it is thick enough to reduce the gallium radiation down to an insignificant level but not too thick to prevent unnecessary loss of intensity from the indium radiation. The aluminium attenuator supplied by BRUKER and meant to be used for experiments with indium radiation had a thickness of 0.75 mm. Nevertheless, an effort was taken to determine an optimal attenuator thickness for the diffractometer setup. The most straightforward method to determine the spectral purity of the primary X-ray beam would be to perform energy dispersive X-ray (EDX) spectroscopy. However, this of course requires an EDX spectroscope or similar hardware. Instead, the fact that the gallium as well as the indium Kα radiation each generate independent diffraction patterns, which are well separated due to the big enough difference in wavelengths, was utilised. Datasets on a standard ylide test crystal were recorded with the same measuring strategy but different attenuator thicknesses (see Figure 1-4). These datasets containing two diffraction patterns each could then be treated as twins with two domains. Determining the twin fraction that corresponds to the reflections caused by gallium radiation indirectly measures the degree of contamination left after attenuation. Because the data reduction software does not allow to use two wavelengths simultaneously, this apparent second domain needed to be described by a second unit cell, which shared the same orientation matrix but had different cell parameters. This new unit cell would then emulate the reflections caused by gallium radiation as if they would have been caused by indium radiation so that all data could be treated within the same wavelength framework. Because

the crystal system of the used ylide test crystal was orthorhombic, the second cell could be easily calculated by multiplying the lengths of the original cell edges with the ratio of wavelengths (equation (1-1)).

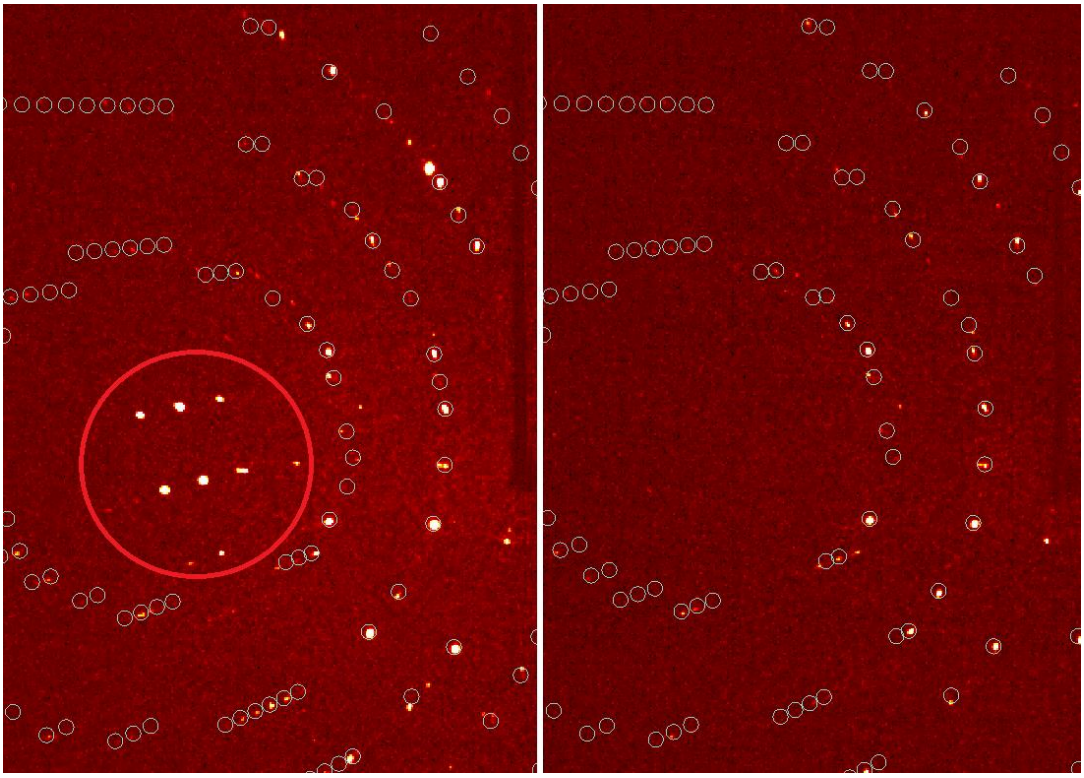

Figure 1-4: Frames recorded on the same ylide test crystal in identical orientations. 10 s exposure time at 37.00 mm detector distance and 100 K. MetalJet source operated at 200 W of electron beam power. The intensity scaling is identical in both frames. Small circles indicate areas where reflections are expected to occur for In radiation. Left: no attenuation; red circle highlights reflections which do not fit to the expected diffraction pattern and are caused by contaminant Ga radiation. Right: Attenuation with 0.95 mm of aluminium.

$$\begin{pmatrix} a' \\ b' \\ c' \end{pmatrix}_{\mathrm{Ga}} = \begin{pmatrix} a \\ b \\ c \end{pmatrix}_{\mathrm{In}} \cdot \frac{\lambda_{\mathrm{In}}}{\lambda_{\mathrm{Ga}}} \qquad (1\text{-}1)$$

The data were then integrated with *SAINT*[83] using both domains and scaled with *TWINABS*.[84] After space group determination and structure solution, an independent atom model (IAM) refinement against unmerged data from both domains up to a resolution of 0.48 Å was performed. The results given in Table 1-1 show a clear trend of increasing data quality and decreasing twin fraction up to an attenuator thickness of 0.95 mm. Beyond that, the data quality

suffers while the twin fraction stays the same within the limits of uncertainty. This showed that attenuation by 0.75 mm of aluminium as proposed by the manufacturer did not suffice to absorb most of the Ga K_α contamination. Hence, future experiments should be performed with 0.95 mm of aluminium instead.

Table 1-1: Results from data collection and twin refinement on an ylide test crystal with different thicknesses of aluminium attenuation.

***d*(Al) [mm]**	**max. resolution (2Θ)**	**R_{int} (0.48 Å)**	**BASF [%]**	**$R1$ ($I>2\sigma(I)$) (0.48 Å)**
0	76.47	4.78	62.8(9)	8.88
0.75	66.05	4.30	0.55(4)	3.99
0.85	67.01	4.09	0.28(4)	3.76
0.95	65.73	3.86	0.12(3)	3.62
1.25	64.51	4.31	0.11(3)	3.84

An independent atom model (IAM) was refined against the data up to 0.48 Å resolution for the sake of data quality assessment. In terms of X-ray structure determination, this is nonsensical as the IAM uses only spherically averaged densities of individual neutral atoms to describe the electron density distribution within a structure and therefore is unable to model density in regions of lone pairs or chemical bonding between atoms. However, the diffractometer was intended to be used for charge density studies specifically aimed at assessing these regions experimentally. For this purpose, diffraction data of highest possible resolution and quality is needed and instead of the IAM approach a multipole model[85] can be refined to yield a more complex description of the electron density distribution. To evaluate the diffractometer's performance in terms of its application for such charge density studies, refinement of a multipole model was attempted. However, using the so far best dataset collected with 0.95 mm aluminium attenuation no satisfying results could be obtained. The fact that the multipole model was unstable and could not be refined hinted at another problem besides the Ga K_α contamination corrupting the data quality.

1.2.2 Determination of spectral contamination by Sn K_α radiation

Blocking Ga K_α radiation by attenuation with aluminium improved the spectral purity of the X-ray beam immensely, however, refinement of a multipole model and therefore experimental charge density studies were still not possible with the obtained data. After the quality of the used ylide crystal had been confirmed with high-resolution diffraction experiments on different diffractometers, the cause of the insufficient data quality had to be connected to the MetalJet source. Up to this point, the tin content of ten percent by weight of the anode alloy had been neglected. It was assumed that it would not contribute to the X-ray beam with the Montel optics being optimised for In K_α radiation. However, from close inspection of the data it became apparent that reflections suffered from intensity asymmetrically tailing towards the beam centre. With increasing resolution this feature became more prominent up to a point where the reflections were actually split. In Figure 1-5 data for a reflection with Miller indices ($\bar{4}\bar{2}9$) is shown. The 3D intensity profile clearly exhibits a smaller peak to the left of the main peak and almost separated from it. The fact that the degree of tailing or separation was dependent on the diffraction angle strongly suggested a spectral impurity to be the cause. Because of the shift towards the beam centre, the contaminant wavelength must have been shorter than that of In K_α radiation.

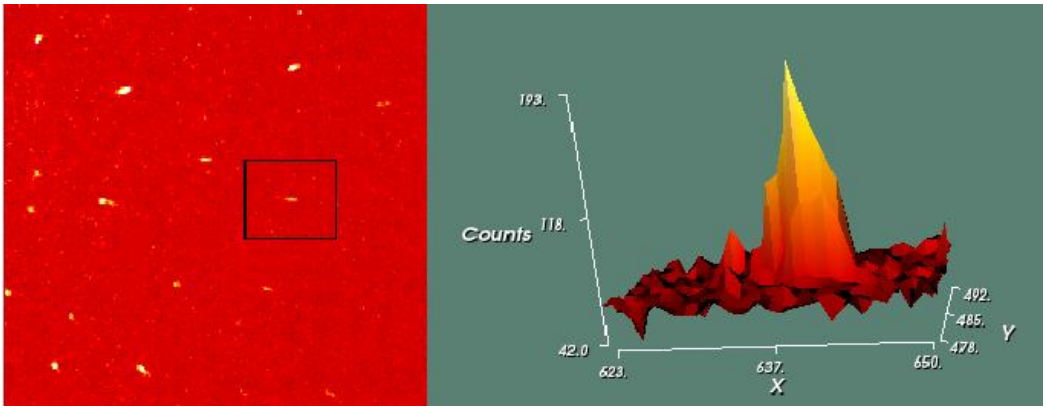

Figure 1-5: Diffraction data recorded on an ylide test crystal. 10 s exposure time at 37.00 mm detector distance and 100 K. MetalJet source operated at 200 W of electron beam power with 1.25 mm of Al attenuation. Left: Magnification of the detector image. The black frame marks the reflection with Miller indices ($\bar{4}\bar{2}9$). Right: 3D intensity profile of the same reflection.

The suspicion that Sn K_α radiation might be the cause was confirmed after a private communication with the group of Prof. Dr. Christian W. Lehmann at the Max-Planck-Institut

für Kohlenforschung in Mülheim, which had also purchased a MetalJet X-ray source. Their source used ExAlloy I2 (47 % Ga, 37 % In, 16 % Sn) as anode material and was also equipped with Montel optics made from INCOATEC optimised for In K_α radiation. The Lehmann group performed EDX analysis on their primary beam with 0.4 mm of aluminium attenuation at 70 kV acceleration voltage and 12.5 W electron beam power and confirmed the spectral impurity to be Sn K_α radiation with a photon energy of 25.27 keV.[52]

If the X-ray optics is not able to separate the characteristic tin radiation from the focused beam, then the only option to get rid of it would be to use attenuation again. In this case, however, this was not straightforward as the unwanted radiation had higher energy. As discussed in the previous chapter absorption coefficients in general become smaller with increasing energy of the radiation to be absorbed. In other words, absorption of the characteristic indium radiation would always be more pronounced than absorption of the Sn K_α line. The only exception to this would be a material, which exhibits an absorption edge in between the two K_α lines. Due to their narrow energy gap, only one element exhibits such a property. With an absorption edge at 24.35 keV palladium could attenuate Sn K_α more efficiently than In K_α (see Figure 1-6). The ratio of the linear absorption coefficients μ_{Pd} (25.3 keV) / μ_{Pd} (24.2 keV) ≈ 4.5 is not particularly great though. Attenuation of the gallium radiation with aluminium would be obsolete if palladium is used as the latter has an even higher absorption coefficient for the Ga K_α line anyway.

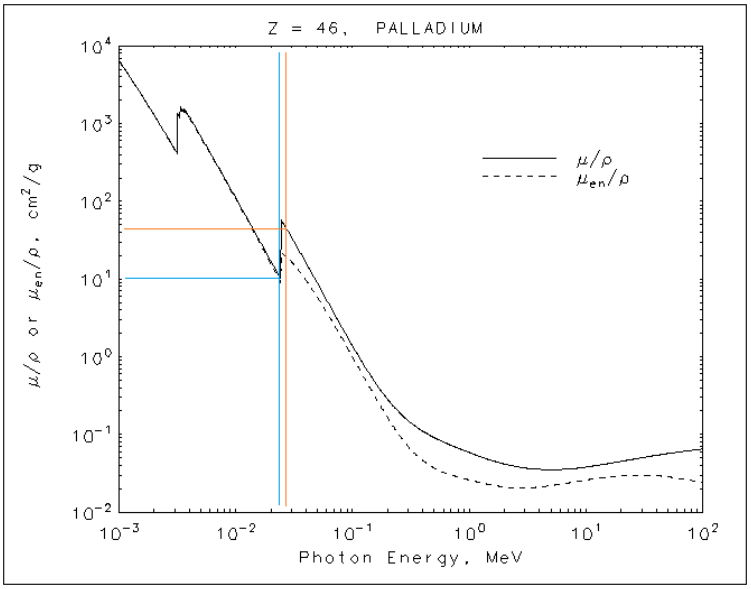

Figure 1-6: Mass attenuation coefficient as a function of photon energy plotted for the element palladium. Blue line: 24 keV. Orange line: 25 keV. Adapted from reference.[82]

Being aware of the spectral impurity caused by tin, several datasets with different thicknesses of palladium attenuation were collected on an ylide test crystal. In contrast to the experiments carried out to determine the contamination by gallium radiation, no optimisation by twin refinement was possible. The wavelengths of In and Sn K_α radiation were too close to each other and therefore the overlap of reflections was too big to reliably determine twin fractions in the same fashion as described before. Instead, a reference dataset was used, which was measured with the same crystal on a diffractometer with a silver IμS 2 source. As a result of this set of experiments, differences in unit cell volume relative to the reference dataset were obtained, which are plotted in Figure 1-7.

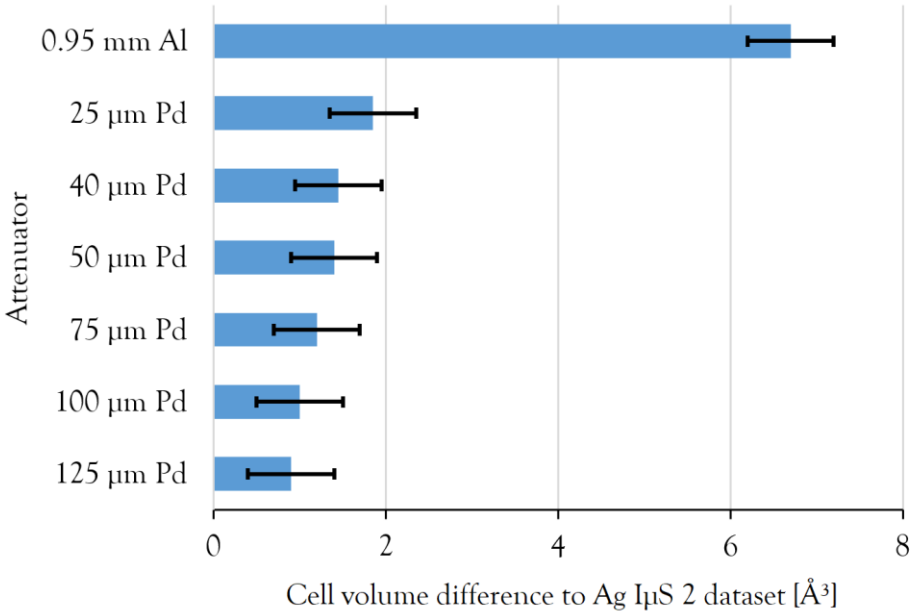

Figure 1-7: Differences in unit cell volumes obtained from datasets with varying attenuation relative to reference data collected with an Ag IμS 2 X-ray source. All data were collected on the same crystal at 110 K. Error bars shown in black.

First of all, despite optimised aluminium thickness, the determined cell volume deviates considerably from the reference when aluminium attenuation is used. If palladium is used, however, it decreases significantly already at the smallest thickness. Increasing the palladium thickness leads to a further but less dramatic decrease. Although all values obtained for palladium attenuation thicker than 40 µm lie within the standard uncertainty, the continuous drop of unit cell volume differences hints at further benefit from thicker attenuation. However, a purely statistical basis for these findings cannot be excluded without measurements that are more precise.

The decrease in unit cell volume differences can be rationalised by the effective blocking of characteristic tin radiation. As described before the Sn K_α radiation has a slightly shorter wavelength leading to reflections shifted towards the beam centre relative to those caused by In K_α radiation. This shift is small and resolution dependent so that only for high-resolution data independent instead of overlapping reflections can be observed. In the latter case, the overlap causes the reflections to become broader and shifts their centroids closer to the beam centre. Since the distances between reflections correspond to distances in reciprocal space, a decrease directly translates to an increase of distances in real space. Hence, the cell parameters and therefore the unit cell volume appear bigger as long as spectral contamination by tin radiation is present.

The next step would be to derive an optimal thickness for the palladium attenuator. However, due to the uncertainties of the results this could not be done reliably. As a consequence of the attenuation the intensity of the MetalJet source also dropped significantly. At 100 µm of Pd, the intensity was only about 50% of that of the reference silver IµS 2 source, which seriously called into question the added value of the MetalJet source. One insight that could be drawn from this though, was that also the alignment procedure of the diffractometer needed to be revisited. During the alignment, the X-ray source is moved with respect to the optics until the intensity in the doubly diffracted beam is maximised. If this is done without palladium attenuation, the alignment will not be optimised for the In K_α line but the contaminated radiation, which passes the optics.

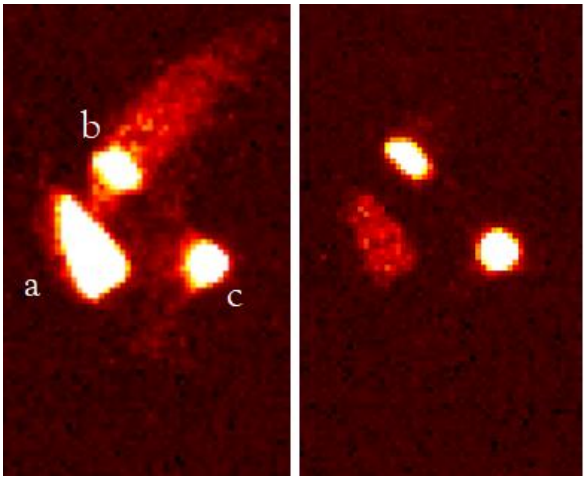

Figure 1-8: Detector images of the uncollimated radiation exiting the Monel optics. a) direct beam b) singly diffracted beam c) doubly diffracted beam. Left: 13.9 mm of aluminium attenuation. Right: 0.6 mm of palladium attenuation.

Figure 1-8 shows two images of the uncollimated radiation, which exits the Montel optics. For the image on the left side, 13.9 mm of aluminium were used as attenuator while the right image was recorded with 0.6 mm of palladium attenuation. For both cases, the absorption with respect to the In K_α line is approximately equal. Nevertheless, pronounced differences can be seen. The smeared out intensity on the left image is most probably due to high-energy contamination as it passed the aluminium attenuator. Most relevant is the asymmetric intensity distribution in the doubly diffracted beam. Ideally, it should be circular as it is, when palladium attenuation is used (right image). Hence it was clear that sufficient palladium attenuation is necessary during alignment.

In an attempt to see, if palladium attenuation was still needed after the improved alignment or if it at least could be reduced in thickness, collimators with different sized entry and exit holes were used to cut off as much of the smeared out intensity around the doubly diffracted beam as possible. Tremendous efforts were made to meticulously align the X-ray source and optics, however, without much success. Instead of a gain in spectral purity, only loss of intensity was achieved.

In summary, it can therefore be said that palladium attenuation cannot be circumvented if high quality data is needed using In K_α radiation from a MetalJet X-ray source with an ExAlloy I1 anode. A sufficiently thick (> 500 µm) attenuator should be used for alignment of source and optic and a thinner attenuator (40 µm to 100 µm) is needed for data collection. Based on these findings and with an appropriately set up diffractometer, a new high-resolution data set of the ylide test crystal was recorded using 40 µm of palladium attenuation. With this a multipole model refinement was possible and gave decent results but still for the price of reduced intensity.

1.2.3 Exchange of Montel optics

In the previous two chapters it was discussed how problematic it is that the X-ray beam is not monochromatic. Methods to reduce this problem and its consequences were discussed and implemented. But instead of just treating the symptoms, one could also try to tackle the root of the problem itself. The X-ray source generates characteristic radiation and bremsstrahlung and the physics of that cannot be altered. One could change the composition of the anode and thereby the emission of characteristic radiation though. This will be discussed in the following chapter. The other possible option to influence the spectral purity of the primary beam is the optics.

Montel optics do not only focus the X-rays in the doubly diffracted beam, they also monochromatise them, as only one wavelength with a small bandwidth should fulfil the necessary diffraction condition to pass the optics. If In and Sn K_α radiation cannot be separated in the setup described in this work, of course the question could be raised, if different optics might be able to do so. At the time of the experiments, INCOATEC had only produced three Montel optics for characteristic indium radiation. The other two were in the possession of BRUKER and the Lehmann group at the Max-Planck-Institut für Kohlenforschung in Mülheim. To test if the optics actually makes a difference, the BRUKER application lab in Karlsruhe lent us theirs for a comparison. In order to quantitatively evaluate the quality of the X-ray beam exiting the optics directly, rather than using the results of a diffraction experiment, a calibrated pin diode was used. The pin diode consists of interchangeable pinholes of different sizes and a photodiode, for which the correlation between the intensity of the incident beam and the resulting photocurrent is known. Repeated measurements with different pinhole diameters allow reliable positioning of the pin diode in the centre of the X-ray beam. In this way not only the photon flux and the flux density can be determined but also the beam shape and therefore the brilliance can be assessed. The latter one is best suited to compare different experimental setups as all parameters of the X-ray beam are taken into account.

Table 1-2: Experimental data for the comparison of Montel optics performance.

pinhole diameter [mm]	**BRUKER optics mean flux density [cps/mm²]**	**Göttingen optics mean flux density [cps/mm²]**	**ratio**
1.128	$1.41 \cdot 10^7$	$1.60 \cdot 10^7$	1.14
0.739	$3.24 \cdot 10^7$	$3.66 \cdot 10^7$	1.13
0.506	$6.69 \cdot 10^7$	$7.53 \cdot 10^7$	1.13
0.293	$1.89 \cdot 10^8$	$2.11 \cdot 10^8$	1.12
0.200	$3.70 \cdot 10^8$	$4.17 \cdot 10^8$	1.13
0.149	$5.57 \cdot 10^8$	$6.67 \cdot 10^8$	1.20
0.098	$9.74 \cdot 10^8$	$1.18 \cdot 10^9$	1.22
0.077	$1.21 \cdot 10^9$	$1.50 \cdot 10^9$	1.24
0.048	$1.87 \cdot 10^9$	$2.56 \cdot 10^9$	1.37
0.028	$2.39 \cdot 10^9$	$3.49 \cdot 10^9$	1.46

With the aid of INCOATEC the original optics from Göttingen were characterised first as they were already installed in the setup according to the optimised alignment procedure described in the previous chapter. After that, the optics was exchanged for those lent by BRUKER and great care was taken to perform a meticulous alignment of all components again. Subsequently the measurements with the pin diode were repeated. Results for both optics are compared in Table 1-2 and show slightly better performance of the original Montel optics.

These data were fitted to model the intensity distribution along the beam radius assuming a circular beam shape. From this fit, the beam diameter could be determined in terms of the beam's width at half of the maximum intensity (FWHM). As the measurements of the mean flux densities already suggested, the X-ray beam shaped by the original optics was more focused. With a diameter of 44 µm it is about 15 % more narrow than the beam shaped by the optics lent by BRUKER. Table 1-3 lists also the derived peak brightness for both cases and as expected based on all prior findings, the original optics is superior here as well.

Table 1-3: Results of the data analysis.

	BRUKER optics	**Göttingen optics**
beam FWHM [µm]	52	44
peak brilliance [photons/(s·mm²·mrad²·0.1% BW)]	$3.503 \cdot 10^8$	$5.353 \cdot 10^8$

The comparison made it clear that the original optics outperforms the one lent by BRUKER in all aspects. Based on these results one can conclude that the optics cannot be the cause for the suboptimal performance of the diffractometer. Hence, the optics was once again changed to restore the status quo.

1.2.4 Exchange of alloy

With the Montel optics being ruled out as a possible tool to separate Sn from In K_α radiation the only option left to get rid of the characteristic tin radiation without attenuation was to exclude tin from the anode material. If it is not even generated in the first place, it cannot contaminate the X-ray beam. While this seems obvious, exchanging the anode material is not straightforward. A new tin-free but still indium and gallium based alloy needs to have a melting point below room temperature and must remain liquid in a pressure range from 1 to 200 bar. It must also possess

fitting rheological parameters to be compatible with the alloy cyclisation system and to form a jet with laminar flow reliably once ejected in the vacuum chamber of the X-ray source. After discussion with the manufacturers of the diffractometer and arguing for the necessity of a tin-free anode, a potential substitute was sourced and EXCILLUM AB started testing the stability of the MetalJet source under operation with the new alloy. After those tests went successful, the original ExAlloy I1 was exchanged for ExAlloy I3 (65 % Ga, 25 % In). To avoid contamination with leftovers from the old alloy, the alloy pump as well as the low-pressure bellow and the high-pressure tubing were replaced. After the system was restarted and aligned, data on a set of crystals were collected (details discussed in chapter 1.3). The results indeed showed improved quality compared to previously collected data. With this not only the previous indications that Sn K_α radiation poses a problem were confirmed, but also the so far best performance of the diffractometer was achieved.

1.2.5 120 kV upgrade preparations

All the measures described in the previous chapters addressed the problems of spectral purity and alignment of the X-ray beam path. With these approaches, the usable fraction of the full emission spectrum of the source was optimised. Another way to further increase the intensity of the X-ray beam would be to increase the overall raw intensity of the source. This can be done by raising either the electron emission current or the acceleration voltage. In both cases, more energy per time would be deposited on the anode. While the emission current is limited by the cathode, the acceleration voltage can in fact be increased. Apart from the 70 kV generator installed in the discussed setup, the manufacturer also offers a 160 kV generator, which was purchased as well. Of course, the increase in acceleration voltage poses a radiation protection problem. It cannot be assumed that the present radiation shielding would be sufficient when the full emission spectrum becomes more intense and additional bremsstrahlung above 70 keV of energy is emitted. As efficient radiation shielding becomes more difficult at higher energies, this has to be considered before a new acceleration voltage is chosen. From theoretical simulations performed at EXCILLUM AB it is expected that the intensity of the In K_α line should increase by a factor of about 1.5 at 120 kV compared to 70 kV accelerating voltage. At 160 kV, another increase of 20 % to 50 % could be possible; however, shielding the 160 keV bremsstrahlung would require lead shielding

more than ten times thicker than for 120 keV radiation. Therefore, operation at only 120 kV was envisaged even when a 160 kV generator would be installed.

To prepare for this change, new radiation shielding of the source was necessary. For this purpose, an estimate of the minimum needed absorber thickness had to be made. Lead was chosen as the absorber material as it has a high atomic number and therefore high absorption coefficient and can easily be shaped due to its high ductility. The toxicity of lead can be tolerated in this case as the final radiation shielding will have no exposed surfaces of lead that could accidently be touched. Only when a disassembly of the source for maintenance is necessary, the lead becomes exposed. The health risk from a high-energy radiation leak would therefore be higher than from the lead. Figure 1-9 shows the mass attenuation coefficient μ/ρ of lead as a function of photon energy. In gamma spectroscopy it is more commonly used than the linear absorption coefficient μ solely for practical reasons, therefore more tabulated values are accessible.[82]

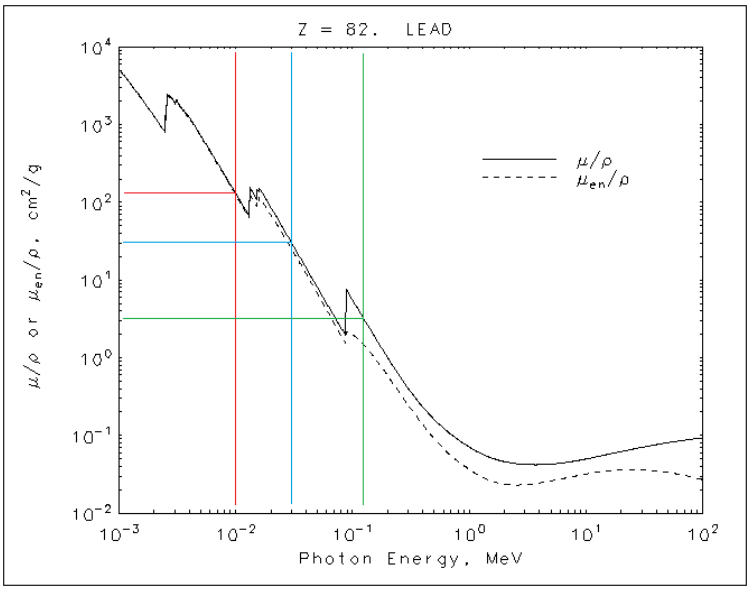

Figure 1-9: Mass attenuation coefficient as a function of photon energy plotted for the element lead. Red line: 10 keV. Blue line: 30 keV. Green line: 120 keV. Adapted from reference.[82]

The exponential decrease of the intensity due to absorption can be described by the Lambert-Beer law (equation (1-2)). If the mass attenuation coefficient instead of the linear absorption coefficient is used, the absorber thickness has to be multiplied by the density of the material giving the area density ϱd of the material. The source intensity I_0 is unknown but only the relative decrease of it is of interest, so that I_{rel} can easily be calculated according to equation (1-3).

$$I = I_0 \cdot e^{-\mu d} = I_0 \cdot e^{-\frac{\mu}{\varrho} \cdot \varrho d} \tag{1-2}$$

$$I_{rel} = \frac{I}{I_0} = e^{-\frac{\mu}{\varrho} \cdot \varrho d} \tag{1-3}$$

Attenuation factors I_{rel} were calculated for lead thicknesses of 2 mm, 2.5 mm and 3 mm. The most reasonable results were obtained for 2.5 mm of lead and are listed in Table 1-4. By far the most intense radiation emitted from the source are the characteristic K_α lines. At 457 W (160 kV, 2.857 mA) electron beam power, their intensities are on the order of 10^{11} to 10^{12}.[58] The calculated attenuation factors for these wavelengths are therefore more than sufficient for the discussed source running at 428.5 W (120 kV, 3.571 mA). Due to the conservation of energy, the energy of the bremsstrahlung cannot be higher than the kinetic energy of the electron (equation (1-4)). Therefore, a maximum energy or frequency and hence a minimum wavelength for the bremsstrahlung spectrum exists (equation (1-5)).

Table 1-4: Calculated attenuation factors I_{rel} for different photon energies for 2.5 mm lead shielding. ϱ (Pb) = 11.35 g/cm³.

	Ga Kα	**In Kα**	**bremsstrahlung**
estimated energy [keV]	10	30	120
μ/ϱ **(Pb) [cm²/g]**[82]	130.6	30.32	3.1
I_{rel}	$1.2 \cdot 10^{-161}$	$4.3 \cdot 10^{-38}$	$1.5 \cdot 10^{-4}$

$$U \cdot e = h \cdot \nu \tag{1-4}$$

$$\nu_{max} = \frac{U \cdot e}{h} \quad \text{or} \quad \lambda_{min} = \frac{h \cdot c}{U \cdot e} \tag{1-5}$$

The intensity distribution of the bremsstrahlung is described by Kramers' law[86] given in equation (1-6). It shows that the amount of energy emitted in a certain wavelength range increases with the wavelength. This is due to the fact that it is much more likely for an electron to emit several low-energy photons in successive collisions than to emit its total energy at once. The calculated attenuation factor for the high-energy limit is therefore sufficient.

$$dE(\lambda) = const \cdot \left(\frac{\lambda}{\lambda_{min}} - 1 \right) \frac{1}{\lambda^3} d\lambda \tag{1-6}$$

Based on these calculations a new source housing was constructed with the aid of the faculty's mechanical workshop. A 1 mm thickness stainless steel corpus was made according to the dimensions of the original housing and the insides were layered with 2.5 mm of lead sheets. The only weak spot that cannot be covered in this was the front of the source, where the cathode and several electrical wires are placed. From personal communication with other users of MetalJet sources running at 160 kV acceleration voltage, it became known that especially the slots for the various cables are prone to radiation leaks. The most elegant way to resolve this issue would be to attach a lead labyrinth for the cables to run through while a straight beam path would be blocked. With the source being very sensitive to dislocation, adding weight seemed to be disadvantageous though. Instead, an aluminium frame was placed around the source to which plates of stainless steel and lead can be easily attached if needed. This ensures easy access to the radiation source, e.g., for maintenance purposes when the power of the radiation source can be reduced and the shielding can be taken off. Additionally, the diffractometer was placed on 4 mm of lead to make sure no radiation can exit the system downwards. This is a necessary precaution, because the pumpbox, which is cycling the alloy and controlling the operating parameters connected to the anode, is placed directly below the source so that no sensible radiation shielding can be realised within the diffractometer.
On a final note, it should be pointed out that conservative estimates were made. Then energy of the characteristic radiation was assumed to be higher than it actually is. In addition, absorption due to the steel and parts of the source was not taken into account. Consequently, the net absorption of the radiation shielding will be even higher than discussed.

1.3 Comparison of a gallium-indium MetalJet and a silver IμS X-ray source for routine SC-XRD experiments

1.3.1 Setup of comparison

The MetalJet source offers higher intensity and, if the characteristic radiation of indium is used, also a shorter wavelength than common lab-scale X-ray sources for single crystal diffraction experiments. While more sophisticated techniques such as experimental charge density determinations or high-pressure experiments benefit from this, it was also of interest how the MetalJet X-ray source would compete in a routine data collection compared to a conventional

solid anode X-ray source. Because the X-ray sources could not be changed easily one for the other within one diffractometer, two complete setups needed to be compared to each other.

The MetalJet X-ray source (model D2) from EXCILLUM AB was integrated in a BRUKER D8 Venture safety enclosure together with a four-circle kappa goniometer, a Photon II detector from BRUKER and Montel multilayer optics from INCOATEC. ExAlloy I3 (75 % Ga, 25 % In) was used for the anode at a default pressure of 190 bar. The source was equipped with a 70 kV high voltage generator delivering 200 W of electron beam power. Prior to collection of comparison data, the whole setup was aligned according to the optimised procedures discussed in chapter 1.2.

The second diffractometer used for the comparison had a silver IμS 2 microfocus X-ray source from INCOATEC and was integrated in a BRUKER D8 Quest safety enclosure together with a three-circle goniometer, an APEX II CCD detector from BRUKER with increased phosphor thickness for higher photon efficiency and Montel multilayer optics from INCOATEC. The source was equipped with a 50 kV high voltage generator delivering 30 W of electron beam power.

For the comparison, a set of four crystals was chosen. As no radiation damage was to be expected the same crystals were used for all measurements. Due their lower absorbance, X-rays of shorter wavelength are especially suited for experiments with compounds, which contain heavy atoms. The set of crystals should therefore contain compounds of high density. Because they have already successfully been used in a different comparative study,[87] single crystals of scandium cobalt carbide (Sc_3CoC_4, space group *Immm*), sodium tungstate dihydrate ($Na_2WO_4 \cdot 2H_2O$, space group *Pbca*) and scandium platinum silicide ($Sc_2Pt_9Si_3$, space group *C2/c*) were used. Additionally, a single crystal of [2,2]paracyclophane ($C_{16}H_{16}$, space group $P4_2/mnm$) was also included in the comparison. Although it is not especially suited for the used wavelengths, a plethora of datasets for this compound were already collected on different setups.

Details on the chosen crystals are listed in Table 1-5. The linear absorption coefficients were calculated by SHELXL[88] based on the used wavelength and the chemical composition of each crystal. To be able to directly compare to what extend absorption would occur for the different crystals the value μr was calculated using an effective radius r. Previous work[87] showed that best results are obtained, if r is biased towards the smallest crystal dimension. Therefore, when calculating r as half of the mean value of all crystal dimensions, the shortest crystal dimension was given a weighting factor of five. In case of the scandium cobalt carbide the longest dimension was not included in the calculation. Due to the needle like shape of the crystal it had to be mounted on the goniometer in a way that its largest dimension was more or less aligned with the phi axis. Otherwise, the crystal would reach into the nitrogen stream used for cooling causing

most probably icing and crystal movement during the measurement. With a crystal aligned like this, it is impossible for the crystal to be irradiated along its longest dimensions, because of the goniometer head blocking the X-ray beam. Hence, this dimension does not contribute significantly to the effective radius of the crystal. The comparison of the μr values shows that lower absorption effects can indeed be expected if characteristic indium radiation is used in SC-XRD experiments. The advantage is of course most pronounced for structures with heavier atoms.

Table 1-5: Sizes and absorption properties of the crystals chosen for the collection of comparison datasets.

	crystal size [mm]	r [mm]	μ (Ag K_α) [mm^{-1}]	μ (In K_α) [mm^{-1}]	μr (Ag K_α)	μr (In K_α)
Sc_3CoC_4	1.002×0.058×0.026	0.016	5.03	3.91	0.0788	0.0626
$Sc_2Pt_9Si_3$	0.100×0.058×0.040	0.026	81.2	64.3	2.11	1.67
$Na_2WO_4 \cdot 2H_2O$	0.173×0.122×0.097	0.06	10.17	8.06	0.61	0.48
$C_{16}H_{16}$	0.342×0.234×0.228	0.123	0.047	0.043	0.0057	0.0053

1.3.2 Data collection and analysis

The diffractometers to be compared differed in practically all components. Only the crystals were identical in both setups. The aim of the comparison was therefore not to evaluate the performance of the MetalJet X-ray source itself, as it would be impossible to decouple it from all other diffractometer components, but to assess the performance of the whole diffractometer compared to well established equipment for in-house X-ray diffraction experiments. For the sake of conciseness, only the respective X-ray wavelength (Ag K_α or In K_α) will be mentioned for both setups, however, always referring to the entire diffractometer and not just the X-ray source.

Since the used goniometers had different geometries and the detectors had differently sized active areas, the application of identical measurement strategies was of no benefit. Any fixed strategy would have ultimately favoured one of the two devices over the other. Instead, measurement strategies for all crystals were generated on each diffractometer individually using the strategy optimisation tool included in the APEX 3 software suite. In this way, crystals could also be transferred between diffractometers easily without the need to conserve their orientation. All

datasets obtained with the MetalJet X-ray source were collected with 40µm Pd attenuation. While palladium would not have been necessary after the anode material was exchanged for the tin free ExAlloy I3, attenuation was still needed to suppress characteristic gallium radiation. Using palladium, however, kept the comparability to most datasets collected prior.

The data were integrated with SAINT.[83] Integration was performed with different resolution limits up to the highest resolution achieved in the experiments. From here on the reduced data were treated as individual datasets of different resolutions and scaled with SADABS.[87] After space group determination with XPREP[89] the data quality can already be assessed by means of R_{merge}. The R_{merge} factor is an indicator which relates the intensity deviations of equivalent reflections to the sum of measured intensities and therefore describes the internal consistency of a dataset (see equation (1-7)). Hence the lower the value of R_{merge}, the better the quality of the data ought to be.

$$R_{merge} = \frac{\sum_{hkl} \sum_{j=1}^{n} \left| I_j(hkl) - \langle I(hkl) \rangle \right|}{\sum_{hkl} \sum_{j=1}^{n} I_j(hkl)} \qquad (1\text{-}7)$$

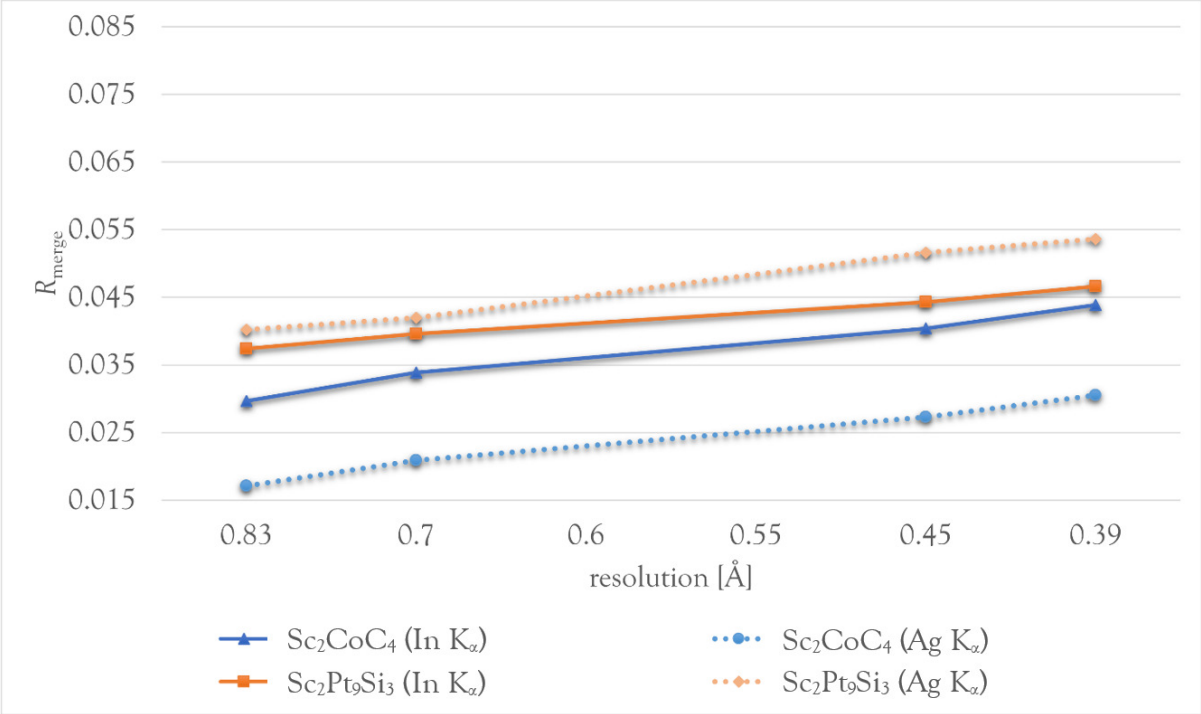

Figure 1-10: Values of R_{merge} obtained for crystals of Sc_2CoC_4 and $Sc_2Pt_9Si_3$. Plotted values correspond to the merging R factors of all data up to the respective resolutions.

In Figure 1-10 the obtained R_{merge} values for integrated data collected on crystals of Sc_2CoC_4 and $Sc_2Pt_9Si_3$ are plotted. While the R_{merge} factor is consistently lower for Sc_2CoC_4 data collected with silver radiation than for data collected with the MetalJet source, the situation is opposite in the case of the scandium platinum silicide. There, data from indium radiation gives a lower R_{merge} value and with increasing resolution the gap between both datasets also increases.

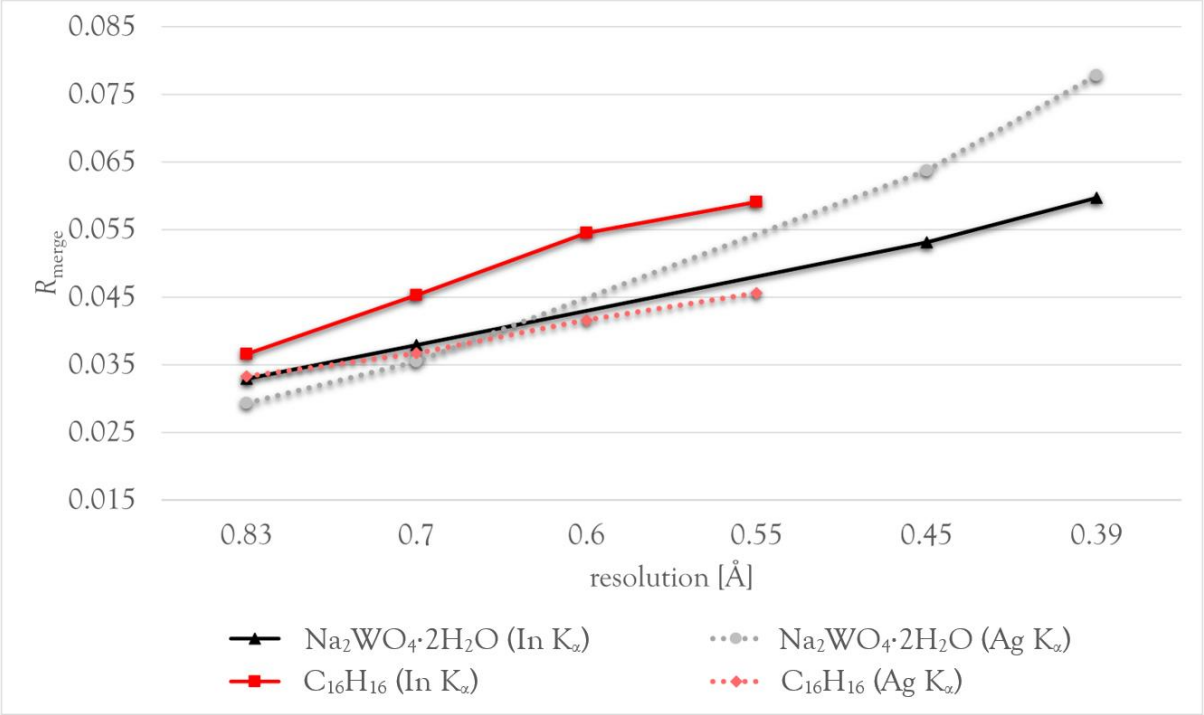

Figure 1-11: Values of R_{merge} obtained for crystals of $Na_2WO_4{\cdot}2H_2O$ and $C_{16}H_{16}$. Plotted values correspond to the merging *R* factors of all data up to the respective resolutions.

The remaining two compounds gave a similarly confusing picture (see Figure 1-11). The [2,2]paracyclophane data show higher R_{merge} factors for the MetalJet experiment at all resolutions. The difference to the silver radiation comparison data becomes bigger with increasing resolution. In the case of the sodium tungstate dihydrate silver radiation yields better quality data up to a resolution of 0.7 Å beyond which the MetalJet diffractometer appears to generate the superior data in terms of merging *R* factors.

The evaluation of the quality of the data obtained so far on the basis of R_{merge} values remains without a clear result concerning the superiority of one of the two diffractometer setups. However, it gives reason to have a closer look at the data and to see if an explanation for the observed outcome can be found.

One important aspect to consider is how the used detectors deal with overexposed frames. The APEX II CCD detector reads out the frame after each exposure time set in the measurement strategy. If an overexposure is detected, the goniometer will drive back to its starting position at the beginning of the exposure time and the frame is recollected with an attenuated and hence less intense X-ray beam. The obtained data are then scaled to the initial intensity. While this works for standard SC-XRD experiments, the scaled data often does not fulfil the necessary quality criteria for experimental charge density studies. The Photon II detector on the other hand collects frames in a shutterless mode. The crystal stays exposed to X-rays while the goniometer moves continuously. The information on diffracted intensities is read out at a frequency of 70 Hz and frames of a certain exposure time are reconstructed from these readouts. In case of an overexposure, it is not possible to retake the frame due to the continues goniometer movement during the experiment. Instead, a so-called fast scan is appended to every experiment in which frames are collected with the shortest possible exposure time while the crystal is rotated 360° around the phi axis. Any reflection, which could not be recorded during the main experiment due to overexposure, will then be substituted by data taken from the fast scan after appropriate scaling. However, experience has shown, that fast scan data severely lacks quality. This can become a problem if the number of independent reflections is low. Unfortunately, this is the case with Sc_3CoC_4 and [2,2]paracyclophane. With these compounds the fractions of overexposed reflections with respect to the number of independent reflections up to a resolution of 0.83 Å amount to 1.75 % and 4.62 %, respectively. This corresponds to the most inner resolution shells being completely overexposed and therefore only poorly determined. The lower R_{merge} values for the data collected with silver radiation and the APEX II CCD detector on both compounds can hence be expected to at least be partially due to a lack of dynamic range with the Photon II detector.

A second aspect, which needs to be addressed is the multiplicity (or redundancy) of the collected data. Due to the larger active area of the Photon II (10×14 cm^2) compared to the APEX II detector (7.5×7.5 cm^2) more reflections can be detected at any given 2θ position. Because of this, inevitably individual reflections will be collected more often and therefore the redundancy of the data will be higher. However, it is known that the R_{merge} factor increases with the multiplicity of the data.[90] Therefore, the redundancy-independent merging R factor R_{rim} has been proposed[91] as shown in equation (1-8). R_{rim} is based on R_{merge} but takes into account a correction for the number n that any reflection hkl has been repeatedly measured.

$$R_{\text{rim}} = \frac{\sum_{hkl} \sqrt{\frac{n}{n-1}} \sum_{j=1}^{n} \left| I_j(hkl) - \langle I(hkl) \rangle \right|}{\sum_{hkl} \sum_{j=1}^{n} I_j(hkl)} \tag{1-8}$$

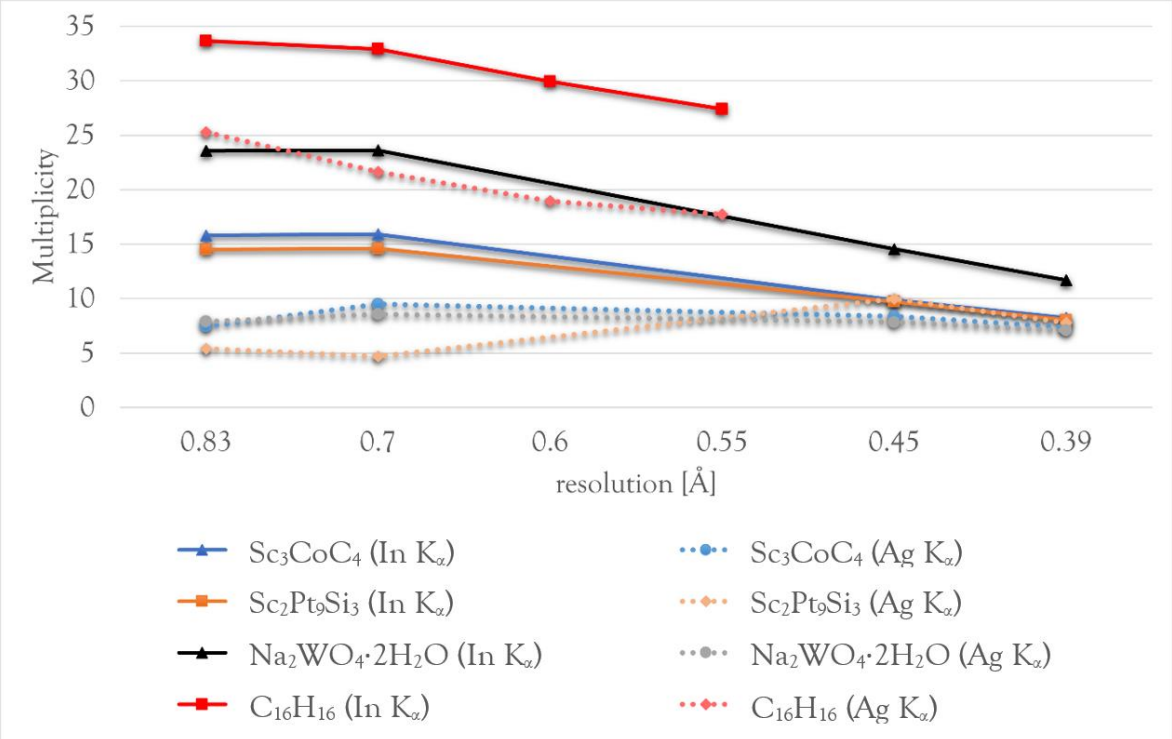

Figure 1-12: Multiplicities of the data of all test crystals. Values correspond to all data up to the respective resolutions.

In Figure 1-12 the multiplicities for all datasets up to the respective resolutions are plotted. In the low resolution regime the multiplicities of data collected with the Photon II detector are higher than for the data collected with the APEX II CCD detector in all cases as expected. While the difference becomes smaller for scandium cobalt carbide and scandium platinum silicide at higher resolution it prevails for the other two compounds. This makes it evident that the R_{merge} factor is not a suitable indicator to compare the present data because of its dependency on multiplicity and hence R_{rim} was investigated. The XPREP[89] software was used to calculate and plot R_{pim} as a function of resolution. The outcome was virtually identical for data on Sc_3CoC_4, $Na_2WO_4{\cdot}2H_2O$ and $C_{16}H_{16}$ from both diffractometers. Only in the case of $Sc_2Pt_9Si_3$ a slight difference was observed. Figure 1-13 shows a superposition of both plots of R_{pim} as generated by XPREP. In the high-resolution regime, the data collected on the Photon II detector has R_{pim} factors around two to three percent lower than the APEX II CCD data.

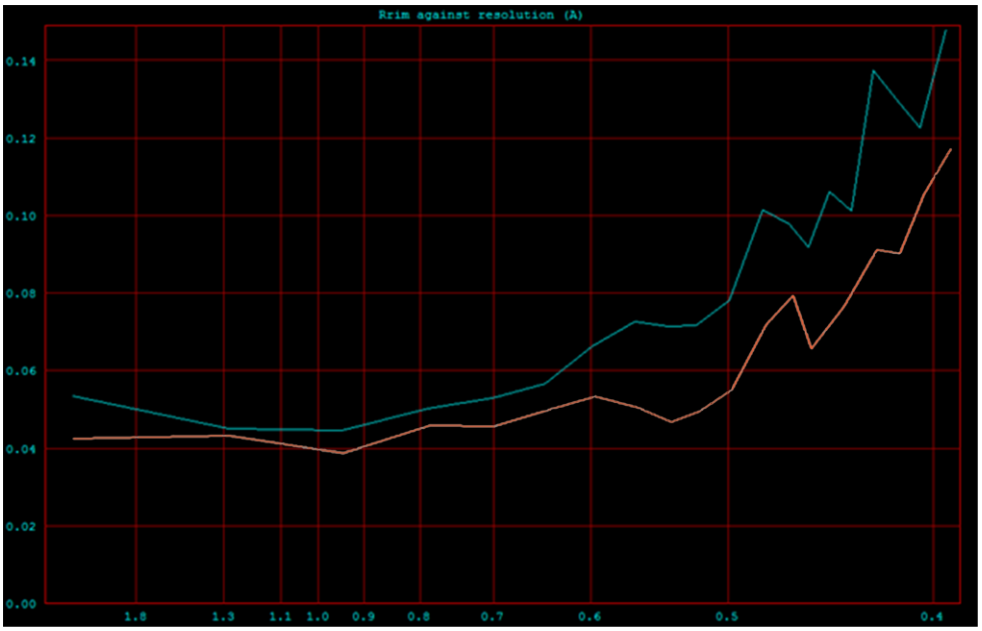

Figure 1-13: R_{rim} for data collected on a crystal of $Sc_2Pt_9Si_3$ plotted as a function of resolution. Turquoise: Data collected with silver IμS 2 X-ray source and APEX II CCD detector. Orange: Data collected with MetalJet X-ray source and Photon II detector.

Apart from *R* factors also the intensity *I* or more precisely the intensity to noise ratio I/σ can be a good indicator to judge the quality of diffraction data. The value of I/σ should be as high as possible so that individual reflections are determined with best possible precision. The level of noise is dependent on a multitude of factors like detector electronics, shutter jitter, goniometer irreproducibility or scattered background radiation and therefore cannot be compared between different diffractometers directly. However, if it is assumed that both diffractometers used in this work are set up so that for each the level of noise is reasonably low, as an approximation its influence on the mean intensity to noise ration can be neglected. Additionally, the detected intensity depends on the photon efficiency of the detector at the respective photon energy. While the exact photon efficiencies of the detectors are not known, the manufacturer claims unrivalled high efficiency for the Photon II detector at In K_α wavelength.[92] The APEX II CCD detector on the other hand uses an X-ray phosphor with increased thickness to compensate for lower efficiency at higher energies. This still does not allow to compare both detectors, but at least it can be assumed that the photon efficiency of the respective detector should not be the major determinant of the observed $\langle I/\sigma \rangle$ values with both diffractometers. Hence it can be expected that the difference in X-ray source intensity should be reflected in the intensities of measured diffraction peaks for each of the test crystals.

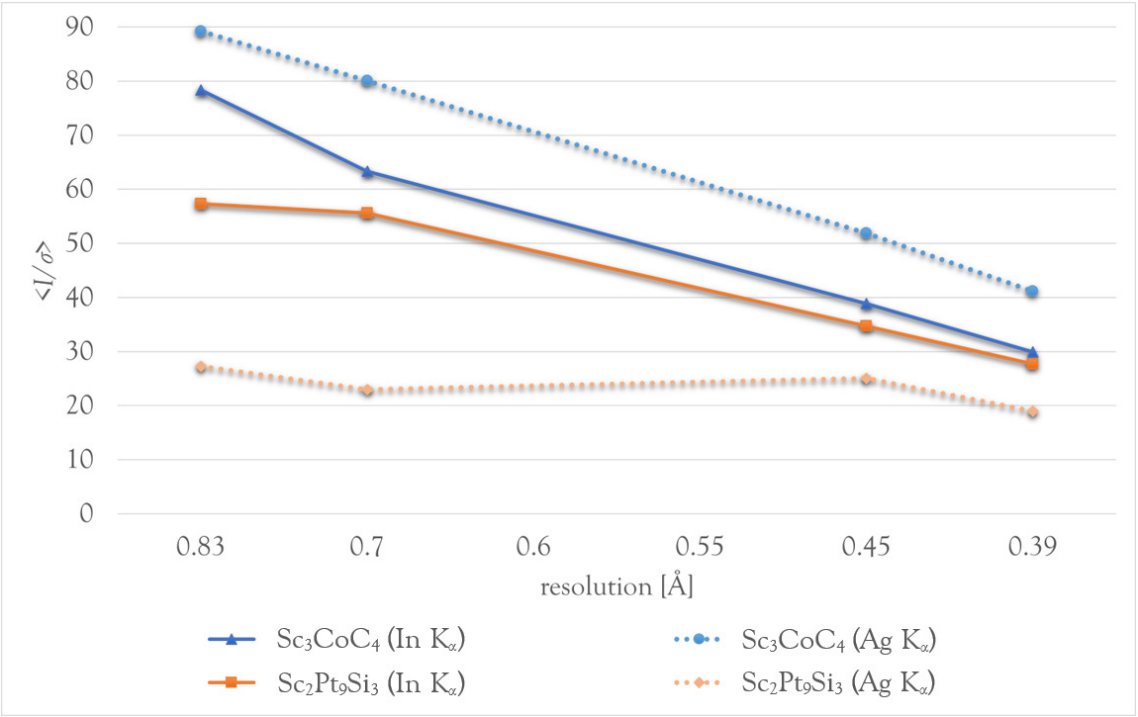

Figure 1-14: Values of <*I*/*σ*> obtained for crystals of Sc_3CoC_4 and $Sc_2Pt_9Si_3$. Plotted values correspond to the mean value of all data up to the respective resolutions.

For the crystal of scandium platinum silicide the expected outcome is observed as shown in Figure 1-14. A significantly higher intensity to noise ratio can be obtained, if the MetalJet X-ray source is used. The sample of scandium cobalt carbide gave the inverse result. Although this seems to be contradiction to the assumption made before, it is most probably caused by the high percentage of overexposed reflections discussed previously. Replacing those reflections, which would contribute high intensities, with low intensity data from a fast scan naturally results in lower <*I*/*σ*> values. Figure 1-15 shows the mean intensity to noise ratio for the remaining two samples. In both cases the values are higher for data collected with the MetalJet X-Ray source. For [2,2]paracyclophane the difference between both datasets is smaller than in all other cases reflecting the fact that this light atom structure shows least interaction with the X-ray radiation as also indicated by the μr values given in Table 1-1.

Although not connected to data quality, another difference that can be observed is the speed of the measurements.

Table 1-6 lists the measurement rates for the highest resolution dataset of each crystal. The values are calculated as the ratio between the number of all collected reflections and the sum of exposure times. These values are overestimates because times for goniometer movements between measurements are not taken into account. Additionally, for data collected on the APEX II CCD

detector also dead time for the read out after each exposure needs to be included to get the real measurement time. Even without this correction, measurement rates are two to four times higher for the MetalJet diffractometer. As discussed before this is most probably due to the larger active area of the Photon II detector and not a feature of the MetalJets high X-ray intensity.

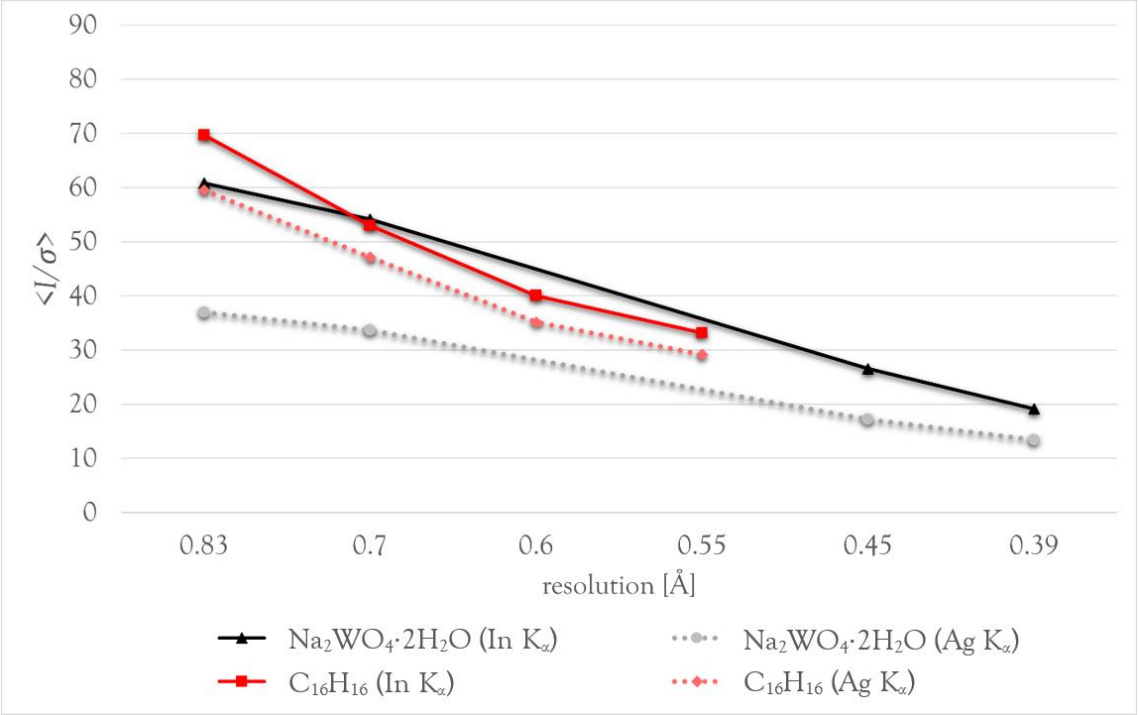

Figure 1-15: Values of $\langle I/\sigma \rangle$ obtained for crystals of $Na_2WO_4 \cdot 2H_2O$ and $C_{16}H_{16}$. Plotted values correspond to the mean value of all data up to the respective resolutions.

Table 1-6: Mean measurement rates for data collection up to a resolution of 0.39 Å or 0.55 Å in the case of $C_{16}H_{16}$.

	Sc_3CoC_4		$Sc_2Pt_9Si_3$		$Na_2WO_4 \cdot 2H_2O$		$C_{16}H_{16}$	
diffractometer	Ag K_α	In K_α	Ag K_α	In K_α	Ag K_α	In K_α	Ag K_α	In K_α
measurement rate [reflections/sec]	0.49	1.08	0.13	0.59	2.99	6.79	0.33	0.90

On a last note, also the completeness of the datasets should be mentioned as it is an important indicator of data quality. For all crystals and over all resolutions data with a completeness higher than 99 % were collected. In most cases even a completeness of 100 % could be reached, if overexposed reflections were replaced by fast scan data.

1.3.3 Independent atom model refinement

In the previous chapter the quality of raw data was discussed in detail. The best data, however, might not be worth much, if it cannot be put to good use. Therefore structure solution was performed on all datasets using direct methods in SHELXT.[93] Independent atom model (IAM) refinement was done with SHELXL[88] in the graphical user interface ShelXle.[94] In the case of sodium tungstate dihydrate, restraints for bond distances and angels of the oxygen-hydrogen bonds were used. Hydrogen atoms in the [2,2]paracyclophane structure were refined using a riding model. Apart from these, no other restraints or constraints were employed in the IAM refinement of any of the structural models. Identical models were refined against data of different resolutions for each of the test crystals. In Table 1-7 selected criteria are listed, which are commonly used to judge the quality of a refined model. Results are given for the maximum resolution achieved and the minimum resolution required for publication of a standard small molecule structure. All results are listed in appendix 5.1.

A good model should describe the experimental data as accurately as possible. Typically, this accuracy is expressed in terms of the differences between the observed structure factors F_{obs} obtained from the experimental data and the calculated structure factors F_{calc} derived from the model. One way to represent the result of the minimisation of these differences during the refinement is the *R*1 factor (see equation (1-9)). A second commonly used indicator is the w*R*2 factor (equation (1-10)), which weights contributions according to the magnitude of the structure factors. The weighting scheme used for the refinement with SHELXL is given in equation (1-11).

$$R1 = \frac{\sum_{hkl}\left||F_{obs}|-|F_{calc}|\right|}{\sum_{hkl}|F_{obs}|} \tag{1-9}$$

$$wR2 = \sqrt{\frac{\sum_{hkl}\left[w\left(F_{obs}^2-F_{calc}^2\right)^2\right]}{\sum_{hkl}\left[w\left(F_{obs}^2\right)^2\right]}} \tag{1-10}$$

$$w^{-1} = \sigma^2\left(F_{obs}^2\right)+(a\cdot P)^2+b\cdot P \text{ with } P = \frac{1}{3}\max\left(0, F_{obs}^2\right)+\frac{2}{3}F_{calc}^2 \tag{1-11}$$

Table 1-7: Selected quality criteria of the final models for lowest and highest resolution data of each test crystal. $\Delta\varrho$ denotes residual electron density.

	resolution [Å]	setup	$R1$ ($I>2\sigma$) [%]	w$R2$ (all data) [%]	$\Delta\varrho$ [eÅ^{-3}]
Sc_3CoC_4	0.83	Ag K_α	1.52	3.97	0.755
		In K_α	1.39	3.29	1.084
	0.39	Ag K_α	1.69	3.66	2.178
		In K_α	1.91	4.69	2.361
$Sc_2Pt_9Si_3$	0.83	Ag K_α	1.52	3.39	2.704
		In K_α	1.34	3.19	2.901
	0.39	Ag K_α	2.93	5.78	13.38
		In K_α	2.30	4.69	14.413
$Na_2WO_4{\cdot}2H_2O$	0.83	Ag K_α	1.14	2.41	0.957
		In K_α	0.81	1.78	0.720
	0.39	Ag K_α	2.94	5.78	5.542
		In K_α	1.78	3.10	4.149
$C_{16}H_{16}$	0.83	Ag K_α	4.10	10.93	0.416
		In K_α	3.96	10.58	0.367
	0.55	Ag K_α	5.00	15.50	0.966
		In K_α	4.59	14.77	0.823

For all metal compounds the R values are low and the w$R2$ factors adopt values of roughly $2{\cdot}R1$ as one would expect. In case of the [2,2]paracyclophane, the R values are significantly higher owing to the lack of heavy atoms in the structure, which would interact more strongly with the characteristic indium or silver radiation. Except for the scandium cobalt carbide, the MetalJet diffractometer data yielded lower R factors. Taking into account that data from identical crystals was refined against identical models, this suggests that the SC-XRD experiments conducted with the MetalJet diffractometer resulted in data of better quality. The fact that this is not true for the crystal of Sc_3CoC_4 is again most likely caused by the substandard quality data taken from fast scans to compensate for overexposures.

Inspecting the values of the residual density $\Delta\varrho$, a more complicated picture arises. Low residuals are a sign of good agreement between the model and the experimental data. High residuals on

the other hand can be either a sign of an insufficient model, caused for example by unnoticed disorder or incorrect atom type assignment, or of data affected by systematic errors like absorption, extinction or problems related to the experimental setup. Because identical models were refined against data from the same crystals, again, differences must result from the data and can therefore be used to compare the performance of the diffractometers relative to each other. For the data at 0.83 Å resolution lower values of residual density were obtained for crystals of $Na_2WO_4 \cdot 2H_2O$ and $C_{16}H_{16}$ with the MetalJet system than with the silver source diffractometer. This is in line with the observations made for the *R* factors. In the cases of the other two compounds the outcome was reversed and lower residual densities resulted from the data collected with the silver source diffractometer. While for scandium cobalt carbide this is most probably connected to the issue of overexposure discussed before, for the crystal of $Sc_2Pt_9Si_3$ this is somewhat surprising. The lower residual density suggests the Ag K_α dataset to be the better one whereas the *R* factors drew the opposite image. It should be noted that the values of residual density for this compound were significantly higher than for all other crystals. For the high-resolution data the residual densities are much higher compared to the obtained values at 0.83 Å. This is expected because with high-resolution data contributions of aspherical valence electron density become more pronounced, which cannot be described adequately by an IAM refinement modeling only spherical electron density distributions. Apart from this, the outcome regarding the performance of the diffractometers remains the same also at higher resolution.

1.3.4 Results of comparison

Two diffractometers were meant to be compared on the basis of a set of four test crystals. Unfortunately, the combination of a low number of independent reflections and unavoidable overexposures rendered the crystal of Sc_3CoC_4 unfit for the comparison. Data collected on the MetalJet diffractometer had systematically lower quality due to these circumstances and Sc_3CoC_4 will therefore be excluded from the comparison.

The quality of the data itself can most straightforward be assessed by the merging *R* factor R_{merge}. However, the values of R_{merge} gave an inconclusive picture regarding the question which diffractometer collected the better data. Owing to the larger active area of the Photon II detector, the data collected with the MetalJet system showed higher multiplicities in all cases, even up to a factor of four compared to the silver IμS 2 system. Because it is known that R_{merge} increases with

increasing multiplicity of the data and because a correlation between multiplicity and R_{merge} could be found in the data collected for this comparison, the redundancy-independent merging *R* factor R_{rim} was analysed instead. Values of R_{rim} were virtually identical for data on $Na_2WO_4 \cdot 2H_2O$ and $C_{16}H_{16}$ from both diffractometers. Only for $Sc_2Pt_9Si_3$ a slightly lower value of R_{rim} was observed for data collected with the MetalJet diffractometer.

Another option to assess data quality is the signal to noise ratio, which in this case is given by the intensity of a reflection relative to the background. Mean values $\langle I/\sigma \rangle$ were compared under the assumption that setup specific contributions to the noise level like detector electronics or scattered background radiation are not affecting the signal to noise ratio in a major way so that for a given crystal it will mainly depend on the intensity of the X-ray source. Consequently, $\langle I/\sigma \rangle$ values for all three crystals were higher for data collected with the more intense MetalJet source as expected. However, it must be pointed out that this cannot solely be attributed to the X-ray source. The assumption that noise levels are of comparable influence regarding $\langle I/\sigma \rangle$ reflects the idea that both diffractometers are adjusted as precisely as possible to provide a fair basis for comparing them as a whole. It most certainly does not mean, that noise levels themselves are comparable. The Photon II detector has the advantage that a non-destructive readout of the frame is possible. Therefore, it can be read out multiple times effectively lowering the noise, which in turn of course increases $\langle I/\sigma \rangle$. Hence, the superior $\langle I/\sigma \rangle$ values have to be attributed to the whole diffractometer rather than just the X-ray source.

To also evaluate the impact of the diffractometers on final structural models the structures were solved and IAM refinements were performed. For each compound an identical model was refined against data from both diffractometers and all resolutions. Except for bond distances and angles involving hydrogen atoms no restraints or constraints were used in the refinements. In all cases lower *R*1 and w*R*2 factors were obtained for models refined against data collected on the MetalJet diffractometer. Although the differences were of the order of only few tenths of a percent, this nevertheless corresponds to the same trend found for $\langle I/\sigma \rangle$ values. For the refined models also the residual densities were analysed. They were lower for MetalJet data in the cases of sodium tungstate dihydrate and [2,2]paracyclophane. For the crystal of scandium platinum silicide, on the other hand, lower residuals were obtained with the data collected on the silver source diffractometer. This result was somewhat surprising as it is the only one that does not align with all other quality indicators. However, the residual densities for $Sc_2Pt_9Si_3$ were around 2 $eÅ^{-3}$ higher than in the other compounds, indicating that this might be connected to an issue specific to $Sc_2Pt_9Si_3$.

Another observation that was made during the comparison was that the rate at which frames are collected on the MetalJet diffractometer is at least two to three times faster than on the silver source system. This is primarily due to the detector and its electronics being able to retrieve the measured data faster. This of course is in no way connected to data quality.

In summary, with exception of the residual density in $Sc_2Pt_9Si_3$, all indicators of data quality and the quality of the refined models suggested that both diffractometers performed equivalently or if not that the MetalJet system was superior. In the latter case, however, the differences in performance were small and mostly due to the detector or at least the combination of detector and X-ray source. It must also be pointed out that the silver source diffractometer used for this comparison is a well-established system but also not up to date. A third generation of INCOATEC microfocus sources (IμS 3) is already available as well as the so called IμS diamond, which features a metal anode layered on a diamond body to make use of its high thermal conductivity allowing for higher electron beam power. In the same vein the APEX II CCD belongs to an old series of detectors and would be exchanged for a detector of the Photon series in any new BRUKER diffractometer. With this in mind it can therefore be argued that the advantage of the MetalJet X-ray source using characteristic indium radiation compared to a solid anode electron impact X-ray source for standard SC-XRD experiments is highly questionable. The higher costs and higher demand for maintenance of the MetalJet source are hardly justified, since within the scope of this work only minute added value to the experimental results could be observed, which can be expected to become insignificant when compared to a state-of-the-art solid anode electron impact X-ray source.

However, this does not mean that the MetalJet In K_α X-ray source is of no use. Rather, its two unique features among lab-scale X-ray sources, namely the high brilliance and the short wavelength, are not of greater benefit for a regular SC-XRD experiment. Only for very small and weakly diffracting crystals, which otherwise would necessitate long exposure times, the MetalJet source might outperform regular solid anode X-ray sources. Its real advantage is expected for more advanced experiments and other techniques apart from diffraction such as X-ray imaging. The short wavelength allows for a higher theoretical achievable resolution important to experimental charge density determination. High-pressure diffraction experiments with diamond anvil cells would also benefit greatly as the number of observable reflections will increase compared to characteristic silver or molybdenum radiation.

1.4 Summary and outlook

A new diffractometer was installed at the University of Göttingen in 2017. It contained a MetalJet X-ray source, which generates X-rays upon impact of electrons on a liquid metal anode. As anode material, ExAlloy I1 (68.5 % Ga, 21.5 % In, 10 % Sn) was used. The aim was to perform so far unprecedented SC-XRD experiments with In K_α radiation.

Over the course of two years, numerous diffraction experiments were performed to stepwise improve the setup of the MetalJet system and to compare it to established diffractometers. Because the X-ray source also generated Ga K_α radiation, aluminium attenuation was needed. As a first step, experiments with ylide crystals were used to experimentally determine the optimal thickness of aluminium needed to attenuate the Ga K_α radiation sufficiently by means of a twin refinement of reflection of both In and Ga K_α radiation and minimising the fractional contribution of the latter. The determined optimal thickness differed from the attenuation suggested by the manufacturer and was corrected accordingly. After that, it became obvious that spectral contamination with Sn K_α radiation posed a problem. Hence, appropriate attenuation for characteristic tin radiation was sought after. Palladium being the only element to show the necessary absorption properties was used as attenuator and optimisation of the attenuator thickness was attempted by monitoring cell parameters of the ylide test crystal. However, it turned out that complete attenuation of the Sn K_α radiation would also decrease the intensity of the In K_α radiation to an unreasonably low level. Instead, only a palladium thickness for an acceptable compromise between Sn K_α attenuation and In K_α intensity could be determined. It can therefore be said that palladium attenuation cannot be circumvented if high quality data is needed using In K_α radiation from a MetalJet X-ray source with an ExAlloy I1 anode. As a result of these experiments a new alignment procedure was developed to assure that X-ray source and optics are set up in a way that is optimised for In K_α radiation.

To exclude the possibility that the optics performed below expected levels, it was compared to another set of Montel optics from the same manufacturer. Both optics were meticulously aligned and characterised by means of a calibrated pin diode. The results showed that in fact the original optics was superior and current state of the art Montel optics were not able to separate In from Sn K_α radiation.

To anyway get rid of the spectral contamination by Sn K_α radiation and avoid palladium attenuation at the same time, the only option was to prevent generation of Sn K_α radiation altogether. In order to do so a tin-free alloy as new anode material was sourced. The whole alloy

cyclisation system of the diffractometer was exchanged so that ExAlloy I3 (65 % Ga, 25 % In) could be used as anode. SC-XRD experiments indeed showed improved data quality and confirmed the spectral contamination by Sn K_α radiation as the reason for problems observed prior. However, attenuation was still needed because of the Ga K_α radiation.

A high-voltage generator was purchased to increase the electron acceleration voltage in the MetalJet source from 70 kV to 120 kV, thereby also increasing the intensity of the X-ray beam. To ensure safety while working with the diffractometer the necessary radiation shielding with increased source power was calculated. Because the original radiation shielding was not designed for higher intensities and 120 kV bremsstrahlung, a new source housing was built and lined with sheets of lead as absorber material. However, the new generator has not yet been installed.

To compare the performance of the MetalJet diffractometer to a well-established lab-scale diffractometer with a silver IμS 2 microfocus source, a set of four crystals was chosen and SC-XRD experiments were performed on both diffractometers. R_{merge}, R_{rim}, $\langle I/\sigma \rangle$, $R1$, w$R2$ and $\Delta\varrho$ were used as indicators to assess the quality of raw data as well as refinement results over a range of resolutions. These comparison experiments showed that data collected with the MetalJet diffractometer was not or only slightly superior to data collected with the other diffractometer. Differences could mainly be attributed to the Photon II detector used in combination with the MetalJet source. It could therefore be said that for standard SC-XRD experiments the MetalJet X-ray source using characteristic indium radiation had no significant benefit over a diffractometer with a conventional solid-state anode X-ray source. However, it is expected that the MetalJets unique features among lab-scale X-ray sources, namely the high brilliance of the X-ray beam and the short wavelength, will be of great benefit for other applications such as experimental charge density determination, high-pressure crystallography or non-diffraction techniques such as X-ray imaging.

Although high-resolution data was collected, only IAM refinements were within the scope of this work. To be able to adequately assess which advantages the MetalJet source might offer for charge density studies, multipole models would need to be refined against high-resolution data. It would also be interesting to perform diffraction experiments under high-pressure with a diamond anvil cell as the shorter wavelength of the characteristic indium radiation appears highly beneficial for this purpose. Maybe even the combination of high-pressure and high-resolution experiments could be possible in a lab-scale.

To eliminate some uncertainties from the comparison presented in this work as well as for a possible future comparison of charge density determinations, diffractometers should be as similar

as possible. While exchanging the X-ray source within on diffractometer would be ideal but also extremely challenging, using at least identical detectors would be advisable as they of course have huge impact on the collected data.

The need for attenuation is a still unsolved problem as any attenuation will inevitably also decrease the intensity of the In K_α radiation. To circumvent this problem a detector could be used, which is able to discriminate the energy of detected photons. Using a tin-free alloy and a detector with an energy cut off such as the Eiger 2R 1M from DECTRIS would render attenuation unnecessary.

Chapter II:
Ducks in space groups: Contributions to education in crystallography

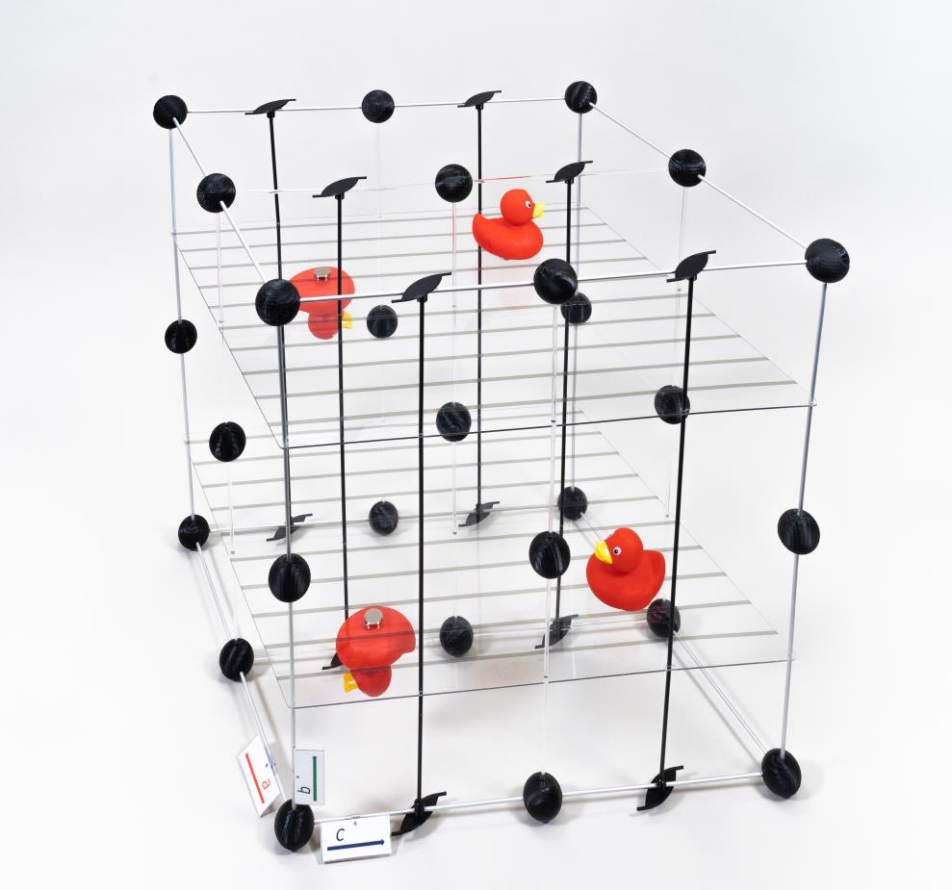

Parts of this chapter have already been published in *Tangible Symmetry Elements and Space Group Models to Guide from Molecular to Solid-State Composition* by Nico Graw, Dietmar Stalke,* *J. Appl. Cryst.* **2021**, *55*, 144-148, DOI: 10.1107/S1600576721012218 and *Ducks in space groups! Students grasping 3D arrangement of symmetry elements with hands-on models* by **Nico Graw**, Dietmar Stalke, *Acta Cryst.* **2021**, *77A*, C765, DOI: 10.1107/S0108767321089327.

2.1 Introduction

Chemistry is a discipline that requires students to have a high degree of three-dimensional imagination.[95] The spatial arrangement of atoms within one molecule determines, if the molecule can have a non-zero dipole moment and therefore influences its properties. Efficacy and effect of drugs are based on molecular recognition processes of three-dimensionally organized molecules and receptors. The way two molecules approach each other during a chemical reaction is naturally governed by their three-dimensional shape, which in turn influences what products are preferably formed or if the reaction can proceed at all due to steric reasons. Moving from individual molecules to bulk material, especially crystalline matter, physical properties such as hardness, refractive indices or thermal expansion are dependent on the proximity of atoms. Structure-property-correlations then allow for predictions and the guided design of new materials.

These few chosen examples underline the immense importance of spatial imagination and symmetry considerations in chemistry and especially in solid-state chemistry and crystallography. Because of this, chemistry students are expected to make symmetry considerations early on in their studies.[96,97] To introduce students to this topic, teaching usually focuses on small molecules,[98–100] for example in the contexts of organic synthesis[101,102] or spectroscopy.[103–105]

However, teaching the introductory courses in general and inorganic chemistry (B.Che.1001 and B.Che.4104) and courses on crystallography (M.Che.1130 and M.Che.1131) at the University of Göttingen over the last few years it has been noticed that precisely these competences of first-year students are increasingly dwindling. Accordingly, more and more time must be spent in undergraduate teaching on introducing them. For these reasons, a project application was submitted to the Lower Saxony Ministry of Science and Culture within the framework of the *Innovation plus* funding programme to address the aforementioned problems. The overall aim of this project was to maintain and train students' abilities for spatial imagination and symmetry recognition. To achieve these goals, the project was divided into three subprojects.

Firstly, a course should be developed, which trains students to translate chemical structures into drawings and *vice versa*. This means not only drawing and interpreting Lewis structures, but also describing topologies such as platonic solids or cyclic systems, which are frequently encountered in chemistry.

Secondly, models of symmetry elements should be designed and built. They should be interactive and tangible so that symmetry operations can be performed by the students themselves.

The third and last subproject was to design and construct models of whole space groups. As with the symmetry elements, these models should be interactive as well. Furthermore, they should aid students in connecting the three-dimensional arrangement of symmetry elements within a unit cell of a given space group to the standardised way space groups are depicted in two dimensions in the International Tables for Crystallography, Section A.[106]

Common to all subprojects is that digital media are not used in teaching. This is based on the evidence that haptic and tactile feedback strengthen the ability of visuospatial thinking.[107,108] Specifically in natural sciences it was shown that tangible 3D models are more effective than virtual 3D models[109] or 2D representations[110,111] in teaching concepts, which require spatiality. Such models often need to be custom-made as they might not be commercially available. For this, 3D printing has become a powerful tool and has already been used for teaching single crystal X-ray diffraction,[112] periodicity and aperiodicity,[113] molecular symmetry,[114] point groups,[115] materials science and engineering[116] and biomolecular self-assembly.[117] Besides the availability of 3D printers, one reason for this is the accessibility of structural data from open access databases and freely available software to convert them into printable files.[118,119]

The application to the *Innovation plus* funding programme was accepted and the results presented in the following chapters were developed within the framework of this project.

2.2 Drawing skill course

Since its introduction in 1916,[120] the Lewis formalism has secured a leading role in representing and communicating chemical structures and processes.[121] For this reason, Lewis structures are commonly introduced to students early on in their studies and many procedures have been described on how Lewis structures can be taught.[122–125] However, from own experience as a student as well as an instructor, drawing, reading and deriving chemical information from a Lewis structure can be a challenging task. This assessment is also widely reflected in the literature.[122,126–130] Additionally, coping with Lewis structures becomes even more difficult if students are confronted with different representations of the same compound, for example, in lecture notes and textbooks. Such a difference could simply result from another choice of perspective. This would be a trivial case and students need to learn how to convert one into the other. Not so trivial, though, are cases in which different depictions at first glance suggest different bonding situations or charge distributions. Typically, this is the case with polyoxoanions and especially the

sulphate ion as shown in Figure 2-1. Representing the sulphate dianion as a Lewis formula adhering to the octet rule results in S-O single bonds and formal charges on all atoms. On the other hand, nobel laureate Linus Pauling advocated an electroneutrality principle that requires minimisation of formal charges resulting in a representation with two S-O double bonds and a negative charge on each of the singly bonded oxygen atoms.[131] He claimed that atoms of heavier elements such as sulphur are not strictly bound by the octet rule due to involvement of d-orbitals in bond formation.[132] Although nowadays there is vast theoretical[133–144] as well as experimental[145] evidence suggesting the S-O bonds to be highly polarised covalent single bonds and not double bonds, depictions with hypervalent sulphur centres are still found in textbooks[146,147] and online resources.[148]

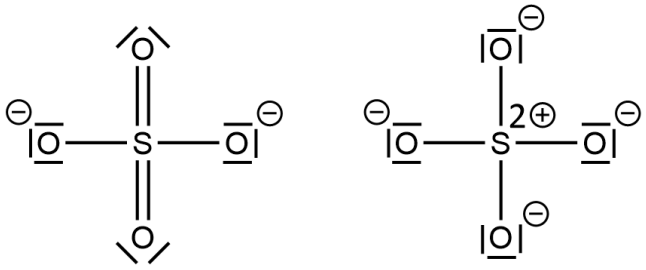

Figure 2-1: Lewis formula of the sulphate ion. Left: hypervalent structure proposed by L. Pauling. Right: accurate depiction of the bonding situation according to the current state of knowledge.[145]

Furthermore, just knowing the toolbox of dots, dashes and arrows available to represent chemical structures[149] does not necessarily mean knowing how to use them correctly. In fact, the latter is not even agreed on within the scientific community. Albeit guidelines and rules are set by the IUPAC,[150] they might not be very practical or representative of a chemist's everyday challenges in writing down structural formulas.[151] Particularly the use of arrows to indicate dative or coordinate bonding has been topic of intense discussions.[152–154]

Apart from Lewis formulas, other forms of representation are also important. Especially in organic chemistry Fischer[155,156] and Newman[157] projections are well established. For transition metal complexes or solid-state inorganic compounds depictions of coordination polyhedra, which do not even need to be electron precise, might be more important.

For these reasons, the project aimed to devise a drawing skill course, which offers guidelines to students on how to draw chemical structures, interconvert different styles of representations and how to interpret them. The outline, implementation and evaluation of this drawing skill course will be discussed in the following chapters.

2.2.1 Presence course

The drawing skill course was planned to be included into the seminars accompanying the lecture on general and inorganic chemistry (B.Che.1001 and B.Che.4104) at the University of Göttingen. Groups of students from all studies related to chemistry, for which this lecture is mandatory, can then be trained in the basics of drawing and interpreting representations of chemical structures. As the basis for this skill course a guideline needed to be developed, which covers IUPAC standards[150,158] and recommendations of the scientific community[151,152] given on the topic as well as the standards present at the faculty of chemistry. As the whole project aimed to use as little digital media as possible, an effort was taken to provide all graphics within the guide as accurate hand drawings. These drawings were not only intended to serve explanatory purposes but also to illustrate to the students how hand-drawn structures should look like.

Starting from the basics of Lewis formulas, it is first explained how dots and dashes represent single and paired electrons. This is followed by the introduction of different kinds of charges, namely ionic charges, partial charges and formal charges. While the first one is trivial in the sense that it is a measurable electric charge carried by an ion, the second one can easily be rationalized by students as a consequence of differences in the electronegativity of bonded atoms. Formal charges, however, can be a conceptual hassle for students. Although the total ionic charge and the sum of formal charges must be identical for any chemical entity, individual formal charges can be void of physical or chemical meaning. They stem from Lewis formulas being electron precise and obeying the octet rule and therefore are purely artificial by nature. Figure 2-2 shows one example from the guide, where the formal charges are in opposition to the qualitative charge distribution one would expect for this molecule due to the electronegativities of the bonding partners.

Based on this, it is shortly discussed how to depict different kinds of bonds including intermolecular interactions and a comment on the use of arrows for donor-acceptor type situations is given.[152–154] This is followed by the introduction of stereochemistry indicators into skeletal formulas using the wedge-and-dash notation and asterisks to denote chirality centres. Additionally, the Newman projection is introduced to train the students' ability to mentally connect different kinds of representations and to interconvert them.

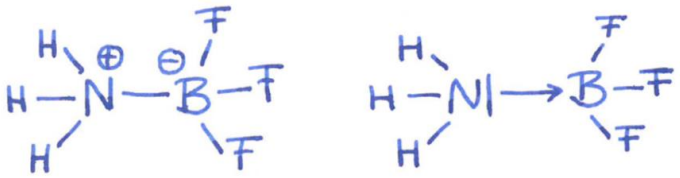

Figure 2-2: Formula of ammonia trifluoroborane adduct. Left: Classic Lewis formula with formal charges. Right: Arrow notation indicating coordinative bonding without the need of formal charges.

Having the basics covered, the guide then moves to cyclic systems. Examples are given for three to eight membered rings. However, the focus is laid on four, five and six membered ones. For these, butterfly, envelope and chair conformations including the arrangement of substituents are discussed in general and with specific examples as shown in Figure 2-3.

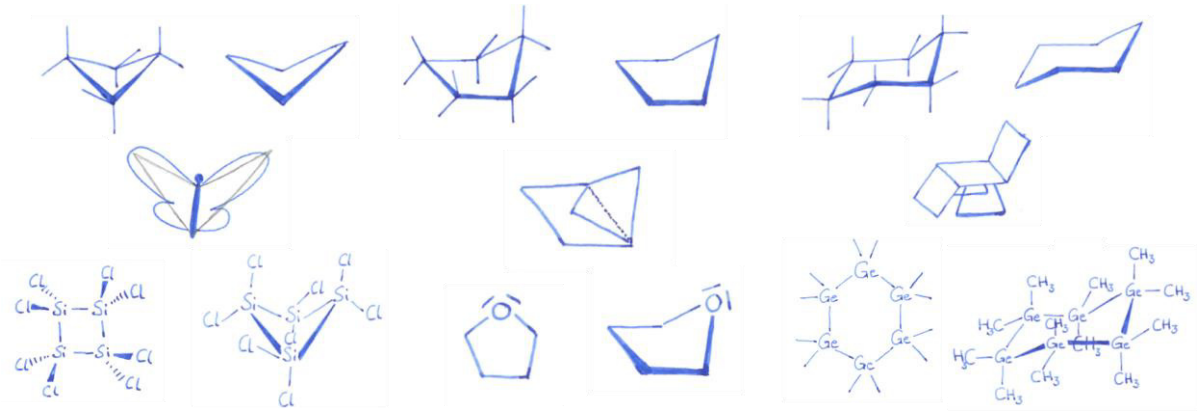

Figure 2-3: Examples of four, five and six membered systems in their respective most common conformation.

A special emphasis is laid on six membered rings adopting the chair conformation, as these are due to high abundance the most relevant ones towards general chemistry education. A very technical description of how to geometrically construct an accurate drawing of a six membered ring in chair conformation[159] was adapted to give more straightforward instructions. At this point, the guide particularly emphasises the importance of being able to convert different forms of representation, in this case chair conformations and skeletal formulas with planar six-membered rings. This is done not only because it trains students' visuospatial thinking, but also because information on chemical reactivity can be deduced from this. E2 reactions in

cyclohexane systems, for example, can only proceed, if the two leaving groups adopt a trans-diaxial position.[147] Arguably, this can easier be assessed from a drawing of the chair conformation.

The guideline then proceeds with aromatic systems. These are by definition planar and can therefore easily be drawn in a plane (provided they are not too large systems). In some cases, however, it might be useful to draw them in a perspective e.g. for molecules like paracyclophanes or to illustrate CH···π interactions as they occur, for example, in solid benzene.[160] While dealing with aromatics, also a short excursus on mesomerism is included. The idea behind the concept of resonance structures is explained and the double-headed arrow is introduced as a descriptor.

To conclude the topic of annular molecules, the students are presented with a collection of chemical structures, which go beyond the structural motifs shown so far. Examples include purely inorganic ring systems such as cyclooctasulphur and related polycations, condensed aromatics, bent molecules like cyclooctatetraene and ice rationalised as an aggregate of six water molecules in a chair conformation like assembly. These are meant to emphasise that more complicated and complex structures can also be understood in terms of smaller subunits and some generalised building principles.

The last part of the guide is dedicated to polyhedra. The tetrahedron, cube, octahedron and icosahedron are introduced as highly symmetric platonic solids and motifs encountered in chemical structures. Subsequently, advice is offered on how to make clear drawings of these polyhedra as shown in Figure 2-4. In the case of the tetrahedron, a distinction is made between the ubiquitous tetrahedral bonding environment, for example with sp^3 hybridised carbon atoms, and genuinely tetrahedral structures such as white phosphorus. Although it is not very common in molecular chemistry, the icosahedron is included because it is a motif that can be found in solid-state compounds. One example that is introduced to the students is the solid-state structure of elemental boron as the α[161] as well as the β[162,163] allotrope can be described in terms of icosahedral B_{12} units.[164]

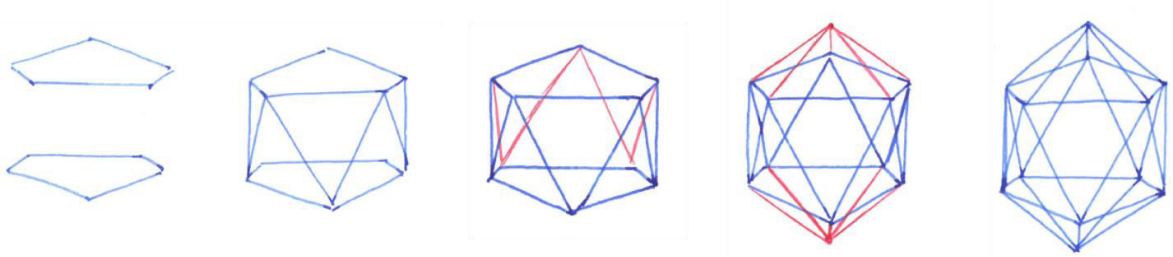

Figure 2-4: Stepwise construction of an icosahedron.

Finally, also the trigonal bipyramid is added to this group of structural archetypes, as it is a very important motif for a lot of group 15 and 16 compounds like phosphorus pentachloride or sulphur tetrachloride and crucial to the discussion of the *Valence Shell Electron Pair Repulsion* (VSEPR) model.[165,166]

In this context, it is also pointed out that structures like the B_{12} icosahedron cannot be interpreted anymore in terms of Lewis formulas the way they were introduced at the beginning. Similarly, molecular compounds with more than four entities (atoms, unpaired electrons or lone pairs) bound to a central atom cannot be depicted by simple lines if one wants to avoid hypervalency. Although the latter case can easily be resolved by using the arrow notation mentioned before, this might lead to unnecessary complexity, if only the overall molecular shape is of interest. For these cases as well as for the B_{12} icosahedron or clusters described by the Wade's rules[167,168] the concept of topological bonds is introduced. A topological bond carries no information on the quality of the interaction, it only indicates that an interaction is present. In this way, chemical connectivities can readily be sketched without having to worry about whether or not the octet rule is violated.

After this guideline on how to properly draw chemical structures had been created, it was handed to the students at the beginning of the 2019/2020 winter term. Students were informed that it is compulsory to study the contents of the guide as they are relevant to the lecture and proper drawings of chemical structures will be expected in the final exam where applicable.

Additionally, new tasks for the seminars were created, further encouraging the students to engage with the subject and to practice drawing chemical structures themselves. This also gave an opportunity to introduce the students to selected research articles asking them to draw featured compounds as, for example, the partially chlorinated carbaborate anion shown in Figure 2-5, which the authors claimed to be the strongest isolable Brønsted acid.[169]

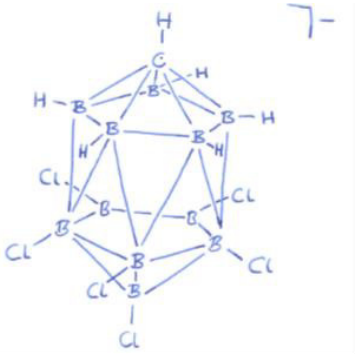

Figure 2-5: Structure of the $CHB_{11}H_5Cl_6^-$ anion.

2.2.2 Digital course

During the 2020/2021 winter term the course was supposed to be repeated. However, due to the SARS-CoV-2 pandemic no teaching in presence was possible. Instead, online tools were used as teaching platforms. Hand drawings can of course be prepared digitally but only if the proper hardware is available. As this cannot be expected to be the case for most students, online teaching undermines the core idea of training students' visuospatial thinking competencies by means of hands-on exercises. Nevertheless, the developed guideline was transformed into an online course for self-study, as the alternative would have been not to offer it at all. In an effort to reduce the students' workload under the circumstances dictated by the pandemic, it was decided not to make the contents of the guideline mandatory for the lecture in the 2020/2021 winter term. Instead, students were repeatedly encouraged to engage with the online guide themselves on a voluntary basis. This posed a problem, however, because the original guide was designed for use in a seminar led by a tutor already familiar with the subject. It therefore focused on presenting accurate hand-drawn structures and offering assistance in creating such drawings. Further explanations and information on chemical context were only given as short comments relying on the tutor to expatiate on in more detail rather than being self-explanatory for the students. To transform the guideline of the original drawing skill course into an online resource suitable for self-study comparable to an inverted classroom model approach,[170] extensive text was added to guide students through the content without a tutor.

The whole course was then embedded within the frame of the lecture on general and inorganic chemistry (B.Che.1001 and B.Che.4104) on the StudIP platform, which is well established at the University of Göttingen. In this way, accessibility of the material by the students is secured.

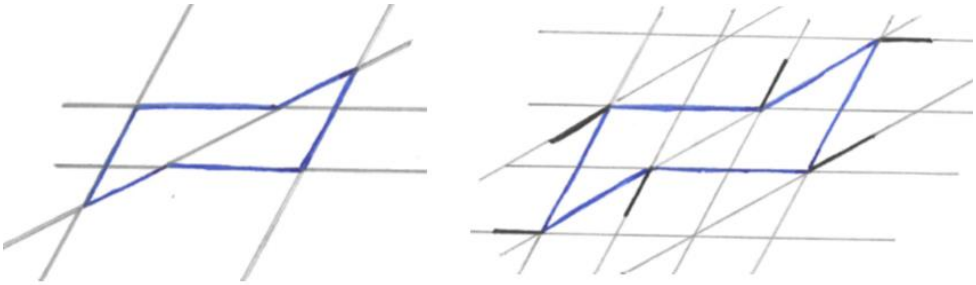

Figure 2-6: Excerpt from the stepwise construction of a six membered ring in chair conformation. Blue: core six membered ring. Black: directionality of bonds to equatorial substituents. Grey: auxiliary lines.

Being anyway reliant on digital media due to the circumstances, it was opportune to make use of the possibilities it offers. For structures, which can be a bit more challenging to draw, such as polyhedra or six membered rings in chair conformation, instead of a series of graphics illustrating the stepwise construction as shown in Figure 2-6, providing a short video emulating a tutor drawing the structure in real time seemed beneficial.

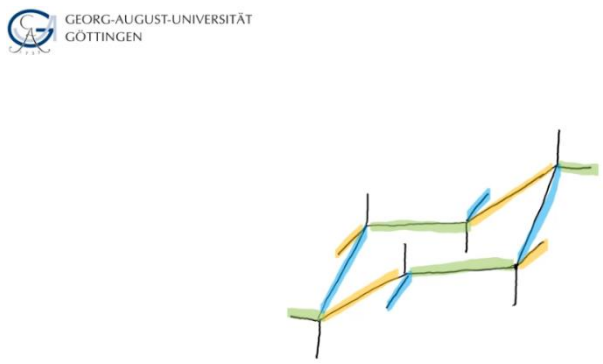

Figure 2-7: Screenshot of a video on how to draw six membered rings in chair conformation. Coloured highlights indicate bonds, which are supposed to be drawn in parallel.

For these reasons, videos were created by screen capturing the process of drawing six membered rings in chair conformation (see Figure 2-7), benzene molecules in different perspectives and tetrahedra as well as octahedra.
After a positive evaluation, which will be discussed in detail in the following chapter, the online course was exported from the lecture and additionally hosted on faculty level as well so that the content is available not only to first year but to all students.

2.2.3 Evaluation

The presence course during the 2019/2020 winter term was meant to be evaluated during the lecture time with the aid of an online questionnaire provided on the *mVote* platform to ensure high participation numbers. However, due to accessibility problems mostly caused by insufficient Wi-Fi coverage in the lecture theatre students were not able to participate equally or complete the questionnaire fully. Therefore, no meaningful results were obtained.
When the course was held for the second time in the following year, it needed to be transformed into an online resource as described in chapter 2.2.2. The lecture on general and inorganic

chemistry was conducted by means of asynchronous online teaching. Therefore, an evaluation during the lecture as planned before was impossible. Instead, students were asked to complete a self-assessment questionnaire embedded in the StudIP course of the lecture to secure accessibility. After an initial assessment was conducted at the beginning of the lecture even before students were given access to the skill course, the survey was repeated at the end of the lecture with an identical questionnaire to see how the results might have changed (the full questionnaire is listed in appendix 5.2.1). Each time, students had one week to complete the questionnaire. Participation of the students was fully anonymous, so that only global differences can be assessed. The questionnaire was provided in German and contained eight questions on self-assessment. For each question students were asked to indicate how much they agree with a given statement on a four-point scale (fully agree, rather agree, rather disagree, fully disagree). The four-point scale was deliberately chosen so that there is no neutral option available, which would allow students to remain indecisive towards the statement. The statements were:

1. I am able to mentally visualise molecules three-dimensionally on the basis of drawings
2. I understand drawings of molecular structures
3. I am able to make drawings of molecular structures myself
4. I am able to interconvert drawings of molecular structures from different perspectives
5. I consider the ability to draw molecular structures to be important for my future professional environment
6. I consider drawings of molecular structures to be important for my future professional environment
7. Drawings of molecular structures are an important tool to communicate with others
8. Drawings of molecular structures contribute to a deeper understanding of chemical concepts

While statements 1 to 4 focus on students' abilities to process representations of chemical structures, the remaining statements address the students' perception of the importance of this ability. These self-assessment questions were followed by three questions on knowledge about platonic solids. Students were asked to pick the correct number of faces of an octahedron, corners of a cube and edges of a tetrahedron out of four possible answers each. The implementation of the survey on the StudIP platform only allowed for analysis of completed surveys. Information on whether participants have discontinued the survey (and if so, at which point) is not available.

The initial survey was completed by 303 participants. Results on the first four statements are shown in Figure 2-8. Statements 1 and 2 evidently show that the majority of students (85.2 % and 85.5 % respectively) see themselves as being able to comprehend drawings of molecular structures already before they started the skill course.

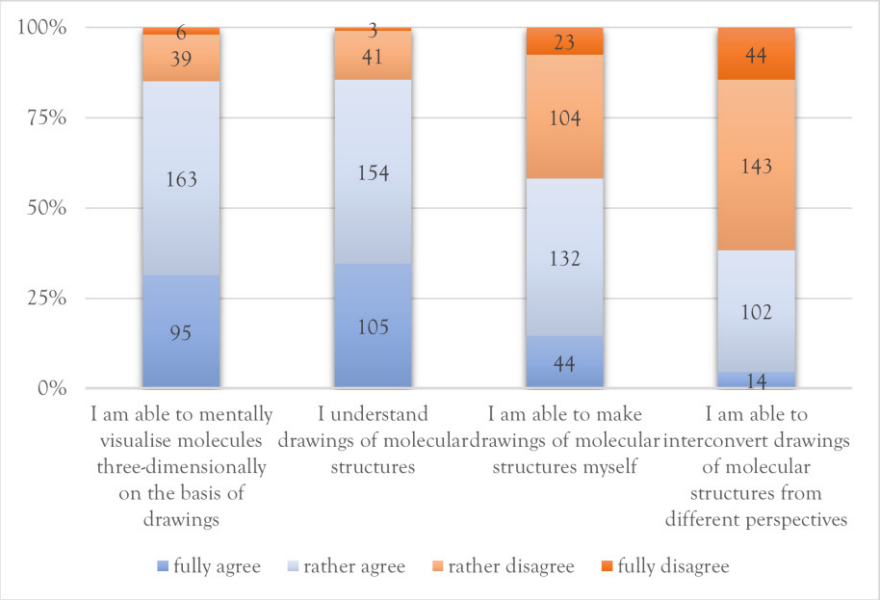

Figure 2-8: Results from introductory self-assessment test on statements 1 to 4.

When it comes to the ability to draw these structures themselves, the percentage of students confident in their skill drops to 58.1 %. Going one step further with the complexity of the task asked for, it is now the majority of students (61.7 %) who disagree with the fourth statement. The results from these first four questions strongly support the preceding assumption, previously based only on teaching experience, that training of drawing skills is necessary. Furthermore, it should be pointed out that 85 % agreement to statements 1 and 2 still leaves 15 % of students, who are not or only slightly able to cope with drawings of molecular structures. With a typical attendance of about 550 students in the lecture on general and inorganic chemistry, this translates to about 80 people, who can follow certain topics only to a limited extent. Though an extensive introduction to the use of structural formulas as part of the lecture itself might not be possible due to a lack of time (and would apparently be redundant for most), this group of students should not be neglected. The drawing skill course being an on-demand resource might be of help in this case as well.

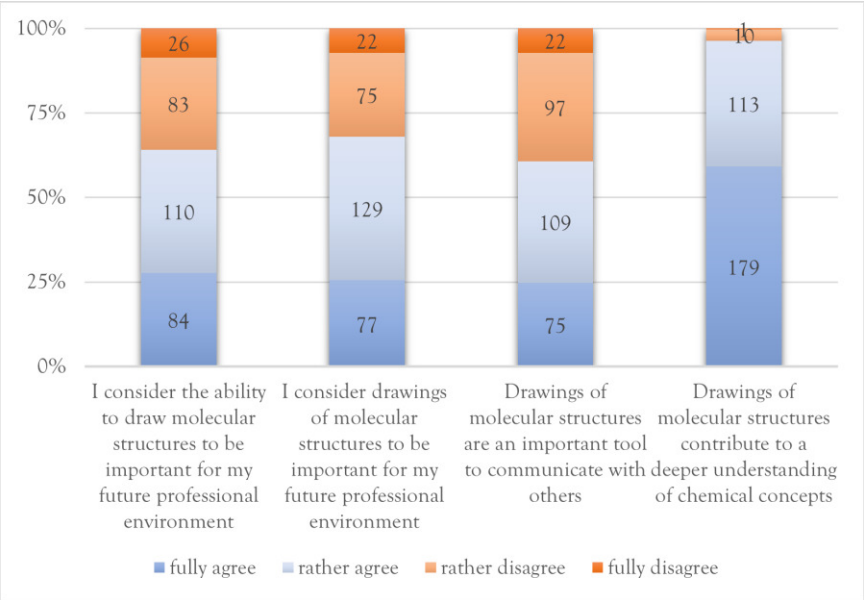

Figure 2-9: Results from introductory self-assessment test on statements 5 to 8.

The agreement to statements 5 to 7 ranges between 60.7 % and 68.0 %, giving an overall consistent picture of how students perceive the importance of being able to deal with structural drawings (see Figure 2-9). One might expect the agreement to be higher as they are attending a chemistry lecture as part of their chosen career path. However, the student body is very diverse in terms of their educational background and the study programmes involved. In the 2020/2021 winter term 30.7% of the attending students were enrolled in chemistry, molecular medicine or biochemistry programmes (including those trained to become high school educators in chemistry), fields where the greatest relevance of structural formulas could be anticipated. 60.3 % were enrolled in biology, biological diversity or geology studies, in which the lecture on general and inorganic chemistry is part of the compulsory curriculum. The remaining 9.0 % belonged to geography, mathematics, physics, social sciences, theology, law, economics, business administration and psychology and have chosen themselves to attend the lecture either as part of the key competency scheme or just out of personal interest. Arguably, drawings of chemical structures will be of less importance to careers in some of these fields. Considering this and the possibly highly vague ideas of ones future professional environment, the agreement on statements 5 to 7 can be rationalised and the actual rate of agreement is of less importance than the consistency of responses to these three statements. Regardless of that, the results on statement 8 show that close to all students (96.4 %) agree to drawings of molecular structures being helpful to understand chemical concepts.

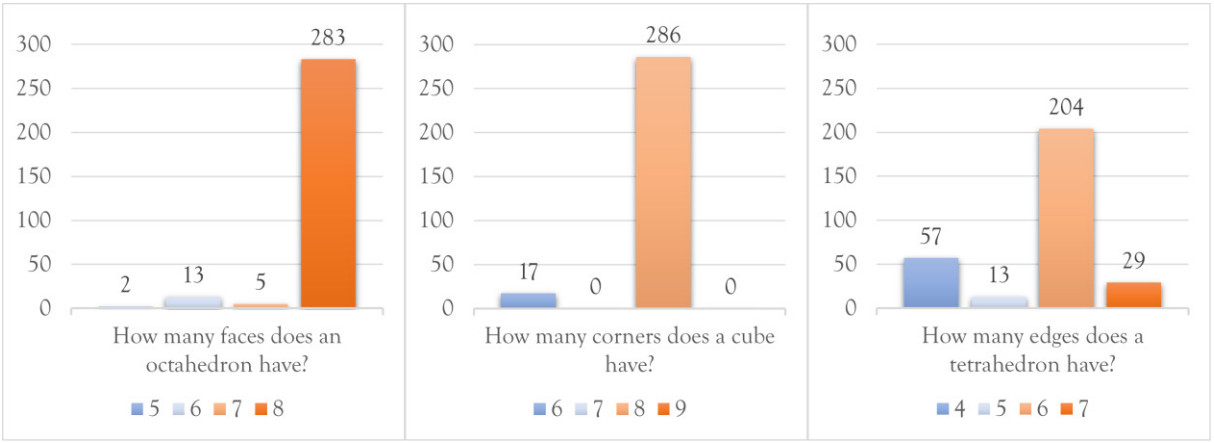

Figure 2-10: Results from introductory questions on knowledge about platonic solids.

To conclude the survey with a set of questions that could be answered unambiguously, knowledge about platonic bodies was tested. The results are shown in Figure 2-10. The highest number of correct answers (286, 94.4 %) was given to the question about the number of corners in a cube followed by the question about the number of faces of an octahedron (283, 93.4 %). Although these numbers are virtually identical, the question about the octahedron shows a greater spread across the wrong answers. This hints at an actual lack of knowledge concerning the octahedron, whereas in the case of the cube, six was the exclusively chosen incorrect answer. Since the number six is commonly associated with cubes due to dice games, this points more towards students not reading the question carefully enough. The third question falls behind with only 204 (67.3 %) correct answers and a wide spread across all wrong answers, again indicating a lack of knowledge about the shape of tetrahedra. Since tetrahedra and octahedra are of particular relevance for chemistry and the description of molecular and solid-state structures as well as coordination compounds, these results also suggest that students could benefit from the outlined skill course. After making the online skill course available to the students, the survey was repeated in the second to last week of the lecture period. Again, students had one week to complete the questionnaire, which contained the exact same questions as before. Additionally, three questions were appended for students to indicate how useful different materials (lecture recordings and slides, seminars, courseware material) were to them with respect to learning to draw and understand chemical structures. Each of these added questions was to be answered on a four-point scale (very helpful, helpful, unhelpful, not helpful at all). Because it was decided that the online skill course is voluntary as mentioned at the beginning of this chapter, a fifth option (I did not use the courseware material) was added to the question about its usefulness.

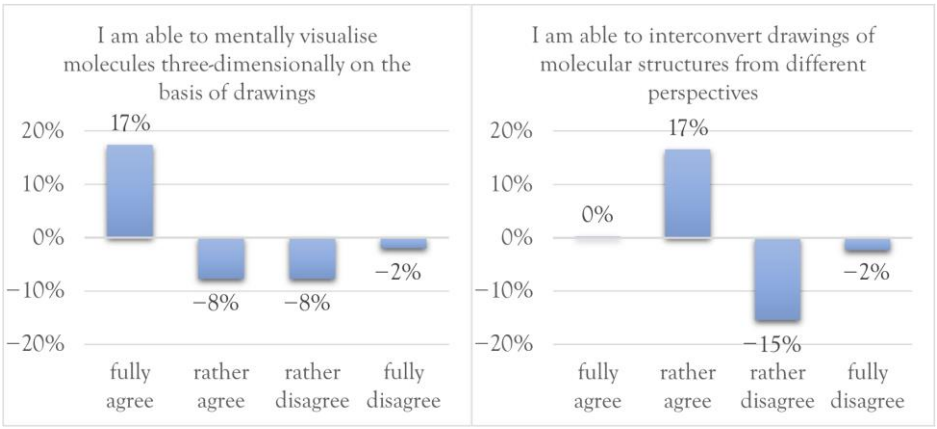

Figure 2-11: Percentage differences in the survey results between the end and the beginning of the lecture on statements 1 (left) and 4 (right).

The second survey was completed by 95 students. This is a drastically reduced number compared to the 303 participants of the introductory survey. Even though the extent of this decline cannot be explained in detail, it is not a surprise. The number of participants should decrease as the number of students who actively participate generally also decreases towards the end of the lecture period. In order to compare the outcomes of both surveys and to see how the students' self-assessment changed after participating in the drawing skill course, the percentage differences for each possible answer were analysed. Figure 2-11 shows exemplary results from statements 1 and 4, while the complete analysis is given in appendix 5.2.2. The results of statements 1 to 4 aiming at students' abilities to process representations of chemical structures are very similar. In all four cases, the percentage of students disagreeing went down. Accordingly, the students' approval of the statements went up, indicating that they improved their (self-perceived) skills by participating in the course.

For statements 5 and 6, both addressing the importance of chemical structures for a future professional environment, the disagreement actually rose, while the importance of structural drawings as a means of communication and teaching is rated higher (see Figure 2-12). These results suggest that students indeed recognise the benefits of such drawings even if they do not consider them as important for their own professional future.

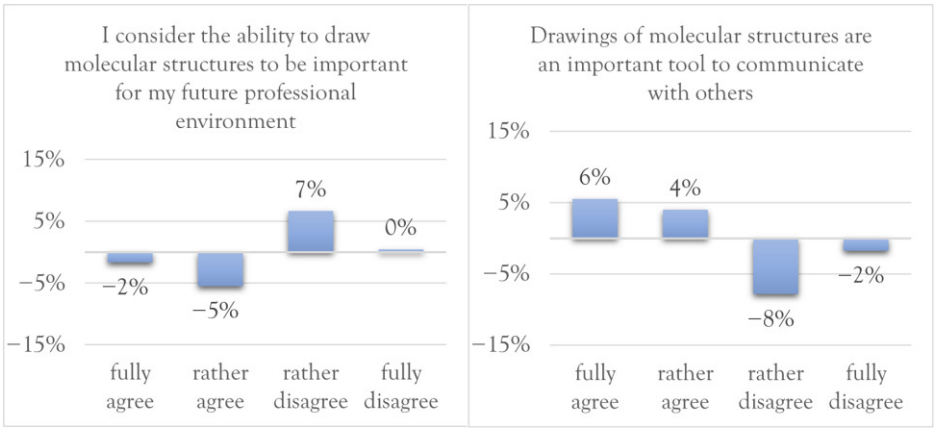

Figure 2-12: Percentage differences in the survey results between the end and the beginning of the lecture on statements 5 (left) and 7 (right).

Regarding the knowledge of platonic solids, there is only a very small improvement (2 %) in the number of correct answers to the question about the number of corners of a cube. However, the percentage of correct answers to this question was already very high during the introductory survey. In the case of the tetrahedron, the mention of the correct answer increased by 14 % while mentions of all incorrect answers decreased. It is somewhat strange, however, that the question about the number of faces in an octahedron was answered incorrectly more often in percentage terms at the end of the lecture. The mention of the correct answer decreased by 7 % and no satisfactory explanation could be found for this.

Regarding the evaluation of different materials available to the students to improve their ability to deal with structural formulas during the lecture period, the majority of students found all of the items asked about either helpful or very helpful (see Figure 2-13). With 69.5 % cumulative percentage the skill course was rated only slightly higher than the lecture slides and recordings (66.3 %). Seminars received the best rating with 72.6 %. It is no surprise that seminars appear to be more helpful to most students as they are interactive and therefore intrinsically more suited to fit to the needs of individual students. It has to be noted though, that while for the lecture materials and the seminars it is true that the remaining students indicated that they had not found them helpful, in the case of the courseware materials, 17 % of the remaining 30.5 % indicated that they had not used the material at all. Taking these students out of the sample results in a cumulative percentage of 83.7 % of students, who used the teaching material and rated it as helpful.

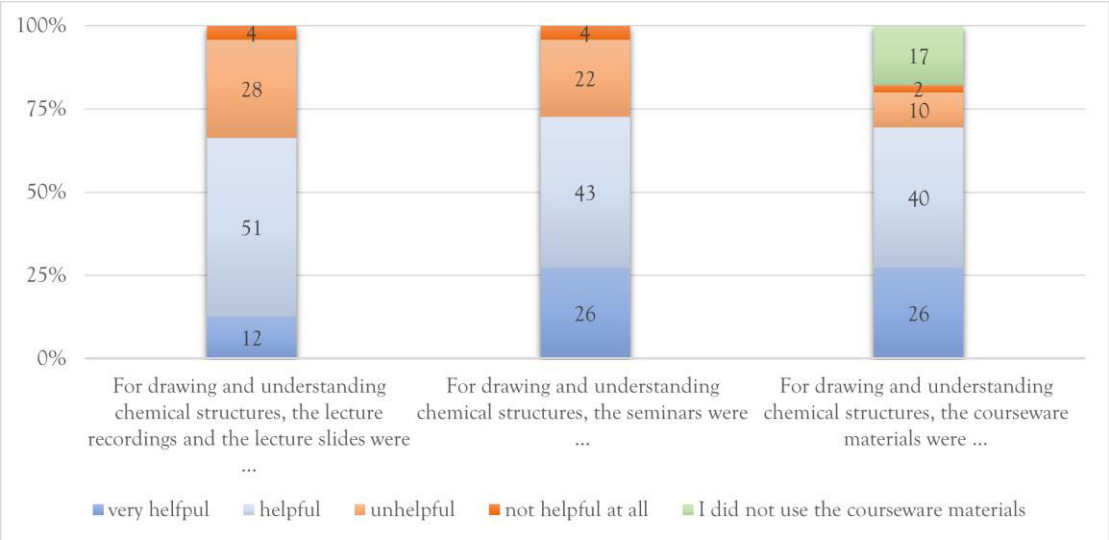

Figure 2-13: Results of the student evaluation of the materials provided to train the ability to process representations of chemical structures.

After completing the questionnaire, students had the possibility to leave feedback on the content of the drawing skill course or to elaborate on why they did not use it. Out of the 95 students who completed the survey, 19 made use of this and left comments. The free text responses were used to generate seven inductive categories, for which the responses were then analysed. These categories are in descending order of the frequency with which they were found [number of mentions]: positive evaluation of the skill course [11], lack of time [5], additional exercises wanted [5], still planning to use it [4], use for exam preparation [3], more details wanted [2], negative evaluation of the skill course [1].

The majority of responses gave positive feedback on the skills course. Those who have not used it yet, gave lack of time and no motivation due to missing self-testing options as reasons. However, most of them also stated that they plan to use it at least as a means of preparing for the exam. Two students asked for the skill course to be more detailed, which kind of contrasts with the fact that others have not had time to work on the course as it is. The sample size is too small though to deduce anything from this. What was mentioned more often, however, was the desire for additional tasks in order to check one's own progress and to provide opportunities to discuss the contents by, for example, integrating them into seminars. This could easily be done as the course was originally designed like that anyway but slimmed down by excluding its exercises from the seminars to reduce the workload. A measure that appears to have been necessary, taking into account the lack of time still mentioned by the students.

As a last indicator, progress statistics were considered. These are automatically generated by the StudIP platform yielding progression rates for all subchapters of the skill course. For comparison, the rates were recorded on 8th of February 2021 and on 13th of January 2022. The first date was chosen at the end of the lecture period, the second about one year later. During this time, progress in all subchapters increased almost constantly by about 5% suggesting that a certain group of students worked on the skill course after the end of the lecture period. While these could be students, who have used the teaching material for the first time to prepare for the exam as indicated by the free text responses, the statistics also show that the last time students accessed the skill course was between 26th of October 2021 and 25th of December 2021 depending on the exact chapter. This indicates that students also use the online resources in the long term.

The validity of the conclusions drawn from this evaluation could be questioned for two major reasons. Firstly, the number of participants differs greatly between the entry and exit surveys. Even if a decrease in the number of participants is reasonable, as already explained, and can even be expected, the composition of the student body changes. Assuming that the results of the surveys are representative, they still represent two different groups of students in terms of their motivation, performance and willingness to learn. It can be assumed that among the participants of the exit survey, those students are proportionally more strongly represented, who already have a higher intrinsic motivation, can cope better with the learning material and perhaps do not need an additional supportive offer such as the skills course. The extent to which the results of the surveys show an improvement in student skills as a result of participation in the course or if it is only due to the omission of the less motivated students from the surveyed group therefore remains questionable. However, it is difficult to include the latter group students in the final survey, as it is hardly possible to motivate someone, who has already decided not to actively participate in the lecture, to participate in a survey. This in itself is evidenced by the survey, as all students would have had the chance to participate if they had wanted to.

Secondly, there is no control group to check the learning effect of students who participate in lectures and seminars but do not have access to the courseware. In principle, the same learning goals could be achievable without the skill course being offered. However, it was not possible to test this due to the time frame required, as it would go beyond the scope of both this thesis and the *Innovation plus* funded project.

Nevertheless, the evaluation over all shows that the skill course was well received by the students and perceived as helpful. Recommendations and measures for improvement could be derived and an online educational resource has been implemented, which, by separating it from the

lecture and making it available at faculty level, can also be of use in the long term and across study cohorts.

2.3 Models of symmetry elements

Regardless of what topic is to be taught, appropriate language is always needed to convey it in a meaningful way. In the case of teaching symmetry to chemistry students based on small molecules as discussed in chapter 2.1, this language is provided by the Schönflies notation. However, it is unfit to describe solid-state structures as it has no means to account for translational symmetry, which is necessary for the description of crystalline matter. Therefore, the Herman-Mauguin notation is used instead. Since students are usually first introduced to Schönflies and only later to Hermann-Mauguin, the need to extend the already learned framework for the description of symmetry with the concept of translation coincides with learning an entirely new notation. Teaching experience shows that students struggle with this, specifically with translational symmetry elements like screw axes and glide planes. There are already electronically supported exercises on symmetry and point groups (for example at symotter.org[171]), but unfortunately they have not proven to be very sustainable for learning, as students might believe they have understood, but later in exercises or exams cannot recall and reproduce this non-persistent knowledge.

In order to remedy this, models of symmetry elements were designed and built to demonstrate the effect of a symmetry operation performed on an object or a set of objects. Having physical models available, students can not only look at the models but also handle them themselves. Through haptics and hand-eye coordination, the mode of action of these symmetry elements is learned in the long term, enters the memory more easily and becomes part of the three-dimensional imagination. Rotary axes and screw axes were chosen as symmetry elements for which models were created. With these two types of symmetry elements, it can readily be demonstrated what difference the presence or absence of a translational component makes.

2.3.1 Axes of rotation

In principle, no dedicated model is needed for the demonstration of pure rotational symmetry. A set of objects that share a common axis of rotation always lies within a plane. If one sets up a

coordinate system with z perpendicular to this plane and thus parallel to the axis of rotation, the description of any rotation can be reduced to a two-dimensional problem, even if the rotation is carried out in three-dimensional space and on three-dimensional objects. Equation (2-1) shows the rotation matrix for a general rotation in three-dimensions.

$$R(a,\beta,\gamma) = \begin{bmatrix} \cos\beta\cos\gamma & \sin a\sin\beta\cos\gamma - \cos a\sin\gamma & \cos a\sin\beta\cos\gamma + \sin a\sin\gamma \\ \cos\beta\sin\gamma & \sin a\sin\beta\sin\gamma + \cos a\cos\gamma & \cos a\sin\beta\sin\gamma - \sin a\cos\gamma \\ -\sin\beta & \sin a\cos\beta & \cos a\cos\beta \end{bmatrix} \qquad (2\text{-}1)$$

Here a, β and γ are the angles of rotation about the axes x, y and z, respectively. If the coordinate system is set up as described, it follows that $a = \beta = 0°$ and thus

$$\cos a = \cos\beta = 1 \qquad \text{and} \qquad \sin a = \sin\beta = 0 \qquad (2\text{-}2)$$

Substituting these conditions into equation (2-1) simplifies the matrix to

$$R_z(\gamma) = \begin{bmatrix} \cos\gamma & -\sin\gamma & 0 \\ \sin\gamma & \cos\gamma & 0 \\ 0 & 0 & 1 \end{bmatrix} \qquad (2\text{-}3)$$

If a point in three-dimensional space represented by a column vector with elements x, y and z is to be rotated around z, the result of this rotation can be obtained by multiplication of the rotation matrix and said vector.

$$\begin{bmatrix} x' \\ y' \\ z' \end{bmatrix} = \begin{bmatrix} \cos\gamma & -\sin\gamma & 0 \\ \sin\gamma & \cos\gamma & 0 \\ 0 & 0 & 1 \end{bmatrix} \begin{bmatrix} x \\ y \\ z \end{bmatrix} = \begin{bmatrix} x\cos\gamma - y\sin\gamma \\ x\sin\gamma + y\cos\gamma \\ z \end{bmatrix} \qquad (2\text{-}4)$$

This shows that $z = z'$ and that the new coordinates x' and y' are independent of z. Hence, the positional change can sufficiently be described in two dimensions. For a practical demonstration of rotational symmetry, it would therefore suffice to arrange any set of objects on a common plane. The condition for rotational symmetry will be met, if all objects are placed evenly spaced at the same distance from a centre point. Depending on the number n of objects, such a setup would represent a rotational axis of n^{th} order. However, presenting a set of objects in this way for example on a table in a lecture hall poses the problem that the audience cannot look at it perpendicular to the plane. This gives only a distorted visual impression, which is contrary to the

aim of promoting better spatial imagination. It therefore has little to no benefit compared to a blackboard drawing. The latter is a truly two-dimensional configuration, though. Formally, there is no axis of rotation but only a centre of rotation about which the rotation is performed (see Figure 2-14). Although it makes no difference to the result in this minimalistic example, differentiating between these and translating between two- and three-dimensional space might be confusing for students later on.

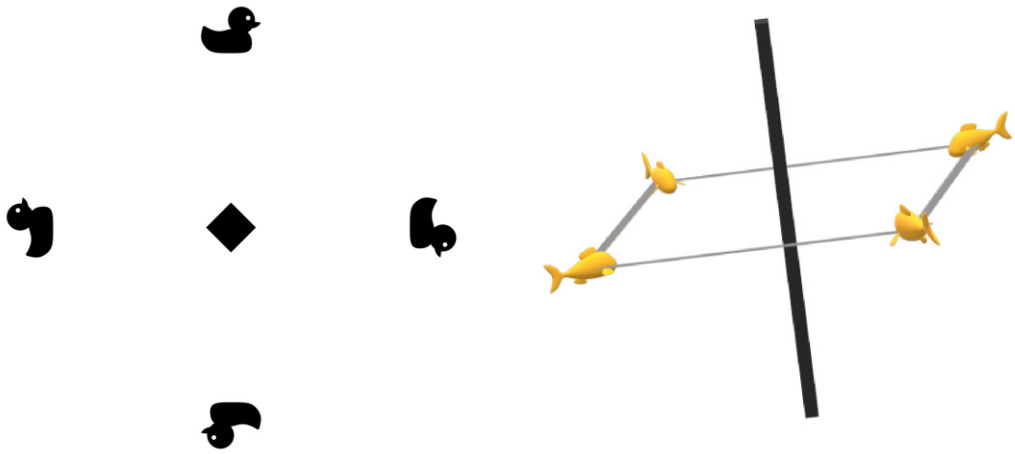

Figure 2-14: Left: Two-dimensional set of ducks around a rotation centre of 4th order. Right: Three-dimensional set of fish around a rotational axis (black) of 4th order. Common plane of fish indicated in grey.

The aim was therefore to construct a model, which allows for the set of objects to be presented in a vertical manner so that the audience could adopt a viewing angle parallel to the rotational axis and at the same time perceive the three-dimensionality. Since the set of objects has to be fixed somewhere, it is self-evident to use the rotational axis itself as an anchor point. This, of course, requires materialising what is physically non-existent. Instead of trying to make this axis as imperceptible as possible, it was actively included in the model design by attaching a front plate to it, which resembles the symbols commonly used to represent rotational axes of different orders. In this way, the students already get introduced to these symbols and can recognize them later when more difficult arrangements of several symmetry elements are discussed. In order to be able to attach objects securely, the front plate needs to be sufficiently thick so that holes can be drilled in the side of the plate. Then the objects only need to be attached to a sturdy metal wire, which can be inserted in those holes and be secured by lock screws. This design allows for easy and quick attachment or detachment of individual components and gives the instructor the freedom to

construct the model step by step and to point out differences between correct and incorrect arrangements.

Figure 2-15: Two kinds of rubber ducks, which were used in this project. The red rubber ducks on the left are achiral, the yellow ones on the right are chiral.

Furthermore, different kinds of objects can be used as long as they are fixed to metal wire of equal diameter. This makes it also possible to demonstrate how the symmetry inherent to the used object might impose restrictions on the symmetry of the whole set up. Within this project rubber ducks were chosen as objects to use, also for the models that will be described in the following chapters. The decision was made in favour of rubber ducks, because they are durable and readily available in a broad variety of shapes and colours. Even chiral and achiral ones can be realised as shown in Figure 2-15.

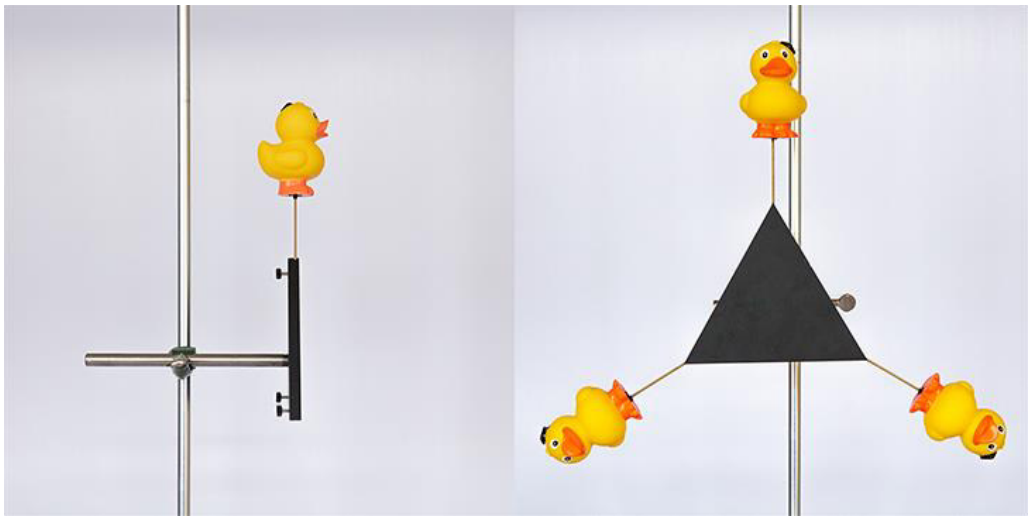

Figure 2-16: Model of a 3-fold rotational axis. Left: Side view of the model revealing lock screws to secure the metal wire of attachable objects. Right: Front view as perceived by the audience.

The models were constructed with the aid of the faculty's mechanical workshop. Front plates were cut from 10 mm thick aluminium sheets to be sturdy but remain lightweight and were

coated black. Holes were drilled in the sides of these plates at angles appropriate to the symmetry to be modelled and fitted with screw locks. A steel rod was attached to the back of each plate allowing for clamping in a standard laboratory stand and thereby also realising the vertical set up of the model (see Figure 2-16). Slight unclamping allows for manual rotation of the model to demonstrate how the configurations of rubber ducks are indistinguishable before and after the symmetry operation is performed if set up correctly.

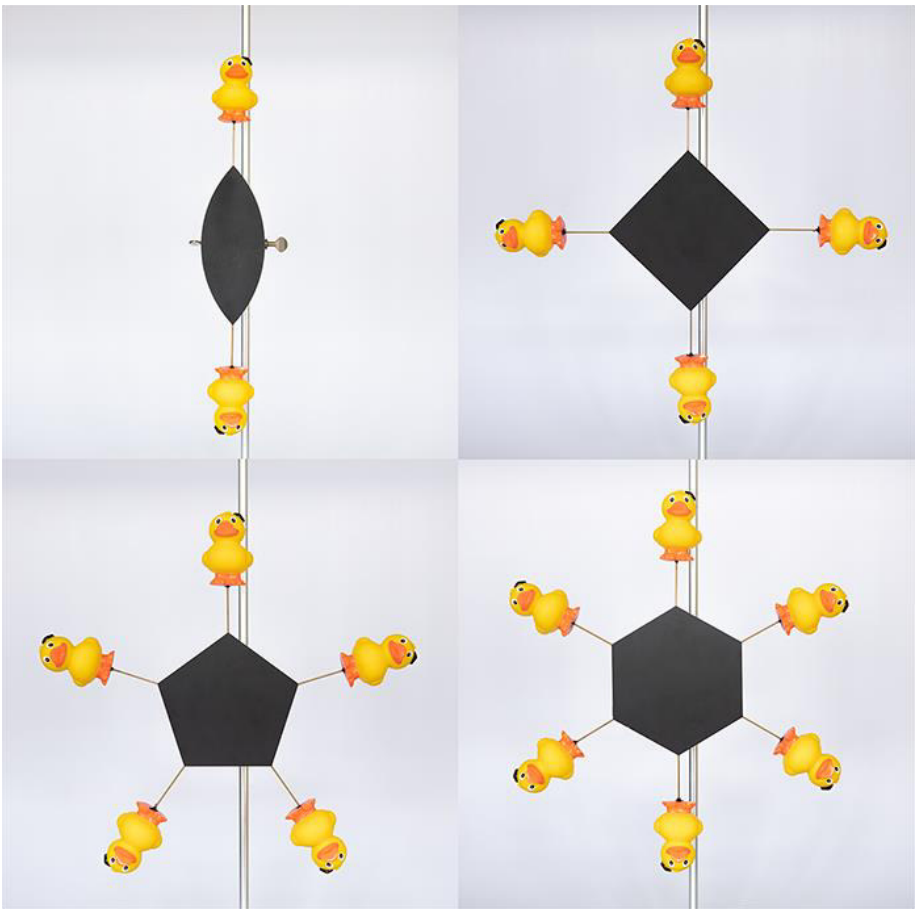

Figure 2-17: Models of 2-, 4-, 5- and 6-fold rotational axes.

Figures 2-16 and 2-17 show all the models of rotational axes built from 2nd to 6th order. Unfortunately, they could only be used once during the lecture on general and inorganic chemistry in presence before online teaching became necessary. Lecture recordings were already prepared before the models were available, so that they were not included in the online materials. However, the models were ready in time for the online lecture on crystallography, for which especially on the topic of symmetry self-learning material was newly prepared. Here, pictures and short videos of the models being rotated could be included.

2.3.2 Screw axes

When moving from rotational axes to screw axis, a model in which the rotational component is performed perpendicular to the direction of view as described in the previous chapter bears no longer an advantage. Screw axes can be understood as the product of the coupling of rotational axes with a translational slide in the direction of these axes. In crystallography, a general screw axis can be denoted as n_m, where n is the order of the rotational component and the subscript m indicates the screw displacement. More precisely, the magnitude of the translational slide is given as the multiple m of the lattice vector. Since the displacement m is only reached after a full rotation of 360°, only a translational slide of the magnitude m/n is carried out for each partial rotation of $360°/n$. For the description of crystalline matter further boundary conditions can be placed. To allow for periodicity, only rotations with $n = 2$, 3, 4 or 6 are possible. As a consequence, m must be smaller than n and an integer. Assuming the axis to be parallel to z so that the rotation is performed about z, the translational slide must be directed along z. It is therefore trivial that, in contrast to pure rotation, the z coordinate of a general point in space can no longer remain unchanged. For a proof, equation (2-3) can be expanded by a translational component T_z to yield the screw axis operation S_z.

$$S_z(\gamma,m,n) = R_z(\gamma)+T_z(m,n) = \begin{bmatrix} \cos\gamma & -\sin\gamma & 0 \\ \sin\gamma & \cos\gamma & 0 \\ 0 & 0 & 1 \end{bmatrix} + \begin{bmatrix} 0 \\ 0 \\ m/n \end{bmatrix} \text{ with } \gamma = \frac{360°}{n} \qquad (2\text{-}5)$$

Applying this operation to a point with the coordinates x, y and z yields

$$\begin{bmatrix} x' \\ y' \\ z' \end{bmatrix} = S_z(\gamma,m,n) \begin{bmatrix} x \\ y \\ z \end{bmatrix} = \begin{bmatrix} x\cos\gamma - y\sin\gamma \\ x\sin\gamma + y\cos\gamma \\ z + m/n \end{bmatrix} \qquad (2\text{-}6)$$

For a screw axis model to emphasise the translation in the direction of the axis, it should be constructed so that the axis is oriented vertically and perpendicular to the viewing direction to ensure that the audience can clearly see the translation. The models were designed based on standard laboratory stands as these fit the just mentioned criteria well and are readily available. To retain the possibility to assemble the model stepwise, a mount was needed to hold the rubber ducks and simultaneously allow for movement along the stand as well as rotation around it. After initial experiments with different kinds of hose clamps, which were supposed to snap onto the

stand but turned out to be either too complicated to construct or too difficult to handle, a new mount was built from scratch. A block of aluminium was fitted with a central hole so it could be slid onto the laboratory stand. Additionally, a locking screw was attached allowing the instructor to fix the block in any position along the stand. With this, the basis of a mount was created, which ensures the freedom of model assembly. To put the rubber ducks in place, a piece of sheet metal was screwed to the aluminium block, on which the ducks or any other objects can be fixed. A set of objects prepared in this way and a laboratory stand at hand, in principle all types of screw axes can be modelled, if the correct number of ducks is arranged in a suitable manner. With certain screw axes (4_2, 6_2, 6_3, 6_4) two or more objects occupy positions at the same height. To be able to accurately model this, special mounts were designed, which have several pieces of sheet metal attached to the same aluminium block (see Figure 2-18). With these, the ducks can be placed at equal height instead of being stacked and displaced by the height of the aluminium blocks.

Figure 2-18: Left: Object mount designed for the screw axis models holding a rubber duck. Right: Special mount for the model of a 6_3 screw axis holding three rubber ducks at equal height and in 120° angles.

It is most straightforward for the height of the laboratory stand to resemble the length of a lattice vector or unit cell edge. To assist the instructor with the placing of the rubber ducks, small markings have been made on the stand to indicate the correct fractions of the total length for each screw axis. To avoid confusion, one laboratory stand for a screw axis model of each order n was prepared. All models were constructed with the aid of the faculty's mechanical workshop and a selection of them is shown in Figure 2-19 (all models are depicted in appendix 5.3).

To unambiguously assign the identity of a screw axis especially in diagrams, a standardised symbolism exists. Because these symbols cannot be included in the models in the same way it was done for the models of rotary axes, a different way was devised to introduce the symbolism to the

students nonetheless. Printouts of all symbols were prepared and fixed to custom mounts, which can be fixed on top of every laboratory stand.

For some screw axes like 3_2 the full screw displacement is a multiple of the respective lattice vector. Retracing the screw mentally necessitates crossing from one unit cell to the next.[172,173] However, all positions must be generated within a cell, otherwise it would not be a unit cell. Due to the periodicity of the crystal lattice, one could simply argue that exiting on one side is equivalent to entering the same unit cell on the opposite site. This line of thought is also a way to grasp the concept of fractional coordinates as soon as students become familiar with those. Nevertheless, modelling the full screw displacement across more than one unit cell might be easier to understand in the beginning. Because the models do not have explicit labelling but only the aforementioned markings on the axis itself, their height might correspond to any multiple of a lattice vector. The number of rubber ducks per axis is anyway variable thanks to the designed mount.

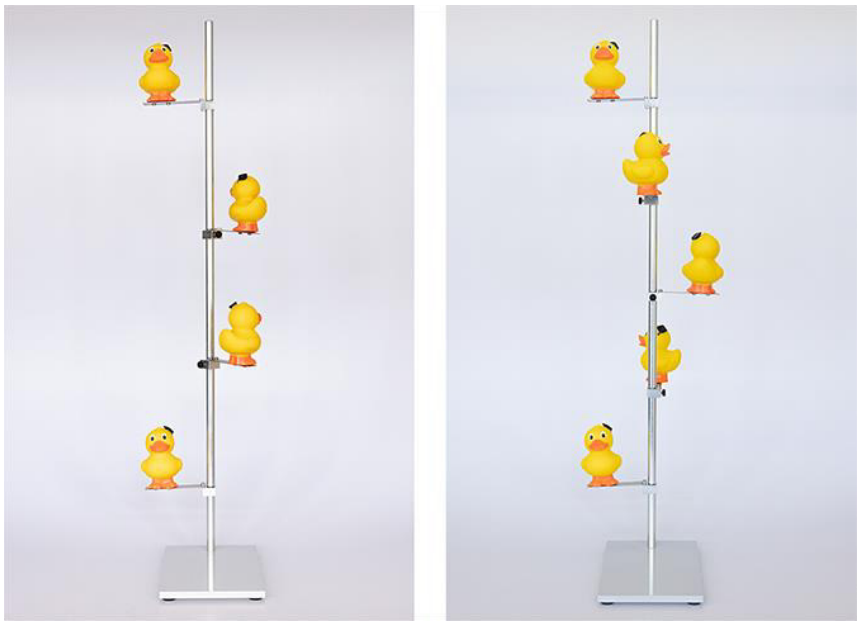

Figure 2-19: Selection of screw axis models. Left: Model of a 3_1 screw axis. Right: Model of a 4_3 screw axis.

Unfortunately, the screw axis models could not be used for in presence teaching due to the SARS-CoV-2 pandemic. The lecture on crystallography was conducted as a combination of screen recordings and prestructured online materials for self-study. Because the topic of symmetry was mostly covered by the latter, which was newly created for the online lecture, photographs of the models were included to illustrate the contents.

2.4 Space group models

Unarguably, space groups are among the more complicated – if not the most complicated – symmetry considerations a chemistry student has to tackle. The importance of physical, three-dimensional models to teach and train ones spatial imagination was laid out before (chapter 2.1). Starting with single molecules, an enormous variety of models in the range from highly specific to general model kits is readily available.[174–178] Moving on to the solid-state, the variety becomes smaller. Besides those, which are commercially available, almost all the models described in the literature focus just on the crystal packing illustrating close-packing of even spheres,[179–192] Bravais lattices[193,194] or archetype structures[181,186,189,190,195] like sodium chloride or rutile. Those are no doubt useful for their own purposes but depending on the individual model, recognizing the symmetry present in the solid-state can be far from easy. Moreover, these models are naturally limited to homoatomic or simple binary compounds. Only one reported model was found, which was more sophisticated in terms of the content to be conveyed, namely the infinity of the crystal lattice.[196] None of them specifically addressed space group symmetry.

The reported models have found little to no recognition within the scientific community based on citation statistics. Searching the literature for accounts of unit cell models of all sorts, 18 reports were found. Excluding citations due to this project, those articles were cited 59 times in total with an average of 3.28 and a median of 2. This apparent lack of interest is also reflected in a decreasing number of students who receive proper crystallographic education.[197] A development which is probably linked to the ever-increasing automation of crystal structure determination. Today, a single crystal diffractometer can be set up in such a way that a crystal structure can be determined completely autonomously from the mounting of the crystal on the goniometer to the structure solution. Availability of such technology may lead to considering crystallographic education as less and less important. If, on the other hand, you rely on black-box techniques, you lose the basis to critically question results.[198] The publication of erroneous results of X-ray structure determinations shows poor knowledge about crystallography on the part of both the authors and the reviewers. Undoubtedly, this should be a no-go to good scientific practice.

These errors show up in a broad range from a simple lack of finesse in structure refinement to completely unjustified claims about new compounds. Misinterpretation of acetate $[CH_3CO_2]^-$ as an "activated" hydrogen carbonate $[O_2C\cdots OH]^-$ lead to questionable claims about carbon dioxide activation pathways,[199,200] actual bromine atoms were mistaken for copper or silver atoms despite

inappropriate structural parameters,[201,202] and an unprecedented, thermally stable cadmium carbonyl complex turned out to contain no cadmium at all.[203,204] Erhard Irmer showed in his PhD thesis[205] that the Inorganic Crystal Structure Database (ICSD)[206] contained 98 structures with presumably incorrect space groups. Two recent examples highlight how poor refinement can slip through unnoticed. In both cases, this negligence does not affect the claims of the respective publication, but because of their implications they will be discussed in a bit more detail.

In the first case,[207] the reported structure suffers from disorder on two lattice solvent molecules and one counter ion, none of them coordinating. The refinement of all these entities suffers from different problems shown in Figure 2-20. In cases a) and b) the vibrational behaviour is simply physically nonsensical, in case c) the applied geometrical restraints appear to be wrong just from visual inspection of the result. The original data was deposited in the CSD[208] on the 28th of September 2020 under reference code 2034513, retrieved on the 23rd of April 2021 and updated by the authors on 24th of April 2021 after the issues became known and widely criticised. The original cif file also contains some statements regarding the alerts prompted by the checkCIF[209,210] validation, showing that the errors were not just overseen but rather accepted as unavoidable (see appendix 5.4.1.1).

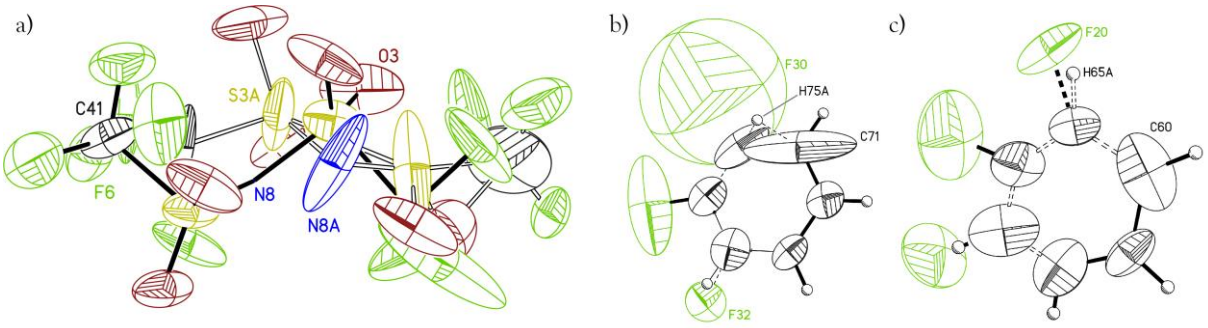

Figure 2-20: a) Triflamide anion refined on two positions. The ADP of N8 is too small to be seen. b) Disorder of *ortho*-difluorobenzene about an inversion centre. H75A is bound to two carbon atoms and the molecule has significant distortions from planarity. c) Disorder of *ortho*-difluorobenzene with geometrical issues. ADPs shown at 50% probability level. ORTEP diagrams were generated from the originally deposited data without modifications.

In the updated refinement the authors corrected all the mentioned problems by refining the disorder of the triflamide anion over three instead of just two positions, correcting the geometrical restraints on the *ortho*-difluorobenzene on a general position and realising that the second lattice solvent disordered about an inversion centre in fact is a molecule of toluene and

not *ortho*-difluorobenzene. However, the updated refinement still has some issues, so a new independent refinement yielding improved model quality was made based on the deposited data, the details of which are discussed in appendices 5.4.1.2 to 5.4.1.4.

In the second case,[211] a disordered thf molecule was removed from the structure by means of the SQUEEZE[212] procedure. When using SQUEEZE, care must be taken not to make unwarranted changes, as effectively electron density is removed from the dataset. As a basic rule, it should only be used if the chemical identity of the disordered entity is unambiguously known and refinement of the disorder is always preferable when possible. With the structure in question, it was stated that it "contained highly disordered thf molecules, which could not be refined properly."[211] Retrieving the data deposited under reference code 1994870 showed that in fact the disorder can easily be modelled over two positions (see Figure 2-21). The final models show nearly identical quality indicators and in both cases unusually high residual electron density between −1.858 eÅ^{-3} and 2.392 eÅ^{-3} is left, indicating a more general problem with the dataset than just a disordered molecule. Furthermore, the results of the SQUEEZE procedure presented in the supporting information claiming to account for approximately three thf molecules per unit cell are inconsistent and highly unlikely for space group $P2_1/c$. Details are discussed in appendix 5.4.2.

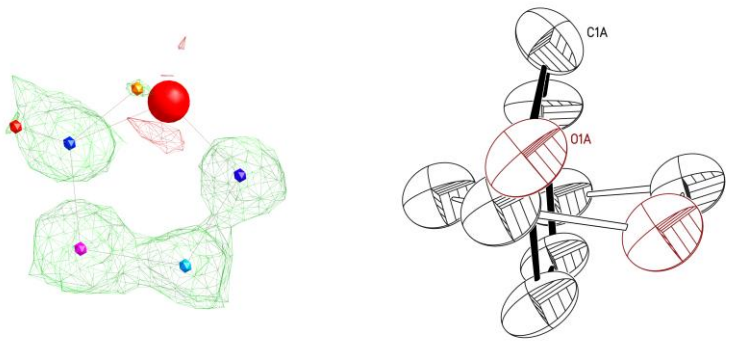

Figure 2-21: Left: Part of the difference electron density map of the deposited structural data before SQUEEZE was applied. Only one oxygen atom (red) was added to the original model. F_o–F_c map: −0.86 eÅ^{-3} to 0.86 eÅ^{-3}. Right: Thf molecule disordered over two positions nearly orthogonal to each other. ADPs shown at 20% probability level and hydrogen atoms omitted for the sake of clarity.

These two cases appear to be examples of poor X-ray structure determinations due to a lack of knowledge. In neither case, the scientific claim of the respective publication was compromised. Nevertheless, they showcase that structure determination is performed and can be accepted for

publication like this. Here only lattice solvent molecules were affected, but an uninformed use of SQUEEZE for example removing an ionic entity would have serious implications for the interpretation of the remaining structure.

Also difficult to understand is the increasing number of publications that describe the observation of second harmonic generation (SHG) responses upon irradiation with a laser for materials with a centrosymmetric crystal structure, [213] although it has already been shown that a centrosymmetric structure cannot exhibit such properties.[214,215] Measurement of SHG responses even became an experimental tool to prove the absence of centrosymmetry.[216,217] Still scientists come forward with their claims and manage to get through peer review, only to be refuted by the scientific community later on. One of these cases was the report of "digylcine zinc dipicrate" crystallising in the centrosymmetric space group $P\bar{1}$ and exhibiting SHG activity.[218] Investigating the cases, it turned out that the space group was correct although the X-ray structure determination was done poorly. However, the compound, which should correctly be described as tetraaquabis(glycine)zinc(II) dipicrate dihydrate, lost water upon laser irradiation causing it to change its composition and thereby also its structure. The SHG response was in fact measured on a different material.[219] Given the impossibility of the experimental outcome, one can expect the authors in such cases to question their findings more carefully.

Clearly, crystallographic education needs to be improved. To contribute to this, the aim was set to construct models of complete space groups. Because space groups themselves are technically infinite arrays of unit cells, for practical reasons models were designed and built to resemble singular unit cells.

2.4.1 Model concept and choice of space groups

The design of the space group models was guided by three criteria: Firstly, the models should be as accurate space group representations as possible. Secondly, they should be maximally transparent and rigid enough to allow for visual inspection from all sides. Symmetry elements should visually resemble the notation used in the International Tables for Crystallography, section A.[106] And thirdly, the models main body should only resemble the symmetry elements within the unit cell of a particular space group. It should be possible to add or remove the physical content of the cell manually.

While the first criterion is rather self-explanatory, the second and third were deliberately chosen for didactical reasons. A mostly transparent model with symmetry elements resembling their own style of notation should, if viewed along one of the crystallographic axes, create a visual impression, which is of high similarity to the two-dimensional depiction of the modelled space group. Such a model would assist students to draw connections between two- and three-dimensional representations of the same space group and therefore help to establish a better understanding of space group depictions in general. Furthermore, it follows already proposed guidelines for the development of visualisation tools in chemistry education[107] by offering visual referential connections, establishing the aforementioned link between two and three dimensions and making multiple representations available in general.

The reasoning behind the third criterion was to emphasise that crystal classes and space groups are only determined by symmetry elements and their relative arrangement. It is a common misconception that the crystal system of a structure is defined by the metrics of its unit cell, when in fact it is the symmetry present enforcing restrictions on cell angles and edges.[220] A unit cell might accidentally adopt a perfectly cubic shape and still be triclinic if the only symmetry element present is a centre of inversion. In other words, while every crystal class and hence space group imposes certain conditions on cell metrics due to symmetry, the metrics themselves do not allow for determination of the crystal class. Furthermore, a unit cell model without chemical content gives instructors and students the possibility to add such content themselves. Placing an object on any position, that is to say a general position, within the unit cell allows to trace how all further positions result from symmetry. Symmetry operations can be performed manually and step by step until all general positions are occupied. This hands-on experience is also suitable to emphasise how symmetry elements impose limitations on the content of the unit cell.[220]

Lastly, a decision had to be made as to which space groups should be modelled. There are 230 possible crystallographic space groups. Modelling them all neither would be practical, nor would it have any educational benefit. A selection should be made that reflects different types of symmetry elements but is not too crowded as for example most of the cubic space groups are, which would be visually challenging simply because of the sheer number of symmetry elements present. Space groups $P\bar{1}$, $P2_1$ and $P2_1/c$ were chosen, as they cover inversion centres, screw axes and glide planes. Furthermore, they exhibit increasing complexity from $P\bar{1}$, to $P2_1/c$ and belong to the five most frequent space groups among structures deposited in the CSD[221] rather than being crystallographic curiosities.

2.4.2 Construction of space group models

As a proof of concept and a means of prototyping, a first attempt was made to create small-scale models with edge lengths between 10 cm and 20 cm. Readily available materials like wooden skewers, packing beads, paper, transparencies and a hot glue gun were used. Though the focus was laid more on feasibility than on accuracy, the prototypes showed that the design criteria discussed in the previous chapter can be met. On the other hand, they also revealed some problems that would arise with larger models. Figure 2-22 shows a small-scale model of space group $P\bar{1}$. This space group can be envisaged as an assembly of spheres in three-dimensional space. Modelling it necessitates to suspend these spheres in some way. In the case of the prototype this was done by building a frame correspondent to the cell edges, on which all spheres not lying on edges or corners were suspended with a thin thread. The thread is barely visible and works fine at this scale, but for a larger model, this method would be unfit due to the higher tension needed to keep a longer piece of thread taut.

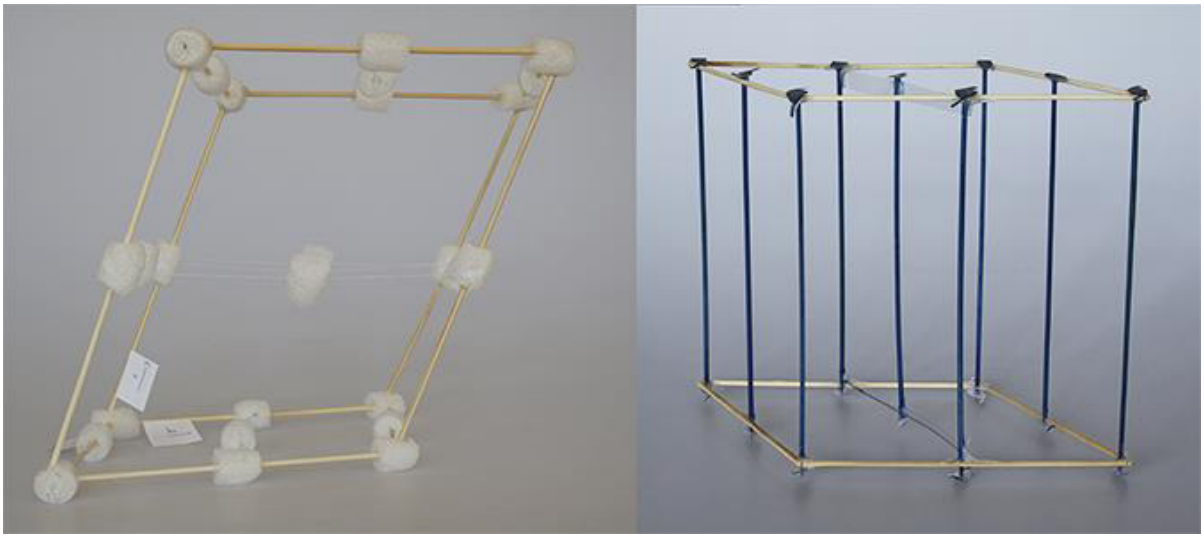

Figure 2-22: Small-scale prototypes of space groups models made from scrap material. Left: model of space group $P\bar{1}$. Centres of inversion represented by packing beads. Right: Model of space groups $P2_1$. Screw axes tainted blue for better differentiation from cell edges.

By convention, a unit cell should always be set up in such a way that its origin is at a location of high symmetry. As a consequence, symmetry elements often coincide with cell edges so that they can be incorporated into the model frame as it was done with the $P2_1$ prototype (see Figure 2-22,

right). However, this does not apply to all symmetry elements and additional means of fixation are needed. More small-scale prototypes are shown in appendix 5.5.1.

Figure 2-23: Small-scale prototypes of space group models. Left: Model assembled from aluminium rods and custom parts made with a filament 3D printer. Right: Whole model printed with a resin 3D printer.

The prepared prototype models are too small for a lecture hall presentation and not sturdy enough to be handled by multiple students. In addition, arranging objects inside them would be challenging. Nevertheless, they are easy to build at reasonably low cost and, if done accurately, are good three-dimensional representations of space groups. For discussions with smaller groups for example during a seminar these models might be very helpful. In order to provide more rigid and consistent models for such a use, space group $P2_1$ was selected as an example to create a virtual model as the basis for 3D printing. Virtual 3D modelling was done with the freely available Tinkercad[222] online CAD resource. Having a filament 3D printer available, it would be highly inefficient to print the model as a whole due to the need of supporting material. Instead, the model was designed to be printed in parts, which can be assembled afterwards. The key here is that the plates, which form the ends of each screw axis, have an extended body with preformed holes already created during the printing process. The connecting parts could also be printed, but aluminium rods of 2 mm diameter were used for convenience and cut to size. The preformed

holes then aid in connecting all parts with correct angles. The object files needed to print the parts for a model as shown in Figure 2-23 were made publicly available as part of the respective publication.[223] If a resin printer is available, it can be more straightforward to print the whole model in one piece.

Based on the prototypes, large-scale and more robust models were constructed, which are more appropriate for a demonstration in a lecture theatre. The cell edges of these range between 40 cm and 60 cm. In general, aluminium rods of 4 or 6 mm diameter were used for the screw axes and cell edges when needed. To differentiate between them, the screw axes were coated black while cell edges remained unpainted. Spheres representing inversions centres and plates to flag screw axes with the appropriate symbols were custom-made by designing virtual 3D models in Tinkercad[222] and 3D printing them using black PLA filament. As with the small-scale model, this gave the opportunity to include preformed cavities right away. In space groups $P\bar{1}$ and $P2_1/c$ an inversion centre is located on every corner of the cell. These could conveniently be used as connectors tying the outer frame of the models together and maintaining correct angles for the respective model. If additional supporting material was needed, e.g. for a face centred inversion centre, colourless transparent polyacrylate rods were used. To represent the glide planes in space group $P2_1/c$ plates of polyacrylate were cut into the appropriate shape and lightly coloured transparent foil was stuck onto the plate in thin stripes to indicate the direction of the translational component of the glide plane. Figure 2-24 shows the completed model of space group $P2_1/c$ alongside the conventional schematic. Due to the size of the model, the perspective of the photograph is slightly distorted, but the resemblance remains. The three-dimensional model can be visually recognised as a counterpart of the two-dimensional depiction and *vice versa*. In Figure 2-24 the model already contains rubber ducks to represent the contents of asymmetric units. The ducks can be easily positioned on top or below the glide planes. They are secured in place with magnets, which allow for easy relocation but are also strong enough to keep the ducks in place when the model is tilted. The model can be placed on any face of the unit cell to enable students to inspect it from all directions (more photographs are shown in appendix 5.5.2).

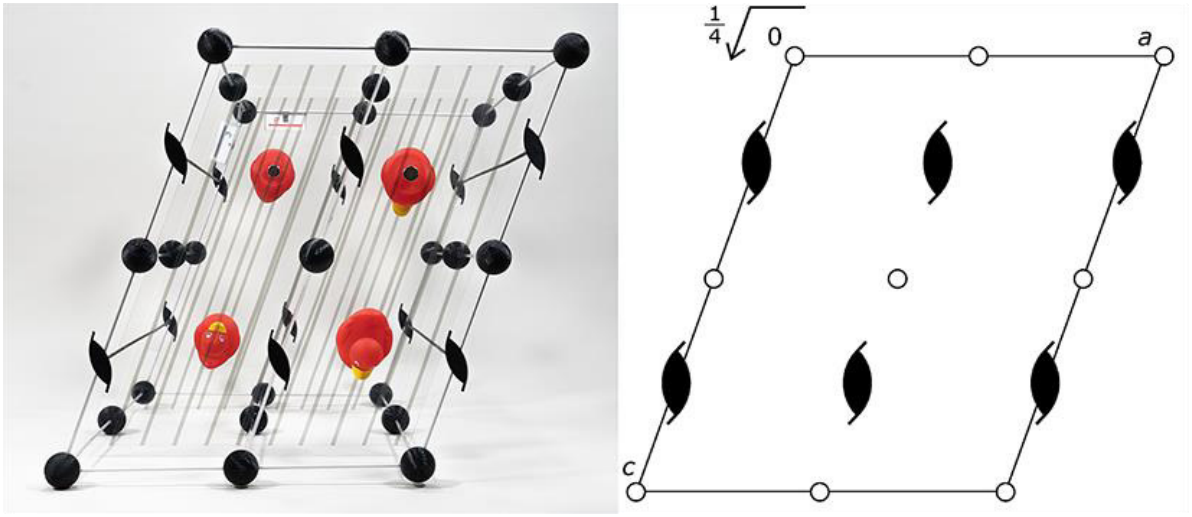

Figure 2-24: Left: Large-scale model of space group $P2_1/c$. View along crystallographic *b* axis. Content of asymmetric unit represented by red rubber ducks. Right: Conventional depiction of space group $P2_1/c$ reproduced from the International Tables for Crystallography, Section A.[106]

Because the space groups $P\bar{1}$ and $P2_1$ do not contain glide planes (or regular mirror planes for that matter) two problems arise with their models: rubber ducks cannot easily be placed inside the model as there is nothing to attach them to and the models lose a source of stability. A frame built only from aluminium rods turned out not to be rigid enough due to the size of these models. To circumvent this problem, plates of polyacrylate were inserted in two opposite faces of each model. This reduced the flexibility of the frameworks significantly and in the case of the $P2_1$ model, it made additional material to support the central screw axis unnecessary. Incorporating solid planes into the models also helps with the problem of how to place the rubber ducks. In case of $P\bar{1}$, the ducks can be fixed to the polyacrylate plates with magnets just as described before. The $P2_1$ model is more complicated because the 2_1 screw axis displaces an object by half of the length of the cell edge. Placing one duck at the bottom of the model therefore necessitates the second duck to be right in the middle. Two ways were devised to deal with this issue. Firstly, a stand was made of transparent polyacrylate, which has the exact height needed to hold the duck at the correct position. Secondly, hooks can be placed onto the polyacrylate plates on each side of the model. Using magnets again allows for free positioning. These hooks can then be used to stretch a thread between them and along the direction of the screw axis. The rubber ducks must be suspended on these threads in a way that they can be moved along it. As the position of the hooks can be altered and the ducks can be moved up and down the thread, in principle any position within the model is accessible (see Figure 2-25). This solution is a bit more elegant than

the stand, as less additional and potentially distracting material in introduced in the model. It grants more freedom and the thread can hardly be seen. However, the stand is most definitely easier to handle. Being able to arrange rubber ducks or other objects freely within the models or to remove them altogether is not only convenient for the instructor but also fulfils the third of the initially formulated criteria.

Furthermore, the models help to illustrate the concept of fractional coordinates. The depiction on the right side of Figure 2-24 only shows the symmetry elements that are located in the *a*,0,*c* plane and a c glide plane at height ¼ *b*. Unlike the two-dimensional depiction, the model can be rotated and viewed along *a* or *c* direction so that it can directly be seen that the glide plane is located at ¼ of the models height (see Figure 5-30 in appendix 5.5.2). In the same vein, it is immediately apparent that a second glide plane at height ¾ *b* exists. This is not explicitly denoted in the two-dimensional depiction, because the two glide planes are related by symmetry and not independent, but students who start to learn about space groups often tend to forget about these. The same applies to all other symmetry elements, which are not located within the depicted plane but are related to them by symmetry.

Figure 2-25: Large-scale model of space group $P2_1$. It is illustrated how the rubber ducks can be positioned anywhere within the unit cell with the aid of thread and magnetic hooks.

Sadly, due to the SARS-CoV-2 pandemic the models could not be used directly for teaching as no courses with matching content were held in presence. Taking pictures of them to include them in the materials for online teaching would not do justice to the basic idea of the models. Therefore, videos were recorded in German and English explaining the models for space groups $P2_1$ and $P2_1/c$ (see Figure 2-26). For contextualisation, first molecular symmetry is discussed using the examples of P_4 and S_8. This is followed by the ionic lattice structures of sodium chloride, caesium chloride and zinc blende emphasising why certain symmetry like an 8-fold rotation is not allowed in the solid-state. In the last part, the space group models are introduced and it is explained step by step how symmetry elements determine the positions of the rubber ducks. The completely assembled models are then compared in detail to the conventional depictions in the International Table for Crystallography, Section A.[106]

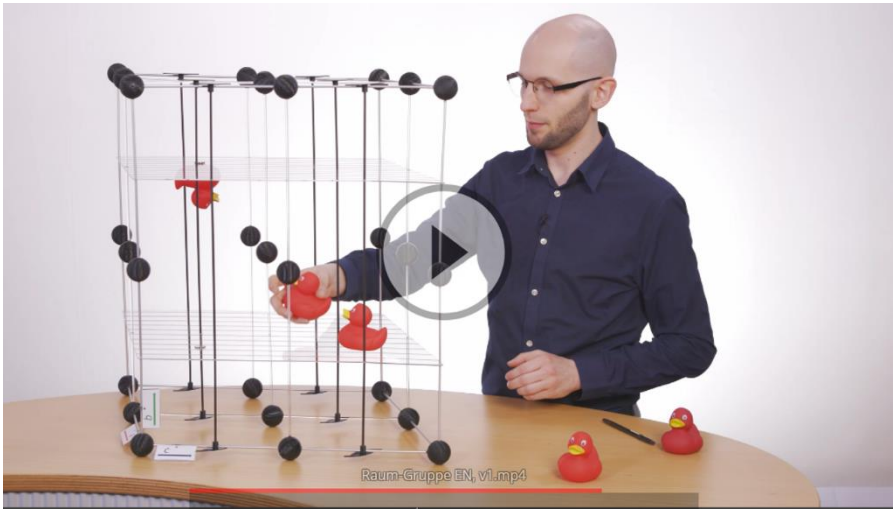

Figure 2-26: Screenshot of a video showing how the model is used to explain the $P2_1/c$ space group symmetry.

To conclude, models of three space groups with increasingly complex symmetry were designed and built. Small or large-scale models can be realised depending on the setting they are meant to be used in. The models themselves only represent an ensemble of symmetry elements, which defines the respective space group, and are limited to one unit cell for practical reasons. The unit cells contents, i.e. the asymmetric units, represented by rubber ducks can be placed in the models step by step to show how the arrangement of objects within the unit cell is governed by symmetry.

2.5 Summary and outlook

The work presented here was done as part of a project funded by the Lower Saxony Ministry of Science and Culture within the framework of the *Innovation plus* funding programme. The main goal of this project was to maintain and train students' abilities for spatial imagination and symmetry recognition. To achieve this, the implementation of a drawing skill course and the construction of three-dimensional models were intended.

A skill course was developed, which covers the basics of chemical formulas and elaborates on various options to illustrate the three dimensionality of chemical structures. The course was initially implemented in existing seminars and later transformed into an online resource following the idea of the inverted classroom model. After positive evaluation, it was implemented faculty wide to be accessible to all students and not just during the introductory lecture on general and inorganic chemistry.

Apart from the course, models of rotational axes, screw axes and space groups were constructed from which especially the latter were unprecedented. The design of all models was guided by two main principles: Firstly, interactivity, so that symmetry, and in particular symmetry operations, can be taught and learned through hands-on experience rather than just being imagined, and secondly, visual resemblance, so that a link can be made between conventional two-dimensional depictions and three-dimensional models. These concepts were successfully realised with all models. However, due to the SARS-CoV-2 pandemic they could not be used for teaching as planned. Instead, pictures and videos were taken to make best possible use of the models in different online teaching approaches. Furthermore, the developed models and the associated teaching approach were transported into the crystallographic community by a publication[223] and conference contribution.[224]

Because the physical nature of the space group models restricts them to one unit cell or at least a very small number of unit cells, one crucial aspect of solid-state structure is not addressed at all: periodicity. While an ideal crystal by definition consists of infinitely many unit cells in any direction, a real crystal is still composed of a virtually infinite number of unit cells. This periodicity has great impact on the properties of solid-state compounds but is mentally hard to grasp like anything else that has to do with infinity. To address this problem and based on the results obtained in this project, a follow-up proposal was submitted to the *Innovation plus* funding programme. The proposed project aims to design virtual models of space groups and crystal structures that allow for an immersive experience by means of virtual reality. Fortunately, the

Lower Saxony Ministry of Science and Culture accepted the proposal and work in this area will be continued.

Chapter III:

Bis(4-methylbenzoxazol-2-yl)methanide based tetrylenes

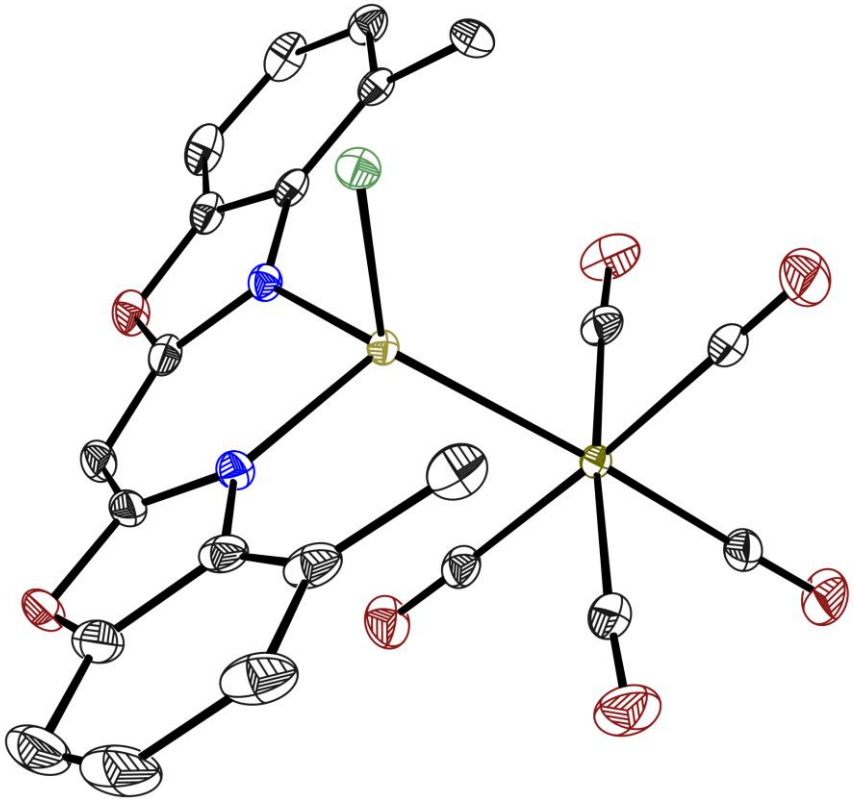

3.1 Introduction

The existence of a *N*-heterocyclic carbene (NHC) was first postulated by Wanzlick in 1960.[225–227] Experimental prove of such a carbene species was shown independently by Wanzlick and Öfele in 1968, when both successfully synthesised the NHC metal complexes shown in Figure 3-1.[228,229] However, isolation of a free *N*-heterocyclic carbene was only successful in 1991 when Arduengo and co-workers reported on the preparation and characterisation of stable 1,3-di-1-adamantylimidazol-2-ylidene (Figure 3-1 c).[230] Since then NHCs have been the topic of extensive research[231,232] and found their way into a multitude of applications in the chemistry of low-valent main group elements[233] organocatalysis,[234] coordination chemistry[235] and transition metal catalysis.[236] Prominent and Noble Prize worthy examples of the latter are, for example, the Grubbs catalysts.[237–239]

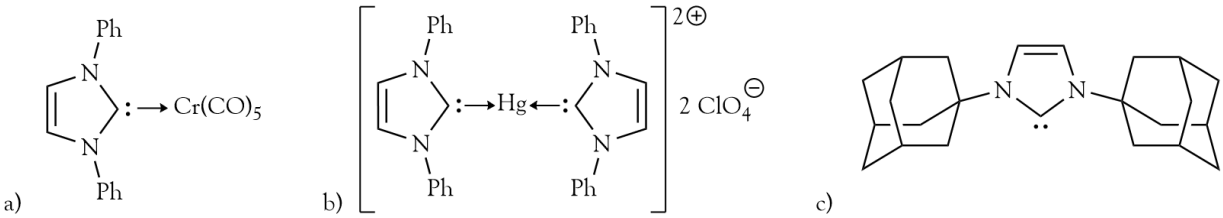

Figure 3-1: Pioneering compounds in NHC chemistry. a) NHC chromium complex prepared by Öfele 1968.[229] b) NHC mercury complex prepared by Wanzlick 1968.[228] c) First isolable free carbene prepared by Arduengo 1991.[230]

Considering the success story of *N*-heterocyclic carbenes, the questions arises as to whether their heavier homologues might exhibit a similarly rich chemistry. Accordingly, over the past 30 years the synthesis and reactivity of group 14 NHC analogues have been at the interest of research.[240,241] A plethora of compounds with different ring sizes has been reported, most of which can be described by the generalised structures shown in Figure 3-2. Of particular interest to this thesis are six membered cyclic systems featuring low-valent *N*-chelated germanium, tin or lead atoms. The current state of research regarding this set of compounds will be discussed in the following chapters.

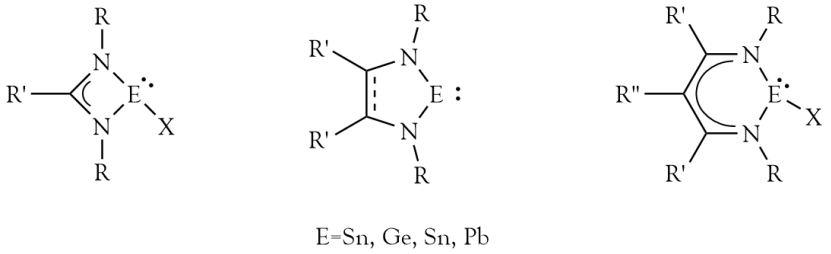

Figure 3-2: Generalised structures of heavy NHC analogues.

3.1.1 *N*-heterocyclic carbene analogues with low-valent group 14 elements

3.1.1.1 Germanium

The first *N*-chelated six membered cyclic germylenes **(Ge-I)** were prepared by the reaction of $GeCl_2$·dioxane with lithium salts of appropriate NacNac ligands in 2001.[242–244] A broad overview of their typical reactivity is sketched in Figure 3-3.

Abstraction of the chloro ligand affords cationic species of type **Ge-II**. While in related species it was observed, that employing $NaBPh_4$ as a chloride scavenger leads to transfer of a phenyl group[245,246] resulting in a **Ge-III** type compound with X=Ph, one report claims to have synthesised the targeted cation in his way starting from $\{HC(CMeNPh)_2\}GeCl$.[244] However, characterisation of $[\{HC(CMeNPh)_2\}Ge][BPh_4]$ was only based on NMR spectroscopic and mass spectrometric analyses. A cationic germylene that could also be characterised by X-ray crystallography could be obtained *via* treatment of $\{HC(CMeNDip)_2\}GeCl$ with $B(C_6F_5)_3$ in the presence of water to form $[\{HC(CMeNDip)_2\}Ge][HO\{B(C_6F_5)_3\}_2]$.[247]

The chloro ligand can be substituted for a triflate, an azide, amides, phosphides, alkoxides or alkyl groups to give complexes of type **Ge-III** by the use of silver triflate,[244] sodium azide,[242,243] lithium amides,[244,248,249] lithium phosphides,[248,250,251] lithium or potassium alkoxides[248,252] or alkyl lithium reagents[253] respectively. While bromo and iodo derivatives are available *via* $GeBr_2$[254] or GeI_2[244] instead of $GeCl_2$·dioxane, the fluoro compound can be accessed by means of reacting **Ge-I** with Me_3SnF.[255] Germylene hydrides were synthesised *via* treatment of **Ge-I** with $K[HBR_3]$,[256,257] AlH_3·NMe_3[258] or LiH_2NBH_3.[252] Sodium borohydride can also be used, however, the resulting species is the corresponding germylene borane adduct, from which the borane can be abstracted in a second step by treatment with trimethylphosphane.[255]

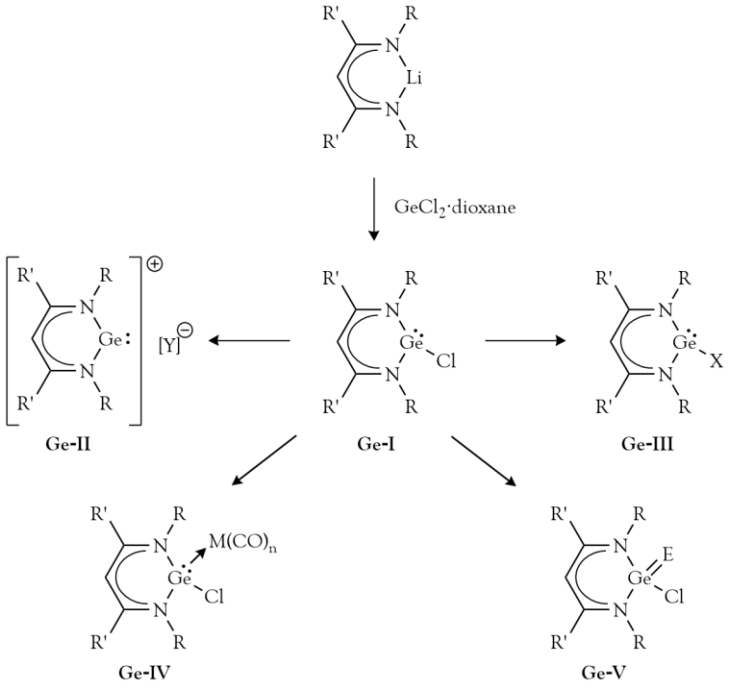

Figure 3-3: Generalised synthesis and reaction pathways for NacNac based germylenes. R=^{i}Pr, Ph, Mes, Dip; R'=Me, ^{t}Bu; X=Me, ^{n}Bu, OMe, O^{i}Pr, O^{t}Bu, O^{s}Bu, NMe_2, $N(SiMe_3)_2$, PH_2, PPh_2, PCy_2, $P(SiMe_3)_2$, OTf, N_3, F, H, OH; Y=BPh_4, $HO\{B(C_6F_5)_3\}_2$; M=Cr, Fe, W; E=S, Se.

With NHCs being frequently used as transition metal ligands, it is only natural to also investigate the properties of germylenes as ligands. Complexes of type **Ge-IV** have been prepared with chromium,[244] iron[259] and tungsten[244,259] carbonyls. Furthermore, also complexes of the analogous iodo germylenes with iron and tungsten carbonyls[259] and of fluoro germylenes with iron tetracarbonyl[260] are reported. In one case also the subsequent substitution of two carbonyl ligands in $W(CO)_6$ was achieved to exclusively yield the *trans* isomer of $NHGe_2W(CO)_4$ with NHGe={HC(CMeNPh)$_2$}GeCl. Notably, in the case of $NHC_2W(CO)_4$ only formation of the *cis* isomer is observed.[261] Apart from metal carbonyls also the coordination to other transition metal complexes has been investigated. The compound [{HC(CMeN^{i}Pr)$_2$}Cu{HC(CMeN^{i}Pr)$_2$}GeCl], for example, features a copper germanium bond and it could be shown that chloro ligand at the germanium atom can be substituted for a methyl group or hydride *via* treatment of the complex with MeLi or K[$HBEt_3$] respectively.[262]

The lone pair of these germylenes can react with elemental sulphur[244,253,263,264] or selenium[244,253,263,265] to obtain the corresponding chalcogenides of type **Ge-V**. Synthesis of the related germanium imine was only successful for {HC(CMeNDip)$_2$}GeF being reacted with trimethylsilyl azide.[255]

The hydroxo germylene **Ge-VI** was first synthesised *via* controlled hydrolysis of **Ge-I** with water in the presence of a NHC to scavenge the liberated hydrogen chloride.[266] A second synthetic route to the hydroxo complex makes use of the C-H acidic methyl group in β position of the ligand. Treatment of the germylene triflate (**Ge-III**, X=OTf) with a NHC results in the deprotonation of the ligand under formal elimination of triflic acid. If water is added in a second step, nucleophilic attack occurs at the germanium atom followed by cleavage of an O-H bond and migration of the proton to the ligand to restore the original bonding situation of the ligand. It was further shown that this reactivity can be extended to phenol, pentafluorophenol and even benzoic acid to yield the germylene ethers or ester respectively.[267]

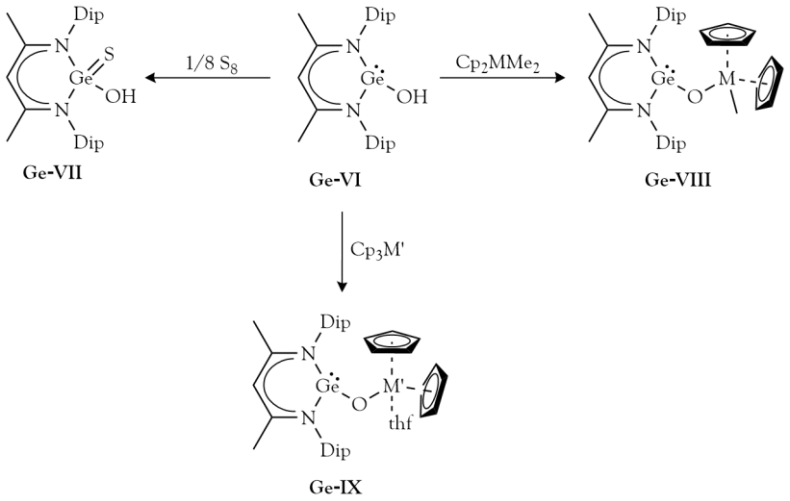

Figure 3-4: Reaction pathways of hydroxo germylene **Ge-VI**. M=Zr, Hf; M'=Y, Yb.

Reacting **Ge-VI** with elemental sulphur leads to oxidation of the germanium atom just as described for compounds of type **Ge-V**. In the case of **Ge-VII**, however, it is noteworthy to point out that the product is the germanium analogue of a thiocarboxylic acid in its thione form, for which there is no isolated species in the carbon system (Figure 3-4).[268] Furthermore, the hydroxo germylene can be used to synthesise oxo bridged heterobimetallic complexes **Ge-VIII**[269] and **Ge-IX**.[270] These species have high potential as catalysts, cocatalysts, as molecular models for bulk metal oxides or precursors for the preparation of well-defined bi- and polymetallic heterogeneous catalysts.[271,272]

It is worth to inspect the reactivity of the germylene hydride **Ge-X** in more depth as it showcases some remarkable features (Figure 3-5).[273] Reacting **Ge-X** with elemental sulphur results not only in oxidation of the germanium atom as in **Ge-X** but also in insertion of one sulphur atom into the germanium hydrogen to yield the thiol **Ge-XI**.[257] While transition metal catalysed

hydrogermylation reactions between unsaturated organic compounds and hydrogermanes are long known,[274] **Ge-X** reacts smoothly with alkynes at room temperature in absence of catalysts to the expected germylene substituted alkenes **Ge-XII**.[257] The sterically less hindered analogue {HC(CMeNMes)$_2$}GeH reacts in the same way with phosphaalkyne P≡C^{t}Bu to give a germanium C-phosphaalkenyl complex regioselectively.[256]

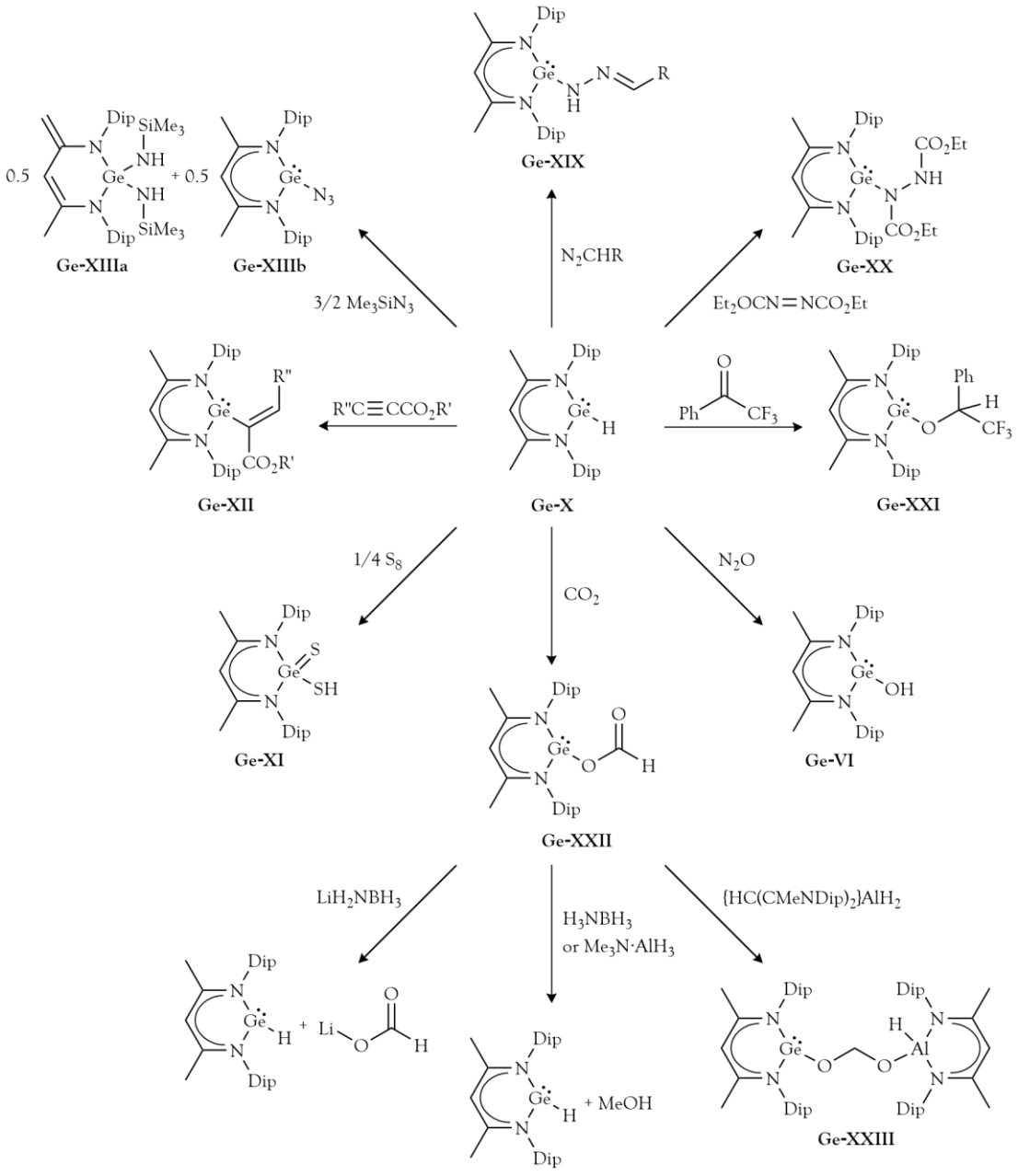

Figure 3-5: Reactivity of germylene hydride **Ge-X**. R=CO$_2$Et, SiMe$_3$; R'= Me, Et, ^{t}Bu; R''=H, CO$_2$Me, CO$_2$^{t}Bu.

Treating **Ge-X** with trimethylsilyl azide does not only give the azide substituted product **Ge-XIIIb** but also in equimolar amounts the germanium(IV) diamide **Ge-XIIIa**. Formation of the latter is expected to proceed *via* initial elimination of N_2 from the azide and subsequent insertion of the resulting nitrene into the germanium hydrogen bond. A second equivalent is then added in an oxidative fashion under involvement of a hydrogen atom migrated from the ligand backbone. However, no detailed mechanistical studies were performed.[275] The reaction of **Ge-X** with diazoalkanes yields germanium(II) substituted hydrazone derivatives **Ge-XIX** formed *via* end-on insertion of the terminal nitrogen atom into the germanium hydrogen bond.[276] Similar reactivity was also observed with a methyl substituted germylene (**Ge-III,** X=Me), however, in this case a hydrogen atom from the ligand backbone migrates to the terminal nitrogen atom instead of the methyl group.[275] Other unsaturated substrates such as diethyl azodicarboxylate or activated ketones give the expected hydrazine derivative **Ge-XX**[276] or germylene ethers **Ge-XXI**[275] as hydrogermylation products. Formally the germanium hydrogen bond is added across the substrate's double bond under retention of the +II oxidation state at germanium. Reaction with nitrous oxide surprisingly does not lead to oxidation of the germanium atom as for example the treatment with sulphur or selenium does but instead yields the germylene hydroxide **Ge-VI**.[275]
Reaction of **Ge-X** with carbon dioxide under ambient conditions yields the germylene ester of formic acid **(Ge-XII)** in a formal 1,2 addition of the germanium hydrogen bond across one of the carbon oxygen double bonds.[256,257] To see if **Ge-XII** could be reduced further to yield C1 products, it was first treated with LiH_2NBH_3 as a hydrogen source. This only gives lithium formate, however, it also regenerates the germylene hydride **Ge-X**.[277] If the parent ammonia borane is used as a reducing agent instead, not only is **Ge-X** is regenerated, but also methanol is obtained after aqueous workup.[277] Later it was shown that also the trimethylamine alane complex can be used as a hydrogen source, whereas with the aluminium hydride complex $[HC(CMeNDip)_2AlH_2$ the reaction seems to stop at intermediate **Ge-XXIII**.[278] Hence, the germylene hydride **Ge-XX** is capable to catalytically transform gaseous carbon dioxide to methanol in presence of atom economic ammonia borane[279,280] as hydrogen source and without the need of expensive and toxic transition metals.
Besides the ones discussed so far only a handful of six membered cyclic *N*-chelated germylenes have been reported, which are not based on the NacNac ligand scaffold (see Figure 3-6). All of them are synthesised by the reaction of the lithiated ligand and $GeCl_2$·dioxane. **Ge-XXIV** has also been prepared by the reaction of the free ligand with $Ge(HMDS)_2$.[281] As already described for other compounds germylene **Ge-XXIV** can be oxidised by elemental sulphur or selenium to

yield the respective germanium +IV chalcogenides.[281] However, due to the reduced steric bulk around the germanium atom these chalcogenides form dimers in the solid-state. **Ge-XXIV** reacts with $Ni(COD)_2$ to form the tetrahedral $[Ni\{Ge(^iPrN)_2C_{10}H_6\}_4]$ complex.[281] The cation of bis(oxazoline) based germylene **Ge-XXV** is accessible *via* treatment with silver hexafluoroantimonate in thf. One solvent molecule stays coordinated to the cation but can be replaced by other donor bases such as PMe_2Ph or pyridine.[282]

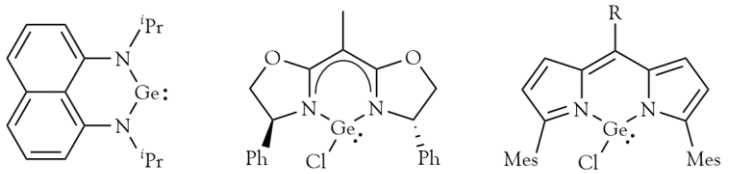

Ge-XXIV **Ge-XXV** **Ge-XXVI**

Figure 3-6: *N*-chelated cyclic germylenes not based on the NacNac ligand scaffold. R=Ph, Mes.

The bis(pyrrolyl)methane based germylene **Ge-XXVI** with R=Mes possesses exceptional stability towards air and water under ambient conditions in the solid-state as well as in solution. Reaction with caesium fluoride yields the fluoro derivative, which shows similar stability.[283] For the phenyl substituted analogue (R=Ph) it could be shown that the chloro ligand can be substituted for alkoxides if the germylene is reacted with the respective alcohols in the presence of caesium carbonate. These alkoxide complexes can then be hydrolysed to obtain a hydroxo germylene. Alternatively, the same hydroxo complex can be obtained by the direct reaction of **Ge-XXVI** with excess caesium carbonate and water. This hydroxo germylene is stable even under physiological conditions and was studied as a potential anti-cancer agent *in vitro* performing comparable to cisplatin. [284]

3.1.1.2 Tin

The chemistry of *N*-chelated six membered cyclic stannylenes is very similar but less extensive compared to the related germylenes. Most compounds are accessible *via* the chloro stannylene **Sn-I** and a general reactivity scheme is give in Figure 3-7. **Sn-I** type compounds themselves can be synthesised from lithiated NacNac precursors and tin(II) chloride.[242–244,285] $SnBr_2$ and SnI_2 react in the same way to yield the respective bromo[254] and iodo derivatives.[244,286]

The cationic stannylene **Sn-II** can be obtained from {HC(CMeNPh)$_2$}SnCl after treatment with NaBPh$_4$ as a chloride abstraction reagent.[244] As with the analogous germylene cation, this claim is only based on NMR spectroscopic and mass spectrometric analyses. Similarly, chloride abstraction with Li[B(C$_6$F$_5$)$_4$] or AlCl$_3$ probably leads to the stannylene cation, but no structural evidence is reported. Finally, reaction of methyl stannylene **Sn-III** (X=Me) with B(C$_6$F$_5$)$_3$ yields [{HC(CMeNDip)$_2$}Sn][MeB(C$_6$F$_5$)$_3$], however, with one solvent molecule of diethyl ether still coordinated to the tin atom.[287]

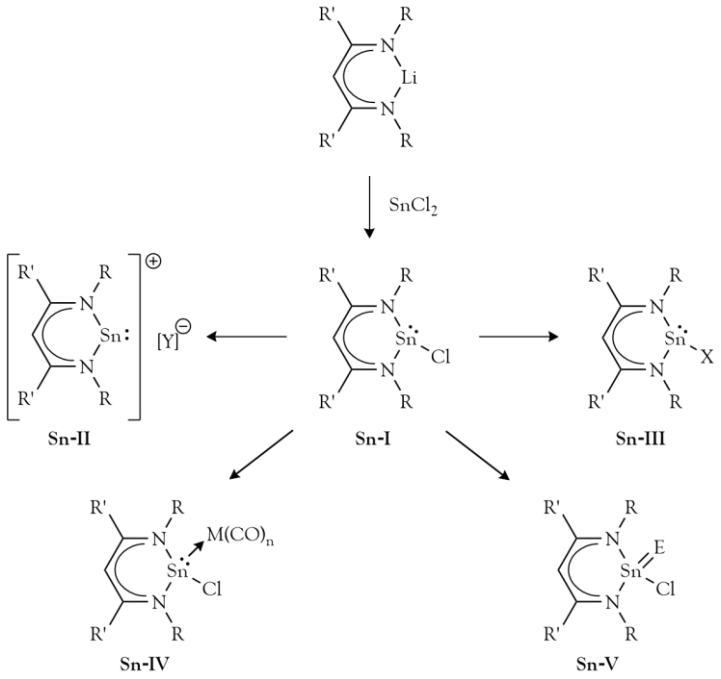

Figure 3-7: Generalised synthesis and reaction pathways for NacNac based stannylenes. R=Ph, Mes, Dip; R'=Me, ^{t}Bu; X=Me, ^{t}Bu, O^{i}Pr, O^{s}Bu, O^{t}Bu, CP, SPh$_3$, NMe$_2$, N^{i}Pr$_2$, NHDip, N(SiMe$_3$)$_2$, PCy$_2$, PPh$_2$, P(SiMe$_3$)$_2$, OTf, N$_3$, F, H, OH; Y=BPh$_4$, MeB(C$_6$F$_5$)$_3$; M=Cr, Fe, W; E=S.

Starting from **Sn-I**, a wide range of substitution reactions has been reported. Stannylene triflates and azides can be obtained *via* salt metathesis with silver triflate[242,244] or sodium azide.[242–244] Transmetalation with lithium alkyls,[242,286] alkoxides,[288–290] triphenylmethanethiolate,[290] amides[244,289,291] or phosphides[251] affords the corresponding stannylene derivatives bearing organic substituents instead of the chloro ligand. The fluoro compound can be accessed by reacting either {HC(CMeNDip)$_2$}SnMe or {HC(CMeNDip)$_2$}SnHMDS with Me$_3$SnF.[286] Using {HC(CMeNDip)$_2$}MgCP as a transfer reagent, the chloro ligand in **Sn-I** can be substituted for the cyaphide ion. [292] Treating **Sn-I** with lithium sulphide or excess potassium hydroxide results in distannylenes bridged by a sulphide or oxide ion respectively.[290] Reaction of **Sn-I** with lithiated

trimethylsilyl diazomethane does not lead to the expected tin(II) diazo or nitrilimine compounds but yields a stannylene and trimethylsilyl substituted carbodiimide after proposed intermolecular rearrangement. This compound can further be reacted with $Fe_2(CO)_9$ to coordinate the lone pair of the stannylene to a $Fe(CO)_4$ fragment.[293] The rather unusual potassium germylenide reagent K[C(Me)CHC(Me)N(Dip)Ge] can be used to prepare a heterodinuclear germylene-stannylene with formal oxidations state +I for Ge and Sn.[294] Like the germylene hydride **Ge-X**, the tin analogue can be synthesised by treatment of **Sn-I** with $AlH_3{\cdot}NMe_3$.[258] In contrary, a hydroxo stannylene of type **Sn-III** is not accessible *via* controlled hydrolysis in presence of NHCs. To obtain such a monomeric tin(II) hydroxide the stannylene amide $\{HC(CMeNDip)_2\}SnNMe_2$ needs to be protected first. This can be achieved by reaction with $Fe_2(CO)_9$ to transfer a $Fe(CO)_4$ fragment onto the stannylene. Addition of water to this complex yields the hydroxo stannylene still coordinated to $Fe(CO)_4$.[295]

While the iron carbonyl fragment is purposely introduced to protect the compounds from oligomerisation, it is also an example of a stannylene employed as a carbene like ligand on a transition metal. Similar complexes of type **Sn-IV** can be synthesised by reaction of **Sn-I** with chromium,[244] tungsten[244] or iron carbonyls.[259,260,296] Also the reaction of **Sn-I** with $K[Fe(\eta^5\text{-}Cp)(CO_2)]$ is reported to give a stannylene iron(0) complex. However, here the stannylene formally is a cation as the reaction proceeds under elimination of KCl.[297]

In contrast to their germanium analogues, chalcogenide compounds of type **Sn-V** are not known. Reaction of **Sn-I** with elemental sulphur is reported but the product appears to be unstable in solution and converts back to the starting materials. With selenium no reactivity is observed.[244] Phosphides of type **Sn-III** ($X=PCy_2$) react with selenium. However, instead of oxidation and formation of the tin(IV) selenide, Se is inserted in the tin phosphorus bond exclusively. In presence of excess selenium, phosphorus but not tin is oxidised. Addition of sulphur leads to scrambling of bridging and terminal chalcogenides and even intermolecular exchange, but no oxidation of the stannylene is observed.[298]

For stannylene alkoxides, amides and hydrides diverse reactivity has been reported. Amides as shown in Figure 3-8 can react with several unsaturated compounds. The dimethylamide reacts with 2-benzoylpyridine or 2,2,2-trifluoroacetophenone *via* 1,2-insertion of the carbonyl moiety into the tin-nitrogen bond to yield the alkoxides **Sn-VII** in a reaction that could be described as aminostannylation.[299] Similar reactivity is observed when **Sn-VI** is reacted with carbon dioxide. The tin-nitrogen moiety adds across one of the carbon-oxygen double bonds to form the stannylene carbamates **Sn-VIII**.[291] In contrast, reactions with terminal alkynes do not proceed

via addition across the triple bond, but instead lead to deprotonation of the alkyne and formation of stannylene acetylides **Sn-IX** together with the corresponding amines.[291,299] If phenylisocyanate is added to **Sn-VI**, no nucleophilic attack of the amide onto the unsaturated carbon atom is observed. Instead the γ-carbon atom in the backbone of a second NacNac ligand forms a new bond with the electrophilic isocyanate carbon atom to yield **Sn-X**.[300]

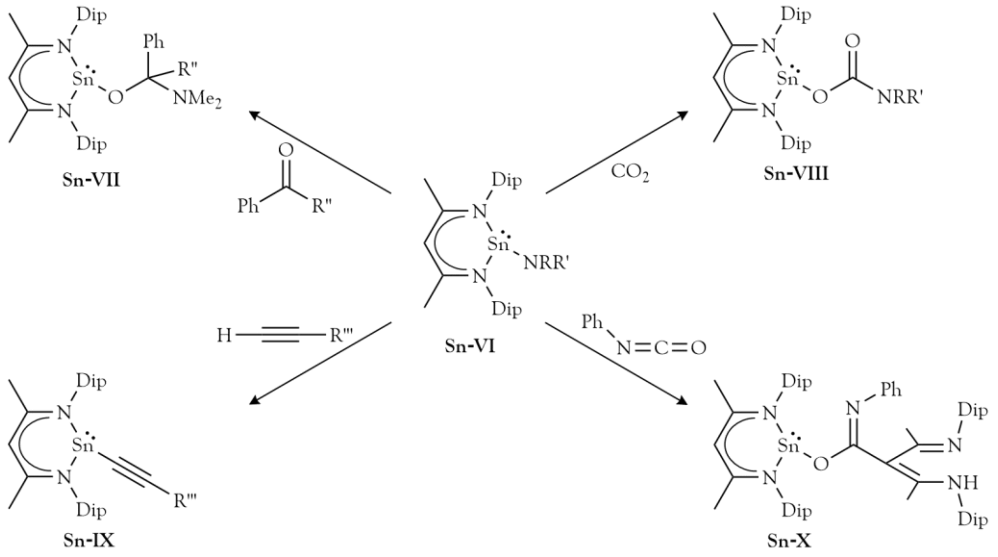

Figure 3-8: Reactivity of stannylene amides **Sn-VI**. R=H, Me, ^{i}Pr; R'=Me, ^{i}Pr, Dip; R''=CF_3, 2-Py; R'''=Ph, CO_2Me, CO_2Et.

Figure 3-9 summarises the reactivity of stannylene alkoxides. They react with carbon dioxide in the same fashion as the amides to give the substituted carbonates **Sn-XII**. However, these carbonates are in equilibrium with the starting materials and readily decompose in absence of CO_2.[301] The isopropoxide derivative (**Sn-XI**, R=O^{i}Pr) reacts with maleic anhydride *via* ring-opening to form stannylene maleate complex **Sn-XIII**.[301] The same compound has also been investigated as an initiator for the living ring-opening polymerisation of racemic lactide.[288] A detailed study has shown that the tin(II) lone pair influences the polymerisation. While repulsive interactions between the lone pairs on tin and oxygen moieties in the monomers are hindering the first propagation steps, thereby causing an induction period prior to the onset of polymerisation, they also introduce heterotacticity into the polymer.[289]

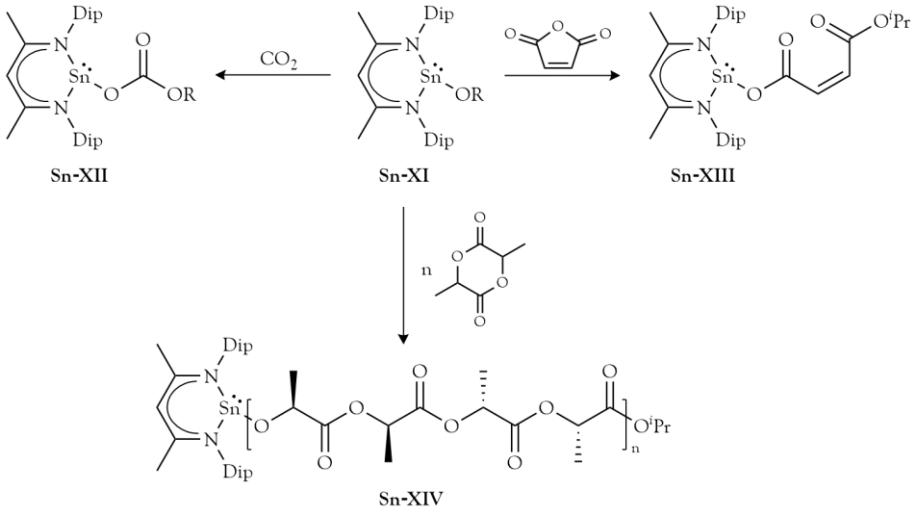

Figure 3-9: Reactivity of stannylene alkoxides **Sn-XI**. R=O^{i}Pr, O^{s}Bu, O^{t}Bu.

Reactivity for stannylene hydride **Sn-XV** with several unsaturated compounds has been reported and is summarised in Figure 3-10. Addition of substituted alkynes leads to *E* and *Z* isomers of the expected hydrostannylation products **(Sn-XVI)**. Isomeric ratios vary between 1:0.7 and 1:1.5 depending on the alkyne esters based on NMR analysis.[302,303] If terminal alkynes are used, vinyl stannylenes **Sn-XVII** are obtained.[303] This is consistent with the reactivity of germylene hydrides towards terminal alkynes as described before and the generally preferred formation of formal anti-Markovnikov products in hydrometallation reactions.[304] Notably, no formation of stannylene acetylides and liberation of dihydrogen is observed as it is the case with stannylene amide **Sn-VI**. Reaction with dicyclohexylcarbodiimide yields the spiro cyclic compound **Sn-XVIII** in which tin as the spiro atom is coordinated by NacNac and the newly formed amidinate ligand.[302] Several symmetric and asymmetric ketones as well as ferrocene carbaldehyde react with **Sn-XV** to form the corresponding stannylene alkoxides **Sn-XIX**.[302,303,305] However, in the cases of pentafluorobenzophenone and perfluorobenzophenone not only the alkoxides **Sn-XXI** are formed, but also fluoro stannylene **Sn-XX** is detected in the reaction mixture in significant amounts (about 40 % based on **Sn-XV**). Moreover, NMR studies show evidence for the presence of fluorinated benzophenones, which underwent fluorine-hydrogen exchange selectively in para position.[305] Lastly, **Sn-XV** is reported to react quantitatively with carbon dioxide at room temperature to yield stannylene formate **Sn-XXII**.[302] In contrast to the germanium analogue, further reactivity of this compound is not reported.

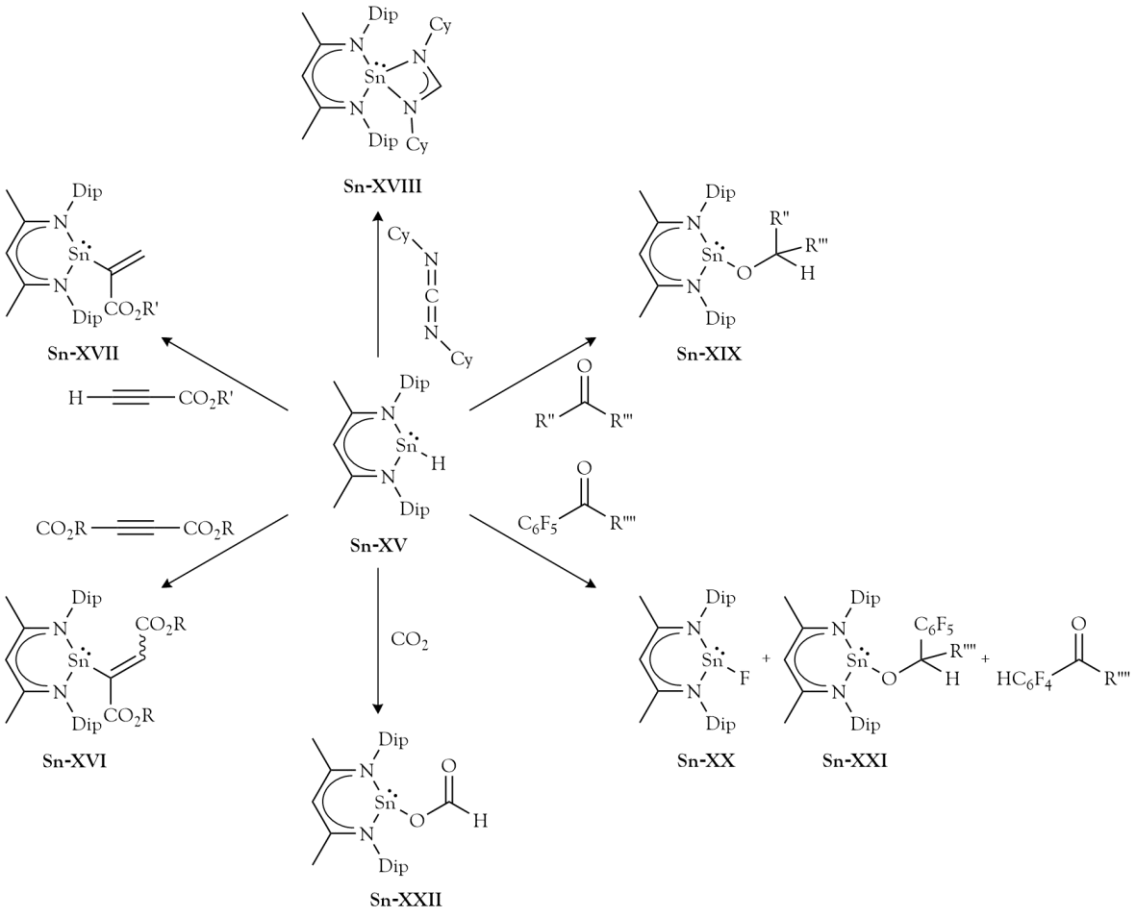

Figure 3-10: Reactivity of stannylene hydride **Sn-XV**. R=Me, Et, ^{t}Bu; R'=Me, Et; R''=^{cy}Pr, Ph, 2-Py, 2-C_4H_3S, Fc; R'''=H, CF_3, ^{cy}Pr, Ph, 2-Py; R''''=Ph, C_6F_5.

Six membered cyclic *N*-chelated stannylenes, which are not based on the NacNac ligand are also known. Figure 3-11 gives an overview of reported compounds. All of them can be synthesised by the reaction of lithiated precursors with $SnCl_2$.[306–310] In case of **Sn-XXIII** also the reaction of the neutral amine with $Sn(HMDS)_2$ is reported.[306,311] **Sn-XXIII** readily forms adducts when treated with $GeAr_2$ or $SnAr_2$ (Ar=2,6-$(Me_2N)_2C_6H_3$) to yield dinuclear complexes.[312] No further reactivity for **Sn-XXIV** is reported and in the case of **Sn-XXV** only substitution of the chloro ligand with silver triflate has been described.[310] The triflate derivative has been found to have an order of magnitude higher fluorescence emission intensity than the chloride precursor. However, this is only observed when silver triflate is used. Control experiments with other metal triflates showed no similar increases. Chiral stannylene **Sn-XXVI** can be transformed into the stannylene cation by treatment with silver triflate or hexafluoroantimonate in thf,[309] but no further reactivity of the cationic species has been reported.

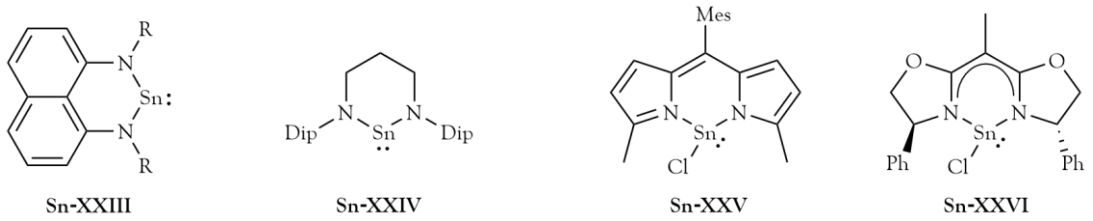

Figure 3-11: *N*-chelated cyclic stannylenes not based on the NacNac ligand scaffold. R=^{i}Pr, $CH_2{}^{t}$Bu, $SiMe_3$, $Si^{i}Pr_3$.

3.1.1.3 Lead

The chemistry of related plumbylenes is considerably less developed. Compounds of the generalised types shown in Figure 3-12 have been reported, but their reactivity remains only vaguely explored. As with the lighter tetrylenes, halo plumbylenes can be obtained from lithiated precursors and lead halides. Syntheses are described for chloro, bromo and iodo derivatives.[313,314] Cationic species of type **Pb-II** are reported and can be obtained by either reacting the chloro plumbylene **Pb-I** with $LiB(C_6F_5)_4$ to yield $[\{HC(CMeNDip)_2\}Pb][B(C_6F_5)_4]$ or the methyl derivative (**Pb-III**, X=Me) with $LiB(C_6F_5)_4$ to yield $[\{HC(CMeNDip)_2\}Pb][MeB(C_6F_5)_4]$.[287] No further reactivity of these species is described.

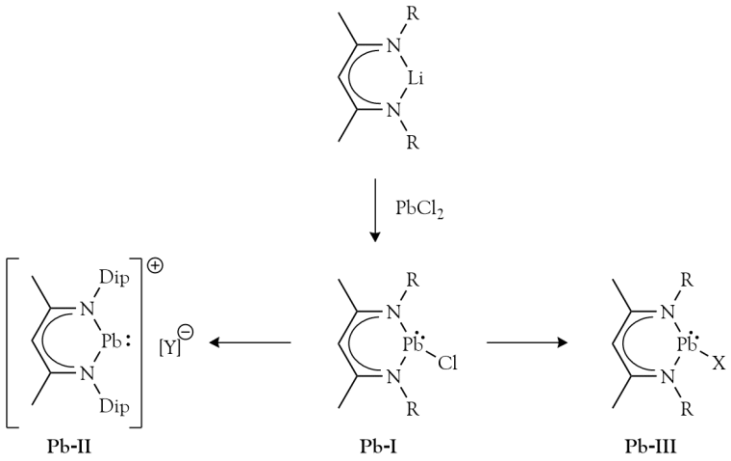

Figure 3-12: Generalised synthesis and reaction pathways for NacNac based plumbylenes. R=Ph, 2,6-$Me_2C_6H_4$, 4-^{i}PrC_6H_4, Dip; X=F, Me, ^{i}Pr, ^{s}Bu, ^{t}Bu, $CH_2{}^{t}$Bu, Ph, Bn, O^{i}Pr, O^{s}Bu, O^{t}Bu, OPh, C≡CPh, NMe_2, $N^{i}Pr_2$, $N(SiMe_3)_2$, NHPh, NHDip, PPh_2, PCy_2, $P(SiMe_3)_2$, OTf; Y=$B(C_6F_5)_4$, $MeB(C_6F_5)_3$.

Similarly to the already discussed germanium and tin compounds, the chloride in **Pb-I** can be substituted for a range of small organic groups. Grignard[315] or lithium reagents[315,316] can be used to introduce alkyl and aryl substituents. Reaction with lithium phenylacetylide yields the expected plumbylene substituted acetylene.[316] Treatment with silver triflate gives the plumbylene triflate, which forms a coordination polymer in the solid-state.[316,317] Plumbylene dimethylamide, diisoproyplamide or anilides are accessible *via* treatment of **Pb-I** with appropriate lithium amides.[300,318] Similarly, reacting **Pb-I** with KHMDS yields plumbylene bis(trimethylsilyl)amide. This is in contrast to the reactivity of analogues germanium and tin compounds, where under the same conditions deprotonation of the NacNac ligand occurs instead of substitution. The plumbylene bis(trimethylsilyl)amide can also be obtained by reaction of free ligand and $Pb(HMDS)_2$.[313] Alkoxides of type **Pb-III** are obtainable from **Pb-I** and potassium alkoxides, if the steric shielding of the NacNac ligand is sufficient.[319] Less sterically hindered ligands such as $\{HC(CMeNR)_2\}^-$ with R=Ph lead to formation of the homoleptic complexes $\{HC(CMeNR)_2\}_2Pb$.[317] In the same way, also plumbylene aryloxides can be synthesised.[320] Alternatively, reaction of the lithium NacNac precursor and lead bis(2,6-di-*tert*-butyl)phenolate directly yields a plumbylene aryloxide of type **Pb-III**. The remaining phenolate ligand can then also be substituted by further reacting it with $LiN(SiMe_3)_2$ or $LiP(SiMe_3)_2$ to obtain the plumbylene amide or phosphide respectively.[321] Other phosphides (R=Ph, Cy) are accessible *via* reaction of **Pb-I** with lithiated precursors $LiPR_2$.[251] Efforts have been taken to synthesise a monomeric plumbylene hydride *via* treatment of **Pb-I** with $K[HBR_3]$, $AlH_3{\cdot}NMe_3$ or $PhSiH_3$. In these reaction only decomposition products such as metallic lead have been obtained so that a **Pb-III** like hydride remains unknown.[318] On the other hand, theoretical investigations show that such a lead(II) hydride, if obtained, would be a far superior catalyst for the reaction with carbon dioxide compared its lighter homologues.[322] Unlike the germylenes and stannylenes no reactivity of **Pb-I** with chalcogenides or towards transition metal complexes has been reported. However, dicyclohexylphosphide of type **Pb-III** ($X=PCy_2$) reacts with sulphur and selenium to form phosphinoselenoites, phosphinodiselenoates and phosphinodithioates. As with its tin counterpart, the oxidation state +II of lead is preserved while the phosphorus is oxidised.[298]

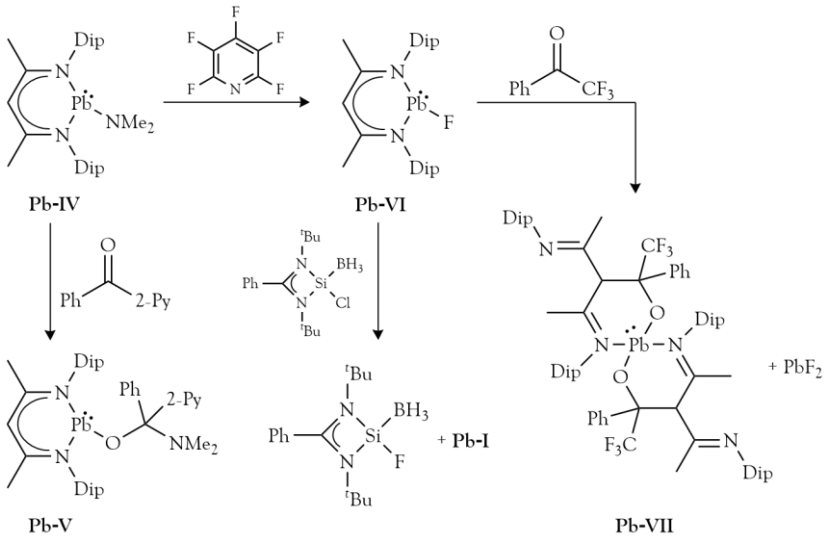

Figure 3-13: Reactivity of plumbylene amide **Pb-IV** and fluoride **Pb-VI**.

Reports on further reactivity of the plumbylenes discussed so far are scarce and summarised in Figures 3-13 and 3-14. Plumbylene dimethylamide **Pb-IV** reacts with 2-benzoyl pyridine to give the alkoxide **Pb-V** as an expected 1,2 addition product.[318] It can also be used synthesise the fluoro plumbylene **Pb-VII** when treated with pentafluoropyridine. This fluoro derivative cannot be obtained by reacting **Pb-I** with Me_3SnF as it has been done with the lighter homologues.[323] **Pb-VII** itself can be used as a fluorinating agent. While fluorination of amidinate stabilised chloro sylilenes has been unsuccessful using other reactants, **Pb-VII** yields the fluoro sylilene under formation of **Pb-I**.[323] Reacting **Pb-VI** with 2,2,2-trifluoroacetophenone does not results in the 1,2-additon of the lead fluorine bond across the carbonyl moiety as it is the case with the lighter homologues. Instead, lead difluoride and a homoleptic lead(II) complex are formed. The latter bears ligands, which result from a carbon-carbon bond formation between the carbonyl group and the γ-position of the NacNac ligand.[323]

In analogy to **Sn-XI**, alkoxides **Pb-VIII** readily react with carbon dioxide to form plumbylene substituted carbonates **Pb-IX**. The respective **Pb-VIII** and **Pb-IX** species form equilibria, which are dependent on the alkoxide group.[319] Furthermore, plumbylene isopropoxide reacts with phenylisocyanate to give carbamate **Pb-X**.[319] Diisopropylamide **Pb-XI** on the other hand reacts with *tert*-butyl isocyanate to form the oxygen bound imino carbamate complex **Pb-XII** regioselectively.[300] If **Pb-XI** is instead reacted with phenylisocyanate, neither carbamate nor imino carbamate is formed. The obtained product **Pb-XIII** is the consequence of carbon-carbon bond formation between the electrophilic isocyanate group and the γ-position of the NacNac ligand.[300] The same outcome is observed in the reaction of stannylene amide **Sn-VI** with phenyl

isocyanate and similar reactivity involving the activation of the γ-carbon atom is described for **Pb-VII**.

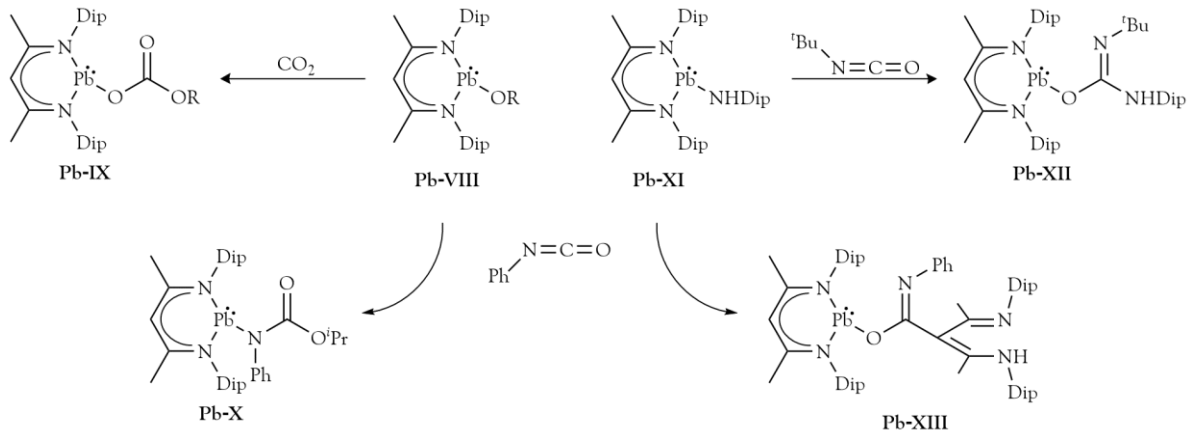

Figure 3-14: Reactivity of plumbylene alkoxides **Pb-VIII** and amide **Pb-XI**. R=^{i}Pr, ^{s}Bu, ^{t}Bu.

Only one non NacNac based six membered cyclic *N*-chelated plumbylene has been reported. It can be synthesised by the reaction of lead(II) chloride with the dilithium salt of 1,3-bis(2,6-diisopropylphenylamino)propane to give what essentially could be described as a saturated analogue of the NacNac based plumbylenes. However, due to the twofold negative charge of the diamido ligand, no additional ligands like chloride are bound to the lead atom.[324] No further reactivity of this compounds has been reported.

3.1.2 Ligands for *N*-heterocyclic tetrylenes

3.1.2.1 Rational design of ligands for low-valent main group compounds

The NacNac ligand has been proven to be a most valuable asset to form compounds with elements all across the periodic table.[325] It can be used to stabilise main group and d-metal complexes in different oxidation states with widespread catalytic applications[326–331] and has been especially advantageous for the stabilisation of low-valent main group compounds such as the tetrylenes discussed in the previous chapters but also beyond.[332–337] One can therefore raise the question, which factors are actually responsible for the ability of the NacNac ligand to stabilise elements in uncommon low oxidations states. Generally speaking, a ligand for this purpose needs to provide sufficient steric shielding to offer kinetic stabilisation and to prevent oligomerisation.[338,339] A second aspect is electronic stabilisation. Theoretical studies have shown that as the principal

quantum number *n* increases, the energetic separation between s and p orbitals becomes larger and hence for metallylenes a singlet ground state is favoured over a triplet one.[340–343] As a consequence the low-valent metal has a lone pair of electrons in an orbital with high s character and a vacant p orbital. In order to stabilise such a state, electron density needs to be donated into the p orbital. The bonding situation of a NacNac tetrylene complex is sketched in Figure 3-15, which shows how the ligand is able to provide these different aspects of stabilisation.

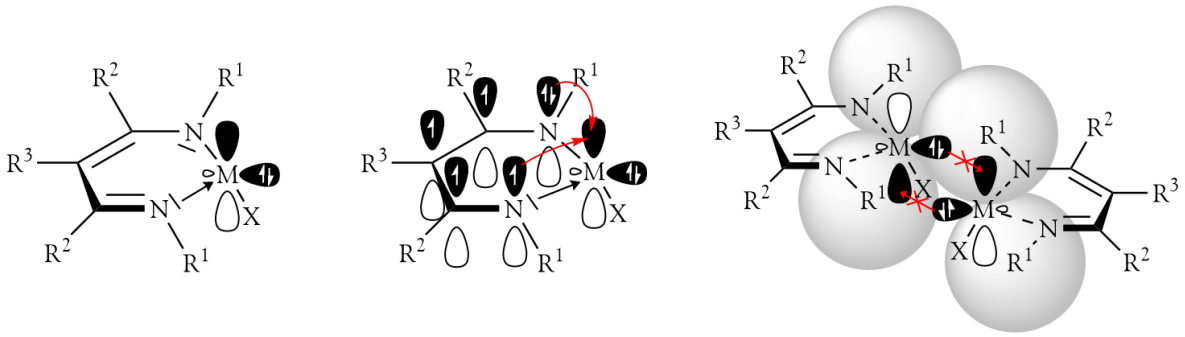

Figure 3-15: General aspects of the stabilising effects of the NacNac ligand in tetrylene complexes. Left: σ bonding between the ligand and the metal fragment. Centre: Electron density donation from the ligand's delocalised π system into the vacant p orbital of the metal fragment. Right: Prevention of dimerization by the steric bulk of substituents R^1.

The metal fragment M is divalent in the sense that it has two electron sharing interactions with substituent X and one of the nitrogen donors. The second nitrogen donor interacts with the metal *via* donation of its lone pair. Because of the conjugated system of double bonds in the ligand backbone, the left part of the figure depicts only one resonance structure. In fact, the system is delocalised and both interactions between nitrogen donors and the metal are equivalent and can be classified as σ bonds. Additionally, donation of electron density from the ligand's π system into the vacant p orbital at the metal is possible. If the metal fragment is located within the ligand plane and the p orbital is oriented accordingly, a conjugated cyclic π system can be formed. Because the ligand's π system contains six electrons, the resulting complex fulfils Hückel's rule. Therefore, the stabilisation of the low oxidation state of the metal is not only attributable to the donation of electron density into the vacant p orbital but also due to resonance stabilisation. The electronic properties of the ligand and thereby also the electron density of the metal can be tuned by choice of the substituents R^1-R^3. However, greater influence results from R^2 and R^3 as these are located within the plane of the ligand, whereas R^1 especially in the case of aryl substituents is often oriented more or less perpendicular to this plane.[328] R^1 takes on a more

important role in the steric shielding of the metal. The right side of figure 3-15 illustrates how the electrophilic p orbital and the nucleophilic lone pair would be able to promote formation of a dimer. However, if the steric bulk of substituents R^1 is sufficient enough, dimerization or even oligomerization is prohibited.

On the other hand, too much steric bulk in R^1 but also R^2 is known to cause bending of the NacNac ligand, which in turn disrupts the delocalisation of its π system and hence lowers the efficiency at which the low-valent metal is stabilised.[328,344] Accordingly, NacNac mimetic ligands have been designed to make use of the described stabilising properties while simultaneously introducing more rigidity into the planar backbone. Bis(benzheterocyclo-2-yl)methanes are one class of such ligands and will be discussed in the following chapter.

3.1.2.2 Beyond NacNac - Bis(benzheterocyclo-2-yl)methanes

As outlined in the previous chapter, NacNac ligands are excellent at stabilising low-valent metal compounds. However, bulky substituents especially at the nitrogen atoms can induce folding in the ligand backbone disrupting the delocalised π system. One way to introduce more rigidity in the ligand and to prevent this folding is to tether the aryl substituents at the nitrogen atoms to the β position in the ligand's backbone (see Figure 3-16). If a heteroatom is used to create this link, bis(benzheterocyclo-2-yl)methanes with extended delocalised π systems are obtained. These compounds were first reported already in the 1950s[345–347] but have not received much attention in coordination chemistry. Apart from one early report on the use as a fluorimetric reagent,[348] systematic studies of bis(benzheterocyclo-2-yl)methanes as chelate ligands started in the 1990s in terms of the preparation of its d-metal complexes.[349–352]

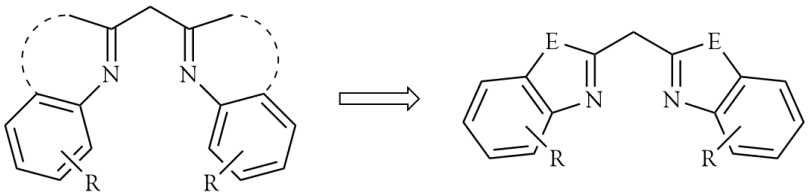

Figure 3-16: Bis(benzheterocyclo-2-yl)methanes rationalised as NacNac mimetics obtained by the introduction of a heteroatom bridge between the imine substituent and the β position in the ligand's backbone.

Work by the Stalke group preceding this thesis laid focus on the preparation of differently substituted bis(benzheterocyclo-2-yl)methanes as ligands for main group metal chemistry.[344,353–355] Bis(benzimidazol-2-yl),[356] bis(benzoxazol-2-yl)[357] and bis(benzothiazol-2-yl)methanes[357] as well as unsymmetrically substituted bis(benzheterocyclo-2-yl)methanes[356] have been synthesised. Each of these could be lithiated or directly reacted with metal alkyls such as, for example, trimethyl aluminium to yield the expected complexes. Substitution of the methylene bridge was also investigated. Replacing the CH_2 unit by an isoelectronic NH group yields the corresponding secondary amines for which preparation of group 1 and 13 complexes was reported as well.[358] The phosphine homologue was studied in more detail. Its aromaticity was assessed by theoretical methods and experimental charge density investigations.[359,360] Despite its tendency to decompose, complexes with alkali metals[359,361] as well as transition metals[361–363] have been reported. Structural analyses of these compounds showed the ability of the bis(benzheterocyclo-2-yl)phosphines to act as *Janus-head* ligands and coordinate different Lewis acids with different donor sites according to the HSAB concept.

In an effort to increase the steric shielding at the coordination site, substituents at the 4-position of bis(benzoxazol-2-yl)methane were introduced and their size gradually increased from methyl[364] to isopropyl[365] and *tert*-butyl groups.[366] Recently, the sterically even more crowded bis(4-benzhydrylbenzoxazol-2-yl)methane has been reported.[367] All of these compounds can be metalated with appropriate alkali metal reagents to yield precursors for the synthesis of main group metal complexes.[368] It is noteworthy that especially potassium salts showed remarkable stability towards stoichiometric amounts of water in controlled hydrolysis experiments.[368,369]

So far these ligands have been used successfully to synthesise complexes with alkaline earth metals[365,366,370] as well as group 13 elements.[364,371] They were even used as ligands in d- and f-metal complexes to study their properties as single molecule magnets.[372–374] With respect to low-valent main group compounds, bis(4-methylbenzoxazol-2-yl)methanide has been used to stabilise the symmetric dialane $[^{Me}BoxAlH]_2$ as well as the asymmetric $[(^{Me}BoxAlH)(^{Dip}NacNacAlH)]$ and the cation of the latter.[375] Carbenoid compounds of group 13 elements in oxidation state +I have been synthesised by the reaction of sodium or potassium salts of the bulky bis(4-benzhydrylbenzoxazol-2-yl)methane with sources of gallium, indium and thallium.[376] Efforts to obtain a bis(benzheterocyclo-2-yl)methane based aluminylene have not been successful so far.

Until now no attempts have been made to synthesise homologues of carbenes by incorporating heavy group 14 elements in oxidation state +II into the bis(benzheterocyclo-2-yl)methane framework.

3.1.3 Scope

In view of the versatile chemistry of the tetrylenes reviewed in chapter 3.1.1, it becomes clear that such compounds constitute intriguing synthetic targets. Hence, considerable research interest is focussed on main group carbenoids. Besides the development of synthetic routes to access these species, this also includes the design of suitable ligand platforms as well as the exploration of their reactivity.

The synthetic work conducted as part of this thesis aims to contribute to this endeavour by investigating the aptitude of the bis(4-methylbenzoxazol-2-yl)methanide ligand to form heavier homologues of *N*-heterocyclic carbenes. The focus will be laid on the preparation and characterisation of complexes containing germanium, tin or lead in oxidation state +II. For this purpose two different synthetic routes will be considered to possibly assess these tetrylenes. Firstly, the parent bis(4-methylbenzoxazol-2-yl)methane shall be converted to alkali metal methanides as precursors for salt metathesis reactions with suitable group 14 reagents. Secondly, the direct reaction of bis(4-methylbenzoxazol-2-yl)methane with germanium, tin or lead amide to yield the envisaged tetrylenes in a concerted deprotonation-metalation reaction will be probed.

Reports of homoleptic tetrylenes bearing two identical NacNac ligands are scarce due to their high steric bulk. If the bis(4-methylbenzoxazol-2-yl)methanide ligand proves to be capable of stabilising the envisaged tetrylenes, it would therefore be of interest to see, if homoleptic complexes could be realised.

Once bis(4-methylbenzoxazol-2-yl)methanide based tetrylenes are obtained, their reactivity shall be investigated. Substitution or abstraction of the remaining halide ligand as well as coordination to d-metal complexes reminiscent of NHCs will be explored.

During this work, unexpected reactivity of potassium bis(4-methylbenzoxazol-2-yl)methanide towards antimony trichloride was observed, yielding a so far unprecedented 1,3-distiba bicyclo[1.1.1]pentane motif. Therefore, efforts were made to further investigate this intriguing compound also by theoretical methods.

3.2 Results and discussion

3.2.1 Synthesis of bis(4-methylbenzoxazol-2-yl)methane

Bis(4-methylbenzoxazol-2-yl)methane (**I**) was prepared according to a published procedure.[364] Starting from the commercially available 2-amino-3-methylphenol a C3 linker is needed. For this reason malononitrile is converted to the more active ethylbisimidate dihydrochloride by reacting it with ethanol and hydrochloric acid in 1,4-dioxane.[377] Refluxing this linker with two equivalents of 2-amino-3-methylphenol in methanol gave **I** in 44 % yield after crystallisation from the reaction mixture (Figure 3-17). The reaction proceeds *via* a twofold cyclocondensation under liberation of ammonia and ethanol.

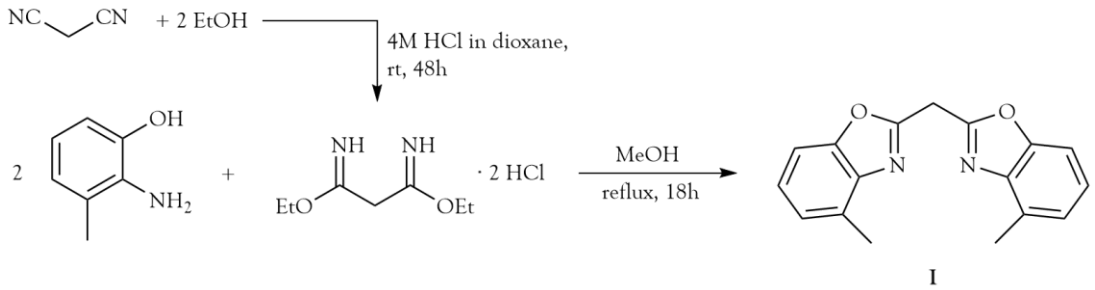

Figure 3-17: Synthesis of ^{Me}BoxH (**I**) by cyclocondensation of 2-amino-3-methylphenol and ethylbisimidate dihydrochloride.

3.2.2 Synthesis of potassium bis(4-methylbenzoxazol-2-yl)methanide

Alkali salts of bis(heterocyclo-2-yl)methanes have already been proven to be good precursors for salt metathesis reactions.[367,371,374] While the lithium methanide can easily be prepared by the use of, for example, butyl lithium, formation of lithium chloride during the subsequent metathesis reaction might lead to unwanted co-complexation. Because such co-complexation tends to be less likely for potassium chloride possibly due to its lower solubility in the used solvents, potassium bis(4-methylbenzoxazol-2-yl)methanide (**II**) was chosen as the precursor. **II** was prepared according to a modified published procedure.[368] Bis(4-methylbenzoxazol-2-yl)methane (**I**) was dissolved in thf and treated with a slide excess of potassium hydride at room temperature (Figure 3-18). After the evolution of hydrogen had ceased and the solution had been stirred for

two hours, all volatiles were removed *in vacuo* to obtain **II** as a yellow powder in high yield (> 90 %). One molecule of thf stays coordinated to the potassium ion and cannot be removed under vacuum at room temperature.

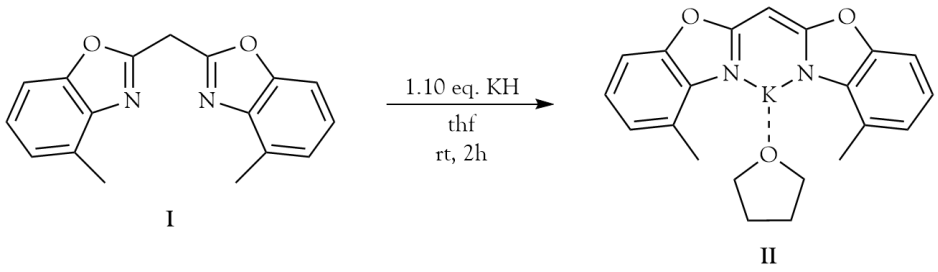

Figure 3-18: Synthesis of ^{Me}BoxK **(II)** by deprotonation with potassium hydride in thf.

3.2.3 Synthesis of {bis(4-methylbenzoxazol-2-yl)methanide}germanium(II) chloride

The examples discussed in chapter 3.1.1 as well as results from previous work of the Stalke group[367,371] formed a reasonable basis to assume that bis(4-methylbenzoxazol-2-yl)methane based tetrylenes might be accessible *via* salt metathesis of potassium precursor **II** and suitable group 14 halides. Thus, $GeCl_2$·dioxane was added to a clear solution of potassium precursor **II** in thf at room temperature (Figure 3-19). Immediately after addition formation of a precipitate was observed, which is assumed to be potassium chloride. After 24 hours of stirring, the reaction mixture was centrifuged and the solution phase separated from the precipitate. Removing all volatiles *in vacuo* yielded the germylene ^{Me}BoxGeCl **(III)** as a yellow powder in 35 % yield. Compound **III** is stable for months if stored as a solid under inert atmosphere at room temperature.

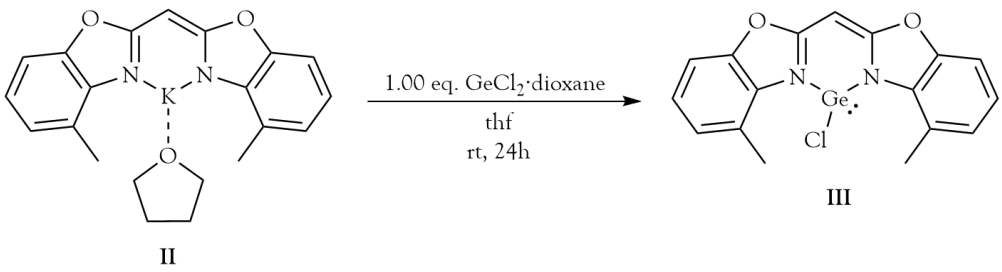

Figure 3-19: Synthesis of ^{Me}BoxGeCl **(III)** by salt metathesis of **II** and $GeCl_2$·dioxane in thf.

The low yield is most probably due to the poor solubility of **III** and can be increased by repeated extraction of the solid residue with thf. If unreacted potassium precursor **II** was present in the product indicated by NMR analysis, separation of **II** and **III** was possible by extraction of **III** with toluene as the potassium salt is virtually insoluble under these conditions.

Comparison of the ^{1}H-NMR spectra of ^{Me}BoxH (**I**), ^{Me}BoxK (**II**) and ^{Me}BoxGeCl (**III**) (Figure 3-20) shows that upon deprotonation the chemical shift of the bridging CH group in ^{Me}BoxK remains mostly unchanged (**I**: 4.68 ppm, **II**: 4.65 ppm) while the methyl (**I**: 2.54 ppm, **II**: 2.41 ppm) and aryl protons (**I**: 7.36-7.08 ppm, **II**: 6.88-6.57 ppm) are shifted upfield. This can be explained by the formation of a delocalised π system across the whole ligand facilitating the shifting of the newly introduced negative charge away from the CH bridge towards the aryl systems. Consequently, the increased electron density causes a stronger shielding of the protons.

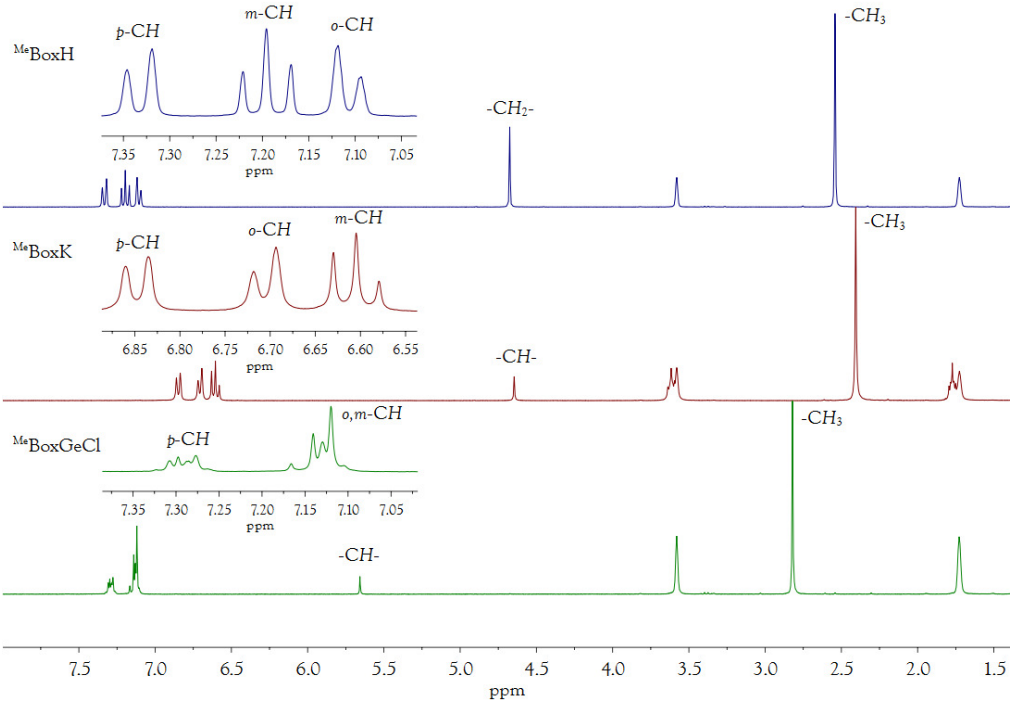

Figure 3-20: Stacked ^{1}H-NMR spectra (300 MHz, thf-d$_8$) of ^{Me}BoxH (**I**), ^{Me}BoxK (**II**) and ^{Me}BoxGeCl (**III**). Ortho, meta and para positions are relative to the methyl groups. Resonances at 3.58 ppm and 1.73 ppm belong to the solvent.

Replacing the potassium cation with the formal GeCl^{+} fragment causes all resonances to shift downfield significantly relative to **II**. Hence, the electron density across the aromatic systems must have been depleted upon coordination of germanium chloride. This suggests that the ligand donates electron density to stabilise the low oxidation state of germanium. The resonances of the aromatic protons overlap and form a more complicated multiplet. The bridging CH group shifts

to 5.66 ppm indicating that the electronic situation in ^{Me}BoxGeCl is distinctly different from the one in ^{Me}BoxK. A possible explanation for this shift would be that the vacant p orbital of the germanium atom is indeed incorporated into the ligand's π system. For a shift of roughly 1 ppm the local change in electron density at the position of the CH group in question must be significant. It can therefore be assumed that the six membered C_3N_2Ge ring indeed forms a conjugated system to provide a good basis for electron density delocalisation.

Yellow plate shaped crystals suitable for single crystal X-ray diffraction analysis were obtained by vapour diffusion of pentane into concentrated solutions of **III** in thf at −25°C after a few days. Compound **III** crystallised in the monoclinic space group $P2_1/c$ (polymorph A) with one molecule in the asymmetric unit. A second polymorph (B) was obtained by crystallisation of **III** from dcm instead of thf. This polymorph crystallised in the triclinic space group $P\bar{1}$ and contained two molecules in the asymmetric unit (Figure 3-21). Both polymorphs contained only ^{Me}BoxGeCl and no lattice solvent molecules or other chemical entities.

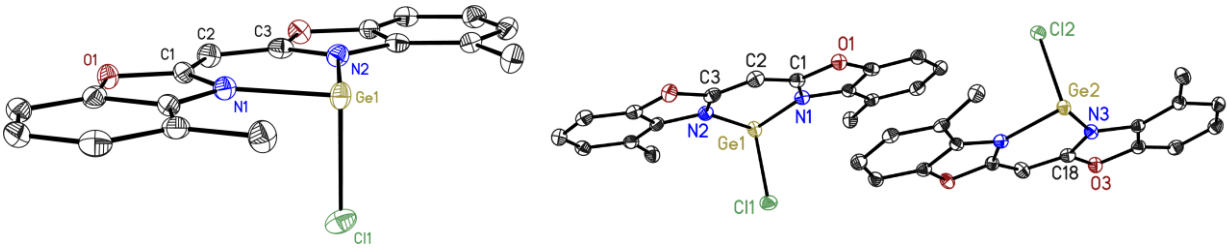

Figure 3-21: Left: Asymmetric unit of ^{Me}BoxGeCl **(III)** (polymorph A) crystallised from thf/pentane. Right: Asymmetric unit of ^{Me}BoxGeCl **(III)** (polymorph B) crystallised from dcm. Anisotropic displacement parameters are depicted at the 50 % probability level. Hydrogen atoms are omitted for clarity.

The molecular structures in both polymorphs are for the most part identical. Therefore only the structure of polymorph A will be discussed in detail. The Ge1-N1 and Ge1-N2 distances are 1.995(2) Å and 1.997(2) Å and thus are identical within the margin of error. They also lie well within the reported values (1.933 Å to 2.021 Å) for cyclic C_3N_2Ge systems with one chloride ligand at the germanium atom (appendix 5.6, Figure 5-31). The equal distances are a first indication of efficient delocalisation. Even more important is the planarity of the central six membered ring. The germanium atom is dislocated only 0.126(3) Å from the C_3N_2 plane. For example, in the compound {HC(CMeNPh)$_2$}GeCl the same dislocation amounts to 0.528 Å.[263] In the same vein the angle between the two planes defined by the benzoxazole subunits in

^{Me}BoxGeCl is quite small at 4.62°, while the corresponding angle in {HC(CMeNPh)$_2$}GeCl measures 14.49°.[263] Hence, it can be seen that the germanium atom is well embedded in the ligand system and the conjugated system works to stabilise the low oxidation state as intended. The crystal structure also indicates a stereoactive lone pair at the germanium atom causing the chloride ligand to adopt almost a 90° angle with respect to the nitrogen atoms. The closest intermolecular contact between germanium and another atom can be found at 3.515 Å. This is the distance between a germanium and a carbon atom of a benzene moiety due to π-π stacking interactions between the ligands. The shortest distance between two germanium atoms is 7.359 Å so that any form of a germanium-germanium interaction can be excluded. Hence, the relatively small steric protection offered by the methyl groups in ^{Me}Box is sufficient to prevent dimerization of the synthesised germylene. This is in contrast to the related gallium compound [^{Me}BoxGa], which readily reacts with itself to form di- and trinuclear species.[354] The monomeric species was also detected by LIFDI mass spectrometry performed with a solution of **III** in thf. The mass spectrum also contains peaks of low intensity, which might indicate formation of dimeric species, but no chemically meaningful constitution could be assigned to those.

In one instance during crystallisation of freshly prepared ^{Me}BoxGeCl, a few yellow, block shaped crystals were obtained, which differed visually from the majority of plate like crystals of the product. Single crystal X-ray diffraction analysis revealed the crystallised species to be an oxygen bridged digermylene (Figure 3-22). (^{Me}BoxGe)$_2$O (**IV**) is most probably formed *via* hydrolysis of **III** due to impurities of water and precedent for such reactivity of chloro germylenes is known.[378]

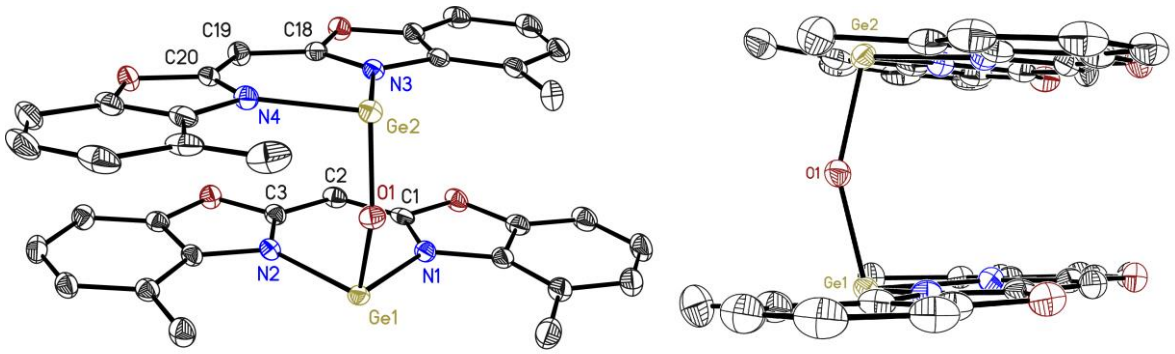

Figure 3-22: Asymmetric unit of (^{Me}BoxGe)$_2$O (**IV**) crystallised from thf/pentane shown from different perspectives. Anisotropic displacement parameters are depicted at the 50 % probability level. Hydrogen atoms are omitted for clarity.

The whole molecule is disordered about its centre of mass with the minor position occupied by roughly 2 % of the molecules. Although the occupation is small, the disorder nevertheless influences the obtained structural parameters due to the strong overlap of both positions. Great care needs to be taken, if structural parameters are to be discussed in such a case. However, some general observations can be made. The two ^{Me}Box ligands deviate by about 6.5° from being parallel and are twisted around the oxo bridge. The Ge1-O1-Ge2 angle (153.24(12)°) is comparable to the values (147.2°, 154.4°, 154.9°)[379,380] of the only three *N*,*N*'-chelated digermylene oxides, which have been reported so far. Interestingly, the dislocations (0.026 Å and 0.069 Å) of the germanium atoms in **IV** from the respective C_3N_2 planes are even smaller than in **III**. Because only a few crystals of this compound were obtained once as a minor side product and no dedicated synthesis was performed, no further analytical data on (^{Me}BoxGe)$_2$O has been obtained. Efforts to synthesise the analogues ^{Me}BoxGeI from GeI_2 under the same conditions failed due to decomposition resulting in intractable product mixtures. Because ^{Me}BoxGeI constitutes a promising starting material for reduction to obtain Ge(+I) species, future attempts to obtain this compound might repeat the reaction at a lower temperature. Alternatively, reaction of ^{Me}BoxGeMe or ^{Me}BoxGeH with elemental iodine might lead to the desired product as it was shown that these approaches gave better results than simple salt metathesis in related aluminium compounds.[354] However, oxidation of germanium might also occur under such conditions.

3.2.4 Synthesis of {bis(4-methylbenzoxazol-2-yl)methanide}tin(II) chloride

Inspired by the results on germanium compound **III** the analogous reaction between ^{Me}BoxK and tin(II) chloride was performed. Both starting materials were suspended in thf and stirred at room temperature for 24 hours (Figure 3-23). However, after the solvent was removed only educts were recovered and no signs of a reaction taking place were observed. The absence of reactivity is attributed to the poor solubility of tin(II) chloride in thf at room temperature. Therefore, the reaction was repeated and heated to reflux. After 48 hours the cloudy reaction mixture was cooled down and all solids were separated by filtration. The resulting clear filtrate was dried *in vacuo* and a light yellow powder was obtained. NMR analysis revealed this powder to be a mixture of free ligand **I** (15-20 % on a molar basis) and a second component likely to be the desired product. This mixture was washed with pentane (1×5 mL) to dissolve and separate the free ligand. The remaining solid was dried under reduced pressure and target compound **V** was obtained as a

yellow powder with a yield of 16 %. Compound **V** is stable for months if stored as a solid under inert atmosphere at room temperature. The ^{1}H-NMR and ^{13}C-NMR spectra of ^{Me}BoxSnCl are very similar to ^{Me}BoxGeCl. The bridging CH group has a ^{1}H chemical shift of 5.43 ppm indicating efficient electron delocalisation in the central six membered C_3N_2Sn ring.

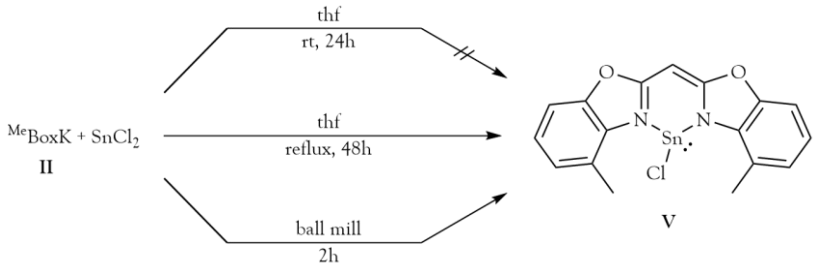

Figure 3-23: Different reaction conditions tested for the synthesis of ^{Me}BoxSnCl (**V**).

Yellow block shaped crystals suitable for single crystal X-ray diffraction analysis were obtained by vapour diffusion of pentane into concentrated solutions of **V** in thf at −25°C after a few days. Compound **V** crystallised in the monoclinic space group $P2_1/c$ with one molecule in the asymmetric unit (Figure 3-24). ^{Me}BoxSnCl is isomorphous to polymorphic form A of ^{Me}BoxGeCl.

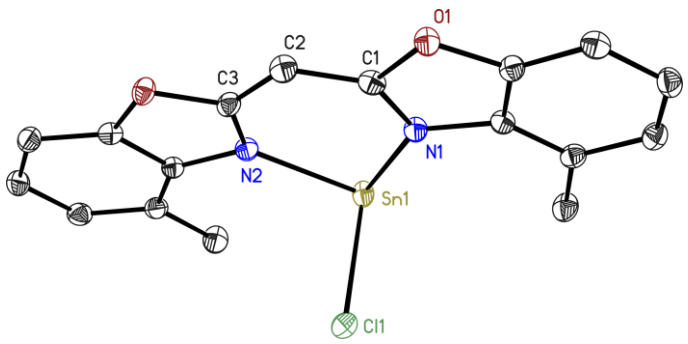

Figure 3-24: Asymmetric unit of ^{Me}BoxSnCl (**V**) crystallised from thf/pentane. Anisotropic displacement parameters are depicted at the 50 % probability level. Hydrogen atoms are omitted for clarity.

The Sn1-N1 and Sn1-N2 distances (2.2073(16) Å, 2.2064(16) Å) are identical within the margin of error. This supports the interpretation of the ^{1}H-NMR spectrum with respect to a well conjugated C_3N_2Sn ring. Both these distances as well as the Sn1-Cl1 distance (2.5060(9) Å) are larger than corresponding distances in ^{Me}BoxGeCl (see Table 3-1) due to the increased radius of the tin(II) cation, but lie well within reported values (2.103 Å to 2.318 Å) for cyclic C_3N_2Sn systems with one chloride ligand at the tin atom (appendix 5.6, Figure 5-32). The dislocation of

the metal from the C_3N_2 plane is even smaller (0.040(2) Å) than in ^{Me}BoxGeCl, suggesting a better fit of the tin(II) cation. In the related compound {HC(CMeNPh)$_2$}SnCl the same dislocation amounts to 0.495 Å.[244] Both benzoxazole subunits of the ^{Me}Box ligand are bent towards the chloride with a butterfly folding angle of 6.43°. This folding is more pronounced than in ^{Me}BoxGeCl (4.62°) but still less than half as big as in {HC(CMeNPh)$_2$}SnCl (13.71°).[244] The trigonal pyramidal environment around the tin atom and the angles between the chloride and both nitrogen atoms being almost 90° indicate a stereoactive lone pair as expected for tin in oxidation state +II. Because **III** and **V** are isostructural also no intermolecular interaction between two tin atoms are observed.

Table 3-1: Comparison of selected structural parameters for ^{Me}BoxGeCl and ^{Me}BoxSnCl. [a]Values obtained from polymorph A. [b]Mean values obtained from the two independent molecules in polymorph B.

distances and angles	**^{Me}BoxGeCl (A)[a]**	**^{Me}BoxGeCl (B)[b]**	**^{Me}BoxSnCl**
M-Cl1 [Å]	2.3366(8)	2.3316(10)	2.5060(9)
M-N1 [Å]	1.995(2)	1.999(2)	2.2073(16)
M-N2 [Å]	1.997(2)	2.002(2)	2.2064(16)
N1-M-N2 [°]	88.69(9)	88.66(10)	84.63(6)
N1-M-Cl1 [°]	94.60(7)	94.75(7)	92.30(4)
N2-M-Cl1 [°]	93.46(7)	93.50(7)	90.56(4)
dislocation of M [Å]	0.126(3)	0.161(4)	0.040(2)

The observation of free ligand as a side product might suggest the presence of water in the solvent causing hydrolysis of either ^{Me}BoxK or ^{Me}BoxSnCl. While the presence of miniscule amounts of water cannot be excluded, although all solvents have been thoroughly dried according to established protocols, reaction with water seems rather unlikely. The high stability of differently substituted potassium bis(benzoxazol-2-yl)methanides has been experimentally investigated.[368,369] The formation of (^{Me}BoxGe)$_2$O on the other hand suggests that hydrolysis occurs preferentially at the chloride site and not the ligand backbone. However, (^{Me}BoxGe)$_2$O was not proven to be the product of the reaction between ^{Me}BoxGeCl and water and either way it is unclear whether these assumptions would hold at elevated temperature. In order to avoid all these factors, the reaction between tin(II) chloride and ^{Me}BoxK was repeated in a ball mill without any solvent.

Both compounds were placed into a grinding bowl made of zirconium dioxide together with grinding balls of the same material. The bowl was sealed under argon atmosphere and placed in a *PULVERISETTE 7* planetary mill. The mill was run for 120 minutes at 500 rpm in intervals of 2 minutes separated by resting periods of 4 minutes. After the reaction was completed, the grinding bowl was transferred into a glove box. ^{1}H-NMR analysis of the crude product showed a mixture of free ligand ^{Me}BoxH and ^{Me}BoxSnCl. Accordingly, it was first washed with pentane (3×5 mL) to separate ^{Me}BoxH from the mixture before the remaining solid was extracted with thf (3×10 mL) to separate the product from insoluble potassium chloride. Removing all volatiles from the combined thf extracts yielded ^{Me}BoxSnCl as a yellow powder in roughly 50 % yield. The solubility of **V** in thf and other common organic solvents is low, which might also be a reason for the moderate yield.

When the reaction is performed in solution the solvent or impurities therein are the most likely cause of hydrolysis and the formation of ^{Me}BoxH. Therefore, it is puzzling to see that even in the absence of any solvent ^{Me}BoxH is formed. Since all starting materials have been checked for impurities of water or ^{Me}BoxH, the proton source remains unclear. However, the amount of free ligand was in the range of 10-15 % on a molar basis over several ball milling experiments, which is about 5 % lower than what was observed, when the reaction is performed in solution.

Considering the lower rate of hydrolysis, the fact that no solvent is needed, the higher yield and the substantially shorter reaction time, ball milling is the clearly preferable method of synthesising ^{Me}BoxSnCl.

3.2.5 Attempted synthesis of {bis(4-methylbenzoxazol-2-yl)methanide}lead(II) [X]$^{-}$

With the germanium and tin compounds **III** and **V** in hands, it was the obvious next step to also attempt the synthesis of ^{Me}BoxPbCl. Stirring lead(II) chloride and ^{Me}BoxK in thf for 24 hours at room temperature lead to no reaction (Figure 3-25). This was most probably due to the low solubility of lead(II) chloride. Lead(II) bromide and nitrate were also tested under these conditions but gave the same results.

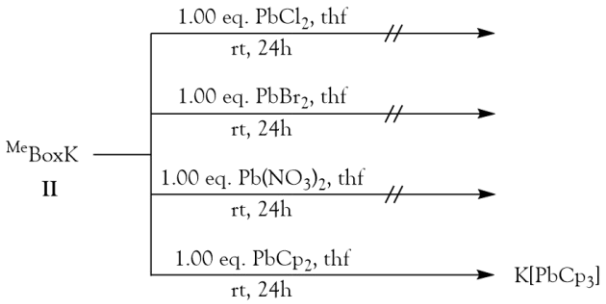

Figure 3-25: Different reaction conditions tested for the synthesis of ^{Me}BoxPbX compounds.

As solubility seemed to be the limiting factor, a more soluble lead(II) source was sought after. Plumbocene was chosen as a promising reagent, but the original method of preparation[381] was noted by later reports to be rather troublesome: "Particular care should be taken in disposing of the black residue produced after sublimation of [$PbCp_2$]. Air exposure can lead to spontaneous ignition in an extremely exothermic reaction followed by explosion. Do not try and fight the fire (rather like the back of a jet engine)."[382] To avoid this, plumbocene was freshly prepared loosely based on an alternative protocol (Figure 3-26).[383] Sodium cyclopentadienide and lead(II) chloride were mixed and a small amount of toluene was added to create a thick slurry. The mixture was heated to 120°C for 24 hours before all volatiles were removed *in vacuo*. The residue was subjected to a Soxhlet extraction with toluene. After the extract was dried under reduced pressure, plumbocene was obtained as a bright yellow powder.

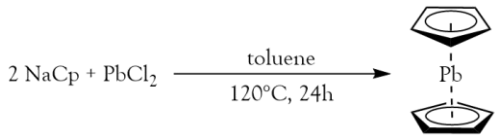

Figure 3-26: Synthesis of plumbocene.

Reaction of plumbocene with ^{Me}BoxK in thf at room temperature lead to a mixture of products, which could not be identified by NMR analysis. Crystals suitable for single crystal X-ray diffraction analysis were grown by vapour diffusion of pentane into thf solutions of the crude product at −25°C. The obtained data showed twinning of the crystals and suffered from disorder. No satisfactory model could be obtained, however, the identity of the crystallised species could be determined to be K[$PbCp_3$]. While the product ^{Me}BoxPbCp stays elusive, formation of K[$PbCp_3$] could be a hint that the envisaged reaction took place. Formally, the sole side product would be potassium cyclopentadienide, which could react with plumbocene to give K[$PbCp_3$].

The success with the solid-state synthesis of ^{Me}BoxSnCl *via* ball milling suggested applying the same method also to the synthesis of ^{Me}BoxPbCl. Therefore, $PbCl_2$ and ^{Me}BoxK were placed into a grinding bowl made of zirconium dioxide together with grinding balls of the same material. The bowl was sealed under argon atmosphere and placed in a *PULVERISETTE 7* planetary mill. The mill was run for 120 minutes at 500 rpm in intervals of 2 minutes separated by resting periods of 4 minutes. After the milling was completed, the grinding bowl was transferred to a glove box. The light yellow powder obtained was suspended in thf in an attempt to separate soluble compounds from potassium chloride. However, the solution immediately underwent a colour change from yellow to red and became slightly yellow again over the course of several hours. Presumably the formed product decomposed in solution. ^{1}H-NMR analysis in thf-d_8 of the crude product showed a mixture of ^{Me}BoxH and ^{Me}BoxK of 1:3 on a molar basis.
Due to these findings, no further experiments were performed to synthesise ^{Me}BoxPbCl in solution at elevated temperature, as it was done for the analogues tin compound.

3.2.6 Synthesis of {bis(4-methylbenzoxazol-2-yl)methanide}germanium(II) bis(trimethylsilyl)amide

The synthesis of ^{Me}BoxGeCl and ^{Me}BoxSnCl was successful, however, both compounds showed only low solubility in common organic solvents. One possibility to improve the solubility was to substitute the chloride ligand. Group 14 compounds with excellent solubility in organic solvents are the bis(trimethylsilyl)amides. Hence, substitution of the chloride in ^{Me}BoxGeCl for such an amide should increase the solubility of the compound significantly. Reaction of ^{Me}BoxGeCl with, for example, Li(HMDS) would most probably give the envisaged product. However, it could also be possible to react the free ligand directly with $Ge(HMDS)_2$ as a germanium(II) source and a deprotonation agent at the same time. Therefore, germanium(II) bis(trimethylsilyl)amide **(VI)** was freshly prepared according to a published procedure (Figure 3-27).[384] Germanium(II) chloride dioxane complex was reacted with lithium bis(trimethylsilyl)amide in thf at room temperature. After this mixture was stirred for two and a half hours, all volatiles were removed *in vacuo*. The residue was extracted with pentane and the extract dried under reduced pressure to give **VI** as an orange-red oily liquid in 74 % yield. NMR analysis gave comparable results to published data and **VI** was used without further purification.

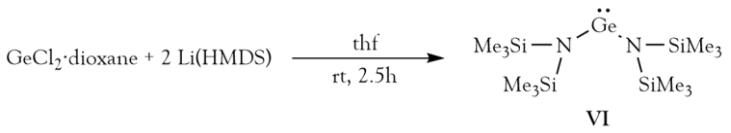

VI

Figure 3-27: Synthesis of germanium(II) bis(trimethylsilyl)amide **(VI)**.

The next step was to react $Ge(HMDS)_2$ with ^{Me}BoxH (Figure 3-28). Mixing both compounds in thf at room temperature gave a clear orange solution, which turned lighter in colour over time. After one day of stirring, all volatiles were removed under reduced pressure to obtain {bis(4-methylbenzoxazol-2-yl)methanide}germanium(II) bis(trimethylsilyl)amide **(VII)** as a yellow powder in 55 % yield. **VII** is soluble in chloroform, dichloromethane, thf, benzene, toluene and to some extend even in pentane as well as hexane. Hence, the solubility of ^{Me}BoxGe(HMDS) is significantly improved compared to ^{Me}BoxGeCl as intended. If impurities of unreacted starting materials are detected in the obtained yellow powder, it might be washed with pentane. This lowers the yield, as the product is also dissolved to some extent, however, it is still higher than for ^{Me}BoxGeCl (35 %). Compound **VII** is stable for months if stored as a solid under inert atmosphere at room temperature.

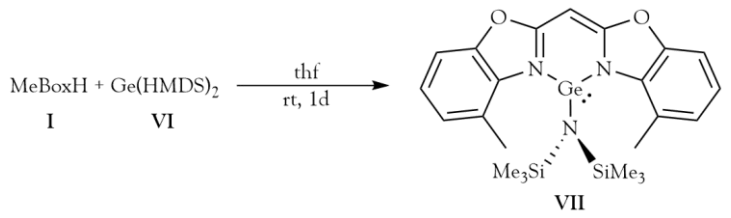

VII

Figure 3-28: Simultaneous deprotonation-metalation reaction between ^{Me}BoxH **(I)** and $Ge(HMDS)_2$ **(VI)** for the synthesis of {bis(4-methylbenzoxazol-2-yl)methanide}germanium(II) bis(trimethylsilyl)amide **(VII)**.

^{1}H- and ^{13}C-NMR analysis of ^{Me}BoxGe(HMDS) gave results very similar to those for ^{Me}BoxGeCl with respect to the bis(4-methylbenzoxazol-2-yl)methanide ligand and additional resonances for the trimethylsilyl groups. In the ^{1}H-NMR spectrum the resonance of the methyl groups is unchanged, while the resonances of the aromatic protons are shifted upfield by about 0.1 ppm. The chemical shift of the bridging CH group can be found at 5.36 ppm. Compared to the corresponding resonance in ^{Me}BoxGeCl (5.66 ppm) this could be an indication of a slightly less well developed conjugated π system in the central C_3N_2Ge ring. LIFDI mass spectrometry confirmed the monomeric nature of **VII** in thf, with the molecular ion peak being the most

intense. The recorded mass spectrum also featured peaks at 715.9 m/z and 1020.0 m/z (54 % and 33 % relative intensity, respectively), which according to their isotope pattern might be species containing two germanium atoms. However, these species cannot be the result of just dimerization and ligand scrambling as the corresponding mass does not match the detected values. No chemically meaningful composition could be derived to explain these peaks.

Yellow block shaped crystals suitable for single crystal X-ray diffraction analysis were obtained from concentrated solutions of **VII** in pentane at −25°C after a few days. Compound **VII** crystallised in the triclinic space group $P\bar{1}$ with one molecule in the asymmetric unit (Figure 3-29). The Ge1-N1 and Ge1-N2 distances (2.0710(14) Å, 2.0782(14) Å) are slightly different from each other and larger than the corresponding distances in ^{Me}BoxGeCl (see Table 3-2). As a consequence, the N1-Ge1-N2 angle becomes more acute. This supports the interpretation of the ^{1}H-NMR spectrum with respect to a less well conjugated C_3N_2Ge ring. Surprisingly though, the dislocation of Ge1 from the C_3N_2 plane (0.032(2) Å) is significantly smaller than in ^{Me}BoxGeCl. The ^{Me}Box ligand itself is only very slightly twisted with an angle of 2.17°. The germanium atom has a trigonal pyramidal coordination environment as expected for germanium in oxidation state +II.

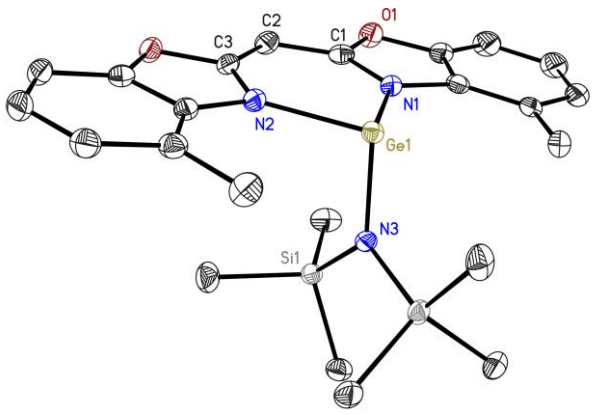

Figure 3-29: Asymmetric unit of ^{Me}BoxGe(HMDS) (**VII**) crystallised from pentane. Anisotropic displacement parameters are depicted at the 50 % probability level. Hydrogen atoms are omitted for clarity.

Table 3-2: Selected structural parameters for the comparison of ^{Me}BoxGeCl and ^{Me}BoxGe(HMDS). [a]Values obtained from polymorphic form A. [b]Mean values obtained from the two independent molecules in polymorph B.

distances and angles	**^{Me}BoxGeCl (A)[a]**	**^{Me}BoxGeCl (B)[b]**	**^{Me}BoxGe(HMDS)**
Ge1-N1 [Å]	1.995(2)	1.999(2)	2.0710(14)
Ge1-N2 [Å]	1.997(2)	2.002(2)	2.0782(14)
N1-Ge1-N2 [°]	88.69(9)	88.66(10)	86.66(6)
sum of angles around Ge1 [°]	276.75(23)	276.91(24)	285.39(16)
dislocation of Ge1 [Å]	0.126(3)	0.161(4)	0.032(2)

One could expect the high steric demand of the bis(trimethylsilyl)amide to force the germanium atom away from the ligands binding pocket. While this is true with respect to the elongated nitrogen-germanium distances, the planarity of the six membered C_3N_2Ge ring is preserved. Apparently, the inclusion of germanium in the conjugated π system is favourable enough, so that dislocation below the ligand plane is prevented. Therefore, the steric influence of the amide can hardly explain the observed changes in the ^{1}H-NMR spectrum relative to ^{Me}BoxGeCl. Instead, an electronic influence might be the reason. The amide can be expected to exhibit a +M effect. Hence, it donates electron density to the germanium atom and aids in the stabilisation of its low oxidation state, so that in return less electron density is accepted from the bis(4-methylbenzoxazol-2-yl)methanide. The observed changes can therefore be understood as a consequence of reduced acceptance of electron density for electronic reasons rather than decreased donation due to structural reasons.

3.2.7 Synthesis of {bis(4-methylbenzoxazol-2-yl)methanide}tin(II) bis(trimethylsilyl)amide

The successful synthesis of ^{Me}BoxGe(HMDS) gave good reason to try to synthesise the higher homologues. Therefore, $Sn(HMDS)_2$ **(VIII)** was freshly prepared in the same way as $Ge(HMDS)_2$, but starting from tin(II) chloride. $Sn(HMDS)_2$ was then reacted with ^{Me}BoxH at room temperature in thf (Figure 3-30). The initially clear orange-red solution turned lighter in colour over time. After one day of stirring, all volatiles were removed under reduced pressure to obtain {bis(4-methylbenzoxazol-2-yl)methanide}tin(II) bis(trimethylsilyl)amide **(IX)** as a yellow powder in

79 % yield. **IX** has high solubility in chloroform, dichloromethane, thf, benzene and toluene. Like ^{Me}BoxGe(HMDS) it dissolves to some extend in pentane or hexane. Impurities of unreacted starting materials might be washed away with pentane. However, due to the solubility of the product, the yield will be decreased. Compound **IX** is stable for months if stored as a solid under inert atmosphere at room temperature.

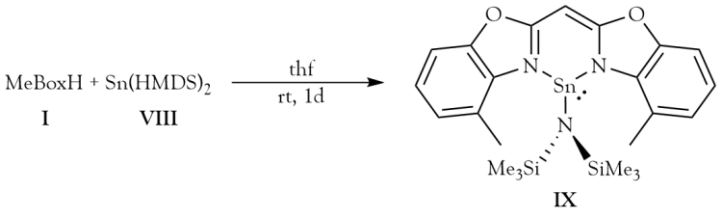

Figure 3-30: Simultaneous deprotonation-metalation reaction between ^{Me}BoxH (**I**) and Sn(HMDS)$_2$ (**VIII**) for the synthesis of {bis(4-methylbenzoxazol-2-yl)methanide}tin(II) bis(trimethylsilyl)amide (**IX**).

The ^{1}H- and ^{13}C-NMR spectra of ^{Me}BoxSn(HMDS) are similar to those of ^{Me}BoxGe(HMDS) and ^{Me}BoxSnCl. All observed resonance shifts are only of small magnitude (0.1 ppm to 0.3 ppm). Analysis of a solution of **IX** in thf by LIFDI mass spectrometry confirmed its monomeric nature (557.4 *m/z*). Apart from the molecular ion peak, the spectrum contained small peaks at 807.8 *m/z* (4 % relative intensity), which according to its isotope pattern most probably corresponds to a species containing two tin atoms, and at 674.0 *m/z* (3 % relative intensity). The latter corresponds to the homoleptic compound (^{Me}Box)$_2$Sn.

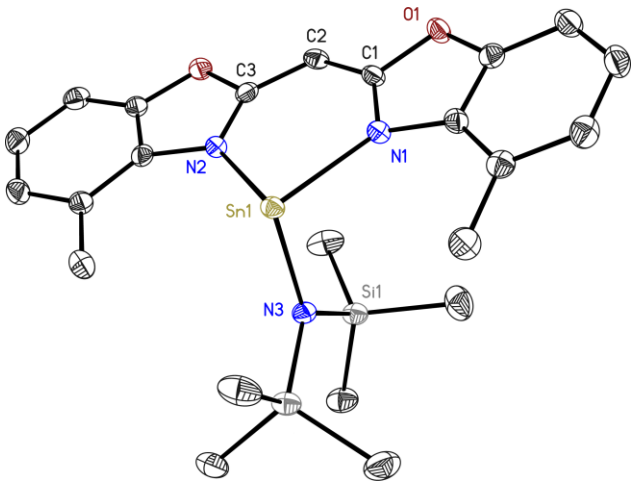

Figure 3-31: Asymmetric unit of ^{Me}BoxSn(HMDS) (**IX**) crystallised from pentane. Anisotropic displacement parameters are depicted at the 50 % probability level. Hydrogen atoms are omitted for clarity.

Yellow block shaped crystals suitable for single crystal X-ray diffraction analysis were obtained from concentrated solutions of **IX** in pentane at −25°C after a few days. Compound **IX** crystallised in the triclinic space group $P\bar{1}$ with one molecule in the asymmetric unit (Figure 3-31). The Sn1-N1 and Sn1-N2 distances (2.2733(17) Å, 2.2698(17) Å) are equal within the margin of error and larger than the corresponding distances in ^{Me}BoxSnCl (see Table 3-3). As a consequence, the N1-Sn1-N2 angle becomes more acute. The sum of angles around Sn1 is bigger than in ^{Me}BoxSnCl reflecting the higher steric demand of the amide and the overall trigonal pyramidal environment is a strong indicator for a stereoactive lone pair.

Table 3-3: Selected structural parameters for the comparison of ^{Me}BoxSnCl, ^{Me}BoxGe(HMDS) and ^{Me}BoxSn(HMDS).

distances and angles	**^{Me}BoxSnCl**	**^{Me}BoxGe(HMDS)**	**^{Me}BoxSn(HMDS)**
M1-N1 [Å]	2.2073(16)	2.0710(14)	2.2733(17)
M1-N2 [Å]	2.2064(16)	2.0782(14)	2.2698(17)
N1-M1-N2 [°]	84.63(6)	86.66(6)	82.90(6)
sum of angles around M1 [°]	267.49(14)	285.39(16)	280.10(18)
dislocation of M1 [Å]	0.040(2)	0.032(2)	0.196(3)

Both benzoxazole subunits of the ^{Me}Box ligand are bent away from the amide with a butterfly folding angle of 11.6°, which is significantly bigger than in ^{Me}BoxSnCl and almost as big as in {HC(CMeNPh)$_2$}SnCl (13.71°).[244] The dislocation of the tin atom from the C_3N_2 plane amounts to 0.196(3) Å. This value is not only bigger than in ^{Me}BoxSnCl or ^{Me}BoxGe(HMDS), the tin atom is also dislocated in the opposite direction. With all these deviations from planarity, more pronounced changes in the NMR spectra of ^{Me}BoxSn(HMDS) would be expected with respect to ^{Me}BoxGeCl, ^{Me}BoxSnCl or ^{Me}BoxGe(HMDS). Assuming that the structure of **IX** in solution is less distorted to be in accordance with the NMR data, the reason for the observed bending and dislocation must be in the solid-state. Therefore, interactions in the solid-state were investigated and indeed formation of π-π stacked dimers is observed as shown in Figure 3-32. The distances between the two molecules are between 3.3 Å and 3.6 Å. The benzoxazole units of both molecules are bent towards each other presumably because of the attractive π-π stacking interaction.

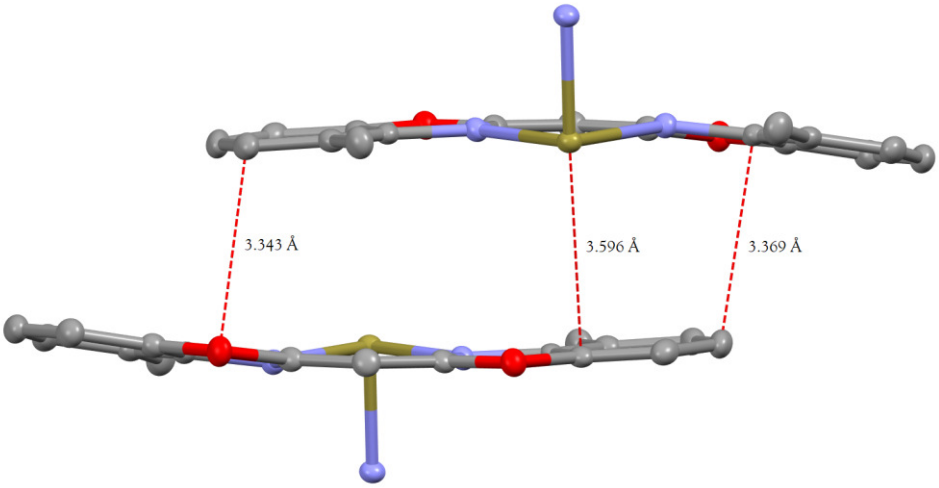

Figure 3-32: Two neighbouring molecules of ^{Me}BoxSn(HMDS) **(IX)** in the solid-state. Anisotropic displacement parameters are depicted at the 50 % probability level. Hydrogen atoms and trimethylsilyl groups are omitted for clarity. Dashed red lines indicate the shortest distance between the respective atoms.

This might also explain the dislocation of the tin atom, if it is pulled towards the neighbouring molecule due to attractive interactions. In fact, the shortest distance between the tin atom and a carbon atom in the neighbouring molecule is 3.596 Å, which is shorter than the sum of their van der Waals radii (3.87 Å).[385] It can therefore be assumed, that the relative high degree of non-planarity of the ^{Me}BoxH ligand in ^{Me}BoxSn(HMDS) is due to interactions in the solid-state and does not represent the structure of isolated or solvated molecule in solution. Although dimers are formed, no tin-tin interaction is observed. Both tin atoms in the dimer are separated by more than 6 Å, because the two molecules are rotated by 180° against each other.

3.2.8 Synthesis of {bis(4-methylbenzoxazol-2-yl)methanide}lead(II) bis(trimethylsilyl)amide

Firstly, $Pb(HMDS)_2$ **(X)** was freshly prepared from lithium bis(trimethylsilyl)amide and lead(II) chloride in analogy to its lighter congeners. $Pb(HMDS)_2$ was then reacted with ^{Me}BoxH at room temperature in thf (Figure 3-33). The mixture was stirred for 24 hours before all volatiles were removed *in vacuo* and {bis(4-methylbenzoxazol-2-yl)methanide}lead(II) bis(trimethylsilyl)amide **(XI)** was obtained as a yellow powder in 73 % yield. Like the lighter homologues, **IX** shows high solubility in chloroform, dichloromethane, thf, benzene and toluene and is partially soluble in

pentane or hexane. Impurities of unreacted starting materials might be washed away with pentane. However, due to the solubility of the product, the yield will be decreased. Compound **XI** is stable for month if stored as a solid under inert atmosphere at room temperature.

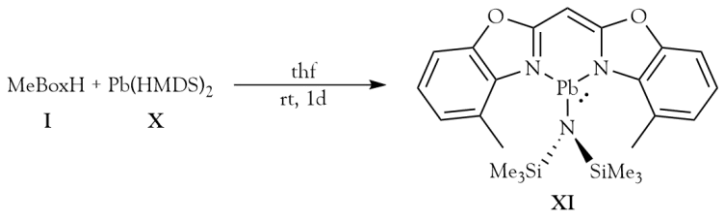

XI

Figure 3-33: Simultaneous deprotonation-metalation reaction between ^{Me}BoxH (**I**) and Pb(HMDS)$_2$ (**X**) for the synthesis of {bis(4-methylbenzoxazol-2-yl)methanide}lead(II) bis(trimethylsilyl)amide (**XI**).

NMR analysis of ^{Me}BoxPb(HMDS) gave results similar to ^{Me}BoxGe(HMDS) and ^{Me}BoxSn(HMDS). Shifts in the resonances are minor except for the bridging CH group. At 5.18 ppm it is more strongly shielded than in the other compounds (**VII**: 5.36 ppm, **IX**: 5.43 ppm), indicating less conjugation in the central heterocycle. The LIFDI mass spectrum contained only one peak at 762.0 *m/z*, which corresponds to the homoleptic compound (^{Me}Box)$_2$Pb. This is rather surprising as the compound was characterised as ^{Me}BoxPb(HMDS) by ^{1}H- and ^{13}C-NMR. Furthermore, authentic samples of (^{Me}Box)$_2$Pb were also synthesised as part of this thesis (see chapter 3.2.11) so that both compounds can unambiguously be differentiated. Nevertheless, the homoleptic compound was exclusively detected.

Yellow plate shaped crystals suitable for single crystal X-ray diffraction analysis were obtained from concentrated solutions of **XI** in pentane at −25°C after a few days. Compound **XI** crystallised in the triclinic space group $P\bar{1}$ (polymorph A) with one molecule in the asymmetric unit (Figure 3-34). This polymorph is isomorphous to the structure of ^{Me}BoxSn(HMDS). A second polymorph (B) was obtained by crystallisation of **XI** from dcm in the form of yellow blocks. This polymorph crystallised in the triclinic space group $P\bar{1}$ with one molecule in the asymmetric unit as well but differs in the three dimensional arrangement of molecules.

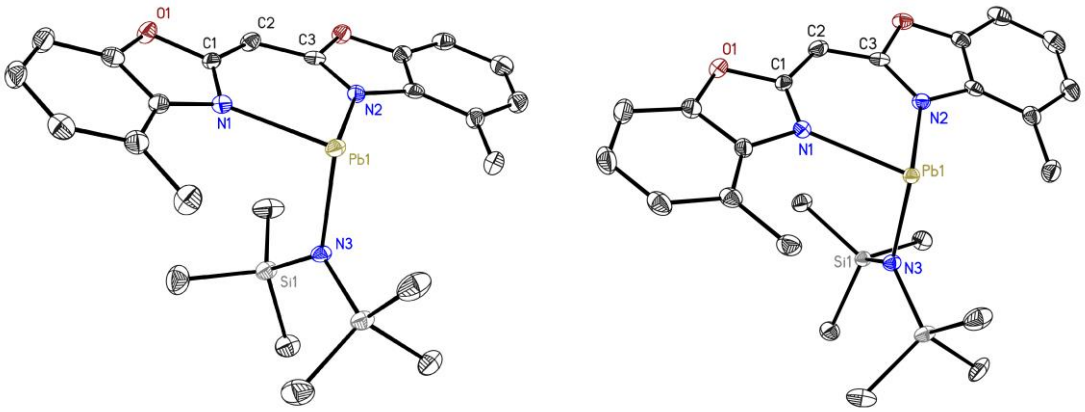

Figure 3-34: Left: Asymmetric unit of ^{Me}BoxPb(HMDS) (**XI**) (polymorph A) crystallised from pentane. Right: Asymmetric unit of ^{Me}BoxPb(HMDS) (**XI**) (polymorph B) crystallised from dcm. Anisotropic displacement parameters are depicted at the 50 % probability level. Hydrogen atoms are omitted for clarity.

The Pb1-N1 and Pb1-N2 distances (**XI**(A): 2.391(3) Å, 2.383(3) Å; **XI**(B): 2.3965(19) Å, 2.3956(19) Å) are very similar or equal within the margin of error depending on the polymorph. Due to the increased ionic radius of the Pb(II) cation the N1-Pb1-N2 angle (**XI**(A): 80.58(9)°; **XI**(B): 80.04(7)°) is more acute than the corresponding angle in the lighter homologues. The sum of angles around Pb1 (**XI**(A): 277.73(27)°; **XI**(B): 278.64(21)°) is the smallest among this group of compounds. This is somewhat surprising as one would expect the lone pair of lead(II) to have predominantly s character and be less stereochemically active due to the inert pair effect. As a consequence the coordination environment should change from trigonal pyramidal to trigonal planar. In Table 3-4 all angles around the metal atom in the characterised structures are compared. While the *N*,*N*' bite angle of the ligand decreases with increasing size of the metal, the angles between the amide substituent and the ^{Me}Box ligand all lie within 1° of each other.

Table 3-4: Selected angles for the comparison of ^{Me}BoxGe(HMDS), ^{Me}BoxSn(HMDS) and ^{Me}BoxPb(HMDS).

	N1-M1-N2 [°]	N1-M1-N3 [°]	N2-M1-N3 [°]
^{Me}BoxGe(HMDS)	86.66(6)	99.24(5)	99.49(5)
^{Me}BoxSn(HMDS)	82.90(6)	98.49(6)	98.71(6)
^{Me}BoxPb(HMDS) (A)	80.58(9)	98.51(9)	98.64(9)
^{Me}BoxPb(HMDS) (B)	80.04(7)	98.97(7)	99.63(7)

Due to the energy gap between s and p orbitals increasing with atom size, the varying s character of the lone pair would be expected to be reflected in less acute angles. Because this is not the case, the metal lone pairs seems not to be a determining factor for the structure of these compounds. Rather, it seems that the structure is determined by the geometry of the vacant p orbitals at the metal(II) centre as depicted in Figure 3-35. This would rationalise the almost constant N1-M1-N3 and N2-M1-N3 angles as predefined by the 90° angle between the p orbitals. In fact, for the chloride analogues, where repulsive interactions between ^{Me}Box and the chloride are expected to be much smaller than between ^{Me}Box and the amide, the corresponding angles are even closer to 90°. It also shows that the σ donation of the amide and the π donation of the ^{Me}Box ligand would compete for the same orbital, further supporting the argument made in chapter 3.2.6 that the amide indirectly influences the electron density in the ^{Me}Box ligand.

Because polymorph A of **XI** is isomorphous to ^{Me}BoxSn(HMDS), it shows the same π-π stacking interactions resulting in the formation of dimers. Accordingly, the ^{Me}Box ligand shows a similar butterfly folding angle (**XI**(A): 10.49°, **IX**: 11.6°) and the lead atom is dislocated above the ligand plane (**XI**(A): 0.224(4) Å, **IX**: 0.196(3) Å). The distances between the two molecules are between 3.3 Å and 3.6 Å. In polymorph B of **XI** the planes defined by the benzoxazole subunits intersect at a smaller angle (6.86°) and are twisted against each other instead of forming a butterfly fold. The lead atom is again dislocated above the ligand plane, but only by 0.173(3)°Å. π-π stacked dimers are also observed in this polymorph. An excerpt of the solid-state structure is shown in Figure 3-36.

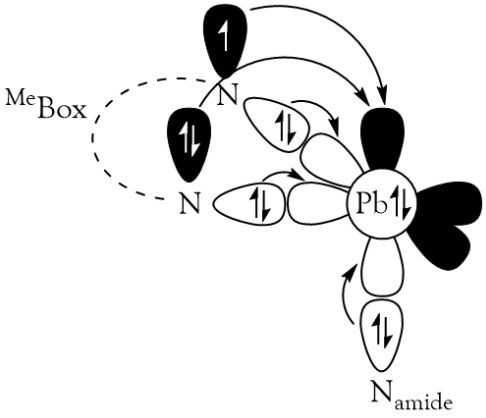

Figure 3-35: Schematic depiction of the bonding interactions between a non-hybridised lead (II) cation and the three nitrogen donors in ^{Me}BoxPb(HMDS).

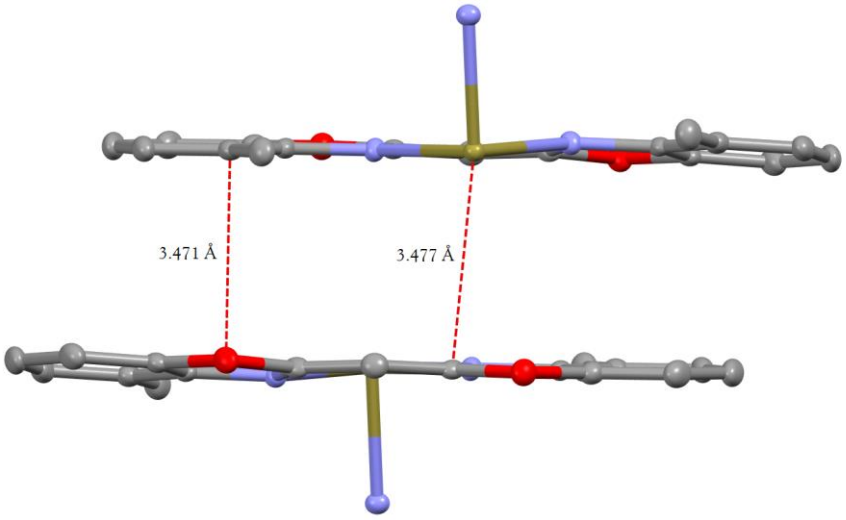

Figure 3-36: Intermolecular interactions in the solid-state structure of ^{Me}BoxPb(HMDS) **(XI)** (polymorph B). Anisotropic displacement parameters are depicted at the 50 % probability level. Hydrogen atoms and trimethylsilyl groups are omitted for clarity. Dashed red lines indicate the shortest distance between the respective atoms.

The two molecules of a dimer are separated by distances between 3.47 Å and 3.48 Å and almost parallel as indicated by a 0.5° intersection angle of the ^{Me}Box ligand planes. Comparing both polymorphs the overlap between the π systems of both molecules seems to be bigger in polymorph B. This probably prevents the butterfly folding as otherwise the outer perimeter of the molecules would be too close to each other.

Because no other structure of a {bis(4-methylbenzoxazol-2-yl)methanide}lead(II) complex is known, it cannot be said, if the dislocation of the lead atom from the ligand plane is only due to the solid-state interactions or if lead might not fit in the binding pocket in general. In the case of tin, the structure of ^{Me}BoxSnCl served as a reference. The ^{1}H-NMR analysis also gave indication that the lead atom is less well embedded in the ligand system than the lighter homologues.

3.2.9 Attempted synthesis of bis{bis(4-methylbenzoxazol-2-yl)methanide}germanium(II)

Curious if also a homoleptic germylene with two bis(4-methylbenzoxazol-2-yl)methanide ligands could be synthesised, two equivalents of the free ligand ^{Me}BoxH **(I)** were reacted with germanium(II) bis(trimethylsilyl)amide **(VI)** in thf at room temperature (Figure 3-37). After 24

hours of stirring all volatiles were removed *in vacuo*. The residue was washed with pentane and again dried under reduced pressure.

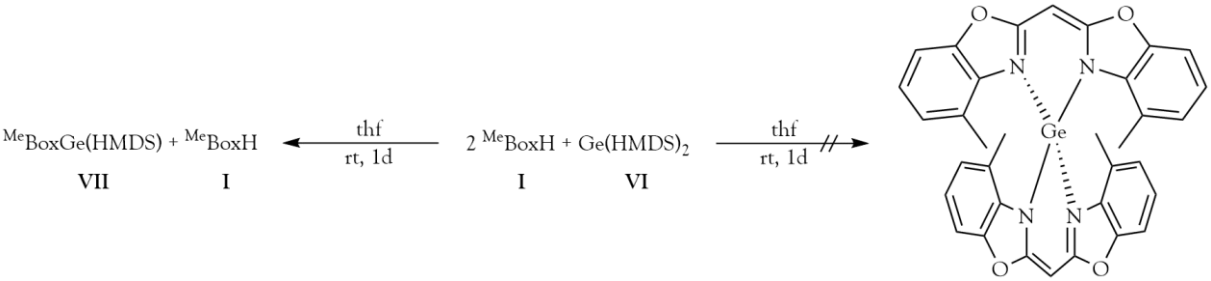

Figure 3-37: Simultaneous deprotonation-metalation reaction between ^{Me}BoxH **(I)** and $Ge(HMDS)_2$ **(VI)** for the attempted synthesis of a homoleptic germylene with two bis(4-methylbenzoxazol-2-yl)methanide ligands.

The obtained light yellow powder was analysed by ^{1}H- and ^{13}C-NMR spectroscopy. Both spectra showed the obtained powder to be a mixture of unreacted ^{Me}BoxH and {bis(4-methylbenzoxazol-2-yl)methanide}germanium(II) bis(trimethylsilyl)amide **(VII)**. The resonances for the bridging CH groups and the methyl groups do not overlap in the ^{1}H-NMR spectrum so that they could be integrated separately. The integrals give a 1:1 ratio of **I** and **VII** suggesting that the reactions stops after one equivalent of bis(4-methylbenzoxazol-2-yl)methane is consumed. Hence, it appears that formation homoleptic $(^{Me}Box)_2Ge$ is not viable. This is most probably due to steric reasons as the two ligands might be too close to each other when coordinated to a germanium atom.

3.2.10 Synthesis of bis{bis(4-methylbenzoxazol-2-yl)methanide}tin(II)

Although the synthesis of $(^{Me}Box)_2Ge$ was not successful, heavier homologues might be accessible due to the increased size of the metal. Therefore, two equivalents of the free ligand ^{Me}BoxH **(I)** were reacted with tin(II) bis(trimethylsilyl)amide **(VIII)** in thf at room temperature (Figure 3-38). After 24 hours of stirring all volatiles were removed *in vacuo*. The residue was washed with pentane and again dried under reduced pressure to give $(^{Me}Box)_2Sn$ **(XII)** in high yield (83 %). Compound **XII** is stable for month if stored as a solid under inert atmosphere at room temperature.

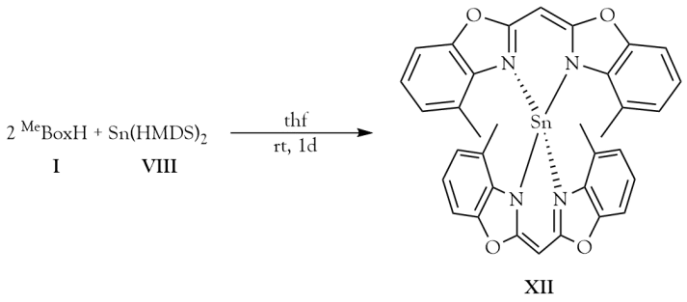

Figure 3-38: Simultaneous deprotonation-metalation reaction between ^{Me}BoxH (**I**) and Sn(HMDS)$_2$ (**VIII**) for the synthesis of bis{bis(4-methylbenzoxazol-2-yl)methanide}tin(II) (**XII**).

The ^{1}H-NMR spectrum of **XII** showed resonances for the methyl groups and the bridging CH group with chemical shifts indistinguishable from the ones in ^{Me}BoxK. The resonances of the aromatic protons are detected in the same range of chemical shifts, but the order of the individual protons changed. In Figure 3-39 ^{1}H-NMR spectra of ^{Me}BoxK, ^{Me}BoxSnCl and (^{Me}Box)$_2$Sn are compared. This clearly shows, how the electronic situation in the conjugated π system of the ligand changes upon coordination of the SnCl$^+$ fragment and how this change is reversed, if the chloride ligand is formally substituted for a second bis(4-methylbenzoxazol-2-yl)methanide.

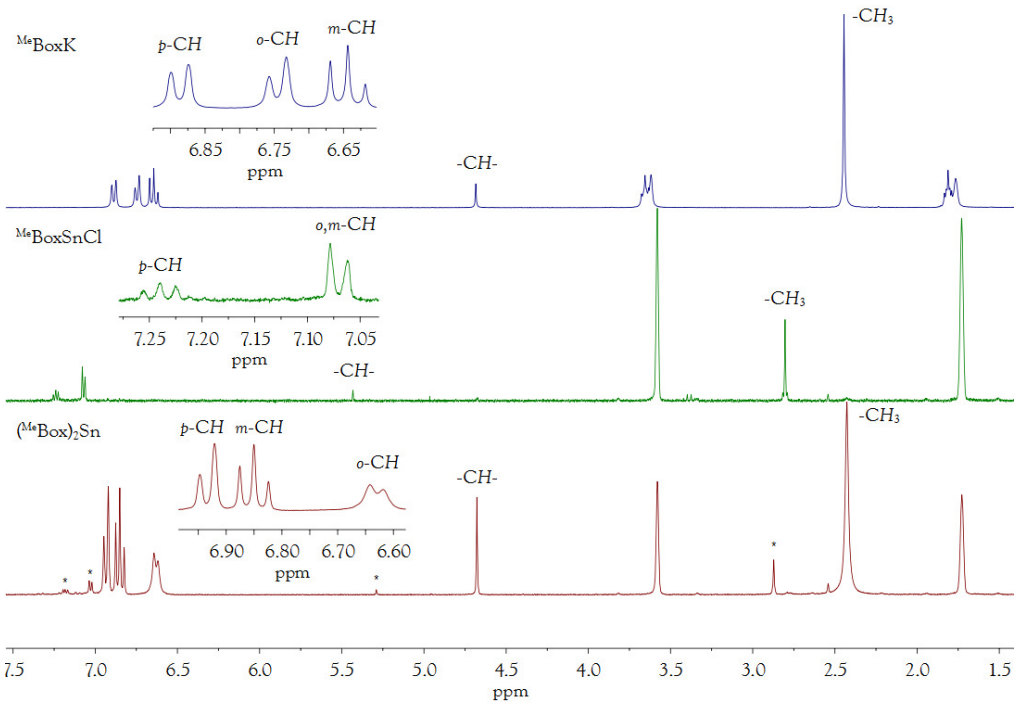

Figure 3-39: Stacked ^{1}H-NMR spectra (300 MHz, thf-d$_8$) of ^{Me}BoxK (**II**), ^{Me}BoxSnCl (**V**) and (^{Me}Box)$_2$Sn (**XII**). Ortho, meta and para positions are relative to the methyl groups. Resonances at 3.58 ppm and 1.73 ppm belong to the solvent. Resonances marked with an asterisk belong to small impurities of ^{Me}BoxSn(HMDS) (**IX**).

The resonance of the CH groups in (^{Me}Box)$_2$Sn (4.68 ppm) is a strong indicator that the tin atom is not embedded in a planar C_3N_2Sn six membered ring anymore. Interestingly, in the ^{13}C-NMR spectrum the same trend is not observed. The resonance of the bridging carbon (62.30 ppm) is more similar to ^{Me}BoxSnCl (61.81 ppm) than to ^{Me}BoxK (56.99 ppm). From these findings it can be concluded, that the tin atom in (^{Me}Box)$_2$Sn must be chelated between two {bis(4-methylbenzoxazol-2-yl)methanides, which at least on the NMR time scale are equivalent in solution.

Yellow block shaped crystals suitable for single crystal X-ray diffraction analysis were obtained by vapour diffusion of pentane into concentrated solutions of **XII** in dcm at −25°C after a few days. Compound **XII** crystallised in the monoclinic space group $P2_1/n$ with one molecule in the asymmetric unit (Figure 3-40). In the solid-state the two methanide ligands are crystallographically independent and also show no non-crystallographic symmetry. Both ligands show rather strong deviations from planarity compared to the heteroleptic complexes described in this thesis with butterfly folding angles of 14.14° and 19.73°. They are bent away from each other with distances between the ligands ranging from 3.074 Å (C3-C18) to about 4 Å at the outer perimeters. The tin-nitrogen distances are all different but can be divided into two shorter (Sn1-N2: 2.2348(16) Å, Sn1-N3: 2.2392(16) Å) and two longer (Sn1-N4: 2.4208(16) Å, Sn1-N1: 2.4280(16) Å) ones. The tin atom is dislocated by 1.319(2) Å and 1.269(2) Å from the planes defined by C1-C2-C3-N1-N2 and C18-C19-C20-N3-N4 respectively. To describe the coordination of the tin atom, the Addison parameter τ can be used. [386] τ is defined as the absolute value of the difference between the two biggest angles of the coordination centre divided by 60°. It adopts the values 0 or 1 for ideal square pyramidal or ideal trigonal pyramidal symmetry respectively. Values in between indicate the continuous transition from one geometry into the other. In the case of (^{Me}Box)$_2$Sn τ equals 0.89. Therefore, the coordination environment of the tin atom is best described as a distorted disphenoid derived from a trigonal bipyramid with one vertex occupied by the tin(II) lone pair.

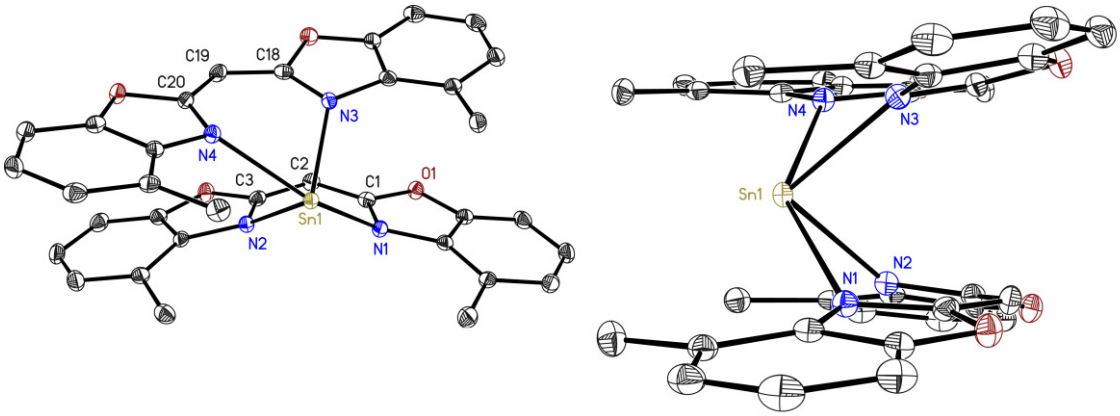

Figure 3-40: Asymmetric unit of (^{Me}Box)$_2$Sn **(XII)** shown from different perspectives. Anisotropic displacement parameters are depicted at the 50 % probability level. Hydrogen atoms are omitted for clarity.

The crystal structure confirmed what had already been expected based on the NMR data. The tin atom in (^{Me}Box)$_2$Sn is no longer part of the conjugated π system of the ligand. The ligands are inequivalent but can be expected to equilibrate in solution. The shortest tin-tin distance is 9.482 Å, hence any interaction can be excluded. In addition, no formation of dedicated dimers in the solid-state is observed. Therefore, the bending of the ligands is assumed to be the result of repulsion caused by the proximity of the ligands enforced after coordination to the tin(II) centre. LIFDI mass spectroscopy gave a molecular ion peak at 674.0 *m/z* supporting the monomeric nature of the compound also in solution. Additionally, a peak at 807.8 *m/z* was observed with 24 % relative intensity. Its isotope pattern suggests a species with more than one tin atom, but no chemically meaningful composition could be derived.

3.2.11 Synthesis of bis{bis(4-methylbenzoxazol-2-yl)methanide}lead(II)

Since the synthesis of (^{Me}Box)$_2$Sn was successful and mass spectrometry already indicated its existence, the lead homologue ought to be accessible as well. Therefore, two equivalents of the free ligand ^{Me}BoxH **(I)** were reacted with lead(II) bis(trimethylsilyl)amide **(X)** in thf at room temperature (Figure 3-41). After 24 hours of stirring all volatiles were removed *in vacuo*. The residue was washed with pentane and again dried under reduced pressure to give (^{Me}Box)$_2$Pb **(XIII)** in high yield (88 %). Compound **XIII** is stable for months if stored as a solid under inert atmosphere at room temperature.

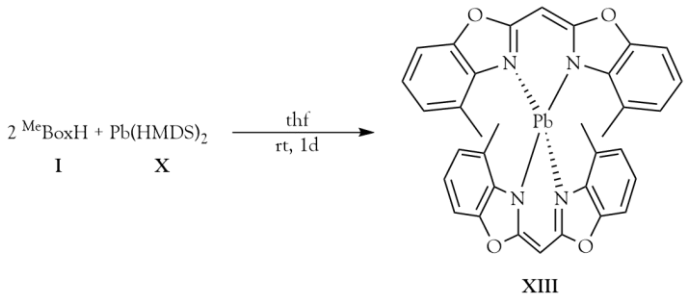

Figure 3-41: Simultaneous deprotonation-metalation reaction between ^{Me}BoxH (**I**) and Pb(HMDS)$_2$ (**X**) for the synthesis of bis{bis(4-methylbenzoxazol-2-yl)methanide}lead(II) (**XIII**).

The ^{1}H- and ^{13}C-NMR spectra of **XIII** showed resonances with only minute changes in chemical shift compared to those observed for (^{Me}Box)$_2$Sn. The most prominent difference can be seen in the ^{1}H chemical shift of the bridging CH group, which is shifted upfield from 4.68 ppm in (^{Me}Box)$_2$Sn to 4.27 ppm in (^{Me}Box)$_2$Pb. The same trend was also observed when ^{Me}BoxSn(HMDS) and ^{Me}BoxPb(HMDS) were compared. Overall, as with the tin compound, the NMR data indicate that the lead atom is not embedded in a planar C_3N_2Pb six membered ring, but chelated by two {bis(4-methylbenzoxazol-2-yl)methanides, which at least on the NMR time scale are equivalent in solution. LIFDI mass spectrometry gave a clean spectrum with only peak at 762.0 m/z corresponding to the molecular ion.

Yellow-orange block shaped crystals suitable for single crystal X-ray diffraction analysis were obtained by vapour diffusion of pentane into concentrated solutions of **XIII** in thf at −25°C after a few days. Compound **XIII** crystallised in the monoclinic space group $P2_1/n$ with one molecule in the asymmetric unit (Figure 3-42). The structure is isomorphous with that of (^{Me}Box)$_2$Sn. Hence, the lead(II) centre is coordinated by four nitrogen atoms at different distances. Details and a comparison to (^{Me}Box)$_2$Sn are given in Table 3-5. Both ligands are bent away from each other with distances between 3.130 Å (C3-C18) and around 3.8 Å at the outer perimeters and butterfly folding angles of 12.32° and 17.62°. These are slightly smaller than in (^{Me}Box)$_2$Sn, indicating that the greater separation between the ligands granted by the increased radius of the lead(II) ion allows the ligands to relax towards planarity. Due to the isomorphism of both structures no interactions between to lead atoms or formations of dimers in general is observed.

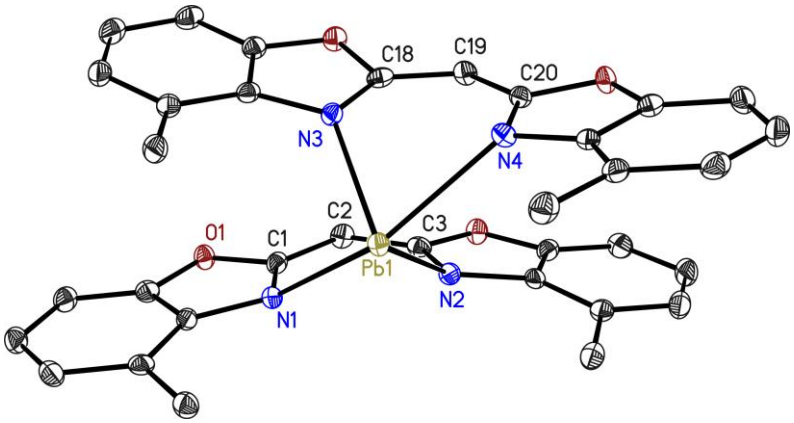

Figure 3-42: Asymmetric unit of (^{Me}Box)$_2$Pb **(XII)** shown from different perspectives. Anisotropic displacement parameters are depicted at the 50 % probability level. Hydrogen atoms are omitted for clarity.

Table 3-5: Comparison of selected structural parameters for (^{Me}Box)$_2$Sn and (^{Me}Box)$_2$Pb.

distances and angles	**(^{Me}Box)$_2$Sn**	**(^{Me}Box)$_2$Pb**
M-N1 [Å]	2.4280(16)	2.512(2)
M-N2 [Å]	2.2348(16)	2.342(2)
M-N3 [Å]	2.2392(16)	2.345(2)
M-N4 [Å]	2.4208(16)	2.523(2)
N1-M-N2 [°]	74.60(6)	73.35(8)
N3-M-N4 [°]	75.01(6)	72.77(8)
N1-M-N4 [°]	145.31(5)	142.82(8)
N2-M-N3 [°]	91.70(6)	90.45(8)
Addison parameter τ[386]	0.89	0.87
dislocation of M [Å]	1.319(2) and 1.269(2)	1.337(4) and 1.407(4)

3.2.12 Synthesis of {bis(4-benzhydrylbenzoxazol-2-yl)methanide}germanium(II) chloride

The chloro germylene **III** and stannylene **V** both lack solubility in common organic solvents. While substitution with a bis(trimethylsilyl)amide greatly increases solubility, the chloro compounds constitute a more versatile platform for further reactivity. In order to test whether the solubility of the chloro germylene could be increased when the size of the substituents in 4 position is increased, bis(4-benzhydrylbenzoxazol-2-yl)methane was synthesised. The synthetic pathway illustrated in Figure 3-43 was reported in previous work of the Stalke group.[367]

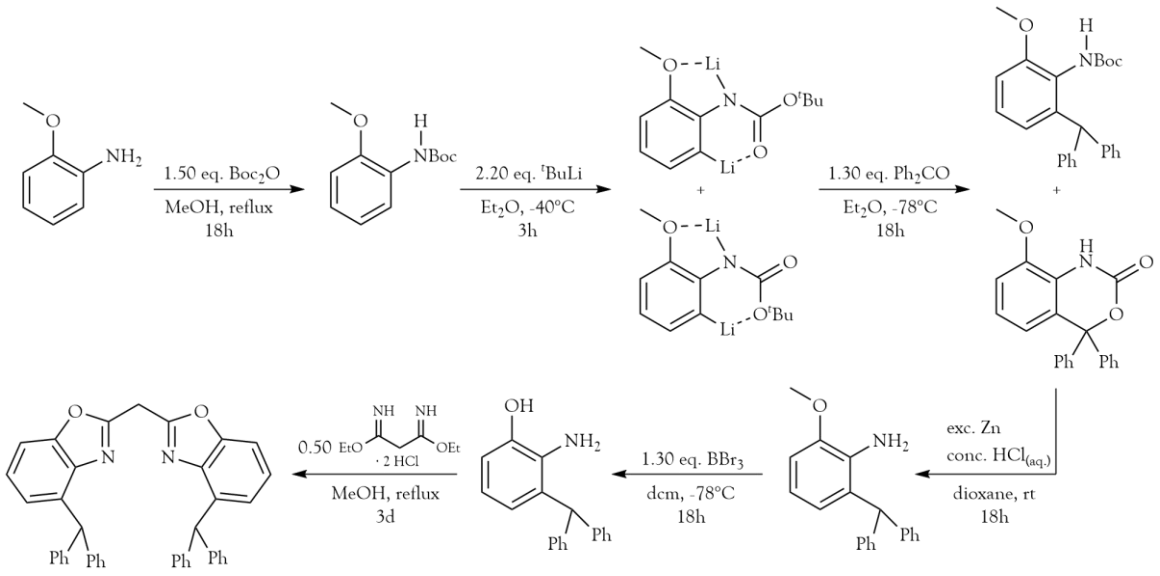

Figure 3-43: Synthesis of bis(4-benzhydrylbenzoxazol-2-yl)methane. [367]

Once bis(4-benzhydrylbenzoxazol-2-yl)methane had been synthesised, it was converted to its potassium salt by reaction with potassium hydride in thf. After 24 hours of stirring, the yellow solution was dried *in vacuo* to yield potassium bis(4-benzhydrylbenzoxazol-2-yl)methanide as a powder. In analogy to the synthesis of ^{Me}BoxGeCl the potassium precursor was used for a salt metathesis reaction with $GeCl_2$·dioxane. Both educts were dissolved in thf and the mixture was stirred for 24 hours at room temperature (Figure 3-44). Afterwards the mixture as filtered and the filtrate was dried *in vacuo* to obtain {bis(4-benzhydrylbenzoxazol-2-yl)methanide}germanium(II) chloride (**XV**) as a pale yellow powder in good yield (64 %). Compound **XV** is stable for months if stored as a solid under inert atmosphere at room temperature.

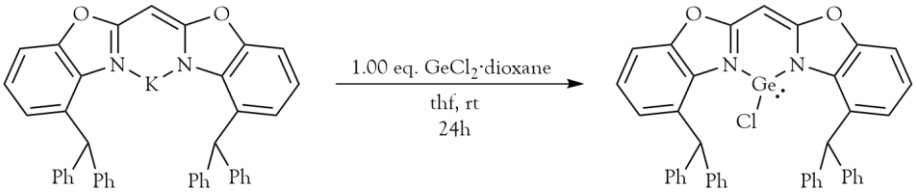

XIV

Figure 3-44: Synthesis of {bis(4-benzhydrylbenzoxazol-2-yl)methanide}germanium(II) chloride (**XIV**) by salt metathesis of potassium bis(4-benzhydrylbenzoxazol-2-yl)methanide and $GeCl_2$·dioxane in thf.

Surprisingly, the solubility of ^{Bzh}BoxGeCl in thf does not appear to be drastically different from that of ^{Me}BoxGeCl. However, it is sufficient to characterise a solution of it in deuterated thf by ^{1}H- and ^{13}C-NMR spectroscopy. The ^{1}H resonance of the bridging CH group is observed at 5.63 ppm. This is comparable to the values obtained for the other heteroleptic tetrylenes synthesised as part of this thesis, but more downfield shifted than most of them. The resonance of the protons in benzhydrylic position is detected at 6.51 ppm while most of the resonances in the aromatic region of the spectrum overlap. NMR data was additionally collected for ^{Bzh}BoxGeCl dissolved in deuterated benzene, in which the compound indeed showed much higher solubility. In this solvent, resonances from the aromatic protons in the benzoxazole units can be separated from the ones of the benzhydrylic groups so that the identity of the compound can be confirmed. Overall, the ^{1}H- and ^{13}C-NMR data compare very well to the data reported on group 13 carbenoids based on the bis(4-benzhydrylbenzoxazol-2-yl)methanide ligand.[376]

Colourless block shaped crystals suitable for single crystal X-ray diffraction analysis were obtained by vapour diffusion of pentane into concentrated solutions of **XIV** in thf at −25°C after a few days. Compound **XIV** crystallised in the triclinic space group $P\bar{1}$ with one molecule of ^{Bzh}BoxGeCl and two molecules of non-coordinating thf in the asymmetric unit (Figure 3-45). The Ge1-N1 (2.022(2) Å) and Ge1-N2 (2.012(2) Å) distances are very similar to each other and only slightly elongated compared ^{Me}BoxGeCl. The ligand is moderately twisted with a torsion angle of 18.91°, which is most probably induced by the benzhydryl substituents. However, this distortion does not seem to have a great effect on the coordination of germanium. The dislocation of the germanium atom from the C_3N_2 plane is 0.191(3) Å. This is bigger than in ^{Me}BoxGeCl (0.126(3) Å), but still significantly smaller than in the related NacNac compounds {HC(CMeNPh)$_2$}GeCl (0.528 Å)[263] or {HC(CMeNDip)$_2$}GeCl (0.564 Å).[242]

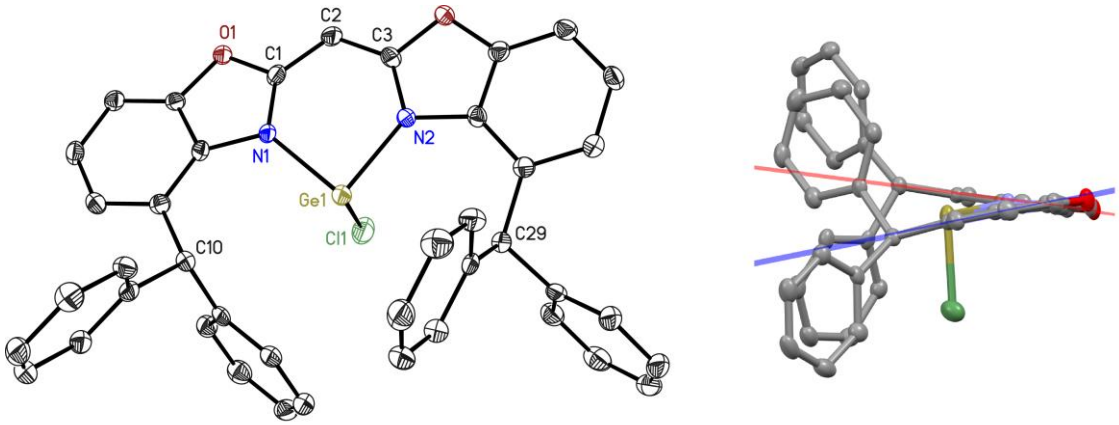

Figure 3-45: Asymmetric unit of ^{Bzh}BoxGeCl (**XIV**) crystallised from thf/pentane shown from different perspectives. The red and the blue plane are fitted to the respective benzoxazole subunits to showcase the torsion within the ligand. Anisotropic displacement parameters are depicted at the 50 % probability level. Hydrogen atoms and two molecules of lattice solvent (thf) are omitted for clarity.

NMR and crystal structure analysis shows that the germanium atom is well embedded in the ligand system and its local environment is very similar to the on found in ^{Me}BoxGeCl. While the big benzhydryl substituents offer great steric protection of the germanium(II) centre, they also induce distortion in the ligand. The solubility of ^{Bzh}BoxGeCl is increased in benzene, and probably in aromatic solvents in general, but not in thf compared to ^{Me}BoxGeCl. Because it was already shown for the bis(4-methylbenzoxazol-2-yl)methane based ligand that the sterically less demanding methyl groups suffice to stabilise monomeric germylene complexes, and heavier homologues, the increased solubility and steric bulk do not justify the disproportionately more laborious synthesis - at least not within the scope of his thesis. Therefore, no further experiments with ^{Bzh}BoxGeCl or then ^{Bzh}Box ligand were conducted.

3.2.13 Attempted synthesis of the {bis(4-methylbenzoxazol-2-yl)methanide}germanium(II) cation

Reports of cationic six membered *N*-heterocyclic germylenes are scarce.[244,247] Hence, it was intriguing to see, if the bis(4-methylbenzoxazol-2-yl)methanide would be able to stabilise such a cationic species. In a first experiment, ^{Me}BoxGeCl (**III**) was reacted with silver tetrafluoroborate in thf in an attempt to abstract the chloride by precipitation of silver chloride (Figure 3-46). The anticipated product would be a {bis(4-methylbenzoxazol-2-yl)methanide}germanium(II) cation with a non-coordinating tetrafluoroborate counter ion.

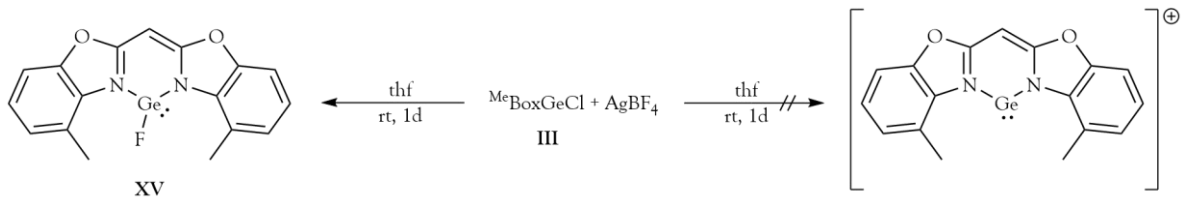

Figure 3-46: Attempted synthesis of a {bis(4-methylbenzoxazol-2-yl)methanide}germanium(II) cation by chloride abstraction with a silver(I) source instead leading to the formation of {bis(4-methylbenzoxazol-2-yl)methanide}germanium(II) fluoride (**XV**).

However, the reaction did not proceed as planned. After stirring the mixture for 24 hours, it was centrifuged and decanted to separate all solids. The remaining clear solution was dried *in vacuo* to obtain a yellow powder.

Vapour diffusion of pentane into a solution of the obtained powder in thf at −25°C lead to formation of colourless, block shaped crystals, which were analysed by single crystal X-ray diffraction. The obtained compound crystallised in the monoclinic space group $P2_1/c$ with two molecules in the asymmetric unit (Figure 3-47). The structure solution clearly indicated, that the envisaged cation was not obtained. After careful refinement of the structure, it became apparent that the substituent at the germanium atom is disordered and is best described by shared occupation between a chlorine and a fluorine atom. Notably, although the space group is the same, the cell parameters for this co-crystal differ from those obtained for both polymorphs of pure ^{Me}BoxGeCl. Due to the co-crystallisation of both halides, ^{Me}BoxGeF could not be characterised unambiguously by NMR spectroscopy.

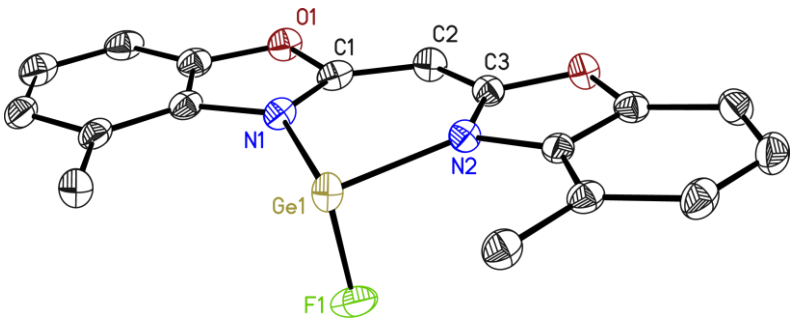

Figure 3-47: Half of the asymmetric unit of ^{Me}BoxGeF **(XV)** crystallised from thf/pentane. Anisotropic displacement parameters are depicted at the 50 % probability level. Hydrogen atoms and disorder are omitted for clarity.

Because of the disorder, all structural parameters of the disordered moieties have to be discussed with great care. The mean germanium-fluorine distance from both molecules in the asymmetric unit is 1.794(17) Å. This compares well to corresponding distances in other *N*,*N* chelated germanium(II) fluorides (1.800 Å-1.805 Å), of which only four have been reported and structurally characterised so far.[255,387,388] The germanium atom is dislocated 0.318(3) Å from the C_3N_2 plane. This is almost three times as large as in ^{Me}BoxGeCl **(III)** and close to the dislocation found in {HC(CMeNDip)$_2$}GeCl (0.377 Å).[255] No π-π stacking or formation of dedicated dimers or oligomers is observed. Accordingly, the ligand is mostly planar with a butterfly folding angle of 4.5° between the benzoxazole subunits.

Although ^{Me}BoxGeF itself is an interesting compound, the aim remained to synthesise the {bis(4-methylbenzoxazol-2-yl)methanide}germanium(II) cation. As an alternative to silver chloride precipitation, ^{Me}BoxGeCl was reacted with trimethylsilyl triflate as a chloride abstraction agent (Figure 3-48). The triflate might than be exchanged for a weakly coordinating anion.

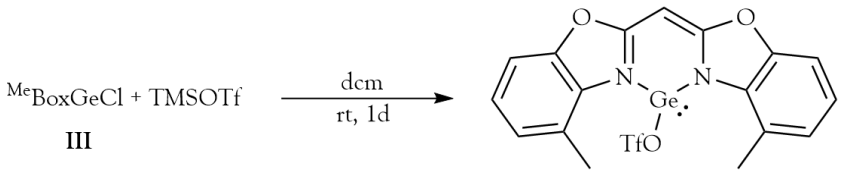

Figure 3-48: Synthesis of {bis(4-methylbenzoxazol-2-yl)methanide}germanium(II) triflate **(XVI)** *via* chloride abstraction from {bis(4-methylbenzoxazol-2-yl)methanide}germanium(II) chloride **(III)** with trimethylsilyl triflate.

^{Me}BoxGeCl was suspended in dcm and one equivalent of trimethylsilyl triflate was added. The mixture was stirred for 24 hours at room temperature before all volatiles were removed under

reduced pressure. NMR analysis of the residue dissolved in deuterated thf indicated that no reaction took place as the ^{1}H-NMR spectrum was identical to the one of ^{Me}BoxGeCl regarding resonances corresponding to the aromatic protons as well as the bridging CH group. ^{19}F-NMR analysis gave a singular resonance at −79.46 ppm, for which the assignment to a chemical species is rather difficult. ^{19}F chemical shifts for TMSOTf, the triflate anion or triflic acid have all been reported to occur in the range from −76 ppm to −80 ppm in deuterated benzene, chloroform or nitromethane.[389–391] For the related compound {HC(CMeNDip)$_2$}GeOTf based on the NacNac ligand, two different ^{19}F chemical shifts in deuterated benzene (−77.5 ppm[250] and −76.5 ppm.[267]) have been reported. References for chemical shifts in thf are not available, because TMSOTf initiates the cationic polymerisation of it.[390]Therefore, a freshly prepared solution of TMSOTf in deuterated thf was analysed by ^{1}H- and ^{19}F-NMR directly after mixing. The ^{1}H-NMR spectrum contained a resonance at 0.49 ppm corresponding to the silicon bound methyl groups, whereas the ^{19}F-NMR spectrum showed one strong resonance at −78.5 ppm and a second weaker resonance with a chemical shift of −76.4 ppm. It is assumed that the first resonance corresponds to TMSOTf, while the latter might be caused by free triflate ions formed by the reaction of TMSOTf with thf. However, with all the chemical shifts being very similar and the literature even reporting different shifts for the same compound in the same solvent no reliable assignment based on ^{19}F-NMR spectroscopy can be made. Somewhat more reliable is the observation that the NMR sample of the reaction product formed an extremely viscous mass in the NMR tube within 24 hours. This can be taken as indication that at least no quantitative reaction between ^{Me}BoxGeCl and TMSOTf took place as enough TMSOTf must have been present in the portion of the residue used for analysis to polymerise the sample.

The reaction was repeated under the same conditions but with two equivalents of trimethylsilyl triflate. After 24 hours of stirring at room temperature the reaction was stopped and volatiles were removed *in vacuo*. ^{1}H-NMR analysis of the residue gave a complicated spectrum with three resonances between 5.95 ppm and 5.50 ppm possibly corresponding to bridging CH groups of the bis(4-methylbenzoxazol-2-yl)methanide ligand in different chemical species but none of them identical to ^{Me}BoxGeCl. Additionally, unreacted TMSOTf with a chemical shift of 0.49 ppm is observed. The ^{19}F-NMR spectrum gave the same resonance already observed for the reaction of ^{Me}BoxGeCl with one equivalent of TMSOTf.

In an attempt to crystallise components from the apparent mixture of compounds present in the residue, it was dissolved in thf or dcm. Vapour phase diffusion of pentane at −25°C in both cases led to the formation of tiny, needle shaped crystals. However, the crystals were too thin and

delicate to be analysed by single crystal X-ray diffraction. They either broke during manipulation or were too small to collect sufficient diffraction data on them.

Because no reliable conclusions from NMR data could be drawn and no work up procedure was found to separate the reaction products from each other, no statement on the success of the reaction can be made.

3.2.14 Synthesis of Pentacarbonyl{chloro[bis(4-methylbenzoxazol-2-yl)methanide]germylene} tungsten(0)

To see if ^{Me}BoxGeCl behaves like a heavy NHC and acts as a ligand in a d-metal complex, it was mixed with tungsten hexacarbonyl, suspended in thf and stirred for 24 hours under UV radiation (Figure 3-49). After that, all volatiles were removed under reduced pressure to yield the product as a light yellow powder.

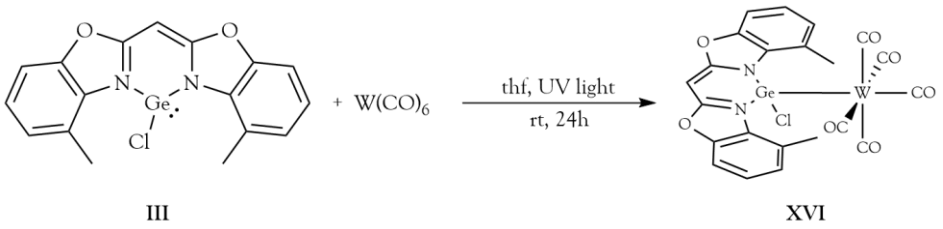

Figure 3-49: Synthesis of ^{Me}BoxGe(Cl)W(CO)$_5$ **(XVI)** by the reaction of **III** and W(CO)$_6$ in thf.

^{1}H-NMR analysis showed that in thf solution two species are present. One is the starting material, ^{Me}BoxGeCl, the other one is assigned to complex **XVI**. Resonances of the methyl groups and the aromatic protons are shifted downfield relative to ^{Me}BoxGeCl. A separate resonance for the bridging CH group is not observed. Integration of the spectrum gives a ratio of roughly 3:1 between free and complexed ^{Me}BoxGeCl. While it could be possible that this observation is the result of an incomplete reaction, it could also be caused by dissociation of the complex in the rather dilute NMR sample. The latter explanation is supported by the analysis of the compound *via* LIFDI mass spectrometry, which gave only the molecular ion peak expected for complex **XVI** at 709.8 *m/z* and no peaks corresponding to ^{Me}BoxGeCl or tungsten hexacarbonyl.

Yellow plate shaped crystals suitable for single crystal X-ray diffraction analysis were obtained by vapour diffusion of pentane into concentrated solutions of **XVI** in thf at −25°C after a few days. Compound **XVI** crystallised in the triclinic space group $P\bar{1}$ with one molecule in the asymmetric

unit (Figure 3-50). In Table 3-6 selected structural parameters of ^{Me}BoxGe(Cl)W(CO)$_5$, the already reported {HC(CMeNPh)$_2$}Ge(Cl)W(CO)$_5$[259] and the free germylene ^{Me}BoxGeCl are compared.

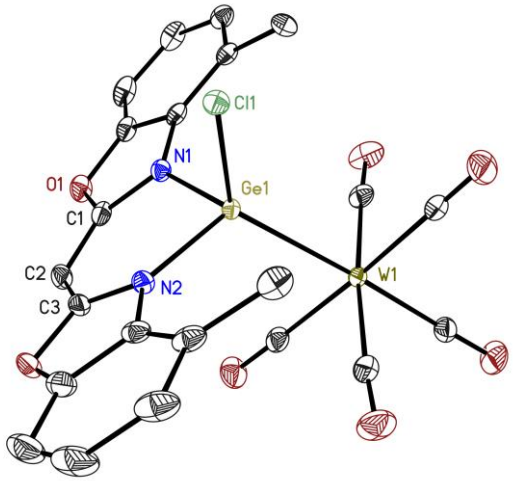

Figure 3-50: Asymmetric unit of ^{Me}BoxGe(Cl)W(CO)$_5$ **(XVI)** crystallised from thf/pentane. Anisotropic displacement parameters are depicted at the 50 % probability level. Hydrogen atoms are omitted for clarity.

Ge1-N1 and Ge1-N2 distances are equal within the margin of error and similar to the distances in ^{Me}BoxGeCl. All angles around the germanium atom become bigger upon coordination of ^{Me}BoxGeCl to the tungsten pentacarbonyl fragment. While it might seem contra intuitive that an increase in coordination number leads to a widening of angles, it can be rationalised assuming that the repulsive action of the lone pair is reduced by donation of electron density to the metal carbonyl. The dislocation of the germanium centre from the C_3N_2 plane is increased to 0.493(2) Å, which is comparable to but greater than in {HC(CMeNPh)$_2$}Ge(Cl)W(CO)$_5$. The tungsten-germanium distance (2.5633(8) Å) is at the shorter edge of reported values (see appendix 5.6, Figure 5-33) and shorter than what is expected for a tungsten-germanium single bond (2.59 Å-2.67 Å).[259] The tungsten-carbon distances in {HC(CMeNPh)$_2$}Ge(Cl)W(CO)$_5$ and ^{Me}BoxGe(Cl)W(CO)$_5$ are all equal within the margin of error. A trans influence can be observed as the carbon monoxide ligand in *trans* position relative to the germylene is about 4 pm closer to the tungsten centre than the other carbon monoxide ligands. The carbon-oxygen distance (1.148(2) Å) is slightly elongated compared to the mean value for the respective distances of the *cis* arranged ligands (1.141(2) Å). These findings are consistent with a strong σ-donor and weak π-acceptor character of germylene **III**.

Table 3-6: Comparison of selected structural parameters for ^{Me}BoxGeCl, ^{Me}BoxGe(Cl)W(CO)$_5$ and {HC(CMeNPh)$_2$}Ge(Cl)W(CO)$_5$.[259] [a]Values obtained from polymorphic form A. [b]Mean values for all four tungsten-carbon distances.

distances and angles	^{Me}BoxGeCl[a]	^{Me}BoxGe(Cl)W(CO)$_5$	{HC(CMeNPh)$_2$}Ge(Cl)W(CO)$_5$
Ge1-Cl1 [Å]	2.3366(8)	2.19528(16)	2.258(1)
Ge1-N1 [Å]	1.995(2)	1.9551(15)	1.929(3)
Ge1-N2 [Å]	1.997(2)	1.9528(16)	1.923(3)
Ge1-W1 [Å]	-	2.5633(8)	2.567(5)
W1-*trans*CO [Å]	-	2.001(2)	1.995(5)
W1-*cis*CO [Å][b]	-	2.042(2)	2.038(5)
N1-Ge1-N2 [°]	88.69(9)	91.94(6)	93.90(13)
N1-Ge1-Cl1 [°]	94.60(7)	98.78(5)	96.64(9)
N2-Ge1-Cl1 [°]	93.46(7)	97.08(5)	98.08(10)
W1-Ge1-Cl1 [°]	-	130.05(2)	112.34(3)
dislocation of Ge1 [Å]	0.126(3)	0.493(2)	0.462

If germylene **III** is indeed a strong σ-donor but weak π-acceptor, the electron density at the tungsten atom should be higher than in tungsten hexacarbonyl. Hence, π backbonding becomes more pronounced so that one could expect to observe a red shift of the stretching frequency for the carbon monoxide ligands. In order to test this assumption, a solid sample of complex **XVI** was analysed by ATR-FTIR spectroscopy. The recorded spectrum is shown in Figure 3-51. For a pentacarbonyl complex with approximate C_{4v} symmetry such as ^{Me}BoxGe(Cl)W(CO)$_5$, three IR active carbonyl stretching bands are expected in theory and a weaker band (A_1 mode) should be 140 cm^{-1} to 150 cm^{-1} higher in energy than the strongest absorption band (E mode).[392] In fact, all three bands can be observed in the recorded IR spectrum at 2071 cm^{-1} (A_1'), 1989 cm^{-1} (A_1'') and 1913 cm^{-1} (E) and the A_1' and E modes are separated by 158 cm^{-1}. The absorption band of the E mode is very broad and asymmetric, which is most probably caused by the Christiansen effect.[393–395] The measured values compare well to the reported absorption bands for {HC(CMeNPh)$_2$}Ge(Cl)W(CO)$_5$ (2072 cm^{-1}, 1984 cm^{-1}, 1943 cm^{-1}).[259] The carbonyl stretching frequency in the parent tungsten hexacarbonyl is reported to be 1997 cm^{-1}.[396] Hence, the IR spectrum confirms that the solid sample contains no tungsten hexacarbonyl or at least not in

significant amounts. This supports the assumption made before that the complex might dissociate in solution to give rise to the discussed NMR data. The IR spectrum also shows the expected red shift of the carbonyl stretching frequency from 1997 cm^{-1} to 1913 cm^{-1} due to the strong σ-donation from the germylene.

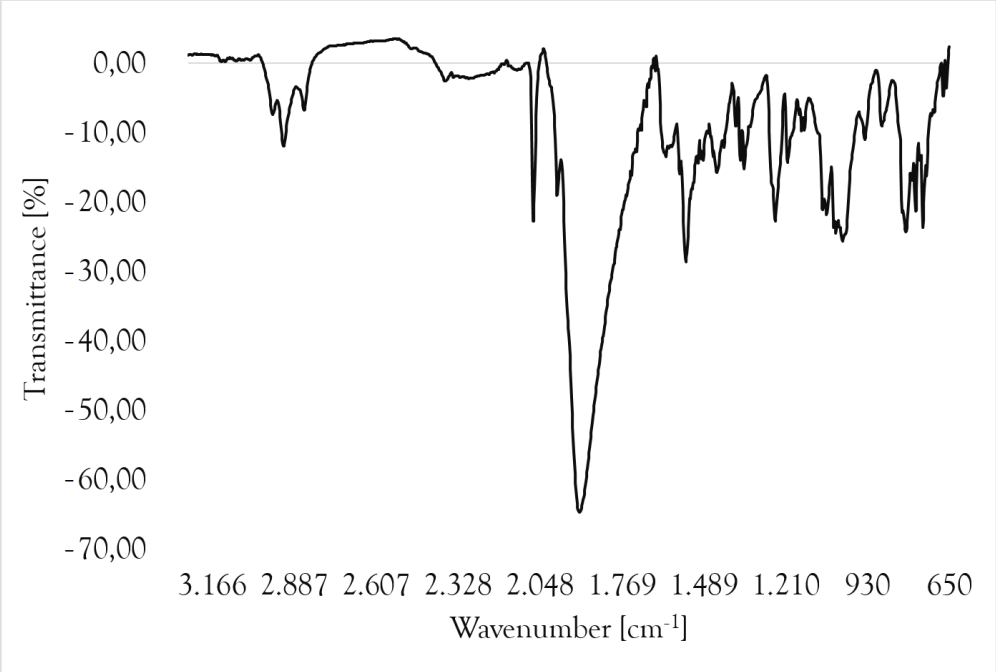

Figure 3-51: ATR-FTIR spectrum recorded on a solid sample of ^{Me}BoxGe(Cl)W(CO)$_5$ **(XVI)**.

3.2.15 Synthesis of {bis(4-methylbenzoxazol-2-yl)methanide}germanium(II) diphenylphosphide

A straightforward method to substitute the chloride ligand in ^{Me}BoxGeCl would be to react the latter with lithium alkyls or comparable reagents. As it was already shown that ^{Me}BoxGeCl acts as a σ-donor ligand, it might be interesting to incorporate a second donation side into the compound to enable new coordination motifs. Therefore, diphenyl phosphine was chosen as a proof of principle example for an additional donor functionality to be introduced. ^{Me}BoxGeCl was reacted with lithium diphenylphosphide in thf (Figure 3-52). The mixture was stirred for 24 hours before all volatiles were removed *in vacuo* to give a sticky, oily orange residue.

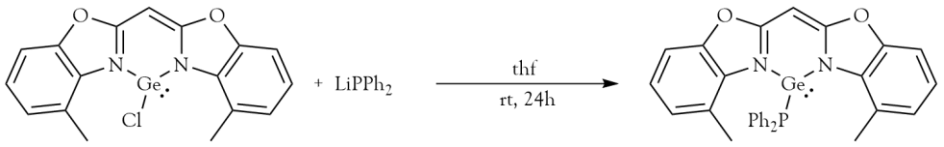

III XVII

Figure 3-52: Synthesis of ^{Me}BoxGePPh$_2$ **(XVII)** by the reaction of **III** and LiPPh$_2$ in thf.

^{1}H- and ^{13}C-NMR analysis of the residue resulted in complicated spectra stemming from multiple species. Three sets of ^{1}H resonances for the methyl and bridging CH groups can be separated, whereas the resonances of aromatic protons are largely overlapping. Additionally, small amounts of bis(4-methylbenzoxazol-2-yl)methane seem to be present as well. The ^{31}P-NMR spectrum, however, shows only one resonance at −16.5 ppm. This is similar to the reported ^{31}P chemical shift of −14.9 ppm for the related compound {HC(CMeNDip)$_2$}GePPh$_2$.[248] Hence, it can be suspected that the reaction proceeded as intended but also caused the formation of several side products. All efforts to isolate any of the multiple species by means of extraction or crystallisation so far were unsuccessful.

3.2.16 Synthesis of 2,2,4,4,5,5-hexa(4-methylbenzoxazol-2-yl)-1,3-distibabicyclo[1.1.1]pentane

Out of curiosity if the bis(4-methylbenzoxazol-2-yl)methanide ligand could also be used to synthesise complexes with group 15 elements, potassium bis(4-methylbenzoxazol-2-yl)methanide was reacted with antimony trichloride in equimolar amounts (Figure 3-53). Upon addition of SbCl$_3$ the reaction mixture changed its colour within minutes from yellow to orange and finally brown accompanied by the formation of a precipitate.

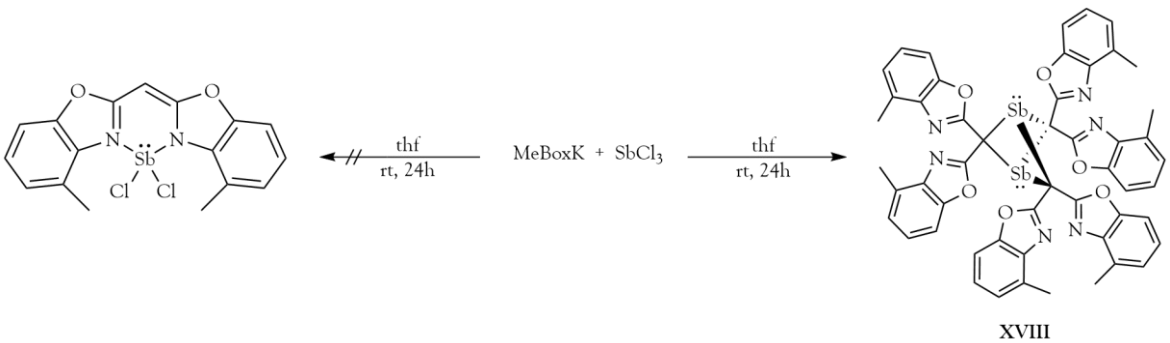

XVIII

Figure 3-53: Attempted synthesis of ^{Me}BoxSbCl$_2$ by reaction of **III** and SbCl$_3$ in thf, which instead led to the formation of (^{Me}Box)$_3$Sb$_2$ **(XVIII)**.

After the mixture had been stirred for 24 hours it was filtrated. From the filtrate yellow block shaped crystals formed at room temperature within one day. The crystals were analysed by single crystal X-ray diffraction and revealed the completely unexpected formation of 2,2,4,4,5,5-hexa(4-methylbenzoxazol-2-yl)-1,3-distibabicyclo[1.1.1]pentane (**XVIII**). **XVIII** crystallises in the trigonal space group $R\bar{3}c$ with only a third of the molecule in the asymmetric unit (Figure 3-54). The molecule is located on a threefold inversion axis along the Sb1-Sb1A vector. Each C1 atom resides on a proper twofold rotational axes, all of which cross in the centre of the molecule. The *c* glide planes run along the angle bisector of the twofold axes and intersect both antimony atoms.

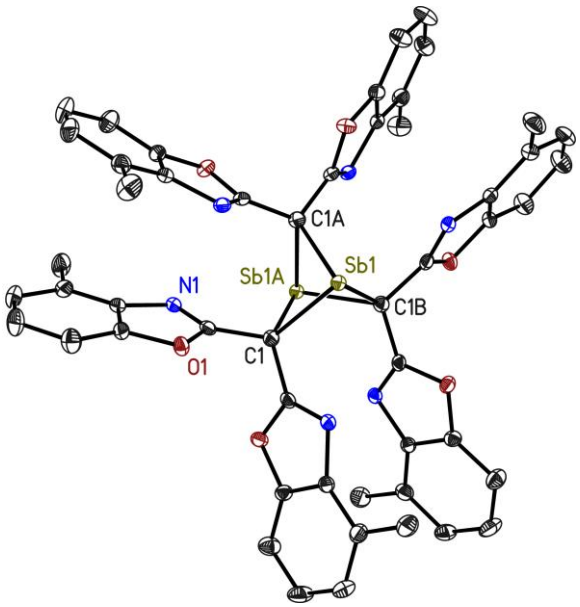

Figure 3-54: Molecular structure of (^{Me}Box)$_3$Sb$_2$ (**XVIII**) in the solid-state. The asymmetric unit contains only on third of the molecule. Anisotropic displacement parameters are depicted at the 50 % probability level. Hydrogen atoms are omitted for clarity.

The Sb1-C1 distance (2.226(2) Å) is more on the longer end of reported values for trivalent antimony compounds but not unusual (see appendix 5.6, Figure 5-34). The separation between both antimony atoms is 3.0522(6) Å, which is significantly shorter than the sum of their van der Waals radii (4.12 Å).[397] The Sb1-C1-Sb1A angle measures only 86.55°.

Compound **XVIII** evaded further experimental characterisation so far. Due to its insolubility in thf, diethyl ether, chloroform, dichloromethane, benzene, toluene, pentane, hexane, acetonitrile, acetone and isopropyl alcohol neither NMR spectroscopy nor LIFDI mass spectrometry could be performed.

The reaction was repeated with differing stoichiometries as well as at different temperatures but always with the same outcome. At the end of the reaction a brownish suspension was formed. Most of the product readily precipitated so that it could not be separated from the potassium chloride that is also formed during the reaction. Removing the volatiles under reduced pressure yielded a brown residue, which appeared powdery but if some force is applied with a spatula or by means of mortar and pistil it behaves more like an oily paste. This behaviour is not changed even after drying the residue at 150°C *in vacuo* for five hours. Residual solvent is therefore unlikely to be the cause. The only identifiable component that could be extracted from this residue was bis(4-methylbenzoxazol-2-yl)methane, which is probably formed *via* hydrolysis of ^{Me}BoxK by *in situ* generated hydrochloric acid. In order to scavenge the formed acid, the reaction was carried out with an excess of potassium hydride, which led to the immediate decomposition of antimony trichloride. Alternatively, the non-nucleophilic Hünig's base was used. It had no influence on the visual proceeding of the reaction. If it actually aided in the prevention of hydrolysis and potentially increased the yield of **XVIII** cannot be assessed due to the lack of options to analyse the residue. An attempt to purify the compound by sublimation was unsuccessful. Up to a temperature of 150°C at a pressure of 10^{-3} mbar no change occurred.

The powder obtained by filtration of the crude reaction mixture was dried *in vacuo* and analysed by powder X-ray diffraction. Measurements were performed on a BRUKER D8 Advance diffractometer with a copper X-ray source, a Göbel mirror and an Eiger2 detector in Bragg-Brentano geometry operated in reflection at room temperature. Samples were either prepared and sealed in an argon filled glove box or applied to the sample holder under ambient conditions. In both cases identical spectra were obtained. Repeated measurements of the same sample over two hours also showed no signs of deterioration. Hence, the compound is stable towards oxygen and moisture at least on the timescale of hours. The experimental spectra were analysed using the software Match!.[398] Comparison to powder spectra of **I**, **II** and **XVIII**, which were calculated based on their respective single crystal structure evidenced that the powder consists of the free ligand ^{Me}Box (**I**) as well as the product (^{Me}Box)$_3$Sb$_2$ (**XVIII**). Additional peaks in the powder diffraction pattern could be explained by the presence of potassium chloride by comparison to powder data stored in the Crystallography Open Database,[399] which is the expected second product of the reaction. In Figure 3-55 the experimental powder spectrum and the expected patterns for ^{Me}Box, (^{Me}Box)$_3$Sb$_2$ and KCl are shown. The calculated patterns for ^{Me}Box and (^{Me}Box)$_3$Sb$_2$ show a deviation from the recorded spectrum that increases with resolution. This is caused because the single crystal data were collected at 100 K while the powder

data were collected at 300 K. Due to the different temperatures also the unit cell parameters will differ. If the unit cell is expanded at 300 K relative to 100 K the structure will have a bigger d spacing causing the Bragg peaks to be shifted to lower 2Θ values. Apart from this shift, the recorded powder spectrum matches well with the expected pattern of this three component mixture. Quantification of the individual phases was not yet successful as this would require a more accurate fit of experimental and calculated patterns.

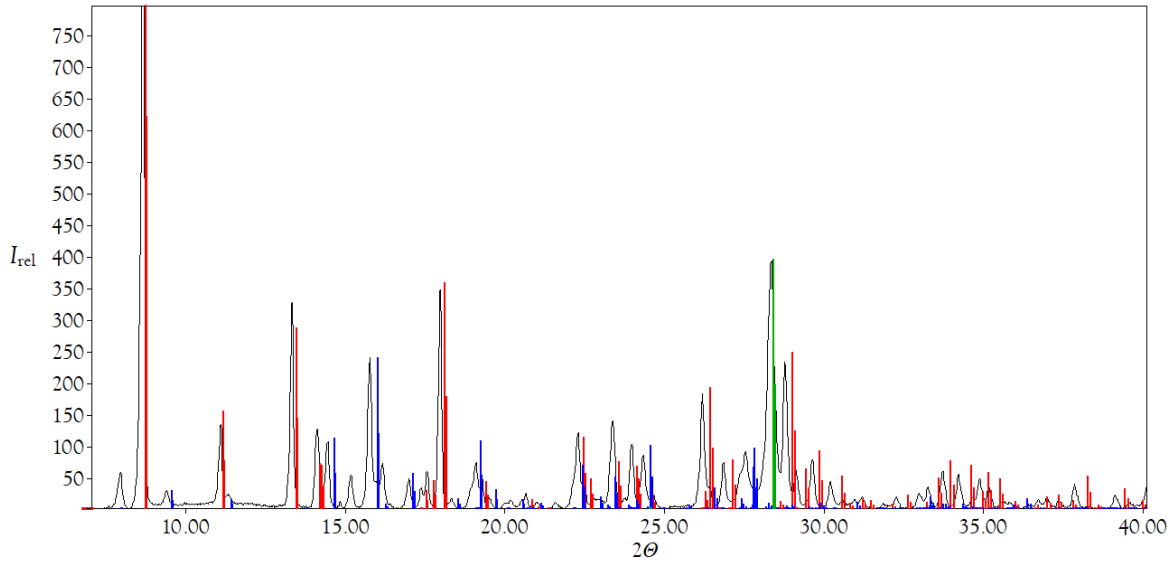

Figure 3-55: Powder X-ray diffraction pattern of the crude product obtained from the synthesis of (^{Me}Box)$_3$Sb$_2$ **(XVIII)**. The expected patterns for ^{Me}Box (blue), (^{Me}Box)$_3$Sb$_2$ (red) and KCl (green) are overlaid.

Antimony halide complexes of the type (NacNac)SbX$_2$ are known, but also with NacNac ligands unusual reactivity towards antimony(III) halides was observed depending on the substitution of the ligand.[400,401] However, no 1,3-distibabicyclo[1.1.1]pentane motif has been described. In fact, isolated bicyclo[1.1.1]pentanes with group 15 elements in 1 and 3 positions have so far not been reported at all. It is hypothesised that initially a [^{Me}BoxSbCl$_2$] type complex is formed, which further reacts with a second equivalent the same species under liberation of HCl. The *in situ* generated hydrochloric acid would also explain the presence of ^{Me}BoxH.

In order to gain further insight into the bonding situation of this compound, an investigation of its electron density distribution would be ideal. Since a single crystal of sufficient quality and diffracting power to collect high-resolution diffraction data could not be obtained, periodic density functional theory was engaged. Calculations were performed with the CRYSTAL17[402] software at the PBE0/POB-DZVP level of theory[403] additionally applying Grimme's D3

correction.[404] Atomic coordinates were taken from the experimentally determined single crystal X-ray structure and kept frozen during modelling. The periodic wave function obtained in this way was further used to derive a periodic electron density distribution, which could be analysed according to Bader's QTAIM formalism[405] implemented in the TOPOND14[406] program integrated with CRYSTAL17. Abramov's expression[407] was used to derive local kinetic and potential energy densities. For comparison, also gas phase calculations with the same atomic coordinates were performed at the B3LYP/x2c-TZVPall level of theory with Gaussian. Topological analysis of the charge density distribution was carried out with the AIMAll software.[408]

Table 3-7: Selected results of the topological analysis of the theoretically derived periodic electron density distribution of **XVIII**. Values obtained from gas phase calculations are given in brackets. $\varrho(r)$: electron density; $\nabla^2\varrho(r)$: Laplacian of electron density; ε: ellipticity; $V(r_{cp})$: potential energy density; $G(r_{cp})$: kinetic energy density.

bond	$\varrho(r)$ [eÅ^{-3}]	$\nabla^2\varrho(r)$ [eÅ^{-5}]	ε	$\lvert V(r_{cp})\rvert/G(r_{cp})$
Sb1-C1	0.620 (0.642)	2.219 (2.056)	0.000 (0.087)	1.58 (1.63)
C1-C2	1.839 (1.871)	−17.544 (−18.019)	0.069 (0.073)	4.40 (4.36)
C2-O1	1.865 (1.943)	−10.334 (−15.096)	0.041 (0.101)	2.38 (2.57)
C2-N1	2.541 (2.665)	−29.150 (−33.896)	0.291 (0.309)	3.09 (3.16)
C5-H5	2.529 (2.578)	−39.633 (−42.400)	0.004 (0.021)	6.54 (7.48)

The values obtained from the topological analysis at the bond critical point of each bond path allow to characterise the bonding interaction between the respective atoms.[409] In general, high values of electron density and a negative Laplacian are indicative of shared-shell interactions, whereas low electron density and a positive Laplacian point towards closed-shell interactions. This differentiation can also be made based on the ratio of the absolute value of the potential energy density and the kinetic energy density $|V(r_{cp})|/G(r_{cp})$. For covalent bonds, this ratio should adopt values greater than two, while closed-shell interactions give values smaller than one. These classifications are not strict as transitions between different interaction types are fluent and hence an intermediate range $1 < |V(r_{cp})|/G(r_{cp}) < 2$ can also be defined.

Results of the topological analysis are listed in appendix 5.6 for both electron density distributions derived from periodic (Table 5-6) as well gas phase (Table 5-7) calculations. Selected results are summarised in Table 3-7. With high electron density and negative values of the Laplacian at the bond critical points all intermolecular interactions can be classified as covalent, except for the carbon-antimony bond. In that case, the electron density is small and the Laplacian becomes positive. However, the ratio of the absolute value of the potential energy density and the kinetic energy density is 1.58 (1.63 in the gas phase calculation) and thus in the intermediate range between shared and closed-shell interactions. No indications of any interaction between the antimony atoms could be observed.

3.3 Summary and outlook

With the present work, the applicability of bis(benzoxazol-2-yl)methane based ligands in main group metal organic chemistry was extended to group 14 of the periodic table. Bis(4-methylbenzoxazol-2-yl)methanide complexes of germanium, tin and lead in oxidation +II could successfully be synthesised, isolated and characterised. A simple salt metathesis approach using potassium bis(4-methylbenzoxazol-2-yl)methanide and element(II) chlorides was successful for germanium and tin. In the latter case elevated temperature or ball milling were necessary for the reaction to proceed though. No reactivity was observed between potassium bis(4-methylbenzoxazol-2-yl)methanide and lead(II) chloride, bromide or nitrate in solution at room temperature. Indications of reactivity towards plumbocene were observed but the mixture of products rendered the reaction unfit. In analogy to the chloro stannylene ball milling might be a viable way to synthesise ^{Me}BoxPbCl, however, it appeared to be unstable in solution and was therefore not investigated further.

The solid-state structures of germylene ^{Me}BoxGeCl and stannylene ^{Me}BoxSnCl were both analysed by single crystal X-ray diffraction and showed, in accordance with NMR data, both molecules to be almost planar with only minor ligand folding or atom displacements. This suggests that the envisaged stabilisation of low oxidation states *via* formation of conjugated π system including the vacant p orbital of the low valent metal fragment is indeed functional. It is also noteworthy, that the relatively small steric demand of the methyl substituents suffices to prevent the dimerization of the synthesised chloro tetrylenes.

While bis(4-methylbenzoxazol-2-yl)methanide at this stage has already been proven to be an excellent ligand for the synthesis of tetrylenes, the chloro complexes suffered from low solubility and mediocre yields. An attempt to overcome these problems was presented by the use of group 14 bis(trimethylsilyl)amides instead of halides as tetrylene precursors. These HMDS compounds were successfully reacted with neutral bis(4-methylbenzoxazol-2-yl)methane to cleanly deprotonate and metalate it in a one pot protocol to afford ^{Me}BoxM(HMDS) (M=Ge, Sn, Pb) in good yields. These amido tetrylenes showed significantly improved solubility in common organic solvents compared their halide analogues. Analysis of the solid-state structures of these compounds revealed higher degrees of distortion in the ligands and bigger dislocations of the group 14 elements from the ligand plane than in the chloride analogues. However, these could

be ascribed to intermolecular interactions in the solid-state. Additionally, it was shown that NMR data suggest that in solution the planarity of the ligand is mostly conserved.

The main objective of the synthetic work presented in this thesis could thus be achieved. Five novel tetrylenes were synthesised and their crystal structures including two additional polymorphs were determined. It was shown to that unlike most NacNac compounds the bis(4-methylbenzoxazol-2-yl)methanide ligand is able to conserve its planarity most probably due the favourable formation of a cyclic conjugated π system including the group 14 element. In further work it would be interesting to assess the electronic situation of the prepared tetrylenes not only indirectly by means of structure analysis but to quantify it by theoretical methods. For the central six membered ring containing the group 14 element it might even be possibly to judge if and to what extend it has the character of a hetero aromatic system.

While for halides such as ^{Me}BoxGeCl and ^{Me}BoxSnCl in general a wide range of protocols for functionalisation are in place, it would be interesting to further investigate the reactivity of amido tetrylenes. As these are available in clean reactions with good yields they pose interesting starting materials. The polar character of the element-nitrogen bond might be employable, for example, in 1,2-additon reaction with unsaturated organic compounds like aldehydes or ketones.

Because heteroleptic tetrylenes of the kind discussed so far have also been described with other chelate ligands, but reports of homoleptic ones are rather rare, the aptitude of the bis(4-methylbenzoxazol-2-yl)methanide ligand was tested to form such homoleptic compounds. The synthesis of the lightest homologue (^{Me}Box)$_2$Ge turned out to be unsuccessful as only one bis(4-methylbenzoxazol-2-yl)methanide ligand coordinates. However, analogue tin and lead complexes could be synthesised and isolated in good yield. Analysis of their solid-state structure revealed that the ligands are very close to each other within in the complexes with distances of only 3.0 Å to 3.1 Å at the nearest points. Hence, it could be observed that the ligands are repelled by each other and deviate from planarity. This was not of concern, however, as in these cases the group 14 elements was anyway not located within the ligand plane.

The geometry of these complexes results in highly directional lone pairs as far as this can be indirectly assessed from their solid-state structures. It would be interesting to test the ability of these compounds to form complexes with transition metals. Due to all four methyl groups pointing in roughly the same direction as the lone pair, these tetrylenes might be fit to form linear complexes, for example, with mercury or gold compounds.

All of the synthesised tetrylenes, homoleptic and heteroleptic, were stable as solids stored under argon for several months. In no case was decomposition or degradation observed over time.

Subsequent to the synthesise of the novel bis(4-methylbenzoxazol-2-yl)methanide based tetrylenes, the reactivity of ^{Me}BoxGeCl was briefly investigated. Attempts to obtain a cationic germylene by chloride abstraction were not successful. Reaction with trimethylsilyl triflate gave a mixture of products, which could not be identified. Treatment of ^{Me}BoxGeCl with silver tetrafluoroborate instead led to the substitution of the chloride with a fluoride. The trivalent germanium(II) fluoride obtained in this way is only the eighth of such species, which have been structurally characterised so far. It is noteworthy, that other protocols for the preparation of such germanium(II) fluorides used harsher conditions and rather unpleasant fluorinating agents such as Me_2SnF_2. As this reaction might proceed *via* intermediate formation of the sought after cation, which then reacts with the tetrafluoroborate anion, the cationic might be accessible if a silver salt with a more robust anion is used instead.

Substitution of the chloride in ^{Me}BoxGeCl with lithium reagents was only exemplary tested with lithium diphenylphosphide. Although no product could be isolated, NMR analysis gave indication that the reaction proceeded as intended and further efforts might very well lead to isolable compounds containing additional phosphine donor sites next to the germylene.

At last, also the aptitude of the germylene to act as a heavy homologue of a NHC was tested in terms of coordination to a d-metal complex. ^{Me}BoxGeCl was successfully reacted with tungsten hexacarbonyl under UV radiation. The germylene coordinated to tungsten under displacement of one carbonyl ligand. The resulting complex was analysed by NMR spectroscopy, LIFDI mass spectroscopy and IR spectroscopy. While NMR data showed that ^{Me}BoxGeCl seems to be the main species in solution, results from mass spectrometry and IR spectroscopy of the solid bulk material strongly support the formation of the complex. It was therefore assumed, that the complex readily dissociates in thf. Additionally the complex could be crystallised and analysed by single crystal X-ray diffraction. In the solid-state structure consequences of the trans influence of the germylene ligand could be observed. Together with the red shift of the carbon monoxide stretching frequency compared to the parent tungsten hexacarbonyl germylene ^{Me}BoxGeCl could be characterised as strong σ-donor and possibly weak π-acceptor ligand.

With this preliminary study to explore the reactivity of ^{Me}BoxGeCl it is clear that more detailed investigations have to be conducted to thoroughly map the possibilities these tetrylenes hold. However, the results obtained so far do show that the bis(4-methylbenzoxazol-2-yl)methanide tetrylenes are very much capable of reactions also known for other *N*,*N*-chelated tetrylenes. Hence, it would be of high interest to see how the compounds described in this work perform in more challenging reactions, for example, with small molecules like carbon dioxide.

Out of curiosity the reactivity of potassium bis(4-methylbenzoxazol-2-yl)methanide towards antimony trichloride was tested. Instead of the expected complex, featuring a $SbCl_2$ fragment in *N,N* binding pocket, 2,2,4,4,5,5-hexa(4-methylbenzoxazol-2-yl)-1,3-distibabicyclo[1.1.1]pentane was formed. The 1,3 hetero substituted bicyclo[1.1.1]pentane motif found in this compound has been unprecedented for group 15 elements so far. The solid-state structure of this compound was determined by single crystal X-ray diffraction and revealed the molecule to be highly symmetric. Further characterisation of this compound was hampered by the fact that it is virtually insoluble. Powder X-ray diffraction of the precipitate obtained from the reaction revealed it to consist of potassium chloride, $(^{Me}Box)_3Sb_2$ and free ligand $^{Me}BoxH$. The latter is most probably formed *via* reaction with *in situ* generated hydrochloric acid. $(^{Me}Box)_3Sb_2$ appears to be stable under ambient atmosphere at room temperature, at least on the time scale of hours. To gain further insight into the bonding situation of this compound a topological analysis of computationally determined electron density distributions in the gas phase and the solid-state has been performed. In both cases no interaction between the antimony atoms is observed. The carbon-antimony bond has intermediate character between a closed and shared shell interaction with a low but positive Laplacian hinting at slightly more electrostatic than covalent bonding.
As soon as a method is found to cleanly obtain this intriguing compound, it would be interesting to see, if it could be used to selectively coordinate Lewis acids of different hardness according to the HSAB scale. The antimony atoms should act as rather soft donors compared to the oxygen or nitrogen atoms in the benzoxazole units. Possibly, two benzoxazole units might even chelate an appropriate Lewis acid. Furthermore, it would be fascinating to see if this compound could be selectively oxidised to a species with two formal Sb(+IV) centres, which might either behave like a diradical or form an intra molecular antimony-antimony bond in a highly constrained environment.

4 Experimental

4.1 General considerations

All reactions were carried out under exclusion of air and moisture using Schlenk techniques or in an Argon filled glovebox unless stated otherwise. Solvents were dried over appropiate drying agents and freshly distilled from sodium/potassium alloy (pentane), potassium (thf), sodium (toluene) or phosphor pentoxide (dcm). The solvents were degassed with minimum three freeze-pump-thaw cycles. The absence of oxygen and moisture was then confirmed by a benzophenone/ketyl test before use.

4.2 Single crystal X-ray diffraction

Crystals were transferred from the mother liquor to perfluorinated polyether oil and examined under a microscope with a polarised light source. If necessary, the X-Temp2 device[410,411] was used for the handling of highly reactive compounds. A suitable crystal was mounted on a glass fibre or a MITEGEN micro loop, mounted on the goniometer and shock cooled in a stream of nitrogen gas. Data were collected on APEX II CCD detectors with either an INCOATEC Mo IμS microfocus source (λ(Mo K_α=0.71073 Å), an INCOATEC Ag IμS microfocus source (λ(Ag K_α=0.56086 Å), or a BRUKER Mo rotating anode (λ(Mo K_α=0.71073 Å) all equipped with INCOATEC multilayer optics. Intensities on the raw frames were integrated with SAINT (v8.30C).[83] Data were scaled with SADABS[87] or TWINABS[84] if the crystal was twinned. If necessary, a 3λ correction[412] was applied. After space group determination with XPREP[89] structures were solved with SHELXT[93] and refined on F^2 with SHELXL[88] in the graphical user interface ShelXle.[94]

4.3 Other characterization

NMR: Deuterated solvents were dried with appropriate drying agents, distilled in *vacuo* and stored over molecular sieves for at least a week before use. Inside of an argon glovebox, NMR tubes with Teflon screw caps were filled with approx. 10mg of sample dissolved in 0.7 mL of deuterated solvent. Spectra were recorded at room temperature at a BRUKER Advance 300, a BRUKER, or a BRUKER Advance 400 MHz NMR spectrometer. All chemical shifts δ are given in ppm, relative

to the residual proton signal of the deuterated solvent. If necessary, assignments of the chemical shifts were checked by two–dimensional correlation spectra.

MS: Mass spectra were recorded at the mass spectrometry facility of the Faculty of Chemistry of the University of Göttingen on a JEOL accuTOF instrument with a LIFDI ion source and an inert-sample application setup under argon atmosphere. Samples were prepared in an argon filled glovebox with a typical concentration of 1 mg/mL dissolved in thf. ESI-MS measurements were not possible as they frequently led to hydrolysis of the compounds.

IR: Infrared spectra were recorded neat on an Agilent Cary 630 ATR-FTIR benchtop spectrometer.

Powder X-ray diffraction: Measurements were performed on a BRUKER D8 Advance diffractometer with a copper X-ray source (λ(Cu K_α=1.54060 Å), a Göbel mirror and an Eiger2 detector in Bragg-Brentano geometry operated in reflection.

4.4 Synthesis and characterization

4.4.1 ^{Me}BoxH – Bis(4-methylbenzoxazol-2-yl)methane **(I)**

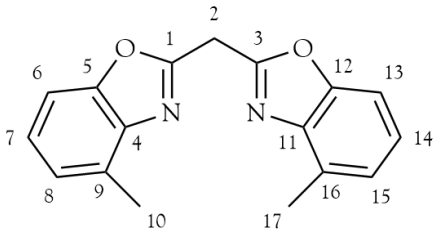

2-Amino-3-methylphenol (5.05 g, 41.0 mmol, 2.00 eq.) and ethylbisimidate dihydrochloride (4.74 g, 20.5 mmol, 1.00 eq.) were weighed into a round bottom flask and suspended in methanol (100 mL). The mixture was stirred and heated to reflux for 18 h and then kept at −25 °C to crystallise the product. The precipitate was filtered off by a Büchner funnel and washed with a saturated aqueous solution of sodium hydrogencarbonate (3×10 mL) and water (3×10 mL). After drying *in vacuo* the product was obtained as a light brown powder.

Chemical formula:	$C_{17}H_{14}N_2O_2$
Molecular weight:	278.31 g/mol
Yield:	2.53 g, 9.09 mmol, 44 %

^{1}H-NMR

(300 MHz, thf-d_8): δ = 7.33 (d, 2H, $^3J_{HH}$ = 8.1 Hz, 6-*H*, 13-*H*), 7.20 (t, 2H, $^3J_{HH}$ = 7.8 Hz, 7-*H*, 14-*H*), 7.11 (d, 2H, $^3J_{HH}$ = 7.4 Hz, 8-*H*, 15-*H*), 4.68 (s, 2H, 2-*H*), 2.54 (s, 6H, 10-C*H*$_3$,17-C*H*$_3$) ppm

(300 MHz, $CDCl_3$): δ = 7.33 (ddd, 2H, $^3J_{HH}$ = 8.0 Hz, $^4J_{HH}$ = 1.3 Hz, $^5J_{HH}$ = 0.7 Hz, 6-*H*, 13-*H*), 7.22 (t, 2H, $^3J_{HH}$ = 8.0 Hz, 7-*H*, 14-*H*), 7.13 (ddd, 2H, $^3J_{HH}$ = 8.0 Hz, $^4J_{HH}$ = 1.3 Hz, $^5J_{HH}$ = 0.7 Hz, 8-*H*, 15-*H*), 4.66 (s, 2H, 2-*H*), 2.62 (s, 6H, 10-C*H*$_3$,17-C*H*$_3$) ppm

^{13}C{^{1}H}-NMR

(75 MHz, $CDCl_3$): δ = 159.15 (1-C,2-C), 151.09 (5-C,12-C), 140.51 (4-C,11-C), 130.76 (9-C,16-C), 125.21 (8-C,15-C), 125.07 (7-C,14-C), 108.12 (6-C,13-C), 29.65 (2-C), 16.63 (10-CH_3, 17-CH_3) ppm

4.4.2 ^{Me}BoxK – Potassium bis(4-methylbenzoxazol-2-yl)methanide (**II**)

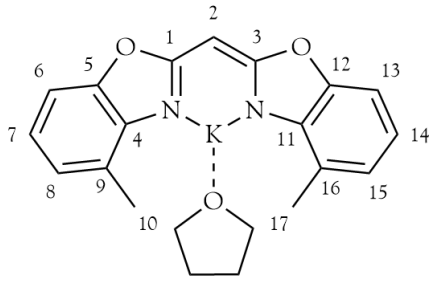

Bis(4-methylbenzoxazol-2-yl)methane (2.00 g, 7.19 mmol, 1.00 eq.) was dissolved in thf (15 mL). Potassium hydride (317 mg, 7.90 mmol, 1.10 eq.) was added at room temperature under vigorous stirring and the mixture turned yellow immediately. After the evolution of gas had ceased, the solution was stirred for 2 h at room temperature before all volatiles were removed *in vacuo* to yield the product as a yellow powder.

Chemical formula:	$C_{17}H_{13}N_2O_2K{\cdot}C_4H_8O$
Molecular weight:	388.51 g/mol
Yield:	2.65 g, 6.83 mmol, 95 %

^{1}H-NMR

(300 MHz, thf-d_8): δ = 6.85 (d, 2H, $^{3}J_{HH}$ = 7.5 Hz, 6-*H*, 13-*H*), 6.71 (d, 2H, $^{3}J_{HH}$ = 7.5 Hz, 8-*H*, 15-*H*), 6.60 (t, 2H, $^{3}J_{HH}$ = 7.5 Hz, 7-*H*, 14-*H*), 4.65 (s, 1H, 2-*H*), 3.62 (m, 4H, thf), 2.41 (s, 6H, 10-C*H*$_3$,17-C*H*$_3$), 1.77 (m, 4H, thf) ppm

^{13}C{^{1}H}-NMR

(75 MHz, thf-d_8): δ = 170.28 (1-C,2-C), 156.56 (5-C,12-C), 146.47 (4-C,11-C), 123.89 (8-C,15-C), 122.52 (9-C,16-C), 118.48 (7-C,14-C), 105.65 (6-C,13-C), 56.99 (2-C), 17.54 (10-CH$_3$, 17-CH$_3$) ppm

4.4.3 ^{Me}BoxGeCl – {Bis(4-methylbenzoxazol-2-yl)methanide}germanium(II) chloride **(III)**

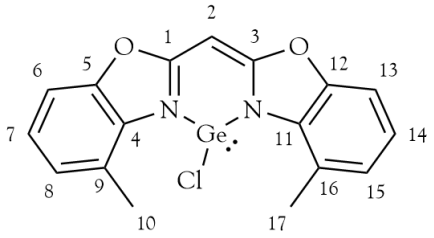

Potassium bis(4-methylbenzoxazol-2-yl)methanide (200 mg, 0.515 mmol, 1.00 eq.) was dissolved in thf (5 mL). To this solution germanium(II) chloride dioxane complex (119 mg, 0.515 mmol, 1.00 eq.) was added at room temperature under vigorous stirring. The initially clear yellow solution immediately became lighter in colour and turned cloudy due to the formation of a white precipitate. The reaction mixture was stirred for 1 d at room temperature before it was centrifuged to separate the precipitate from the solution. Alternatively, the mixture can also be filtered. The clear yellow solution was dried *in vacuo* to obtain the product as a light yellow powder. The yield can be increased by extraction of the precipitate with thf or toluene. Crystals suitable for SC-XRD experiments were grown by vapour diffusion of pentane into solutions of **III** in thf or dcm at −25°C.

Chemical formula:	$C_{17}H_{13}N_2O_2GeCl$
Molecular weight:	385.38 g/mol
Yield:	70 mg, 0.182 mmol, 35 %
^{1}H-NMR	
(300 MHz, thf-d_8):	δ = 7.33-7.25 (m, 2H, 6-*H*, 13-*H*), 7.18-7.08 (m, 4H, 7-*H*, 8-*H*, 14-*H*, 15-*H*), 5.66 (s, 1H, 2-*H*), 2.82 (s, 6H, 10-C*H*$_3$,17-C*H*$_3$) ppm
^{13}C{^{1}H}-NMR	
(75 MHz, thf-d_8):	δ = 134.66 (4-C, 11-C), 127.91 (8-C, 15-C), 124.60 (7-C, 14-C), 108.55 (6-C, 13-C), 62.50 (2-C), 21.05 (10-CH_3, 17-CH_3) ppm
MS (LIFDI[+], thf)	
m/*z* (%):	387.6 (100) $[M+H]^+$

4.4.4 ^{Me}BoxSnCl – {Bis(4-methylbenzoxazol-2-yl)methanide}tin(II) chloride (**V**)

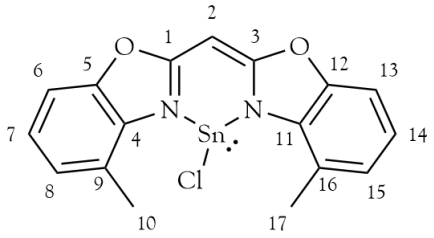

Method A: Potassium bis(4-methylbenzoxazol-2-yl)methanide (210 mg, 0.541 mmol, 1.00 eq.) was dissolved in thf (5 mL). To this solution tin(II) chloride (102 mg, 0.541 mmol, 1.00 eq.) was added at room temperature. The resultant cloudy suspension was heated to reflux and kept at this temperature under vigorous stirring. After 48 h the reaction mixture was cooled down to room temperature. Solids were separated by filtration and extracted with thf (3×3 mL). All extracts were combined with the filtrate and volatiles were removed *in vacuo* to obtain a light yellow powder. This crude product was washed with pentane (2×2 mL) and the remaining solid dried under reduced pressure to obtain the product as a yellow powder. Crystals suitable for SC-XRD experiments were grown by vapour diffusion of pentane into solutions of **V** in thf at −25°C.

Method B: A zirconium oxide grinding bowl was charged with zirconium oxide grinding balls, potassium bis(4-methylbenzoxazol-2-yl)methanide (500 mg, 1.29 mmol, 1.00 eq.) and tin(II) chloride (244 mg, 1.29 mmol, 1.00 eq.). The grinding bowl was sealed under argon atmosphere and placed in a *PULVERISETTE 7* planetary mill. Ball milling was performed at 500 rpm for 2 min followed by a 4 min resting period. This sequence was iterated for a total of 2 h. The crude product was washed with pentane (3×5 mL) and then extracted with thf (3×10 mL). All extracts were combined and volatiles were removed *in vacuo* to obtain the product as a yellow powder.

Chemical formula:	$C_{17}H_{13}N_2O_2SnCl$
Molecular weight:	431.46 g/mol
Yield *(Method A)*:	38 mg, 0.088 mmol, 16 %
Yield *(Method B)*:	275 mg, 0.636 mmol, 49 %

^{1}H-NMR

(300 MHz, thf-d_8): δ = 7.34-7.17 (m, 2H, 6-*H*, 13-*H*), 7.12-7.01 (m, 4H, 7-*H*, 8-*H*, 14-*H*, 15-*H*), 5.43 (s, 1H, 2-*H*), 2.80 (s, 6H, 10-C*H*$_3$,17-C*H*$_3$) ppm

$^{13}C\{^1H\}$-NMR

(75 MHz, thf-d_8): δ = 127.28 (8-C, 15-C), 123.83 (7-C, 14-C), 108.25 (6-C, 13-C), 61.81 (2-C), 21.19 (10-CH_3, 17-CH_3) ppm

4.4.5 ^{Me}BoxPbX – {Bis(4-methylbenzoxazol-2-yl)methanide}lead(II) $[X]^-$

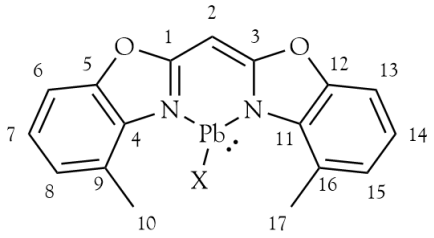

Method A (X=Cl): Potassium bis(4-methylbenzoxazol-2-yl)methanide (150 mg, 0.386 mmol, 1.00 eq.) was dissolved in thf (5 mL). To this solution lead(II) chloride (107 mg, 0.359 mmol, 1.00 eq.) was added at room temperature. The resultant cloudy suspension was vigorously stirred at room temperature. After 24 h all volatiles were removed *in vacuo* to obtain a light yellow powder, which contained only unreacted starting materials.

Method B (X=Br): Equivalent to method A. Lead(II) bromide (142 mg, 0.386 mmol, 1.00 eq.) was used instead of lead(II) chloride.

Method C ($X=NO_3$): Equivalent to method A. Lead(II) nitrate (128 mg, 0.386 mmol, 1.00 eq.) was used instead of lead(II) chloride.

Method D (X=Cp): Equivalent to method A. Di(cyclopentadienyl)lead(II) (130 mg, 0.386 mmol, 1.00 eq.) was used instead of lead(II) chloride. The only identified product was $K[PbCp_3]$

Method E (X=Cl): A zirconium oxide grinding bowl was charged with zirconium oxide grinding balls, potassium bis(4-methylbenzoxazol-2-yl)methanide (500 mg, 1.29 mmol, 1.00 eq.) and lead(II) chloride (358 mg, 1.29 mmol, 1.00 eq.). The grinding bowl was sealed under argon atmosphere and placed in a *PULVERISETTE 7* planetary mill. Ball milling was performed at 500 rpm for 2 min followed by a 4 min resting period. This sequence was iterated for a total of 2 h. Attempts to dissolve the crude product lead to apparent decomposition.

4.4.6 $PbCp_2$ – Di(cyclopentadienyl)lead(II) (plumbocene)

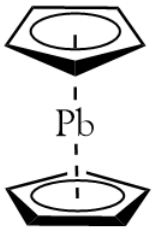

Cyclopentadienyl sodium (1.27 g, 14.4 mmol, 2.00 eq.) and lead(II) chloride (2.00 g, 7.19 mmol, 1.00 eq.) were placed in a schlenk flask. Toluene (5 mL) was added and the resultant red-brown slurry was heated to 120°C. After 24 h the colour of the reaction mixture had changed to yellow-greenish and all volatiles were removed *in vacuo*. The residue was subjected to a Soxhlet extraction with toluene under argon atmosphere resulting in a bright yellow solution. After the solvent of the extract was removed under reduced pressure the product was obtained as a bright yellow powder, which was stored at −25°C until further use.

Chemical formula:	$C_{10}H_{10}Pb$
Molecular weight:	337.39 g/mol
Yield:	1.00 g, 2.96 mmol, 41 %

^{1}H-NMR	
(300 MHz, C_6D_6):	δ = 5.80 (s, 10H) ppm
^{13}C{^{1}H}-NMR	
(75 MHz, C_6D_6):	δ = 111.60 ppm
^{207}Pb-NMR	
(84 MHz, C_6D_6):	δ = −5032 ppm

4.4.7 $Ge(HMDS)_2$ – Germanium(II) bis(trimethylsilyl)amide **(VI)**

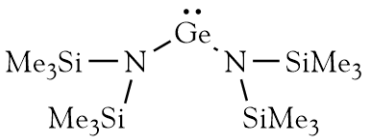

Germanium(II) bis(trimethylsilyl)amide was prepared according to a previously published procedure.[384] Germanium(II) chloride dioxane complex (500 mg, 2.16 mmol, 1.00 eq.) and lithium bis(trimethylsilyl)amide (726 mg, 4.34 mmol, 2.00 eq.) were dissolved in thf (4 mL) and stirred at room temperature for 2.5 h. After the reaction was completed, all volatiles were removed *in vacuo*. The residue was suspended in pentane (3 mL) and filtrated. The clear filtrate was dried under reduced pressure to obtain the product as an orange-red oil, which was stored at −25°C until further use.

Chemical formula:	$C_{12}H_{36}GeN_2Si_4$
Molecular weight:	393.40 g/mol
Yield:	627 mg, 1.59 mmol, 74 %

^{1}H-NMR

(300 MHz, $CDCl_3$): δ = 0.36 (s, $^1J_{CH}$ = 119.1 Hz, $^2J_{SiH}$ = 6.5 Hz, 36H, Si-CH_3) ppm

^{13}C{^{1}H}-NMR

(75 MHz, $CDCl_3$): δ = 5.96 ($^1J_{SiC}$ = 56.9 Hz, Si-CH_3) ppm

4.4.8 ^{Me}BoxGe(HMDS) – {Bis(4-methylbenzoxazol-2-yl)methanide}germanium(II) bis(trimethylsilyl)amide (**VII**)

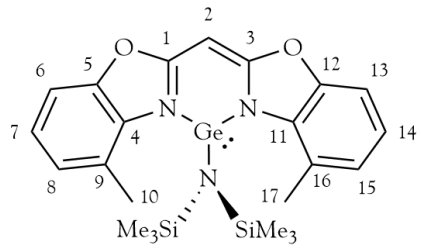

Germanium(II) bis(trimethylsilyl)amide (141 mg, 0.359 mmol, 1.00 eq.) was dissolved in thf (3 mL). To this solution bis(4-methylbenzoxazol-2-yl)methane (100 mg, 0.359 mmol, 1.00 eq.) was added under vigorous stirring. The clear yellow-orange solution was stirred for 1 d at room temperature before all volatiles were removed *in vacuo* to obtain the product as a yellow powder. Impurities of the starting materials can be extracted with pentane, but this will reduce the yield as the product is also soluble. Crystals suitable for SC-XRD experiments were grown from concentrated solutions of **VII** in thf/pentane (2:1.5) at −25°C.

Chemical formula:	$C_{23}H_{31}N_3O_2GeSi_2$
Molecular weight:	510.32 g/mol
Yield:	102 mg, 0.200 mmol, 55 %

^{1}H-NMR

(300 MHz, thf-d_8): δ = 7.22-7.15 (m, 2H, 6-*H*, 13-*H*), 7.08-7.01 (m, 4H, 7-*H*, 8-*H*, 14-*H*, 15-*H*), 5.36 (s, 1H, 2-*H*), 2.85 (s, 6H, 10-C*H*$_3$,17-C*H*$_3$), 0.05 (s, 18H, Si-C*H*$_3$) ppm

^{13}C{^{1}H}-NMR

(75 MHz, thf-d_8): δ = 136.57 (4-C, 11-C), 127.34 (8-C, 15-C), 124.66 (9-C, 16-C), 123.80 (7-C, 14-C), 108.04 (6-C, 13-C), 61.43 (2-C), 22.36 (10-CH$_3$, 17-CH$_3$), 5.47 (Si-CH$_3$) ppm

MS (LIFDI[+], thf)

m/*z* (%): 511.6 (100) $[M]^+$

4.4.9 $Sn(HMDS)_2$ – Tin(II) bis(trimethylsilyl)amide **(VIII)**

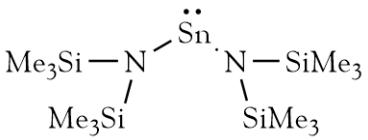

Tin(II) bis(trimethylsilyl)amide was prepared according to a previously published procedure.[384] Lithium bis(trimethylsilyl)amide (2.00 g, 11.9 mmol, 2.00 eq.) and tin(II) chloride (1.13 g, 5.98 mmol, 1.00 eq.) were dissolved in thf (5 mL) and stirred at room temperature for 2.5 h. After the reaction was completed, all volatiles were removed *in vacuo*. The residue was suspended in pentane (3 mL) and filtrated. The clear filtrate was dried under reduced pressure to obtain the product as a red oil, which was stored at −25°C until further use.

Chemical formula:	$C_{12}H_{36}SnN_2Si_4$
Molecular weight:	439.48 g/mol
Yield:	2.38 g, 5.42 mmol, 90 %

^{1}H-NMR

(300 MHz, C_6D_6): δ = 0.29 (s, $^2J_{SiH}$ = 6.3 Hz, 36H, Si-CH_3) ppm

^{13}C{^{1}H}-NMR

(75 MHz, C_6D_6): δ = 5.92 (Si-CH_3) ppm

4.4.10 ^{Me}BoxSn(HMDS) – {Bis(4-methylbenzoxazol-2-yl)methanide}tin(II) bis(trimethylsilyl)amide (**IX**)

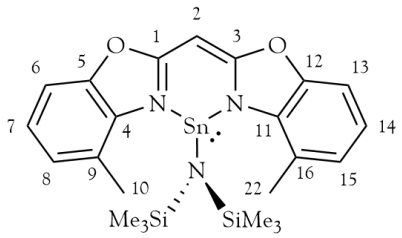

Tin(II) bis(trimethylsilyl)amide (265 mg, 0.603 mmol, 1.00 eq.) was dissolved in thf (5 mL). To this solution bis(4-methylbenzoxazol-2-yl)methane (168 mg, 0.603 mmol, 1.00 eq.) was added under vigorous stirring. The clear orange solution was stirred for 1 d at room temperature before all volatiles were removed *in vacuo* to obtain the product as a yellow powder. Impurities of the starting materials can be extracted with pentane, but this will reduce the yield as the product is also soluble. Crystals suitable for SC-XRD experiments were grown from concentrated solutions of **IX** in pentane at −25°C.

Chemical formula:	$C_{23}H_{31}N_3O_2SnSi_2$
Molecular weight:	556.40 g/mol
Yield:	265 mg, 0.476 mmol, 79 %
^{1}H-NMR	
(300 MHz, C_6D_6):	δ = 6.91-6.80 (m, 2H, 6-*H*, 13-*H*), 6.76-6.67 (m, 4H, 7-*H*, 8-*H*, 14-*H*, 15-*H*), 5.43 (s, 1H, 2-*H*), 2.70 (s, 6H, 10-C*H*$_3$,17-C*H*$_3$), 0.19 (s, $^1J_{CH}$ = 117.6.1 Hz, $^2J_{SiH}$ = 6.3 Hz, 18H, Si-C*H*$_3$) ppm
^{13}C{^{1}H}-NMR	
(75 MHz, C_6D_6):	δ = 166.75 (1-C, 3-C), 148.38 (5-C, 12-C), 138.18 (4-C, 11-C), 126.26 (8-C, 15-C), 123.23 (9-C, 16-C), 122.59 (7-C, 14-C), 107.31 (6-C, 13-C), 61.24 (2-C), 21.49 (10-CH$_3$, 17-CH$_3$), 5.62 (Si-CH$_3$) ppm
MS (LIFDI[+], thf)	
m/z (%):	557.4 (100) $[M]^+$

4.4.11 $Pb(HMDS)_2$ – Lead(II) bis(trimethylsilyl)amide (**X**)

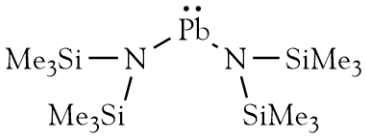

Lead(II) bis(trimethylsilyl)amide was prepared according to a previously published procedure.[384] Lithium bis(trimethylsilyl)amide (1.50 g, 8.99 mmol, 2.00 eq.) and lead(II) chloride (1.25 g, 4.49 mmol, 1.00 eq.) were dissolved in thf (5 mL) and stirred at room temperature for 2.5 h. After the reaction was completed, all volatiles were removed *in vacuo*. The residue was suspended in pentane (3 mL) and filtrated. The clear filtrate was dried under reduced pressure to obtain the product as a red oil, which was stored at −25°C until further use.

Chemical formula:	$C_{12}H_{36}PbN_2Si_4$
Molecular weight:	527.97 g/mol
Yield:	2.25 g, 3,77 mmol, 84 %

^{1}H-NMR	
(300 MHz, C_6D_6):	δ = 0.87 (s, 36H, Si-CH_3) ppm
^{13}C{^{1}H}-NMR	
(75 MHz, C_6D_6):	δ = 5.94 (Si-CH_3) ppm

4.4.12 ^{Me}BoxPb(HMDS) – {Bis(4-methylbenzoxazol-2-yl)methanide}lead(II) bis(trimethylsilyl)amide (**XI**)

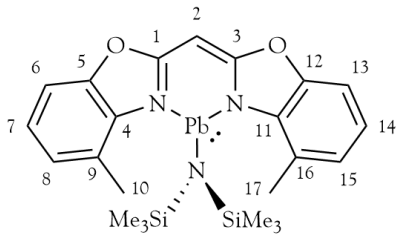

Lead(II) bis(trimethylsilyl)amide (190 mg, 0.359 mmol, 1.00 eq.) was dissolved in thf (3 mL). To this solution bis(4-methylbenzoxazol-2-yl)methane (100 mg, 0.359 mmol, 1.00 eq.) was added under vigorous stirring. The clear yellow-orange solution was stirred for 1 d at room temperature before all volatiles were removed *in vacuo* to obtain the product as a yellow powder. Impurities of the starting materials can be extracted with pentane, but this will reduce the yield as the product is also soluble. Crystals suitable for SC-XRD experiments were grown from concentrated solutions of **XI** in pentane or dcm at −25°C.

Chemical formula:	$C_{23}H_{31}N_3O_2PbSi_2$
Molecular weight:	644.89 g/mol
Yield:	169 mg, 0.262 mmol, 73 %

^{1}H-NMR

(300 MHz, thf-d_8): δ = 7.18-7.11 (m, 2H, 6-*H*, 13-*H*), 7.01-6.92 (m, 4H, 7-*H*, 8-*H*, 14-*H*, 15-*H*), 5.18 (s, 1H, 2-*H*), 2.82 (s, 6H, 10-C*H*$_3$,17-C*H*$_3$), 0.00 (s, $^{1}J_{CH}$ = 116.9 Hz, $^{2}J_{SiH}$ = 6.1 Hz, 18H, Si-C*H*$_3$) ppm

^{13}C{^{1}H}-NMR

(75 MHz, thf-d_8): δ = 149.80 (5-C, 12-C), 139.42 (4-C, 11-C), 126.36 (8-C, 15-C), 123.84 (9-C, 16-C), 122.84 (7-C, 14-C), 107.73 (6-C, 13-C), 62.50 (2-C), 20.29 (10-CH$_3$, 17-CH$_3$), 5.85 (Si-CH$_3$) ppm

MS (LIFDI[+], thf)

m/*z* (%): 762.0 (100) $[C_{34}H_{26}N_4O_4Pb]^+$

[a]For discussion see chapter 3.2.8

4.4.13 (^{Me}Box)$_2$Ge – Bis{bis(4-methylbenzoxazol-2-yl)methanide}germanium(II)

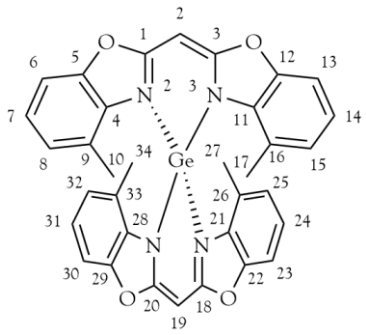

Germanium(II) bis(trimethylsilyl)amide (100 mg, 0.254 mmol, 1.00 eq.) was dissolved in thf (2 mL). To this solution bis(4-methylbenzoxazol-2-yl)methane (141 mg, 0.508 mmol, 2.00 eq.) was added under vigorous stirring. The clear light yellow solution became darker within minutes and was stirred for 1 d at room temperature. All volatiles were removed *in vacuo* and the residue was washed with pentane (2 mL) to obtain a light yellow powder. NMR analysis revealed it to be a 1:1 mixture of ^{Me}BoxGe(HMDS) and bis(4-methylbenzoxazol-2-yl)methane

4.4.14 (^{Me}Box)$_2$Sn – Bis{bis(4-methylbenzoxazol-2-yl)methanide}tin(II) **(XII)**

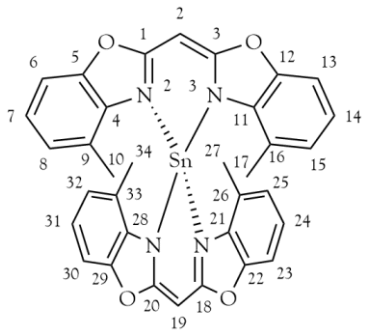

Tin(II) bis(trimethylsilyl)amide (100 mg, 0.227 mmol, 1.00 eq.) was dissolved in thf (3 mL). To this solution bis(4-methylbenzoxazol-2-yl)methane (127 mg, 0.455 mmol, 2.00 eq.) was added under vigorous stirring. The clear yellow-orange solution became lighter in colour and after stirring for 1 d at room temperature a precipitate had formed. All volatiles were removed *in vacuo* and the residue was washed with pentane (1 mL) to obtain the product as a yellow powder. Crystals suitable for SC-XRD experiments were grown from concentrated solutions of **XII** in dcm at −25°C.

Chemical formula:	$C_{34}H_{26}N_4O_4Sn$
Molecular weight:	673.32 g/mol
Yield:	127 mg, 0.188 mmol, 83 %

^{1}H-NMR

(300 MHz, thf-d_8): δ = 6.93 (d, 4H, $^3J_{HH}$ = 7.9 Hz, 6-*H*, 13-*H*, 23-*H*, 30-*H*), 6.85 (t, 4H, $^3J_{HH}$ = 7.7 Hz, 7-*H*, 14-*H*, 24-*H*, 31-*H*), 6.63 (d, 4H, $^3J_{HH}$ = 8.0 Hz, 8-*H*, 15-*H*, 25-*H*, 32-*H*), 4.68 (s, 2H, 2-*H*, 19-*H*), 2.43 (s, 12H, 10-C*H*$_3$,17-C*H*$_3$, 27-C*H*$_3$,34-C*H*$_3$) ppm

^{13}C{^{1}H}-NMR

(75 MHz, thf-d_8): δ = 149.48 (5-C, 12-C, 22-C, 29-C), 139.91 (4-C, 11-C, 21-C, 28-C), 125.63 (8-C, 15-C, 25-C, 32-C), 124.49 (9-C, 16-C, 26-C, 33-C), 122.80 (7-C, 14-C, 24-C, 31-C), 107.40 (6-C, 13-C, 23-C, 30-C), 62.30 (2-C, 19-C), 19.36 (10-CH_3, 17-CH_3, 27-CH_3, 34-CH_3) ppm

MS (LIFDI[+], thf)

m/*z* (%): 674.0 (100) $[M]^+$

4.4.15 (^{Me}Box)$_2$Pb – Bis{bis(4-methylbenzoxazol-2-yl)methanide}lead(II) (**XIII**)

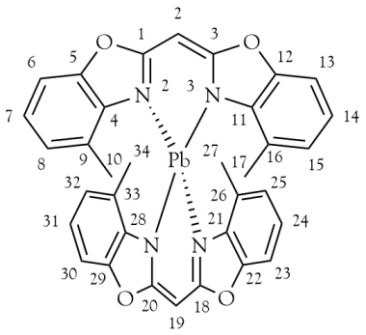

Lead(II) bis(trimethylsilyl)amide (100 mg, 0.189 mmol, 1.00 eq.) was dissolved in thf (3 mL). To this solution bis(4-methylbenzoxazol-2-yl)methane (105 mg, 0.379 mmol, 2.00 eq.) was added under vigorous stirring. The clear yellow solution became darker within minutes and was stirred for 1 d at room temperature. All volatiles were removed *in vacuo* and the residue was washed with pentane (1 mL) to obtain the product as a yellow powder. Crystals suitable for SC-XRD experiments were grown by vapour diffusion of pentane into solutions of **XIII** in thf at −25°C.

Chemical formula:	$C_{34}H_{26}N_4O_4Pb$
Molecular weight:	761.81 g/mol
Yield:	127 mg, 0.166 mmol, 88 %

^{1}H-NMR

(300 MHz, thf-d_8): δ = 6.92 (d, 4H, $^3J_{HH}$ = 7.9 Hz, 6-*H*, 13-*H*, 23-*H*, 30-*H*), 6.75 (t, 4H, $^3J_{HH}$ = 7.8 Hz, 7-*H*, 14-*H*, 24-*H*, 31-*H*), 6.57 (d, 4H, $^3J_{HH}$ = 7.6 Hz, 8-*H*, 15-*H*, 25-*H*, 32-*H*), 4.27 (s, 2H, 2-*H*, 19-*H*), 2.39 (s, 12H, 10-C*H*$_3$,17-C*H*$_3$, 27-C*H*$_3$,34-C*H*$_3$) ppm

^{13}C{^{1}H}-NMR

(75 MHz, thf-d_8): δ = 170.23 (1-C, 3-C, 18-C, 20-C), 150.72 (5-C, 12-C, 22-C, 29-C), 141.07 (4-C, 11-C, 21-C, 28-C), 124.84 (8-C, 15-C, 25-C, 32-C), 124.14 (9-C, 16-C, 26-C, 33-C), 122.34 (7-C, 14-C, 24-C, 31-C), 106.87 (6-C, 13-C, 23-C, 30-C), 64.33(2-C, 19-C), 18.24 (10-CH$_3$, 17-CH$_3$, 27-CH$_3$, 34-CH$_3$) ppm

MS (LIFDI[+], thf)

m/*z* (%): 762.0 (100) $[M]^+$

4.4.16 ^{Bzh}BoxGeCl – {Bis(4-benzhydrylbenzoxazol-2-yl)methanide}germanium(II) chloride **(XIV)**

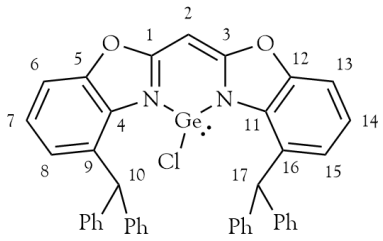

Potassium bis(4-benzhydrylbenzoxazol-2-yl)methanide (213 mg, 0.343 mmol, 1.00 eq.) was dissolved in thf (5 mL). To this solution germanium(II) chloride dioxane complex (80 mg, 0.343 mmol, 1.00 eq.) was added at room temperature under vigorous stirring. The initially clear yellow solution immediately became darker in colour and slowly turned cloudy due to the formation of a white precipitate. The reaction mixture was stirred for 1 d at room temperature before it was filtered. The filtrate was dried under reduced pressure to obtain the product as a pale yellow powder. Crystals suitable for SC-XRD experiments were grown by vapour diffusion of pentane into solutions of **XIV** in thf at −25°C.

Chemical formula:	$C_{41}H_{29}N_2O_2GeCl$
Molecular weight:	689.78 g/mol
Yield:	151 mg, 0.219 mmol, 64 %

^{1}H-NMR

(300 MHz, thf-d_8): δ = 7.38-7.08 (m, 24H, 6-*H*, 7-*H*, 13-*H*, 14-*H*, Ph-H_{20}), 6.87 (d, 2H, $^3J_{HH}$ = 7.9 Hz, 8-*H*, 15-*H*), 6.51 (s, 2H, 10-*H*,17-*H*), 5.63 (s, 1H, 2-*H*) ppm

^{13}C{^{1}H}-NMR

(75 MHz, thf-d_8): δ = 166.19 (1-C, 3-C), 149.12 (5-C, 12-C), 144.56 (Ph-C_{ipso}), 142.70 (Ph-C_{ipso}), 135.56 (4-C, 11-C), 130.99 (Ph-C_{ortho}), 130.84 (5-C, 12-C), 130.79 (Ph-C_{ortho}), 129.43 (Ph-C_{meta}), 129.27 (Ph-C_{meta}), 127.99 (8-C, 15-C), 127.65 (Ph-C_{para}), 124.32 (7-C, 14-C), 108.99 (6-C, 13-C), 62.79 (2-C), 54.54 (10-C, 17-C) ppm

^{1}H-NMR

(300 MHz, C_6D_6): δ = 7.41-7.33 (m, 8H, Ph-H_{ortho}), 7.21-6.99 (m, 12H, Ph-$H_{meta,para}$), 6.90 (dd, 2H, $^3J_{HH}$ = 7.9 Hz, 1.2 Hz, 8-*H*, 15-*H*), 6.77 (dd, 2H,

$^{3}J_{HH}$ = 7.9 Hz, 1.2 Hz, 6-*H*, 13-*H*), 6.74 (s, 2H, 10-*H*,17-*H*), 6.69 (t, 2H, $^{3}J_{HH}$ = 7.9 Hz, 7-*H*, 14-*H*), 5.24 (s, 1H, 2-*H*) ppm

$^{13}C\{^{1}H\}$-NMR

(75 MHz, C_6D_6): δ = 164.93 (1-C, 3-C), 148.20 (5-C, 12-C), 144.09 (Ph-C_{ipso}), 141.93 (Ph-C_{ipso}), 134.87 (4-C, 11-C), 130.53 (Ph-C_{ortho}), 130.28 (5-C, 12-C), 130.23 (Ph-C_{ortho}), 128.84 (Ph-C_{meta}), 128.34 (Ph-C_{meta}), 127.43 (8-C, 15-C), 127.27 (Ph-C_{para}), 127.10 (Ph-C_{para}), 123.48 (7-C, 14-C), 108.10 (6-C, 13-C), 62.95 (2-C), 54.04 (10-C, 17-C) ppm

4.4.17 ^{Me}BoxGeF – {Bis(4-methylbenzoxazol-2-yl)methanide}germanium(II) fluoride (**XV**)

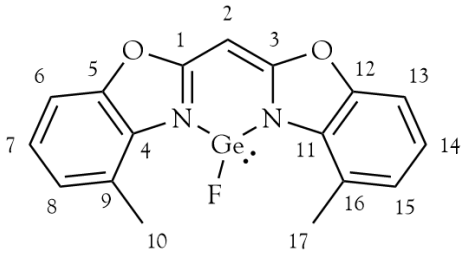

{Bis(4-methylbenzoxazol-2-yl)methanide}germanium(II) chloride (50 mg, 0.130 mmol, 1.00 eq.) was dissolved in thf (5 mL). To this solution silver tetrafluoroborate (30 mg, 0.154 mmol, 1.20 eq.) was added and the mixture was stirred for 1 d at room temperature. Afterwards, the suspension was filtered and the filtrate was dried *in vacuo* to obtain a mixture of the product and {bis(4-methylbenzoxazol-2-yl)methanide}germanium(II) chloride as a yellow powder. Crystals suitable for SC-XRD experiments were grown by vapour diffusion of pentane into solutions of this mixture in thf at −25°C.

Chemical formula:	$C_{17}H_{13}N_2O_2GeF$
Molecular weight:	368.93 g/mol
Yield*:	70 mg, 0.182 mmol, 35 %

Due to the co-crystallisation of ^{Me}BoxGeCl and ^{Me}BoxGeF the latter could not be characterised unambiguously.

*Yield of the fluorinated compound based on the solid-state composition as determined by SC-XRD.

4.4.18 ^{Me}BoxGe(Cl)W(CO)$_5$ – Pentacarbonyl{chloro[bis(4-methylbenzoxazol-2-yl)methanide] germylene}tungsten(0) (**XVI**)

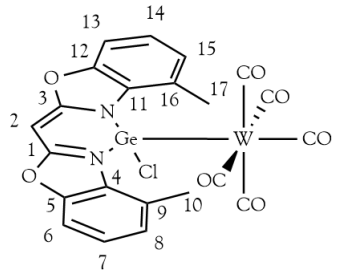

{Bis(4-methylbenzoxazol-2-yl)methanide}germanium(II) chloride (200 mg, 0.519 mmol, 1.00 eq.) was dissolved in thf (5 mL). To this solution tungsten hexacarbonyl (183 mg, 0.519 mmol, 1.00 eq.) was added and the mixture was stirred under UV irradiation for 1 d at room temperature. After that, all volatiles were removed *in vacuo* to obtain the product as a pale yellow powder. Crystals suitable for SC-XRD experiments were grown by vapour diffusion of pentane into solutions of **XVI** in thf at −25°C.

Chemical formula:	$C_{22}H_{13}N_2O_7GeClW$
Molecular weight:	709.27 g/mol
Yield:	354 mg, 0.499 mmol, 96 %
^{1}H-NMR	
(300 MHz, thf-d$_8$):	δ = 7.37-7.32 (m, 2H, 6-*H*, 13-*H*), 7.25-7.18 (m, 4H, 7-*H*, 8-*H*, 14-*H*, 15-*H*), 3.04 (s, 6H, 10-C*H*$_3$,17-C*H*$_3$) ppm
^{13}C{^{1}H}-NMR	
(75 MHz, thf-d$_8$):	δ = 192.8 (CO), 133.24 (4-C, 11-C), 129.32 (8-C, 15-C), 125.05 (7-C, 14-C), 26.09 (10-CH$_3$,17-CH$_3$) ppm
MS (LIFDI[+], thf)	
m/*z* (%):	709.8 (100) $[M]^+$

4.4.19 ^{Me}BoxGePPh$_2$ – {Bis(4-methylbenzoxazol-2-yl)methanide}germanium(II) diphenylphosphide **(XVII)**

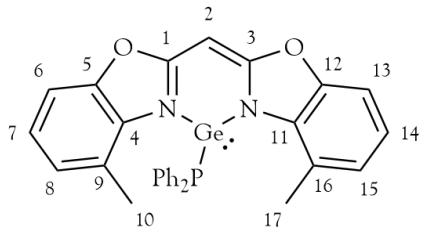

{Bis(4-methylbenzoxazol-2-yl)methanide}germanium(II) chloride (100 mg, 0.260 mmol, 1.00 eq.) was suspended in thf (3 mL). A 0.5 M solution of lithium diphenylphosphide (0.52 mL, 0.260 mmol, 1.00 eq.) was added and the mixture was stirred for 1 d at room temperature. After that, all volatiles were removed *in vacuo* to obtain a sticky, oily orange residue. NMR analysis of this residue gave complicated spectra with multiple overlapping species, which could not be assigned. Efforts to separate individual components from the residue by means of recrystallisation or extraction were unsuccessful as the mixture of products appears to have high solubility in common organic solvents.

Chemical formula:	$C_{29}H_{23}N_2O_2GeP$
Molecular weight:	535.12 g/mol
Yield:	Not determined

4.4.20 (^{Me}Box)$_3$Sb$_2$ – 2,2,4,4,5,5-hexa(4-methylbenzoxazol-2-yl)-1,3-distiba bicyclo[1.1.1] pentane **(XVIII)**

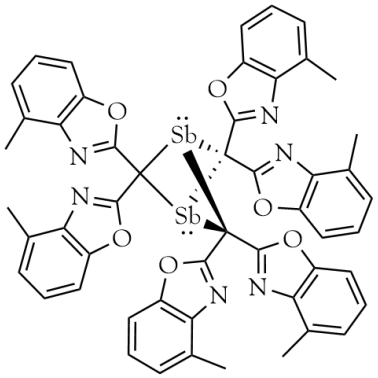

Potassium {bis(4-methylbenzoxazol-2-yl)methanide} (100 mg, 0.257 mmol, 1.00 eq.) was dissolved in thf (5 mL). To this solution antimony trichloride (58 mg, 0.257 mmol, 1.00 eq.) was added and the mixture was stirred for 1 d at room temperature. After filtration the filtrate was kept at room temperature and crystals suitable for SC-XRD experiments grew within 1 d.

Chemical formula:	$C_{51}H_{36}N_6O_6Sb_2$
Molecular weight:	1072.41 g/mol
Yield[a]:	28 mg, 0.026 mmol, 10 %

[a] based on crystallised material

5 Appendix

5.1 Refinement results for the comparison datasets collected with a gallium-indium MetalJet and a silver IμS X-ray source

Table 5-1: Refinement results for Sc_3CoC_4.

resolution [Å]	0.83		0.70		0.45		0.39	
diffractometer	In K_α	Ag K_α	In K_α	Ag K_α	In K_α	Ag K_α	In K_α	Ag K_α
***R*1 (*I*>2*σ*) [%]**	0.0139	0.0152	0.0127	0.0133	0.0158	0.0143	0.0191	0.0169
w*R*2 (all data) [%]	0.0329	0.0397	0.0286	0.0339	0.0363	0.0340	0.0398	0.0366

Table 5-2: Refinement results for $Sc_2Pt_9Si_3$.

resolution [Å]	0.83		0.70		0.45		0.39	
diffractometer	In K_α	Ag K_α	In K_α	Ag K_α	In K_α	Ag K_α	In K_α	Ag K_α
***R*1 (*I*>2*σ*) [%]**	0.0134	0.0152	0.0145	0.0186	0.0203	0.0241	0.0230	0.0293
w*R*2 (all data) [%]	0.0319	0.0339	0.0335	0.0386	0.0423	0.0513	0.0469	0.0590

Table 5-3: Refinement results for $Na_2WO_4 \cdot 2H_2O$.

resolution [Å]	0.83		0.70		0.45		0.39	
diffractometer	In K_α	Ag K_α	In K_α	Ag K_α	In K_α	Ag K_α	In K_α	Ag K_α
***R*1 (*I*>2*σ*) [%]**	0.0081	0.0114	0.0089	0.0128	0.0187	0.0230	0.0178	0.0294
w*R*2 (all data) [%]	0.0178	0.0241	0.0184	0.0271	0.0310	0.0472	0.0310	0.0578

Table 5-4: Refinement results for $C_{16}H_{16}$.

resolution [Å]	0.83		0.70		0.60		0.55	
diffractometer	In K_α	Ag K_α	In K_α	Ag K_α	In K_α	Ag K_α	In K_α	Ag K_α
***R*1 (*I*>2*σ*) [%]**	0.0396	0.0410	0.0447	0.0459	0.0455	0.0487	0.0459	0.0500
w*R*2 (all data) [%]	0.1058	0.1093	0.1369	0.1356	0.1454	0.1498	0.1477	0.1550

5.2 Drawing skill course evaluation

5.2.1 Questionnaire design

The complete questionnaire for evaluation of the drawing skill course contained the following questions (*original German phrasing given in parentheses*):

Questions 1 to 8 had to be answered on a four-point scale (fully agree, rather agree, rather disagree, fully disagree).

1. I am able to mentally visualise molecules three-dimensionally on the basis of drawings (*Aufgrund von Zeichnungen kann ich mir Moleküle dreidimensional vorstellen*)
2. I understand drawings of molecular structures (*Zeichnungen von Molekülstrukturen verstehe ich*)
3. I am able to make drawings of molecular structures myself (*Ich bin selbst in der Lage, Zeichnungen von Molekülstrukturen anzufertigen*)
4. I am able to interconvert drawings of molecular structures from different perspectives (*Ich bin in der Lage, Zeichnungen von Molekülstrukturen aus unterschiedlichen Perspektiven ineinander zu überführen*)
5. I consider the ability to draw molecular structures to be important for my future professional environment (*Die Fähigkeit, Molekülstrukturen darstellen zu können, schätze ich für mein späteres berufliches Umfeld als wichtig ein*)
6. I consider drawings of molecular structures to be important for my future professional environment (*Zeichnungen von Molekülstrukturen schätze ich für mein späteres berufliches Umfeld als wichtig ein*)
7. Drawings of molecular structures are an important tool to communicate with others (*Zeichnungen von Molekülstrukturen sind ein wichtiges Werkzeug, um mit anderen zu kommunizieren*)
8. Drawings of molecular structures contribute to a deeper understanding of chemical concepts (*Zeichnungen von Molekülstrukturen tragen zum tieferen Verständnis chemischer Konzepte bei*)

Questions 9 to 11 each had their own set of possible answers listed in brackets.

9. How many faces does an octahedron have? (*Wie viele Flächen hat ein Oktaeder?)* [5, 6, 7, 8]
10. How many corners does a cube have? (*Wie viele Ecken hat ein Würfel?)* [6, 7, 8, 9]
11. How many edges does a tetrahedron have? (*Wie viele Kanten hat ein Tetraeder?)* [4, 5, 6, 7]

The following questions appeared only in the second survey . Questions 12 to 14 were to be answered on a four-point scale (very helpful, helpful, unhelpful, not helpful at all). Only question 14 had a fifth option (I did not use the courseware material). Questions 15 was an open question.

12. For drawing and understanding chemical structures, the lecture recordings and the lecture slides were ... (*Für das Zeichnen und Verstehen von chemischen Strukturen waren die Vorlesungsaufzeichnungen und die Vorlesungsfolien ...*)

13. For drawing and understanding chemical structures, the seminars were ... (*Für das Zeichnen und Verstehen von chemischen Strukturen waren die Seminare ...*)

14. For drawing and understanding chemical structures, the courseware materials were ... (*Für das Zeichnen und Verstehen von chemischen Strukturen waren die Materialien in der Courseware ...*)

15. Here you have the opportunity to give us feedback on the content of the courseware. If you have used the courseware: What did you like, what didn't you like? If you did not use the courseware: Why not? (*Hier haben Sie die Möglichkeit, uns Rückmeldung zu die Inhalte der Courseware zu geben. Sofern Sie die Courseware genutzt haben: Was hat Ihnen gefallen, was nicht? Falls Sie die Courseware nicht genutzt haben: Warum nicht?*)

5.2.2 Analysis of survey results

Presented are the percentage differences in the survey results between the end and the beginning of the lecture.

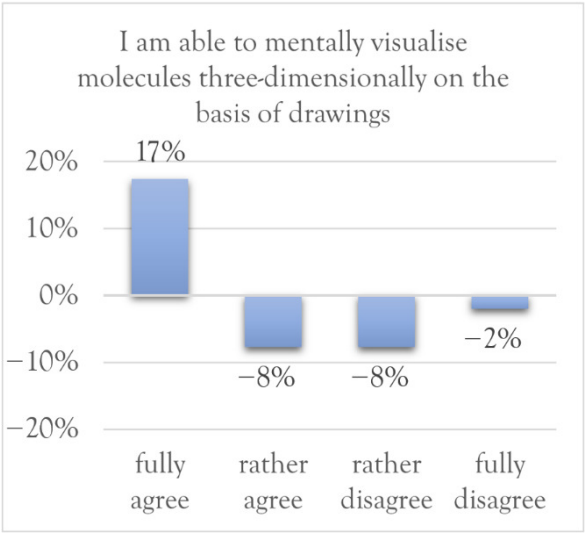

Figure 5-2: Percentage differences in the survey results between the end and the beginning of the lecture on statement 1.

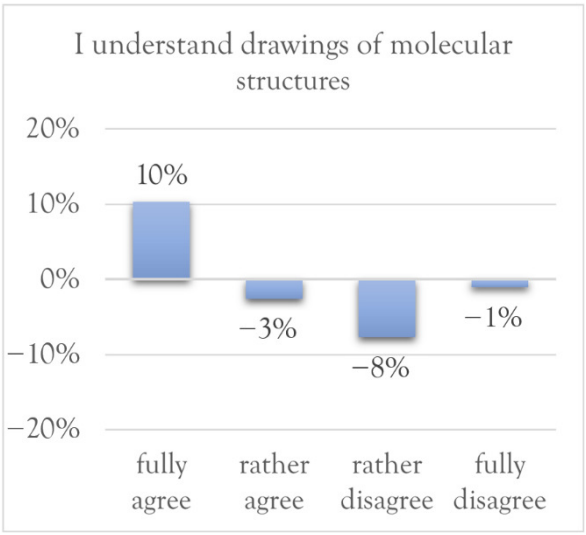

Figure 5-1: Percentage differences in the survey results between the end and the beginning of the lecture on statement 2.

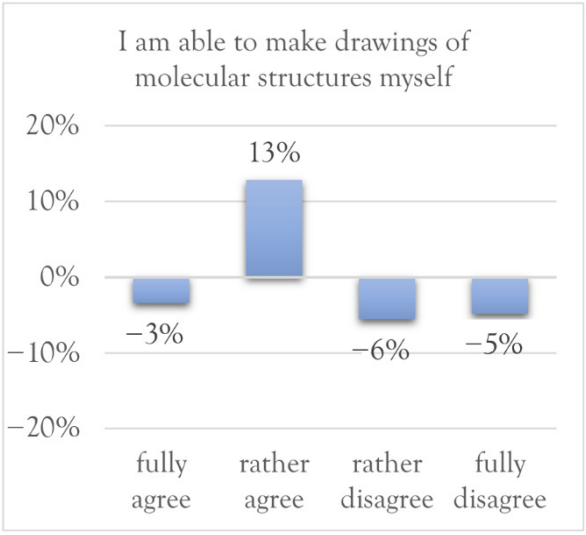

Figure 5-3: Percentage differences in the survey results between the end and the beginning of the lecture on statement 3.

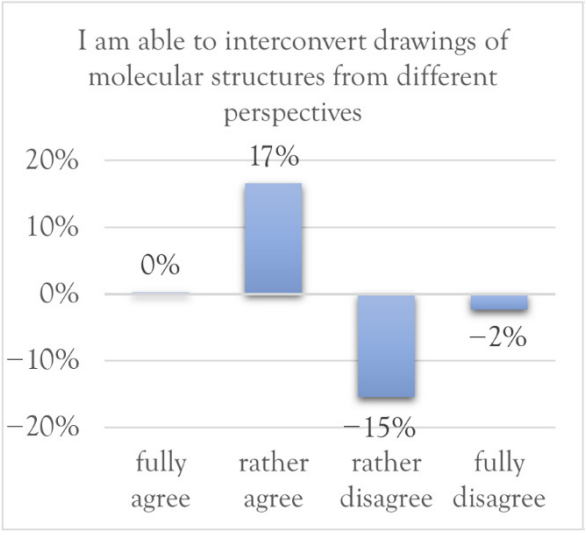

Figure 5-4: Percentage differences in the survey results between the end and the beginning of the lecture on statement 4.

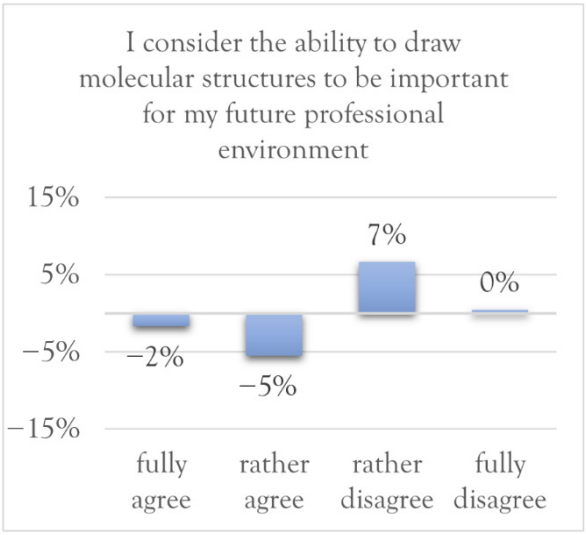

Figure 5-5: Percentage differences in the survey results between the end and the beginning of the lecture on statement 5.

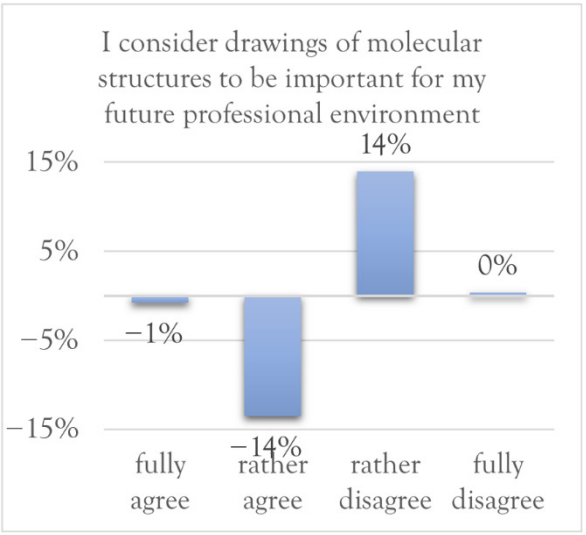

Figure 5-6: Percentage differences in the survey results between the end and the beginning of the lecture on statement 6.

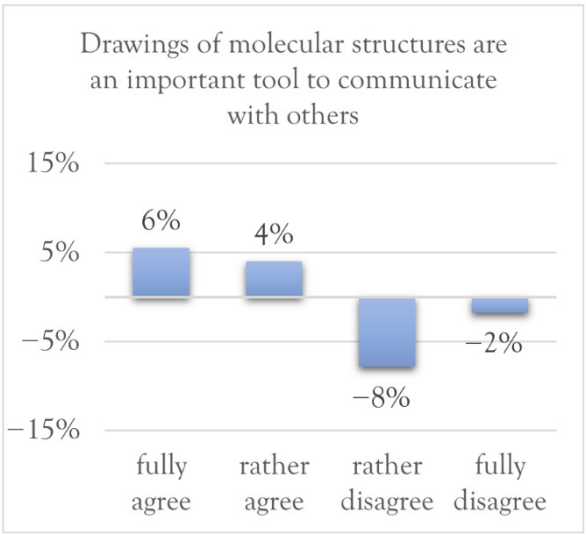

Figure 5-8: Percentage differences in the survey results between the end and the beginning of the lecture on statement 7.

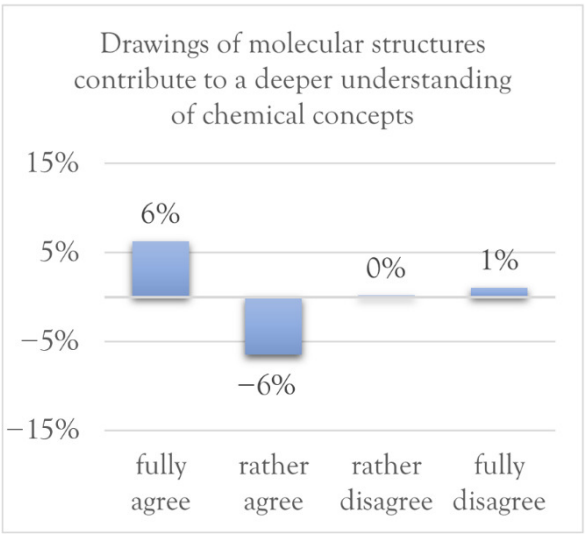

Figure 5-7: Percentage differences in the survey results between the end and the beginning of the lecture on statement 8.

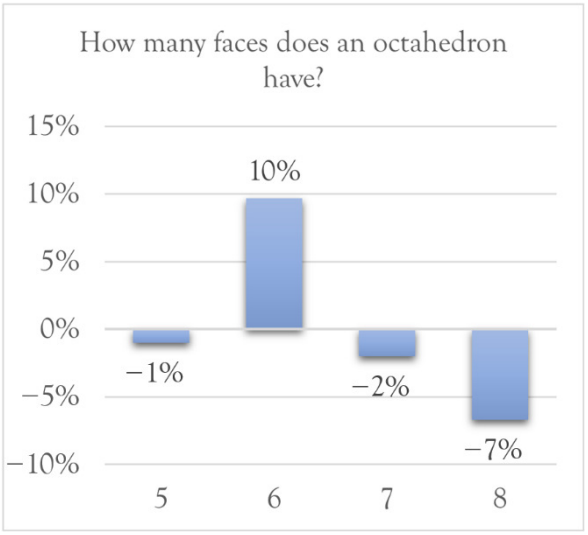

Figure 5-9: Percentage differences in the survey results between the end and the beginning of the lecture on statement 9.

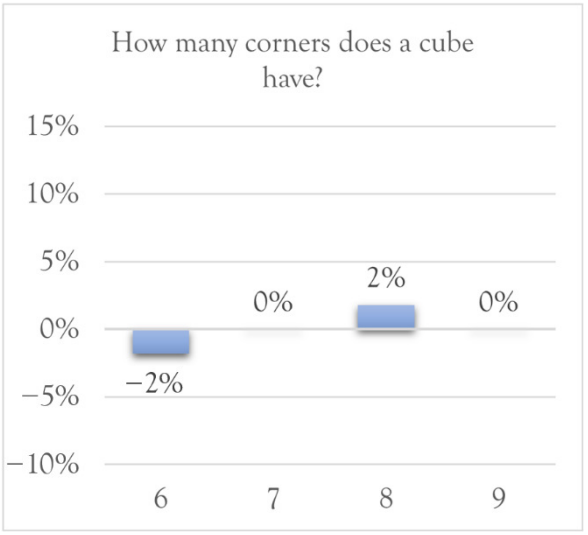

Figure 5-10: Percentage differences in the survey results between the end and the beginning of the lecture on statement 10.

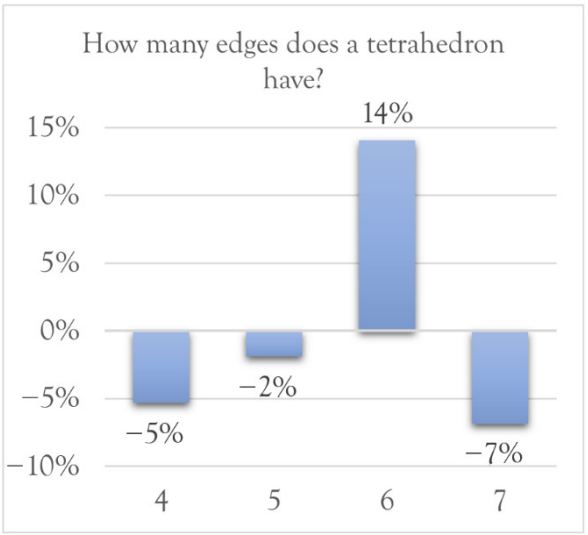

Figure 5-11: Percentage differences in the survey results between the end and the beginning of the lecture on statement 11.

5.2.3 Analysis of free text responses

The following are the free text responses given in the second survey (*original German phrasing given in parentheses*). Expressions that could be assigned to specific topics are marked in colour accordingly. The number of mentions is given in brackets.

Categories analysed for: Exam preparation [3], positive evaluation of the skill course [11], lack of time [5], still planning to use it [4], additional exercises wanted [5], more details wanted [2], negative evaluation of the skill course [1]

- I will definitely use the courseware content to prepare for the exam and I think it will help me a lot. (*Zur Vorbereitung auf die Klausur werde ich die Courseware-Inhalte auf jeden Fall noch nutzen und ich denke sie werden mir sehr helfen.)*
- I found the courseware offer great! (*Ich fand das Courseware Angebot super!*)
- I have not used the courseware yet because I simply have not found the time, but I will definitely use the offer, mainly as exam preparation. (*Ich habe die Courseware bisher noch nicht genutzt, weil ich einfach keine Zeit dazu gefunden habe, aber ich werde das Angebot in jedem Fall noch nutzen, hauptsächlich als Klausurvorbereitung.*)
- I have not had time to use the courseware yet, but I imagine it will be very helpful and I will probably take a look at it before the exam. (*Ich hatte noch keine Zeit um die Courseware zu nutzen, aber ich stelle mich als sehr hilfreich vor und werde es wahrscheinlich vor dem Klausur rein gucken.*)
- I have not used the courseware so far because I did not have the time or motivation for it. It would help me if the contents from it were included in the seminars and the lecture. (*Ich habe bisher die Courseware nicht genutzt, weil ich keine Zeit bzw. Motivation dafür hatte. Es würde mir helfen, wenn die Inhalte daraus in die Seminare und die Vorlesung mit einbezogen würden.*)
- More confused than before with Lewis/VSCR (*Verwirrter als vorher mit Lewis/VSCR*)
- I have used the courseware and have been very happy with the format provided. Many details that were not discussed further in the lecture were picked up here and presented in an understandable way. What could possibly be discussed in more detail are the individual lattice structures of molecules, as well as their special properties. To be honest, I missed that a bit in the courseware. (*Ich habe die Courseware genutzt und bin sehr zufrieden mit dem zur Verfügung gestellten Format gewesen. Viele Einzelheiten, die in der Vorlesung nicht weiter besprochen wurde, wurden hier aufgegriffen und verständlich dargestellt. Was eventuell noch etwas genauer besprochen*

werden könnte, sind die einzelnen Gitterstrukturen von Molekülen, sowie ihre speziellen Eigenschaften. Das hat mir in der Courseware ehrlich gesagt etwas gefehlt.)

- I liked the content of the courseware. It is easy to understand and clearly laid out, which made it fun and helpful for me to work through. (*Die Coursewareinhalte haben mir gut gefallen. Sie sind leicht verständlich und übersichtlich gestaltet, sodass mir die Bearbeitung Spaß gemacht und geholfen hat.)*
- Exercises with solutions would have been helpful. (*Übungsaufgaben mit Lösungen wären hilfreich gewesen.)*
- The courseware was very helpful because the content was communicated in detail and precisely. Thank you for this tool. (*Die Courseware waren sehr hilfreich, da die Inhalte detailliert und präzise kommuniziert wurden. Vielen Dank für dieses Tool.*)
- I did not use the courseware or only started to work on it once, as the chemistry module with the lectures, seminars, vips etc. already filled up my timetable. (*Ich habe die Courseware nicht genutzt bzw. nur einmal angefangen zu bearbeiten, da das Chemiemodul mit den Vorlesungen, Seminaren, Vips etc. meinen Stundenplan zeitlich bereits voll ausgefüllt hat.*)
- I used some of the courseware. However, the time commitment for me was relatively high due to the vips, seminar and worksheet as well as lectures and I lack both time and motivation. Also because it was never discussed. (*Ich habe die Courseware teilweise genutzt. Allerdings war der Zeitaufwand für mich durch die Vips, Seminar und Arbeitsblatt sowie Vorlesungen relativ hoch und sowohl die Zeit als auch die Motivation fehlt mir. Auch weil es nie besprochen wurde.*)
- Not too long, not too short, still well explained. I was able to take something away with me. (*Nicht zu lang, nicht zu kurz, trotzdem gut erklärt. Konnte was mitnehmen.*)
- The courseware was well structured and appropriately set up; there could almost be more content explained in this way. (*Die Courseware war gut strukturiert und passend aufgebaut; es könnten dort fast mehr Inhalte so erklärt angeben werden.)*
- I would wish to be shown more exceptions and especially deeper explanations of why the structure looks the way it does. An overview of the advantages and disadvantages of the different types of presentation would also be helpful. Overall, however, it was very good that the courseware was available in combination with the seminars, as the online lecture meant that there were no opportunities to ask questions. (*Ich würde mir wünschen, mehr Ausnahmen gezeigt zu bekommen und vor allem tiefere Erklärungen dazu, warum die Struktur so aussieht, wie sie aussieht. Ein Überblick über die Vor- und Nachteil der unterschiedlichen Darstellungsarten wäre*

ebenfalls hilfreich. Insgesamt war es aber sehr gut, dass es die Courseware in Kombination mit den Seminaren gab, da durch die online Vorlesung Möglichkeiten zum Rückfragen wegfielen.)

- I found the courseware very helpful. However, I would have liked to see a few more sample exercises where you had to draw a molecule and then check the solution. That somehow came up short. (*Ich fand die Courseware sehr hilfreich. Ich hätte mir jedoch noch einige Beispielaufgaben gewünscht, bei denen man ein Molekül zeichnen sollte und sich danach erst mit der Lösung überprüfen kann. Das kam irgendwie zu kurz.)*
- Maybe some small (voluntary) exercises to practise on. (*Vielleicht noch kleine (freiwillige) Aufgaben zum Üben.)*
- The courseware was extremely helpful because otherwise I would have sat for hours at the laptop googling shapes and structures and in the end only confusing myself even more. It provided clarity and an overview. (*Die Courseware war extrem hilfreich, da ich sonst stundenlang am Laptop gesessen hätte um Formen und Strukturen zu googlen und mich letztendlich nur noch mehr zu verwirren. sie hat Klarheit und Überblick verschafft.)*
- I'll do it later (*mache ich später noch*)

5.3 Models of screw axes

Presented are photographs of models of all screw axes, which are crystallographically relevant and were designed and built within this project.

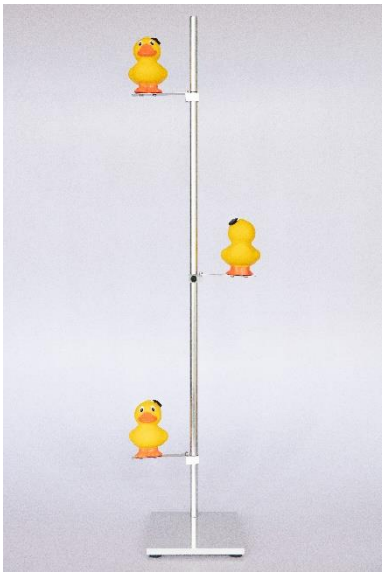

Figure 5-12: Model of a 2_1 screw axis.

Figure 5-13: Model of a 3_1 screw axis.

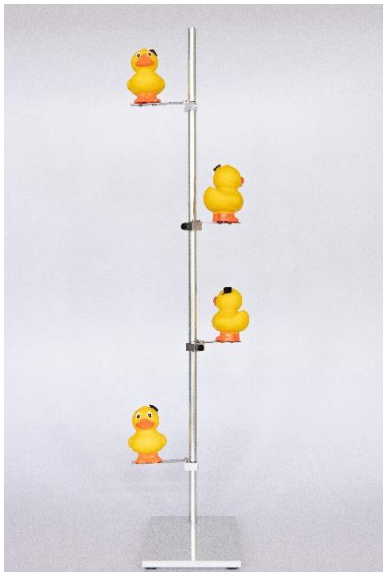

Figure 5-14: Model of a 3_2 screw axis.

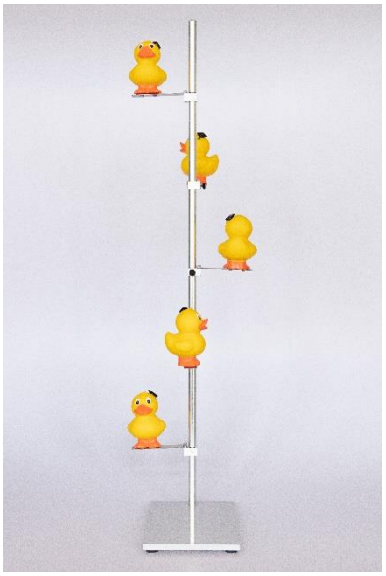

Figure 5-15: Model of a 4_1 screw axis.

Figure 5-16: Model of a 4_2 screw axis.

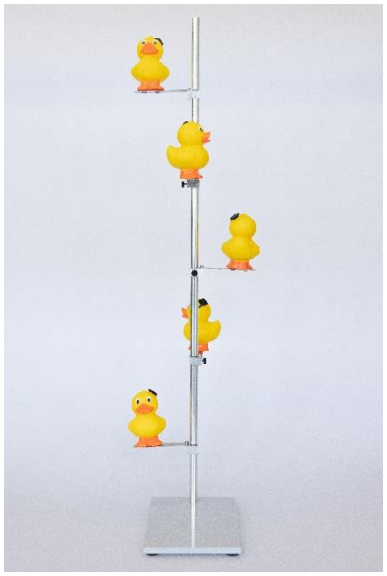

Figure 5-17: Model of a 4_3 screw axis.

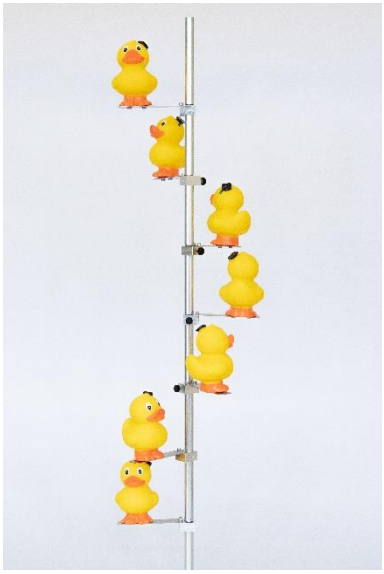

Figure 5-18: Model of a 6_1 screw axis.

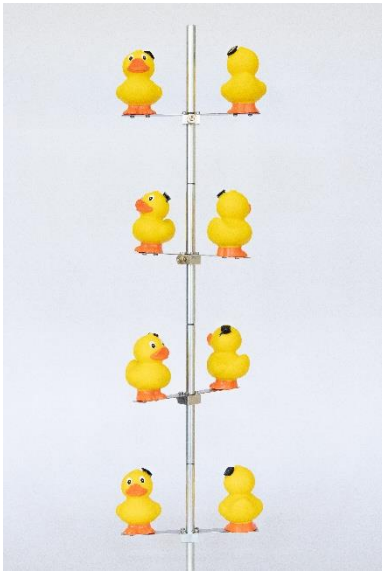

Figure 5-19: Model of a 6_2 screw axis.

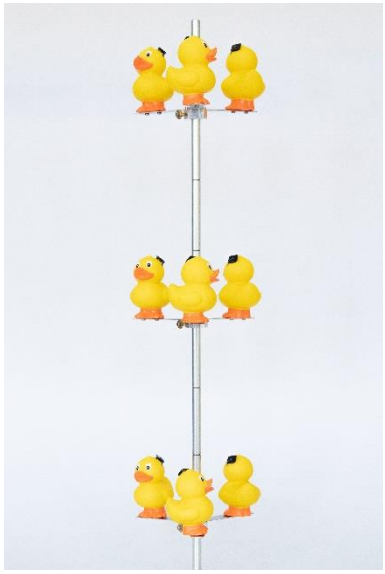

Figure 5-20: Model of a 6_3 screw axis.

Figure 5-21: Model of a 6_4 screw axis.

Figure 5-22: Model of a 6_5 screw axis.

5.4 Discussion of erroneous X-ray structure determinations

5.4.1 Poor modelling of disorder

5.4.1.1 Original structure refinement

Replies given by authors to alerts prompted after checkCIF[209,210] validation as retrieved from the CSD:[208]

```
# start Validation Reply Form
_vrf_PLAT212_shelx
;
PROBLEM: ADP of Atom N8 is N.P.D. or (nearly) 2D.      Please Check
RESPONSE: Despite our best efforts, N8 is represented by a very small
ellipsoid. N8 is part of a fully disordered triflimide anion that has been
atomistically modelled in two parts; its chemical identity is unambiguous.
;
```

"best efforts" in this case describes the use of only one restraint for anisotropic displacement parameters. The used ISOR command has not only an unjustified reduced standard deviation of 1/1000 of the default value, it is also used in exactly the way the ShelXL manual[413] explicitly states not to use it. Instead, restraints on distances and anisotropic displacement parameters should have been used, which restrain the disordered and the non-disordered anions to each other.

```
_vrf_PLAT221_shelx
;
PROBLEM: Solv./Anion Resd 2 F Ueq(max)/Ueq(min)      Range 10.0 Ratio
RESPONSE: The structure contains a total of five residues: the complex of
interest, two non-coordinating anion (one of them disordered) and two solvent
molecules (both of them disordered, one disordered over a special position).
All residues were modelled atomistically. However, the disorder observed
often led to weak electron density maps. This made necessary the use of more
restraints on the model to ensure stable refinement, which in turn led to a
model with larger ellipsoids for some of the atoms in these disordered
residues.
;
```

This comment makes no sense. The use of more restraints does not lead to enlarged ADPs if the restraints are set correctly and the model contains the correct atom types on approximately correct positions. This alert is in fact due to the incorrect modelling of toluene as *ortho*-difluorobenzene.

```
_vrf_PLAT234_shelx
;
PROBLEM: Large Hirshfeld Difference F20A--C63.       0.28 Ang.
RESPONSE: F20A and C63 are both part of a disordered ortho-difluorobenzene
molecule.  Notably, the atom occupying C63 position was modelled in two parts
of similar occupancy: one containing C63 bound to H63A, and one containing
C63A bound to F20A. C63 and C63A are constrained to the same position (EXYZ)
and ellipsoids (EADP), which could explain why a Hirshfeld difference alert
is raised here.
;
```

Constraining the positions and ADPs of C63 and C63A does not explain this alert as it is referring to the ADPs of C63 and F20A. It is a result of the attempt to model the disorder only on the fluorine substituents and not the aromatic core.

```
_vrf_PLAT315_shelx
;
PROBLEM: Singly Bonded Carbon Detected (H-atoms Missing).    C74 Check
RESPONSE: C74 is not missing any H atoms.  It is part of the aromatic ring
of an orthodifluorobenzene molecule and thus bound to two neighbouring C
atoms (C72 and C75) as well as one F atom (F31).
;
# end Validation Reply Form
```

C74 is indeed part of an aromatic ring. This ring is part of a toluene molecule and not *ortho*-difluorobenzene, however, the alert is not due to this misidentification but rather due to the incorrect treatment of disorder about an inversion centre. The geometry is so distorted that C74 is too far away from its neighbouring atom to be recognised by the software as a bonding partner.

Additional uncommented A and B level alerts:

```
221_ALERT_2_B Solv./Anion  Resd 3  C   Ueq(max)/Ueq(min) Range    10.0 Ratio
995_ALERT_1_B Can not Recreate .fcf from Embedded .res & .hkl       ! Check
```

The first alert is equivalent to one already discussed and has the same reasons. The second alert indicates inconsistencies in the data and should therefore be resolved or at least be addressed.

All restraints and constraints used in the refinement:

```
ISOR 0.05 F32 C40A C70 F30
ISOR 0.02 F4 F3
ISOR 0.01 C60 C70
ISOR 0.01 O3A
ISOR 0.001 C40
ISOR 0.0001 N8
EXYZ C63 C63A
EXYZ C65 C65A
EADP C63 C63A
EADP C65 C65A
EXYZ C72 C72A
EXYZ C75 C75A
EADP C72 C72A
EADP C75 C75A
SADI C63 F20A C64 F21 C65 F20 C74 F31 C75 F30 C72 F32
SADI F30 C74 F30 C71 F32 C74 F32 C73
```

Positional constraints and constraints for ADPs need to be justified and should be used carefully as there is the risk to introduce something in the model that is not supported by the data. Some of the ADP restraints have unreasonably small standard deviations.[414] The applied restraints on

distances and ADPs do not suffice for the relatively high degree of disorder in this structure. On a side note, it should also be mentioned that the refinement was performed with a presumably incorrect temperature of 20°C (293 K) influencing the bond distances for all C-H bonds placed using a riding model.

5.4.1.2 Updated structure refinement

Replies given by authors to alerts prompted after checkCIF[209,210] validation as retrieved from the CSD:[208]

```
# start Validation Reply Form
_vrf_PLAT250_shelx
;
PROBLEM: Large U3/U1 Ratio for Average U(i,j) Tensor ....        5.5 Note
RESPONSE: This alert results from the ADPs associated with the overlapping
fragments of the disordered triflimide molecule. Anisotropic refinement in
this case is believed to be justified by the reasonable geometry and ellipsoid
sizes that were produced, and is preferable to isotropic refinement or
anisotropic refinement with strong ISOR restraints.
;
# end Validation Reply Form
```

The alert is rather caused by all of the disorder present in the structure than just the triflamide anion. However, due to the disorder the alert can be accepted.

Additional uncommented A and B level alerts:

```
995_ALERT_1_B Can not Recreate .fcf from Embedded .res & .hkl       ! Check
```

The alert indicates inconsistencies in the data and should therefore be resolved or at least be addressed.

All restraints and constraints used in the refinement:

```
EADP S5B N9
RIGU 0.0001 0.0001 O8A S4A O7A
EADP C37A C37B
RIGU 0.0001 0.0001 F10A C38 F11A F9B
EADP N9 S5B
RIGU 0.0001 0.0001 C44 C41 C43 C42 C40
EADP O10B O10A
SADI 0.0001 F11A F9B F9B F10A
SADI 0.0001 F9B C38 F11A C38 F10A C38
EADP C38A S4A
EADP C38 F11
ISOR 0.02 0.04 F11 F9
ISOR 0.001 0.002 C38A
ISOR 0.001 0.002 N9A
```

```
RIGU 0.001 0.001 F11 C38A F10 F9
ISOR 0.001 0.002 F13A C37A F12A F14A
SADI 0.0001 F10 C38A F11 C38A F9 C38A
SADI 0.0001 F11 F10 F10 F9
RIGU 0.001 0.001 S5 N9 S4
RIGU 0.001 0.001 F16A C41A F15A C44A C40A C43A C42A
DANG 2.41 C50 C48
DFIX 1.38 C45 C46 C47 C48 C48 C49
SADI 0.04 C50 C48 C50 C46 C49 C47 C45 C49 C46 C48 C45 C47
SADI 0.04 C51 C49 C51 C45
DANG 2.52 C51 C45 C51 C49
DFIX 1.39 C50 C45 C50 C49 C46 C47
DANG 2.42 C50 C46
RIGU C51 C50 C45 C46 C47 C48 C49
FLAT C51 C50 C45 C46 C47 C48 C49
DFIX 1.51 C51 C50
SIMU C51 C50 C45 C46 C47 C48 C49
SADI C50 C45 C45 C46 C46 C47 C47 C48 C48 C49 C49 C50
DANG 2.39 C45 C47
DANG 2.4 C46 C48 C47 C49
SADI 0.00001 S5 N9 S4 N9
RIGU 0.0001 0.0001 O7B S4B O8B
RIGU 0.001 0.001 O9A S5A O10A
SADI 0.00001 F11B C38B F10B C38B F9B C38B
SADI 0.00001 F9B F10B F10B F11B
RIGU 0.0001 0.0001 C38B F9B F10B F11B
EADP F9AA F9B
EADP F11B F9
EADP F10 F10B
SADI 0.0001 F14B C37B F12B C37B F13B C37B
SADI 0.0001 F13B F14B F14B F12B
EADP F14B F13A
RIGU 0.0001 0.0001 F13B C37B F14B F12B
EADP N9B N9A
```

Constraints for ADPs need to be justified and should be used carefully as there is the risk to introduce something in the model that is not supported by the data. A lot of the ADP and distance restraints have unreasonably small standard deviations, partly to a degree that effectively makes them constraints.[414]

5.4.1.3 Improved structure refinement

Alerts prompted after checkCIF[209,210] validation

```
250_ALERT_2_B Large U3/U1 Ratio for Average U(i,j) Tensor ....   5.4 Note
```

The alert can be accepted due to relatively high degree of disorder present in the structure.

All restraints and constraints used in the refinement:

```
SIMU 0.01 N1B > F6G
RIGU N1B > F6B
RIGU N1C > F6C
```

```
RIGU N1G > F6G
SIMU 0.01 F1D > C6E
RIGU F1D > C6D
RIGU F1E > C6E
SIMU 0.01 C7F > C6F
RIGU C7F > C6F
FLAT C7F > C6F
SADI 0.0200 N1A S1A N1B^a S1B^a N1C^b S1C^b N1G^c S1G^c
SADI 0.0200 C3F^a C4F^a C4F^a C5F^a
SADI 0.0200 S1A O1A S1B^a O1B^a S1C^b O1C^b S1G^c O1G^c
SADI 0.0200 C1F^a C6F^a C1F^a C2F^a
SADI 0.0200 C2F^a C3F^a C5F^a C6F^a
SADI 0.0200 C5D^a C6D^a C5E^b C6E^b C1D^a C6D^a C4D^a C5D^a =
C3D^a C4D^a C2D^a C3D^a C1D^a C2D^a C4E^b C5E^b C3E^b C4E^b =
C2E^b C3E^b C1E^b C2E^b C1E^b C6E^b
SADI 0.0200 C2A F5A C2B^a F5B^a C2G^c F5G^c C2C^b F5C^b
SADI 0.0200 C2A F6A C2B^a F6B^a C2G^c F6G^c C2C^b F6C^b
SADI 0.0200 N1A S2A N1B^a S2B^a N1C^b S2C^b N1G^c S2G^c
SADI 0.0200 C1A F2A C1B^a F2B^a C1G^c F2G^c C1C^b F2C^b
SADI 0.0200 S1B^a O2B^a S1C^b O2C^b S1A O2A S1G^c O2G^c
SADI 0.0200 S2B^a O3B^a S2C^b O3C^b S2G^c O3G^c S2A O3A
SADI 0.0200 C2A F4A C2B^a F4B^a C2G^c F4G^c C2C^b F4C^b
SADI 0.0200 C1B^a F3B^a C1G^c F3G^c C1A F3A C1C^b F3C^b
SADI 0.0200 S2B^a C2B^a S2C^b C2C^b S2G^c C2G^c S2A C2A
SADI 0.0200 S2B^a O4B^a S2G^c O4G^c S2A O4A S2C^b O4C^b
SADI 0.0200 S1B^a C1B^a S1G^c C1G^c S1A C1A S1C^b C1C^b
SADI 0.0200 C1B^a F1B^a C1G^c F1G^c C1A F1A C1C^b F1C^b
SADI 0.0200 F1D^a C1D^a F2D^a C2D^a F1E^b C1E^b F2E^b C2E^b
SADI 0.0400 S2B^a F5B^a S2C^b F5C^b S2G^c F5G^c S2A F5A
SADI 0.0400 S2B^a F4B^a S2C^b F4C^b S2G^c F4G^c S2A F4A
SADI 0.0400 F2B^a F3B^a F2C^b F3C^b F2G^c F3G^c F2A F3A
SADI 0.0400 N1B^a O1B^a N1G^c O1G^c N1C^b O1C^b N1A O1A
SADI 0.0400 F1B^a F2B^a F1C^b F2C^b F1G^c F2G^c F1A F2A
SADI 0.0400 S1B^a F2B^a S1C^b F2C^b S1G^c F2G^c S1A F2A
SADI 0.0400 O3B^a O4B^a O3G^c O4G^c O3C^b O4C^b O3A O4A
SADI 0.0400 O1B^a C1B^a O1G^c C1G^c O1C^b C1C^b O1A C1A
SADI 0.0400 O3B^a C2B^a O3C^b C2C^b O3G^c C2G^c O3A C2A
SADI 0.0400 S1B^a F1B^a S1G^c F1G^c S1C^b F1C^b S1A F1A
SADI 0.0400 O2B^a C1B^a O2C^b C1C^b O2G^c C1G^c O2A C1A
SADI 0.0400 O1B^a O2B^a O1G^c O2G^c O1C^b O2C^b O1A O2A
SADI 0.0400 F4B^a F6B^a F4C^b F6C^b F4G^c F6G^c F4A F6A
SADI 0.0400 N1B^a C1B^a N1G^c C1G^c N1C^b C1C^b N1A C1A
SADI 0.0400 N1B^a O4B^a N1C^b O4C^b N1G^c O4G^c N1A O4A
SADI 0.0400 N1B^a O3B^a N1C^b O3C^b N1G^c O3G^c N1A O3A
SADI 0.0400 S1B^a F3B^a S1C^b F3C^b S1A F3A S1G^c F3G^c
SADI 0.0400 F4B^a F5B^a F4C^b F5C^b F4A F5A F4G^c F5G^c
SADI 0.0400 S2B^a F6B^a S2C^b F6C^b S2A F6A S2G^c F6G^c
SADI 0.0400 F1A F3A F1B^a F3B^a F1G^c F3G^c F1C^b F3C^b
SADI 0.0400 C1D^a C3D^a C2D^a C4D^a C3D^a C5D^a C4D^a C6D^a =
C1D^a C5D^a C2D^a C6D^a C1E^b C3E^b C2E^b C4E^b C1E^b C5E^b =
C3E^b C5E^b C2E^b C6E^b C4E^b C6E^b
SADI 0.0400 F2D^a C1D^a F2D^a C3D^a F2E^b C1E^b F2E^b C3E^b =
F1D^a C2D^a F1D^a C6D^a F1E^b C2E^b F1E^b C6E^b
SADI 0.0400 F5A F6A F5B^a F6B^a F5C^b F6C^b F5G^c F6G^c
SADI 0.0400 N1B^a C2B^a N1G^c C2G^c N1C^b C2C^b N1A C2A
SADI 0.0400 O4B^a C2B^a O4G^c C2G^c O4C^b C2C^b O4A C2A
SADI 0.0400 S1B^a S2B^a S1G^c S2G^c S1C^b S2C^b S1A S2A
SADI 0.0400 C1F^a C5F^a C1F^a C3F^a
SADI 0.0400 C4F^a C6F^a C2F^a C4F^a
SADI 0.0400 C7F^a C6F^a C7F^a C2F^a
SADI 0.0400 N1B^a O2B^a N1G^c O2G^c N1A O2A N1C^b O2C^b
```

No constraints were used. Default values for the standard deviations of relative distance restraints were not changed. Standard deviations of ADP restraints were not reduced to more than ¼ of the default values.

5.4.1.4 Comparison of refinements

Table 5-5: Comparison of refinement results. Values for original and updated structure refinement results taken from deposited data under reference code 2034513.[207]

	Original structure refinement	**Updated structure refinement**	**This work**
Empirical Formula	$C_{50}H_{34}Cu_2F_{17}N_9O_{10}S_5$	$C_{50.5}H_{36}Cu_2F_{16}N_9O_{10}S_5$	$C_{50.5}H_{36}Cu_2F_{16}N_9O_{10}S_5$
Formula weight [g·mol^{-1}]	1531.2	1520.26	1520.26
Data / Restraints / Parameters	12179 / 111 / 1023	12179 / 359 / 1133	12179 / 2229 / 1213
***R*1 (*I*>2σ (*I*))**	0.0779	0.0688	0.0646
w*R*2 (all data)	0.2256	0.2010	0.1882
max. diff. peak / hole [eÅ^{-3}]	1.699 and −1.382	1.33 and −1.58	1.007 and −1.135

The updated structure refinement makes chemically and physically more sense than the original one and accordingly a model with better quality indicators was obtained. However, the here presented refinement still improved the model significantly based on *R* values and reduced residual density. The here presented model requires 2229 restraints which is a lot more than in the updated published model (359). However, only relative restraints were used, which are inherently milder than direct restraints.[414] All restraints were used with their default standard deviation except for a similar ADP restraints, which were applied at four times the default strength.

5.4.2 Questionable use of SQUEEZE

The authors state in the supporting information:

"The unit cell of 1H−1Cl−1 contained highly disordered thf molecules, which could not be refined properly. Thus, they have been treated as a diffuse contribution to the overall scattering without specific atom positions by SQUEEZE/PLATON. The number of electrons (205) and the void volume (625 Å³) counts for approximately three thf per unit cell."[211]

Evaluation of the data deposited under the reference code 1994870[211] revealed that the asymmetric unit contains one thf molecule, which is disordered over two positions. The disorder can be refined with distance restrains and restraints for the ADPs. The occupancy of the minor positions refined to 0.1225(67) and the refinement converged. The use of SQUEEZE is therefore unjustified.[212]

Furthermore, it is difficult to comprehend the conclusion that the removed electron density corresponds to about three thf molecules. Using the 18 cubic angstrom rule, the volume of one molecule of thf (C_4H_8O)can be estimated to be

$$5\,\frac{\text{non H-atoms}}{\text{thf}}\cdot 18\,\frac{\text{Å}^3}{\text{atom}} = 90\,\frac{\text{Å}^3}{\text{thf}} \tag{5-1}$$

Hence, the void volume could account for

$$\frac{625\,\frac{\text{Å}^3}{\text{unit cell}}}{90\,\frac{\text{Å}^3}{\text{thf}}} \approx 7\,\frac{\text{thf}}{\text{unit cell}} \tag{5-2}$$

On the other hand, the electron count for one molecule of thf is

$$1\,\frac{e^-}{\text{H-atom}}\cdot 8\,\frac{\text{H-atom}}{\text{thf}} + 6\,\frac{e^-}{\text{C-atom}}\cdot 4\,\frac{\text{C-atom}}{\text{thf}} + 8\,\frac{e^-}{\text{O-atom}}\cdot 1\,\frac{\text{O-atom}}{\text{thf}} = 40\,\frac{e^-}{\text{thf}} \tag{5-3}$$

Hence, the number of removed electrons per unit cell should account for

$$\frac{205\,\frac{e^-}{\text{unit cell}}}{40\,\frac{e^-}{\text{thf}}} \approx 5\,\frac{\text{thf}}{\text{unit cell}} \tag{5-4}$$

Both results are far away from the original statement of three thf molecules per unit cell, which therefore cannot be reconstructed. Again, this strongly contradicts the use of the SQUEEZE procedure.

Interestingly, all of these are uneven numbers. Alone for this fact, none of them makes sense. The reported space group is $P2_1/c$ with four asymmetric units per unit cell. Assuming an uneven number of thf molecules therefore results in a non-integer number of thf molecules per asymmetric unit. Disregarding the previous calculations, such a result alone should render the SQUEEZE procedure questionable. Applying it nonetheless shows a lack of fundamental knowledge about space groups. The only cases in which a non-integer number of molecules per asymmetric unit is sensible would be the location of the molecule about a special position (which it not the case here), the location of the molecule on a face, edge or corner of the cell (which it not the case here) or a truly unstochiometric composition of the crystal due to loss of lattice solvent. The latter cannot be excluded but in case decomposition of the crystal took place, it should be addressed in the experimental details of the structure report.

Lastly, the deposited model as well as the new model with refined disorder show unreasonably large maxima in the difference electron density maps of 2.39 e^{-}Å^{-3} and 3.00 e^{-}Å^{-3} respectively. The highest peak in both cases is located close to a *tert*-butyl group but in a positon that cannot be considered as potential disorder (see figure 5-23). Instead, this hints at a more general problem with the quality of the diffraction data also indicated by the high R_{int} value of 10.99 %. Unresolved residual density not belonging to the disordered solvent on its own is another reason not to apply the SQUEEZE procedure as it also impacts the difference electron density in the solvent region.[212]

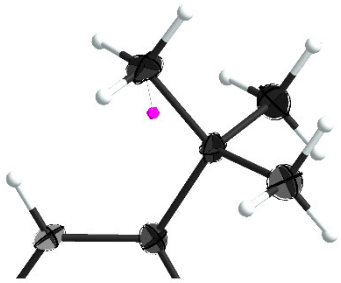

Figure 5-23: Part of the original X-ray structure model showing the highest q-peak (pink) in proximity to a *tert*-butyl group. The q-peak indicates a maximum in the difference electron density accounting for 2.39 e^{-}Å^{-3}.

5.5 Space group models

5.5.1 Small scale prototypes

Figure 5-24: Prototype model of space group $P2_1$. Left: Arbitrary direction. Right: View along crystallographic *b* axis.

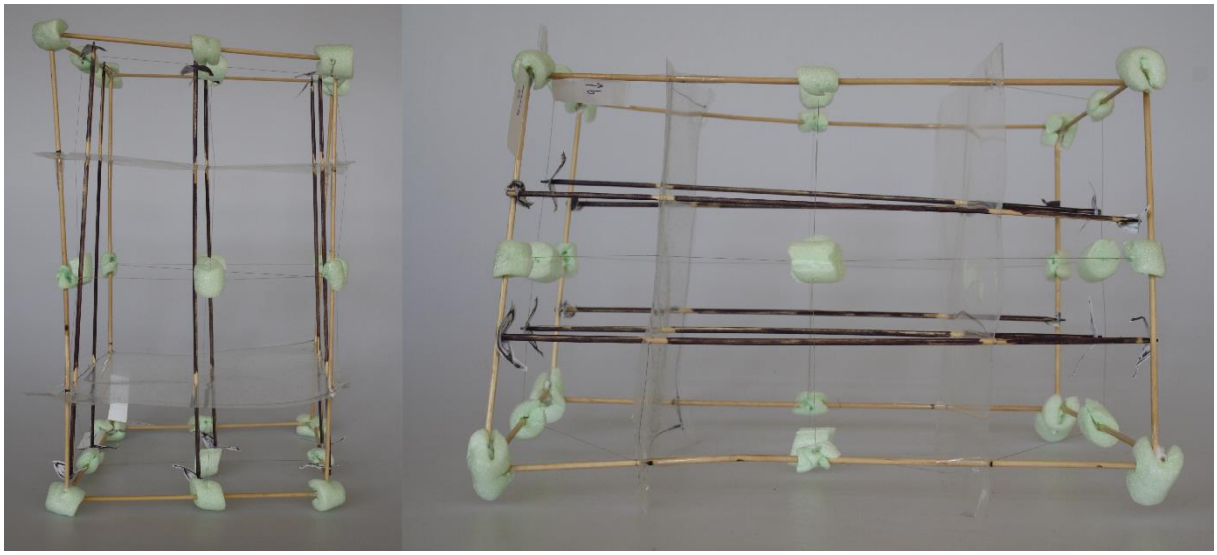

Figure 5-25: Prototype model of space group $P2_1/c$. Left: View along crystallographic *c* axis. Right: View along crystallographic *a* axis.

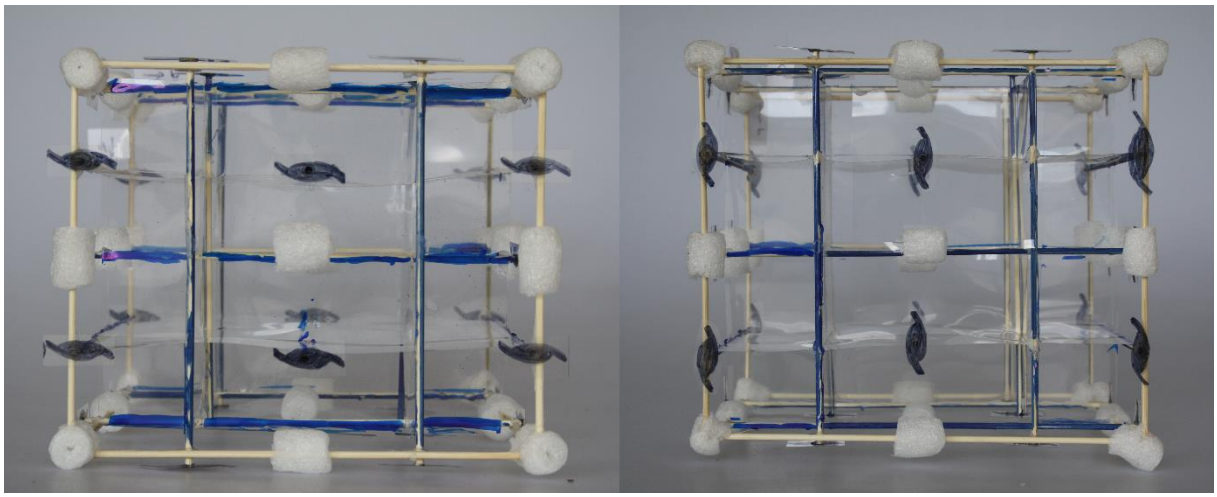

Figure 5-26: Prototype model of space group *Pbca*. Left: View along crystallographic *c* axis. Right: View along crystallographic *a* axis.

5.5.2 Large scale models

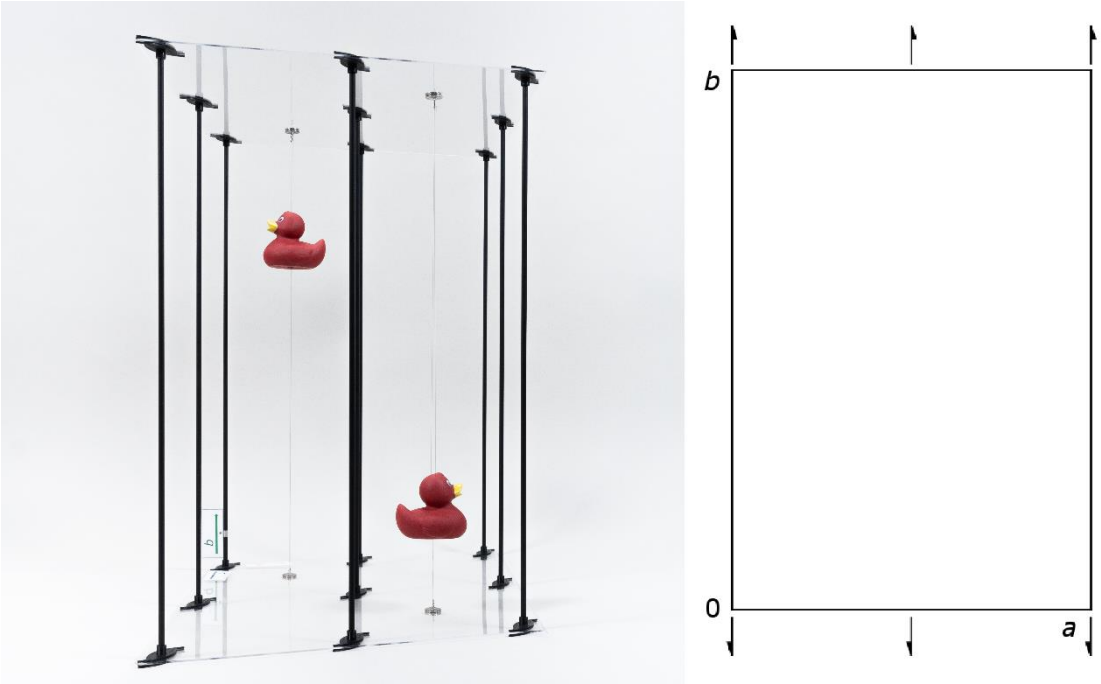

Figure 5-27: Left: Large-scale model of space group $P2_1$. View along crystallographic *c* axis. Content of asymmetric unit represented by red rubber ducks. Right: Conventional depiction of space group $P2_1$ along the same axis reproduced from the International Tables for Crystallography, Section A.[106]

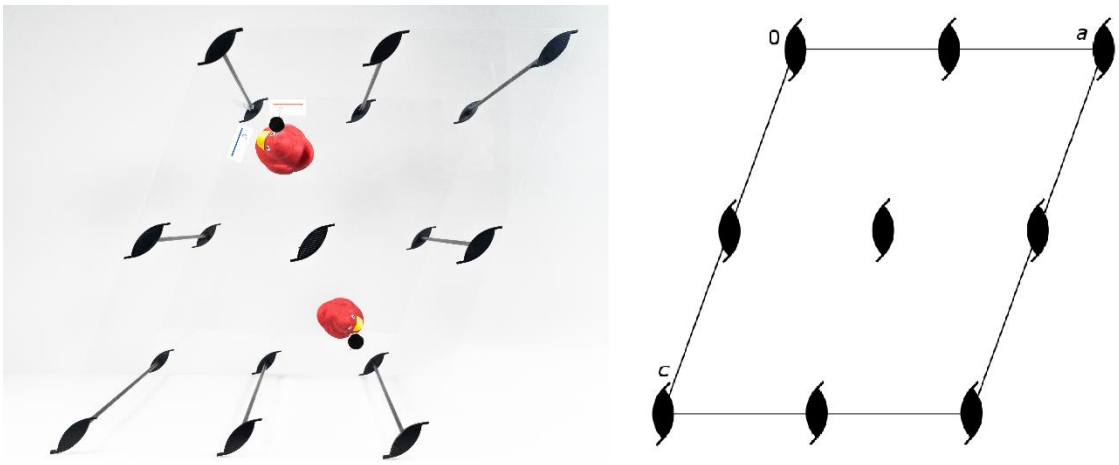

Figure 5-28: Left: Large-scale model of space group $P2_1$. View along crystallographic *c* axis. Content of asymmetric unit represented by red rubber ducks. Right: Conventional depiction of space group $P2_1$ along the same axis reproduced from the International Tables for Crystallography, Section A.[106]

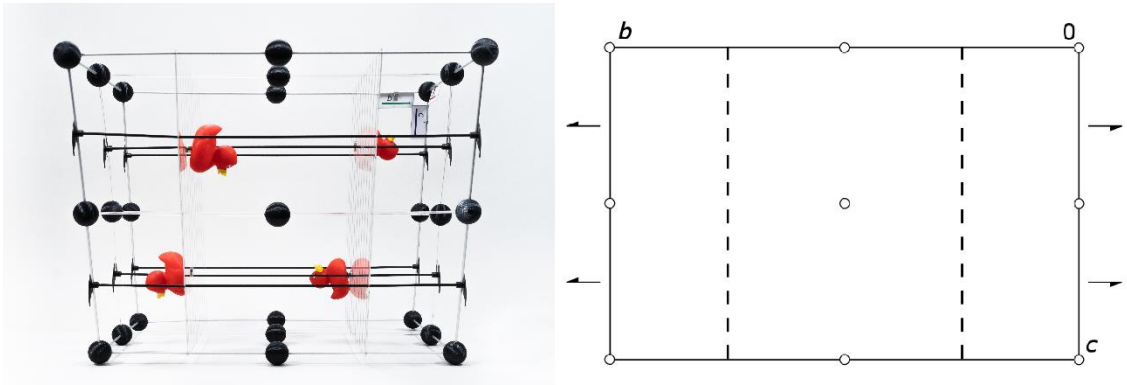

Figure 5-29: Left: Large-scale model of space group $P2_1/c$. View along crystallographic *a* axis. Content of asymmetric unit represented by red rubber ducks. Right: Conventional depiction of space group $P2_1/c$ along the same axis reproduced from the International Tables for Crystallography, Section A.[106]

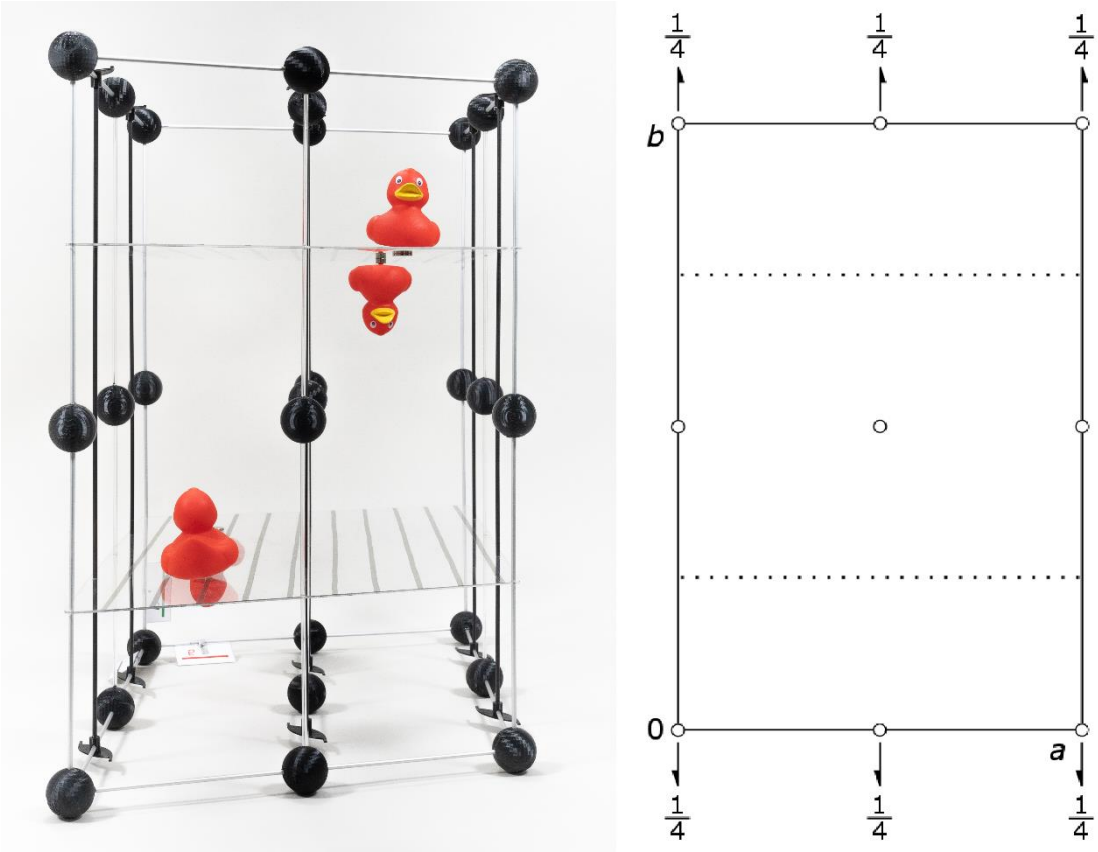

Figure 5-30: Left: Large-scale model of space group $P2_1/c$. View along crystallographic *c* axis. Content of asymmetric unit represented by red rubber ducks. Right: Conventional depiction of space group $P2_1/c$ along the same axis reproduced from the International Tables for Crystallography, Section A.[106]

Photographs of the model of space group $P\bar{1}$ are not included because construction of the model was not completed in time for the photo shooting and due to the size of the models special equipment was needed to take the photographs.

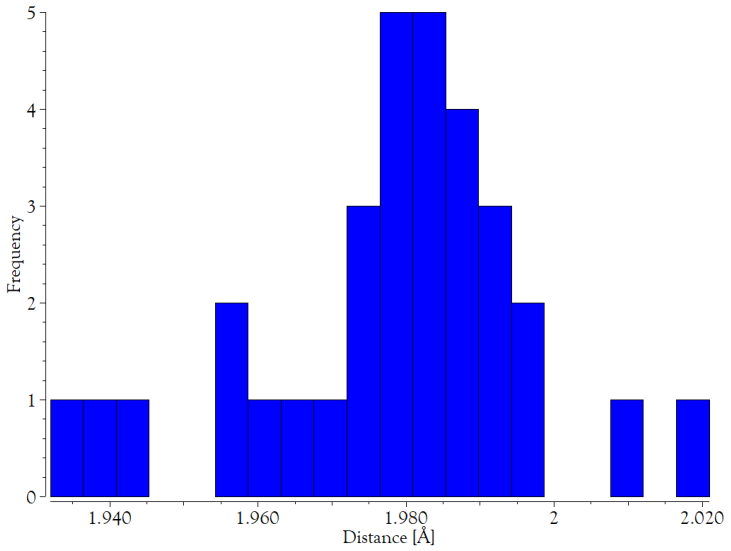

Figure 5-31: Histogram of all germanium-nitrogen distances in *N*,*N*'-chelated six membered cyclic C_3N_2Ge systems with one chloride ligand at the germanium atom reported in the CSD (v4.52).[208]

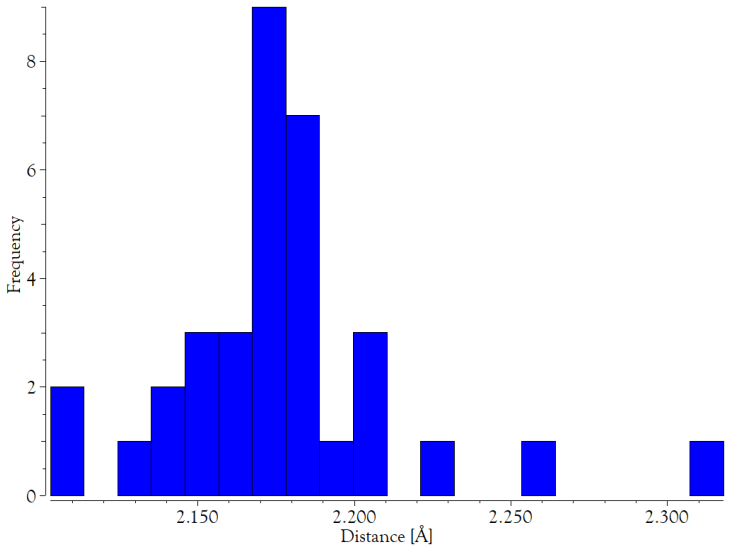

Figure 5-32: Histogram of all tin-nitrogen distances in *N*,*N*'-chelated six membered cyclic C_3N_2Sn systems with one chloride ligand at the tin atom reported in the CSD (v4.52).[208]

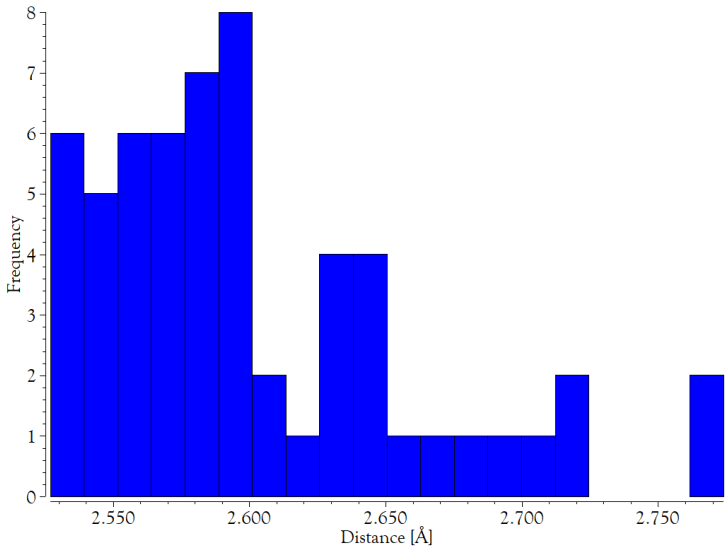

Figure 5-33: Histogram of all germanium-tungsten distances in compounds containing a germanium donor coordinating to a tungsten pentacarbonyl fragment reported in the CSD (v4.52).[208]

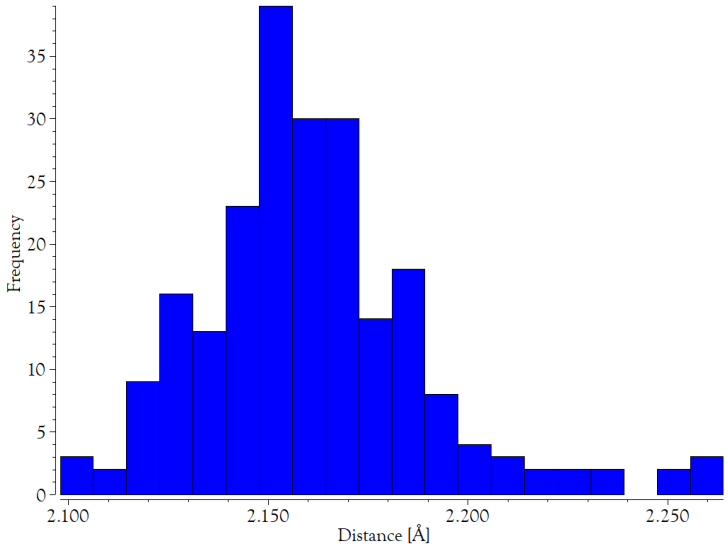

Figure 5-34: Histogram of all carbon-antimony single bond distances in all trivalent antimony compounds bound to three carbon atoms reported in the CSD (v4.52).[208]

Table 5-6: Results of the topological analysis of the theoretically derived periodic electron density distribution of **XVIII**. $\varrho(r)$: electron density; $\nabla^2\varrho(r)$: Laplacian of electron density; ε: ellipticity; $V(r_{cp})$: potential energy density; $G(r_{cp})$: kinetic energy density.

bond	$\varrho(r)$ [eÅ^{-3}]	$\nabla^2\varrho(r)$ [eÅ^{-5}]	ε	$V(r_{cp})$	$\lvert V(r_{cp})\rvert/G(r_{cp})$
Sb1-C1	0.620	2.219	0.000	−0.58	1.58
C1-C2	1.839	−17.544	0.069	−2.25	4.40
C2-O1	1.865	−10.334	0.041	−4.56	2.38
C2-N1	2.541	−29.150	0.291	−5.80	3.09
O1-C4	1.799	−6.400	0.011	−4.67	2.21
N1-C3	1.925	−17.094	0.063	−3.15	3.23
C3-C4	2.201	−23.316	0.244	−3.10	4.22
C3-C8	2.116	−21.956	0.190	−2.93	4.21
C4-C5	2.137	−22.091	0.198	−3.09	4.01
C5-C6	2.099	−21.056	0.181	−2.91	4.05
C6-C7	2.052	−20.447	0.160	−2.77	4.14
C7-C8	2.120	−21.450	0.195	−2.95	4.07
C5-H5	2.529	−39.633	0.004	−4.00	6.54
C6-H6	2.539	−39.929	0.005	−4.08	6.35
C7-H7	2.538	−39.792	0.001	−4.08	6.31
C8-C9	1.709	−15.577	0.030	−1.98	4.45
C9-H9A	2.341	−33.596	0.022	−3.53	5.98
C9-H9B	2.342	−33.589	0.023	−3.57	5.85
C9-H9C	2.347	−33.753	0.024	−3.57	5.93

Table 5-7: Results of the topological analysis of the theoretically derived electron density distribution of an isolated molecule of **XVIII** in the gas phase. $\varrho(r)$: electron density; $\nabla^2\varrho(r)$: Laplacian of electron density; ε: ellipticity; $V(r_{cp})$: potential energy density; $G(r_{cp})$: kinetic energy density.

bond	$\varrho(r)$ [eÅ^{-3}]	$\nabla^2\varrho(r)$ [eÅ^{-5}]	ε	$V(r_{cp})$	$\lvert V(r_{cp})\rvert / G(r_{cp})$
Sb1-C1	0.642	2.056	0.087	−0.63	1.63
C1-C2	1.871	−18.019	0.073	−2.33	4.36
C2-O1	1.943	−15.096	0.101	−4.77	2.57
C2-N1	2.665	−33.896	0.309	−6.48	3.16
O1-C4	1.885	−12.072	0.044	−4.85	2.42
N1-C3	2.012	−19.973	0.078	−3.35	3.43
C3-C4	2.252	−24.796	0.246	−3.21	4.36
C3-C8	2.168	−23.266	0.206	−3.04	4.31
C4-C5	2.194	−23.746	0.226	−3.20	4.17
C5-C6	2.152	−22.511	0.203	−3.03	4.17
C6-C7	2.100	−21.707	0.184	−2.87	4.24
C7-C8	2.174	−22.904	0.212	−3.08	4.17
C5-H5	2.578	−42.400	0.021	−4.05	7.48
C6-H6	2.591	−42.786	0.013	−4.10	7.42
C7-H7	2.584	−42.463	0.018	−4.11	7.21
C8-C9	1.735	−16.015	0.030	−2.00	4.56
C9-H9A	2.370	−35.272	0.018	−3.53	6.64
C9-H9B	2.375	−35.378	0.019	−3.55	6.62
C9-H9C	2.390	−35.839	0.017	−3.53	6.91

6 X-ray crystallographic details

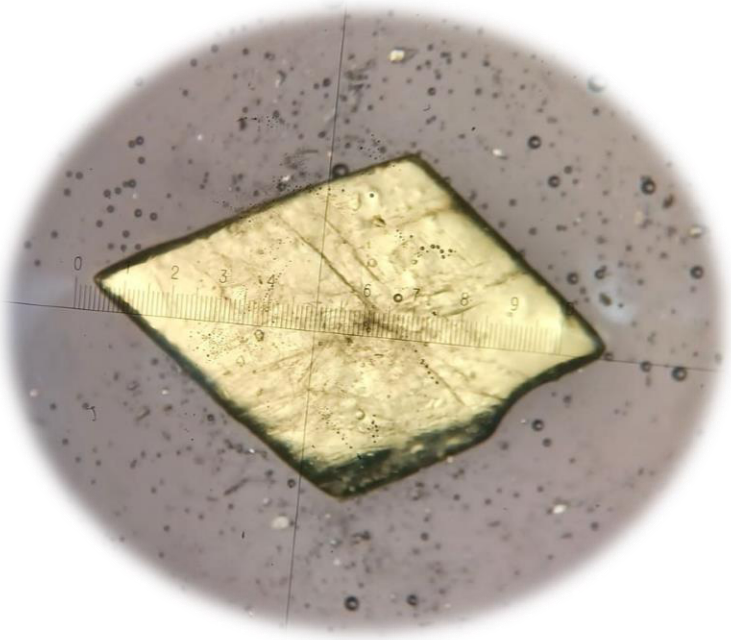

„Chemical crystallography – science, technology or a black art“

David J. Watkin

Data collection as well as structure solution and refinement was done as part of this thesis for all crystal structures presented in the following chapter.

6.1 Crystal structure of ^{Me}BoxGeCl **(III)**: $C_{17}H_{13}N_2O_2GeCl$ (polymorph A)

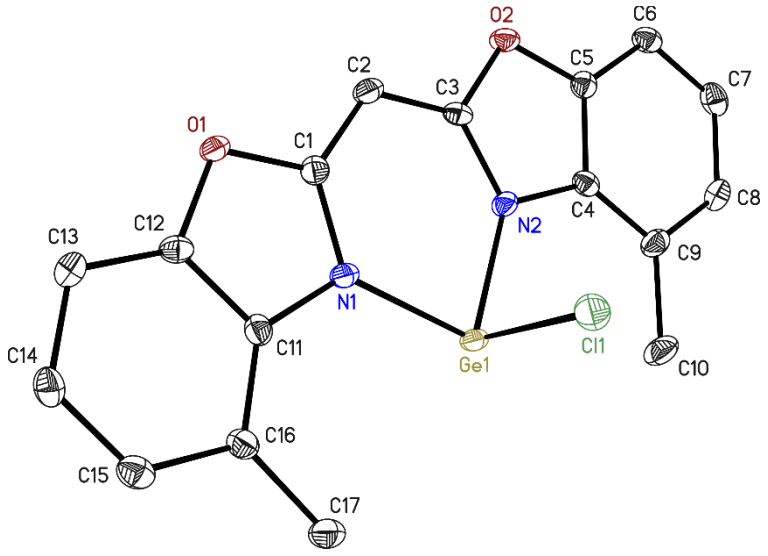

Figure 6-1: Asymmetric unit of ^{Me}BoxGeCl **(III)**. The anisotropic displacement parameters are depicted at the 50% probability level. The hydrogen atoms are omitted for clarity.

Structure code	NG_029_THF_2	**CCDC Number**	–
Empirical Formula	$C_{17}H_{13}N_2O_2GeCl$	**Crystal colour and shape**	yellow plates
Formula weight [g·mol^{-1}]	385.33	Z	4
Sample temperature [K]	100(2)	μ [mm^{-1}]	2.189
Wavelength [Å]	0.71073	F(000)	776
Crystal System	Monoclinic	Θ **range [°]**	2.086 to 25.361
Space group	$P2_1/c$	**Reflections collected**	31046
Unit cell dimensions [Å]	a = 7.966(2)	**Unique Reflections**	2798
	b = 14.646(3)	R_{int}	0.0518
	c = 13.470(2)	**Restraints / Parameters**	0 / 210
	β = 103.41(2)	$R1$ ($I>2\sigma(I)$)	0.0297
Volume [Å^3]	1528.7(6)	w$R2$ **(all data)**	0.0669
Crystal size [mm]	0.249 x 0.062 x 0.035	**max. diff. peak / hole [eÅ^{-3}]**	1.006 and −0.381

6.2 Crystal structure of ^{Me}BoxGeCl (**III**): $C_{17}H_{13}N_2O_2GeCl$ (polymorph B)

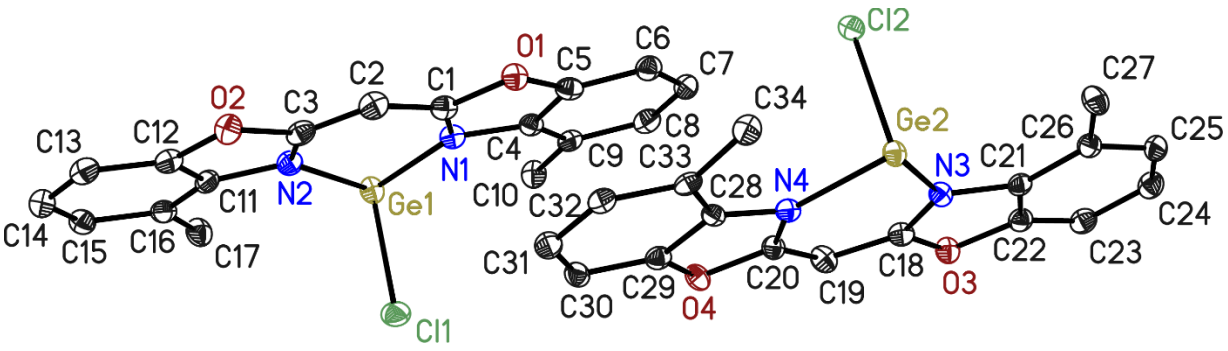

Figure 6-2: Asymmetric unit of ^{Me}BoxGeCl (**III**). The anisotropic displacement parameters are depicted at the 50% probability level. The hydrogen atoms are omitted for clarity.

Structure code	NG_029_DCM	**CCDC Number**	–
Empirical Formula	$C_{17}H_{13}lN_2O_2GeC$	**Crystal colour and shape**	yellow rods
Formula weight [g·mol^{-1}]	385.33	Z	4
Sample temperature [K]	100(2)	μ [mm^{-1}]	2.210
Wavelength [Å]	0.71073	F(000)	776
Crystal System	Triclinic	Θ **range [°]**	1.577 to 26.494
Space group	$P\bar{1}$	**Reflections collected**	49664
Unit cell dimensions [Å]	a = 7.950(2)	**Unique Reflections**	6211
	b = 13.397(3)	R_{int}	0.0353
	c = 14.748(2)	**Restraints / Parameters**	0 / 419
	a = 69.22(2)	$R1$ (I>2σ (I))	0.0323
	β = 89.91(2)	w$R2$ (all data)	0.0882
	γ = 83.77(2)	**max. diff. peak / hole [eÅ^{-3}]**	1.054 and −0.451
Volume [Å^3]	1514.3(6)		
Crystal size [mm]	0.409 x 0.228 x 0.181		

6.3 Crystal structure of (^{Me}BoxGe)$_2$O (**IV**): $C_{34}H_{26}N_4O_5Ge_2$

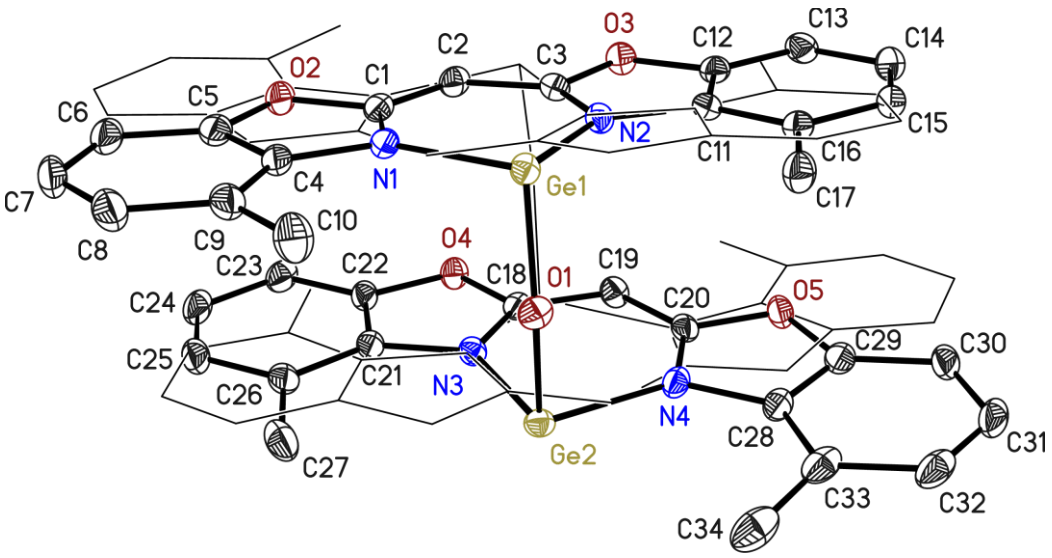

Figure 6-3: Asymmetric unit of (^{Me}BoxGe)$_2$O (**IV**). The anisotropic displacement parameters are depicted at the 50% probability level. The hydrogen atoms are omitted and disordered parts are shown in wireframe format for the sake of clarity.

The whole molecule was disordered over two positions. The occupancy of the minor position refined to 0.0202(8). The disorder was refined with distance restraints and restraints for the anisotropic displacement parameters.

Structure code	NG_029_THF	**CCDC Number**	–
Empirical Formula	$C_{34}H_{26}N_4O_5Ge_2$	**Crystal colour and shape**	yellow blocks
Formula weight [g·mol^{-1}]	715.77	Z	8
Sample temperature [K]	100(2)	μ [mm^{-1}]	2.128
Wavelength [Å]	0.71073	F(000)	2896
Crystal System	Orthorhombic	Θ **range [°]**	1.576 to 25.888
Space group	*Pbca*	**Reflections collected**	63168
Unit cell dimensions [Å]	a = 15.443(2)	**Unique Reflections**	5608
	b = 14.515(2)	R_{int}	0.0460
	c = 25.838(3)	**Restraints / Parameters**	2993 / 816
		$R1$ ($I>2\sigma(I)$)	0.0316
Volume [Å^3]	5791.7(13)	w$R2$ (all data)	0.0794
Crystal size [mm]	0.173 x 0.148 x 0.124	**max. diff. peak / hole [eÅ^{-3}]**	0.498 and −0.389

6.4 Crystal structure of ^{Me}BoxSnCl (V): $C_{17}H_{13}N_2O_2SnCl$

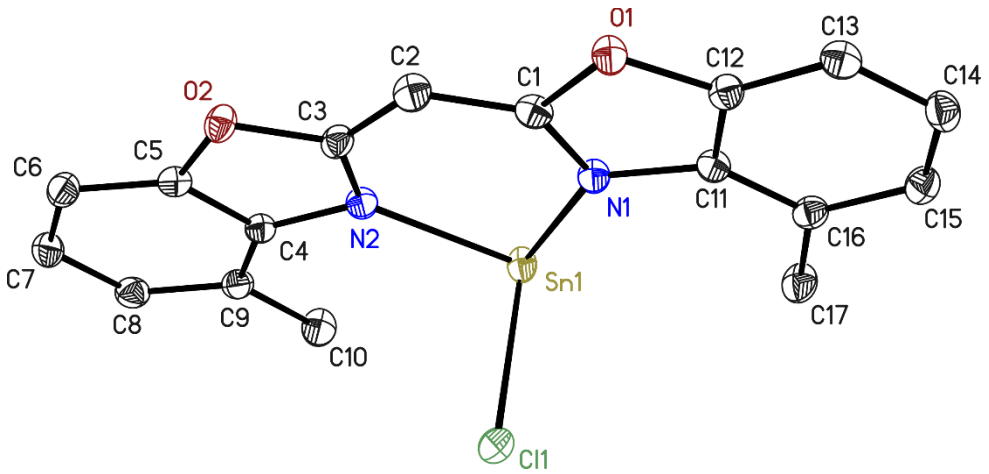

Figure 6-4: Asymmetric unit of ^{Me}BoxSnCl (**V**). The anisotropic displacement parameters are depicted at the 50% probability level. The hydrogen atoms are omitted for clarity.

Structure code	NG_ML_04	**CCDC Number**	–
Empirical Formula	$C_{17}H_{13}N_2O_2SnCl$	**Crystal colour and shape**	yellow blocks
Formula weight [g·mol^{-1}]	431.43	Z	4
Sample temperature [K]	100(2)	μ [mm^{-1}]	1.814
Wavelength [Å]	0.71073	F(000)	848
Crystal System	Monoclinic	Θ **range [°]**	2.066 to 26.548
Space group	$P2_1/c$	**Reflections collected**	46192
Unit cell dimensions [Å]	a = 7.990(3)	**Unique Reflections**	3190
	b = 14.880(5)	R_{int}	0.0275
	c = 13.451(4)	**Restraints / Parameters**	0 / 210
	β = 101.99(2)	$R1$ ($I>2\sigma(I)$)	0.0179
Volume [Å^3]	1564.3(9)	w$R2$ **(all data)**	0.0438
Crystal size [mm]	0.346 x 0.165 x 0.086	**max. diff. peak / hole [eÅ^{-3}]**	0.783 and −0.289

6.5 Crystal structure of ^{Me}BoxGe(HMDS) (**VII**): $C_{23}H_{31}N_3O_2GeSi_2$

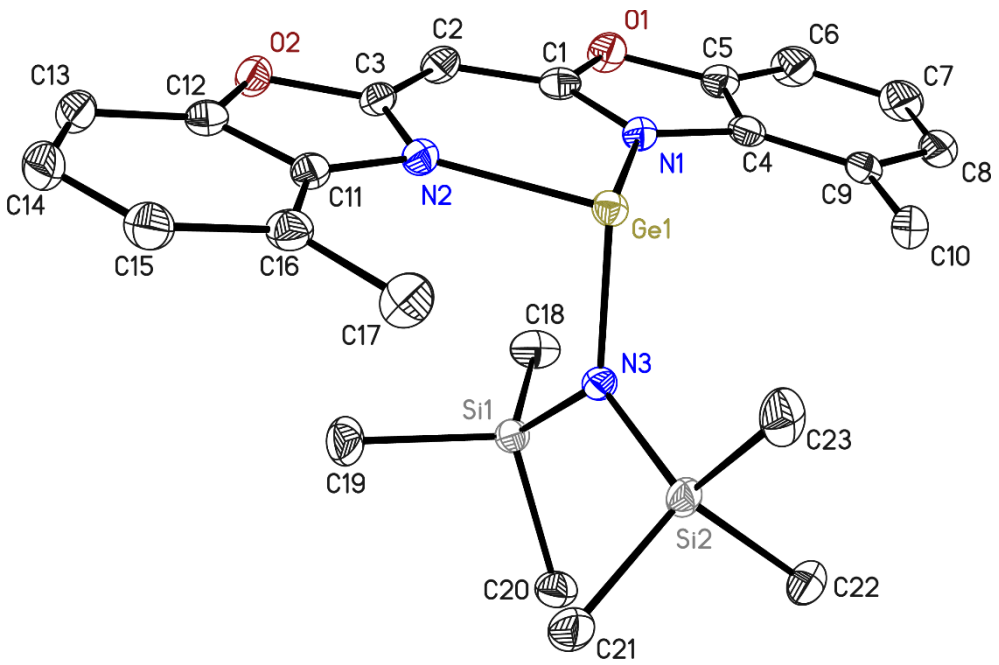

Figure 6-5: Asymmetric unit of ^{Me}BoxGe(HMDS) (**VII**).The anisotropic displacement parameters are depicted at the 50% probability level. The hydrogen atoms are omitted for clarity.

Structure code	NG_ML_05	**CCDC Number**	–
Empirical Formula	$C_{23}H_{31}N_3O_2GeSi_2$	**Crystal colour and shape**	yellow blocks
Formula weight [g·mol^{-1}]	510.28	Z	2
Sample temperature [K]	100(2)	μ [mm^{-1}]	1.386
Wavelength [Å]	0.71073	F(000)	532
Crystal System	Triclinic	Θ **range [°]**	1.541 to 26.396
Space group	$P\bar{1}$	**Reflections collected**	40268
Unit cell dimensions [Å]	a = 9.177(2)	**Unique Reflections**	4957
	b = 10.987(2)	R_{int}	0.0346
	c = 14.420(3)	**Restraints / Parameters**	0 / 288
	a = 67.98(2)	$R1$ ($I>2\sigma(I)$)	0.0219
	β = 73.55(2)	w$R2$ (all data)	0.0556
	γ = 65.62(2)	**max. diff. peak / hole [eÅ^{-3}]**	0.374 and −0.209
Volume [Å^3]	1213.4(5)		
Crystal size [mm]	0.134 x 0.132 x 0.094		

6.6 Crystal structure of ^{Me}BoxSn(HMDS) (**IX**): $C_{23}H_{31}N_3O_2SnSi_2$

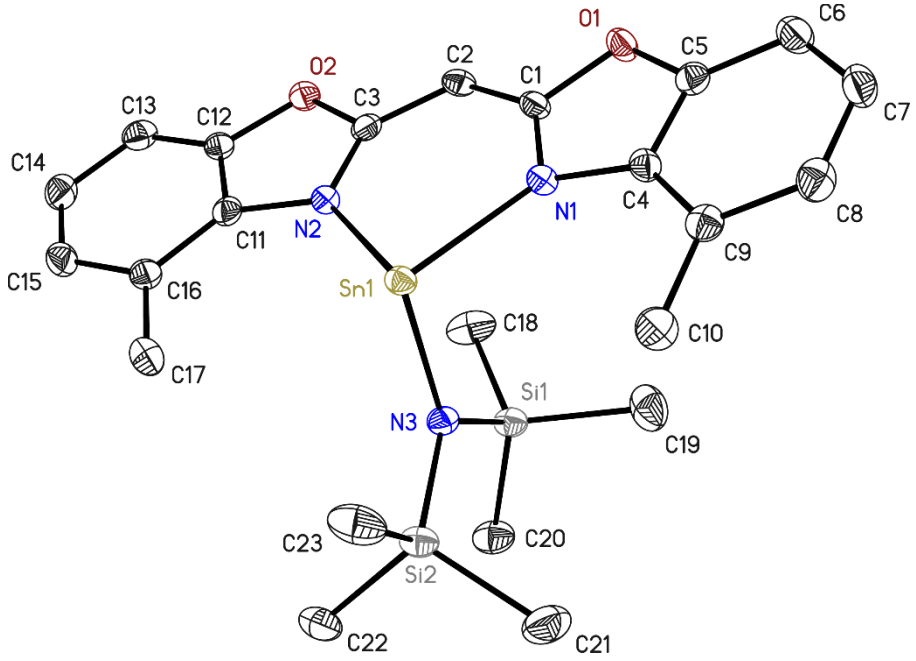

Figure 6-6: Asymmetric unit of ^{Me}BoxSn(HMDS) (**IX**). The anisotropic displacement parameters are depicted at the 50% probability level. The hydrogen atoms are omitted for clarity.

The data were corrected for 3λ contamination.[412]

Structure code	NG_038_Pentan	**CCDC Number**	–
Empirical Formula	$C_{23}H_{31}N_3O_2SnSi_2$	**Crystal colour and shape**	yellow blocks
Formula weight [g·mol^{-1}]	556.38	Z	2
Sample temperature [K]	100(2)	μ [mm^{-1}]	1.131
Wavelength [Å]	0.71073	F(000)	568
Crystal System	Triclinic	Θ **range [°]**	1.308 to 25.362
Space group	$P\bar{1}$	**Reflections collected**	36065
Unit cell dimensions [Å]	a = 8.897(2)	**Unique Reflections**	4611
	b = 9.260(2)	R_{int}	0.0347
	c = 16.214(3)	**Restraints / Parameters**	0 / 288
	α = 98.01(2)	$R1$ ($I>2\sigma(I)$)	0.0193
	β = 102.26(2)	w$R2$ **(all data)**	0.0486
	γ = 100.34(2)	**max. diff. peak / hole [eÅ^{-3}]**	0.440 and −0.340
Volume [Å^3]	1262.1(5)		
Crystal size [mm]	0.129 x 0.102 x 0.039		

6.7 Crystal structure of ^{Me}BoxPb(HMDS) (**XI**): $C_{23}H_{31}N_3O_2PbSi_2$ (polymorph A)

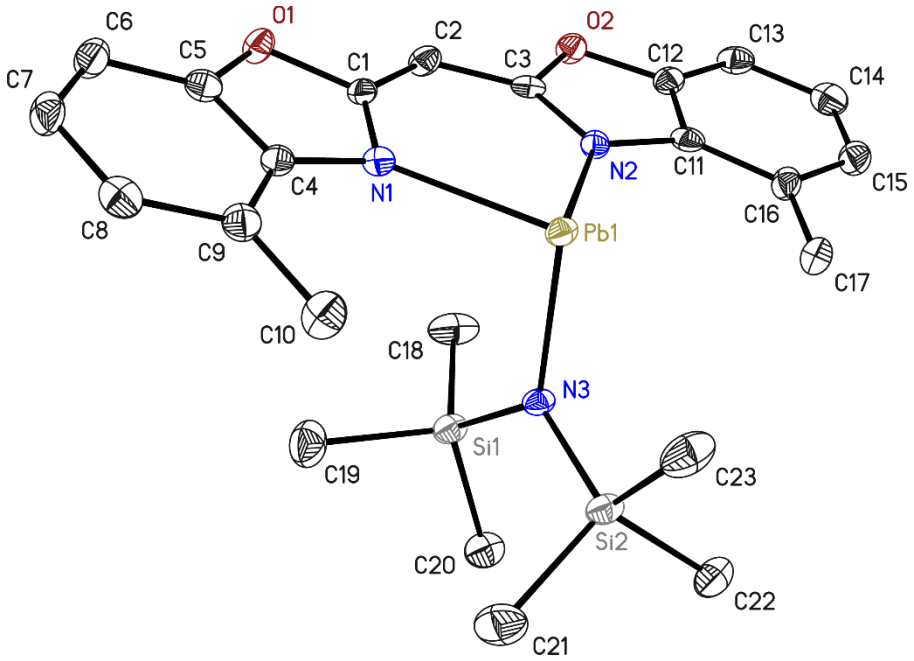

Figure 6-7: Asymmetric unit of ^{Me}BoxPb(HMDS) (**XI**).The anisotropic displacement parameters are depicted at the 50% probability level. The hydrogen atoms are omitted for clarity.

The data were corrected for 3λ contamination.[412]

Structure code	NG_046_Pentan	**CCDC Number**	–
Empirical Formula	$C_{23}H_{31}N_3O_2PbSi_2$	**Crystal colour and shape**	yellow plates
Formula weight [g·mol^{-1}]	644.88	***Z***	2
Sample temperature [K]	100(2)	***μ* [mm^{-1}]**	6.753
Wavelength [Å]	0.71073	***F*(000)**	632
Crystal System	Triclinic	***Θ* range [°]**	1.292 to 26.383
Space group	$P\bar{1}$	**Reflections collected**	33798
Unit cell dimensions [Å]	a = 8.861(2)	**Unique Reflections**	5203
	b = 9.230(2)	R_{int}	0.0557
	c = 16.384(3)	**Restraints / Parameters**	0 / 288
	α = 98.43(2)	***R*1 (*I*>2*σ*(*I*))**	0.0211
	β = 101.78(2)	**w*R*2 (all data)**	0.0432
	γ = 99.44(2)	**max. diff. peak / hole [eÅ^{-3}]**	0.596 and −0.625
Volume [Å^3]	1271.3(5)		
Crystal size [mm]	0.172 x 0.063 x 0.013		

6.8 Crystal structure of ^{Me}BoxPb(HMDS) (**XI**): $C_{23}H_{31}N_3O_2PbSi_2$ (polymorph B)

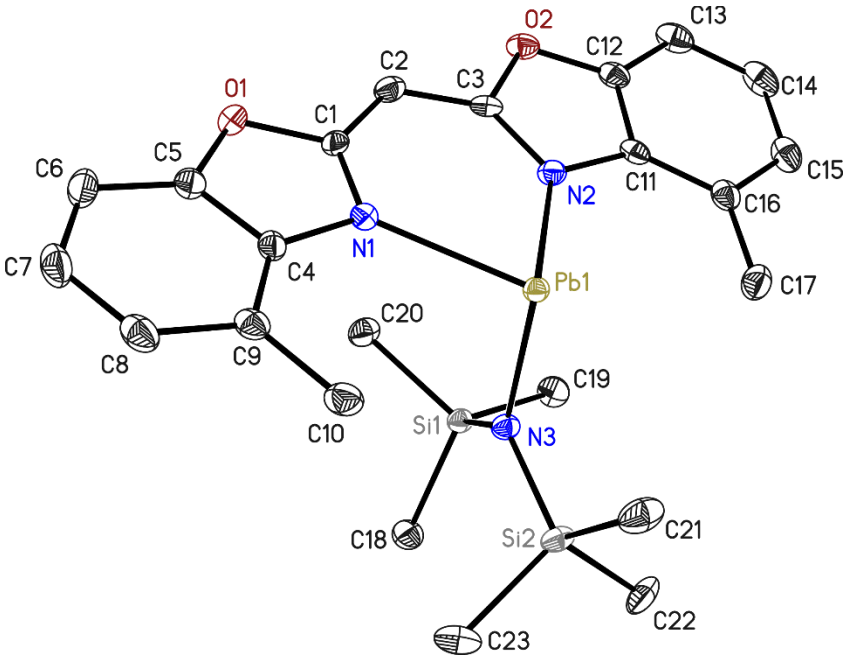

Figure 6-8: Asymmetric unit of ^{Me}BoxPb(HMDS) (**XI**).The anisotropic displacement parameters are depicted at the 50% probability level. The hydrogen atoms are omitted for clarity.

The data were corrected for 3λ contamination.[412]

Structure code	NG_046_DCM	**CCDC Number**	–
Empirical Formula	$C_{23}H_{31}N_3O_2PbSi_2$	**Crystal colour and shape**	yellow blocks
Formula weight [g·mol^{-1}]	644.88	***Z***	2
Sample temperature [K]	100(2)	***μ* [mm^{-1}]**	6.937
Wavelength [Å]	0.71073	***F*(000)**	632
Crystal System	Triclinic	**Θ range [°]**	2.501 to 26.488
Space group	$P\bar{1}$	**Reflections collected**	62561
Unit cell dimensions [Å]	a = 8.591(2)	**Unique Reflections**	5090
	b = 12.611(2)	R_{int}	0.0540
	c = 12.830(3)	**Restraints / Parameters**	0 / 288
	α = 69.91(2)	***R*1 ($I>2\sigma(I)$)**	0.0160
	β = 71.81(2)	**w*R*2 (all data)**	0.0419
	γ = 87.14(2)	**max. diff. peak / hole [eÅ^{-3}]**	1.093 and −0.731
Volume [Å^3]	1237.6(5)		
Crystal size [mm]	0.379 x 0.269 x 0.236		

6.9 Crystal structure of (^{Me}Box)$_2$Sn (**XII**): $C_{34}H_{26}N_4O_4Sn$

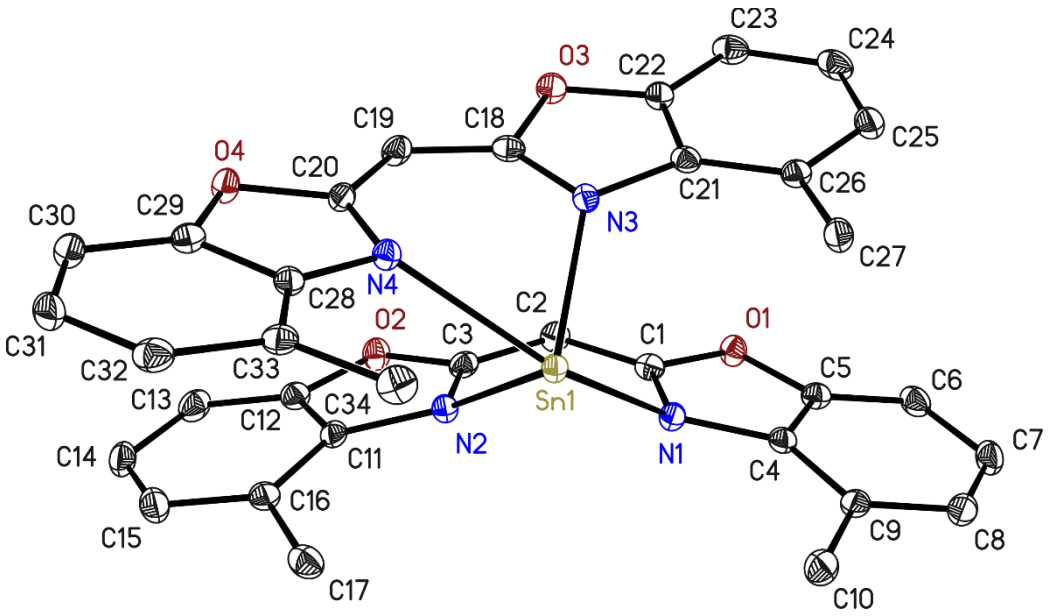

Figure 6-9: Asymmetric unit of (^{Me}Box)$_2$Sn (**XII**). The anisotropic displacement parameters are depicted at the 50% probability level. The hydrogen atoms are omitted for clarity.

The data were collected on a non-merohedral twin. The twin law was −1 0 0.16 0 −1 0 0 0 1. The fractional contribution of the minor twin domain refined to 0.0223(2).

Structure code	NG_045	**CCDC Number**	–
Empirical Formula	$C_{34}H_{26}N_4O_4Sn$	**Crystal colour and shape**	yellow blocks
Formula weight [g·mol^{-1}]	673.28	Z	4
Sample temperature [K]	100(2)	μ [mm^{-1}]	0.959
Wavelength [Å]	0.71073	F(000)	1360
Crystal System	Monoclinic	Θ **range [°]**	1.952 to 26.389
Space group	$P2_1/n$	**Reflections collected**	109303
Unit cell dimensions [Å]	a = 12.785(2)	**Unique Reflections**	5816
	b = 13.939(2)	R_{int}	0.0327
	c = 15.815(3)	**Restraints / Parameters**	0 / 393
	β = 95.79(2)	$R1$ ($I>2\sigma(I)$)	0.0211
Volume [Å^3]	2804.0(8)	w$R2$ (all data)	0.0.589
Crystal size [mm]	0.264 x 0.161 x 125	**max. diff. peak / hole [eÅ^{-3}]**	0.773 and −0.396

6.10 Crystal structure of (^{Me}Box)$_2$Pb (**XIII**): $C_{34}H_{26}N_4O_4Pb$

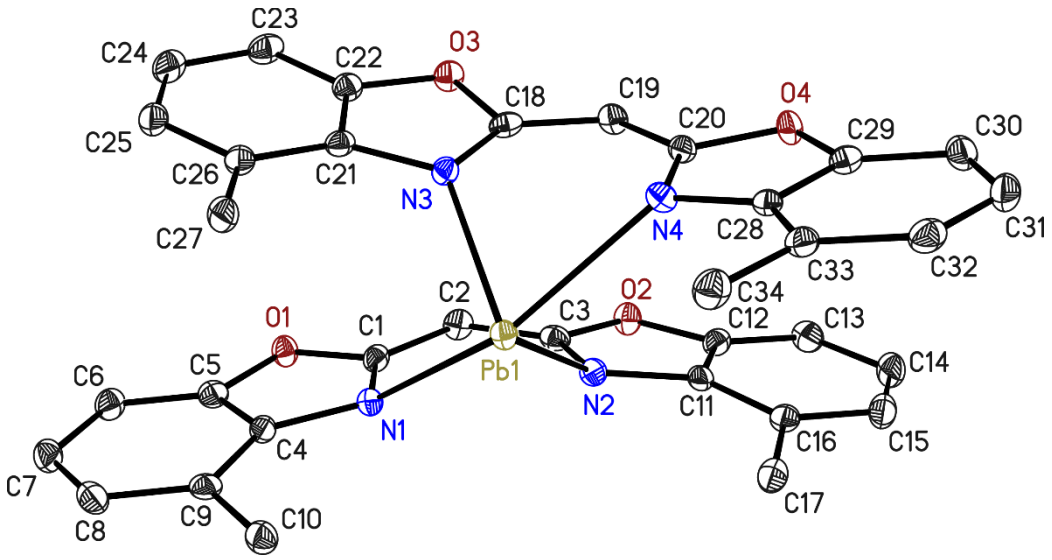

Figure 6-10: Asymmetric unit of (^{Me}Box)$_2$Pb (**XII**). The anisotropic displacement parameters are depicted at the 50% probability level. The hydrogen atoms are omitted for clarity.

Structure code	NG_049	**CCDC Number**	–
Empirical Formula	$C_{34}H_{26}N_4O_4Pb$	**Crystal colour and shape**	yellow blocks
Formula weight [g·mol^{-1}]	761.78	Z	4
Sample temperature [K]	100(2)	μ [mm^{-1}]	6.022
Wavelength [Å]	0.71073	F(000)	1488
Crystal System	Monoclinic	Θ **range [°]**	1.941 to 26.487
Space group	$P2_1/n$	**Reflections collected**	49735
Unit cell dimensions [Å]	a = 12.858(4)	**Unique Reflections**	5806
	b = 13.971(4)	R_{int}	0.0283
	c = 15.814(5)	**Restraints / Parameters**	0 / 392
	β = 96.22(2)	$R1$ ($I>2\sigma(I)$)	0.0183
Volume [Å^3]	2824.1(15)	w$R2$ **(all data)**	0.0436
Crystal size [mm]	0.180 x 0.153 x 0.066	**max. diff. peak / hole [eÅ^{-3}]**	1.099 and −0.777

6.11 Crystal structure of ^{Bzh}BoxGeCl (**XIV**): $C_{41}H_{29}N_2O_2GeCl \cdot 2\ (C_4H_8O)$

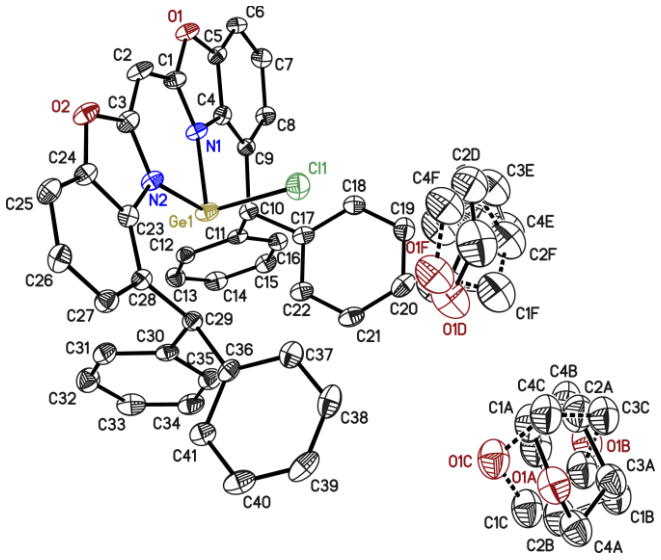

Figure 6-11: Asymmetric unit of ^{Bzh}BoxGeCl (**XIV**). The anisotropic displacement parameters are depicted at the 50% probability level. The hydrogen atoms are omitted for clarity.

The thf molecules was disordered over three positions each. The disorder was refined with distance restraints and restraints for the anisotropic displacement parameters. The occupancies refined to 0.767(3) (O1A–C4A), 0.169(3) (O1B–C4B), 0.064(3) (O1C–C4C), 0.807(3) (O1D–C4D), 0.108(3) (O1F–C4F), 0.087(3) (O1E–C4E).

Structure code	NG_048	**CCDC Number**	–
Empirical Formula	$C_{41}H_{29}N_2O_2GeCl \cdot 2\ (C_4H_8O)$	**Crystal colour and shape**	colourless blocks
Formula weight [g·mol^{-1}]	833.91	Z	2
Sample temperature [K]	100(2)	μ [mm^{-1}]	6.022
Wavelength [Å]	0.71073	F(000)	868
Crystal System	Triclinic	Θ **range [°]**	1.536 to 25.054
Space group	$P\bar{1}$	**Reflections collected**	59544
Unit cell dimensions [Å]	a = 11.218(4)	**Unique Reflections**	7045
	b = 14.351(5)	R_{int}	0.0605
	c = 14.791(5)	**Restraints / Parameters**	1208 / 700
	a = 68.57(2)	$R1$ ($I>2\sigma(I)$)	0.0373
	β = 68.47(2)	w$R2$ **(all data)**	0.0962
	γ = 88.87(2)	**max. diff. peak / hole [eÅ^{-3}]**	0.557 and −0.603
Volume [Å^3]	1990.2(13)		
Crystal size [mm]	0.094 x 0.087 x 0.082		

6.12 Crystal structure of ^{Me}BoxGeF (**XV**): $C_{17}H_{13}N_2O_2GeF$

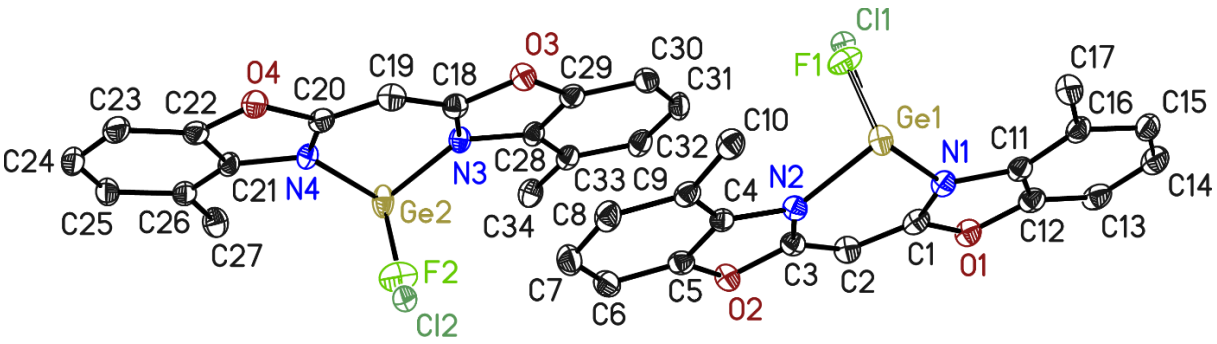

Figure 6-12: Asymmetric unit of ^{Me}BoxGeF (**XV**). The anisotropic displacement parameters are depicted at the 50% probability level. The hydrogen atoms are omitted for clarity.

The compounds co-crystallised with the starting material resulting in a substitutional disorder of the halide. The occupation of the minor position (fluoride) refined to 0.291(7).

Structure code	NG_056_2	**CCDC Number**	–
Empirical Formula	$C_{17}H_{13}N_2O_2GeCl_{0.61}F_{0.29}$	**Crystal colour and shape**	colourless blocks
Formula weight [g·mol^{-1}]	761.10	Z	4
Sample temperature [K]	100(2)	μ [mm^{-1}]	2.178
Wavelength [Å]	0.71073	F(000)	1533
Crystal System	Monoclinic	Θ **range [°]**	1.372 to 26.384
Space group	$P2_1/c$	**Reflections collected**	90911
Unit cell dimensions [Å]	a = 16.404(2)	**Unique Reflections**	6151
	b = 13.051.971(2)	R_{int}	0.0334
	c = 15.510(3)	**Restraints / Parameters**	0 / 438
	β = 115.17(2)	$R1$ ($I>2\sigma(I)$)	0.0328
Volume [Å^3]	3005.2(9)	w$R2$ **(all data)**	0.0736
Crystal size [mm]	0.239 x 0.205 x 0.134	**max. diff. peak / hole [eÅ^{-3}]**	0.479 and −0.536

6.13 Crystal structure of [(^{Me}BoxGeCl)W(CO)$_5$] (**XVI**): $C_{22}H_{13}N_2O_7GeClW$

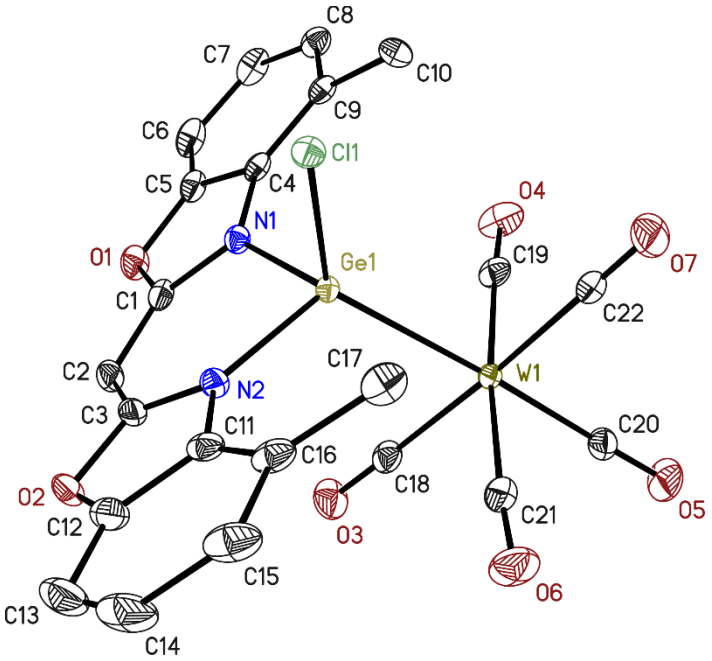

Figure 6-13: Asymmetric unit of [(^{Me}BoxGeCl)W(CO)$_5$] (**XVI**). The anisotropic displacement parameters are depicted at the 50% probability level. The hydrogen atoms are omitted for clarity.

Structure code	NG_ML_9	**CCDC Number**	–
Empirical Formula	$C_{22}H_{13}N_2O_7GeClW$	**Crystal colour and shape**	yellow plates
Formula weight [g·mol^{-1}]	709.23	Z	2
Sample temperature [K]	100(2)	μ [mm^{-1}]	6.590
Wavelength [Å]	0.71073	F(000)	676
Crystal System	Triclinic	Θ **range [°]**	1.737 to 26.426
Space group	$P\bar{1}$	**Reflections collected**	53643
Unit cell dimensions [Å]	a = 9.943(2)	**Unique Reflections**	4639
	b = 10.466(2)	R_{int}	0.0335
	c = 12.022(3)	**Restraints / Parameters**	0 / 309
	α = 79.44(2)	$R1$ ($I>2\sigma(I)$)	0.0110
	β = 79.40(2)	w$R2$ (all data)	0.0278
	γ = 67.67(2)	**max. diff. peak / hole [eÅ^{-3}]**	0.542 and −0.576
Volume [Å^3]	1128.6(5)		
Crystal size [mm]	0.281 x 0.220 x 0.213		

6.14 Crystal structure of (^{Me}Box)$_3$Sb$_2$ (**XVIII**): $C_{51}H_{36}N_6O_6Sb_2$

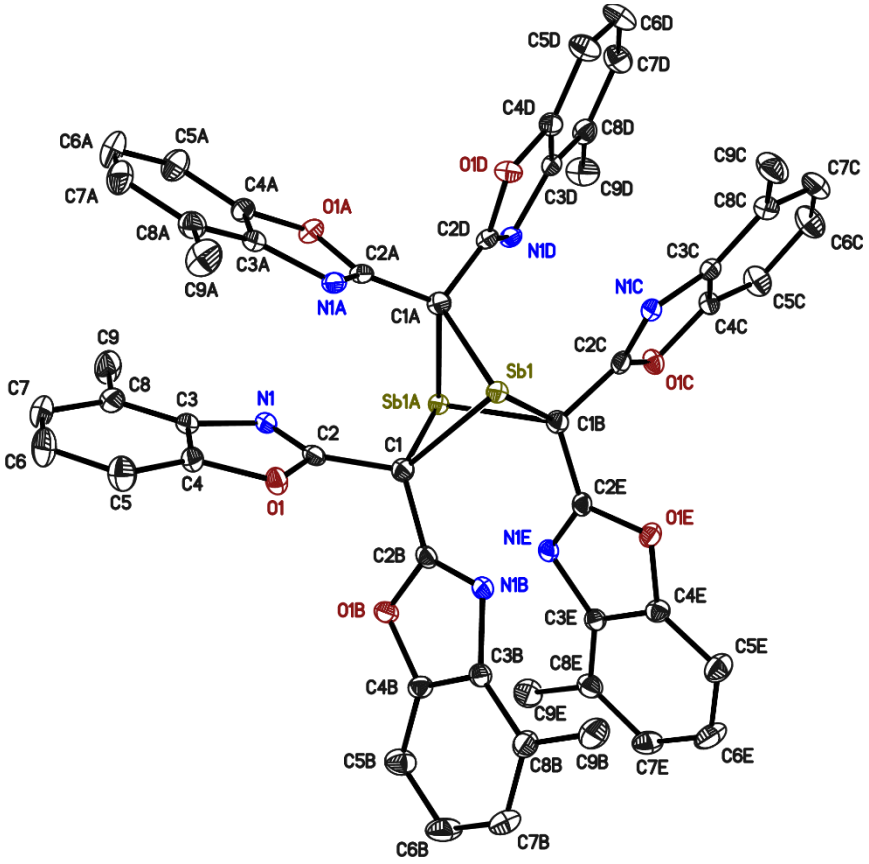

Figure 6-14: Molecular structure of (^{Me}Box)$_3$Sb$_2$ (**XVIII**). The asymmetric unit contains only one third of the molecule. The anisotropic displacement parameters are depicted at the 50% probability level. The hydrogen atoms are omitted for clarity.

Structure code	NG_030	**CCDC Number**	–
Empirical Formula	$C_{51}H_{36}N_6O_6Sb_2$	**Crystal colour and shape**	yellow blocks
Formula weight [g·mol^{-1}]	1072.36	Z	6
Sample temperature [K]	100(2)	μ [mm^{-1}]	1.312
Wavelength [Å]	0.71073	F(000)	3204
Crystal System	Trigonal	Θ **range [°]**	2.017 to 25.360
Space group	$R\bar{3}c$	**Reflections collected**	44913
Unit cell dimensions [Å]	a = 15.813(2)	**Unique Reflections**	1329
	c = 29.903(4)	R_{int}	0.0253
Volume [Å^3]	6475.5(19)	**Restraints / Parameters**	0 / 100
Crystal size [mm]	0.165 x 0.159 x 0.129	$R1$ ($I>2\sigma(I)$)	0.0214
		w$R2$ (all data)	0.0604
		max. diff. peak / hole [eÅ^{-3}]	1.392 and −0.750

6.15 Crystallographic service measurements

I would like to thank Prof. Dr. h.c. mult. Dr. rer. nat. em. Herbert W. Roesky (University of Göttingen) and his postdoctoral fellows Dr. Mingdong Zhong, Dr. Samja Banerjee, Dr. Arun Kumar and Dr. Mohd Nazish as well as Dr. Kartik Chandra Mondal (IIT Madras) and Dr. Sudipta Roy (IISER Tirupati) for entrusting me with their crystals and for the opportunity they gave me to contribute to their research through crystallographic analyses.

Data collection as well as structure solution and refinement was done as part of this thesis for all crystal structures presented in this chapter except for the structures discussed in subchapters 6.15.2.5 and 6.15.2.6. In those cases, data collection was performed at the Indian Institute of Technology (IIT) Madras, India and the raw data was provided for further processing and analysis.

6.15.1 Service Dr. Mingdong Zhong

6.15.1.1 Crystal structure of NG_MZ_Al3: $C_{40}H_{63}AlCl_2N_2$

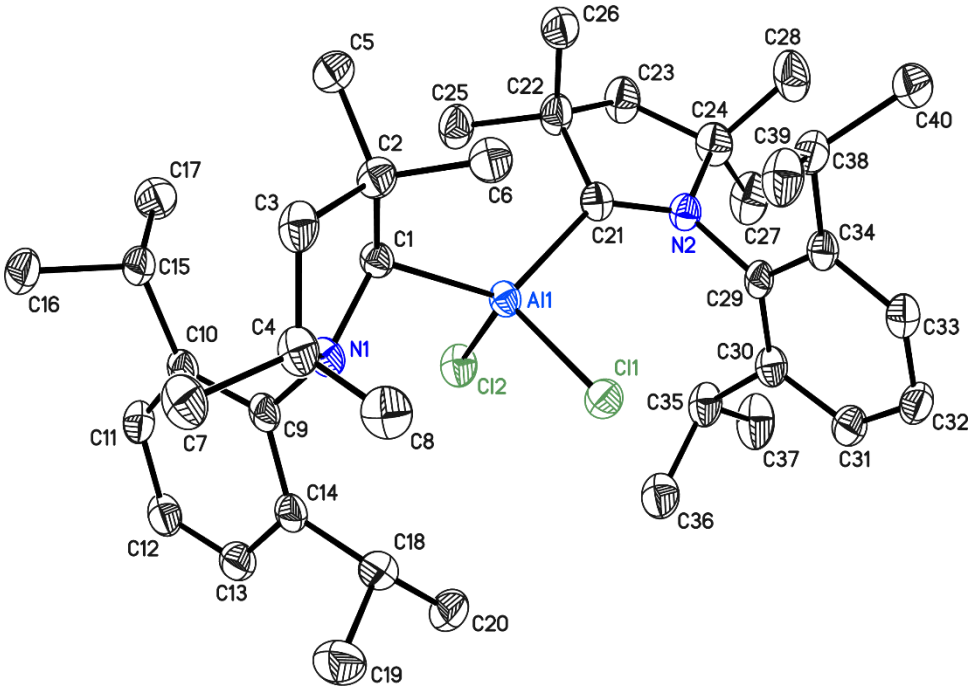

Figure 6-15: Asymmetric unit of NG_MZ_Al3. The anisotropic displacement parameters are depicted at the 50% probability level. The hydrogen atoms are omitted for clarity.

The highest residual density peaks could be interpreted as disorder of nearly the whole molecule. However, the occupancy of the minor position refined to 0.03(1). Therefore, the final refinement was done without treatment of disorder.

Structure code	NG_MZ_Al3	**CCDC Number**	1898149
Empirical Formula	$C_{40}H_{63}AlCl_2N_2$	**Crystal colour and shape**	yellow blocks
Formula weight [g·mol^{-1}]	669.80	Z	4
Sample temperature [K]	100(2)	μ [mm^{-1}]	0.220
Wavelength [Å]	0.71073	F(000)	1456
Crystal System	Monoclinic	Θ **range [°]**	1.665 to 26.065
Space group	$P2_1/c$	**Reflections collected**	64170
Unit cell dimensions [Å]	a = 12.642(2)	**Unique Reflections**	7634
	b = 19.368(3)	R_{int}	0.0566
	c = 16.983(3)	**Restraints / Parameters**	0 / 422
	β = 111.80(2)	$R1$ ($I>2\sigma(I)$)	0.0443
Volume [Å^3]	3860.9(12)	w$R2$ **(all data)**	0.1202
Crystal size [mm]	0.270 x 0.110 x 0.100	**max. diff. peak / hole [eÅ^{-3}]**	0.407 and −0.292

6.15.1.2 Crystal structure of NG_MZ_113: $C_{24}H_{41}AlClNO$

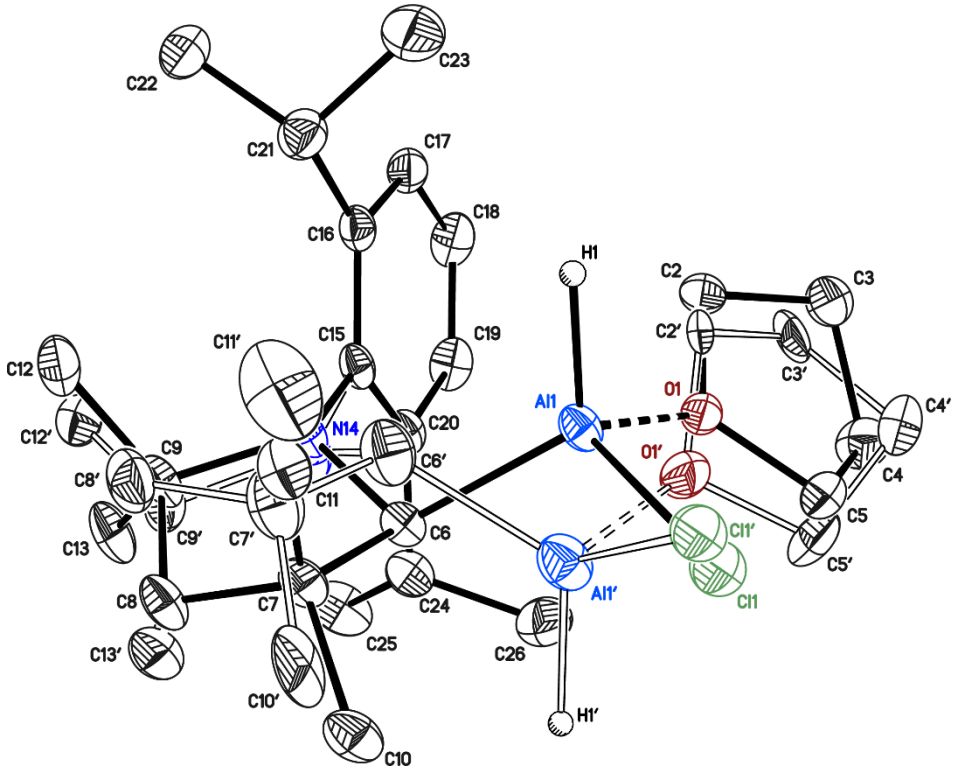

Figure 6-16: Asymmetric unit of NG_MZ_113. The anisotropic displacement parameters are depicted at the 50% probability level. The hydrogen atoms are omitted for clarity.

Parts of the molecule (Cl1-N14) were disordered over two positions. The occupancy of the minor position refined to 0.1230(17). All disordered groups were refined with distance restraints and restraints for the anisotropic displacement parameters. The anisotropic displacement parameters of the two positions of the chloride atoms were constrained to be identically. The metal bound hydrogen atom (H1) was refined freely.

Structure code	NG_MZ_113	**CCDC Number**	1898150
Empirical Formula	$C_{24}H_{41}AlClNO$	**Crystal colour and shape**	colourless blocks
Formula weight [g·mol^{-1}]	422.01	Z	4
Sample temperature [K]	100(2)	μ [mm^{-1}]	0.203
Wavelength [Å]	0.71073	F(000)	920
Crystal System	Monoclinic	Θ **range [°]**	1.830 to 26.433
Space group	$P2_1/c$	**Reflections collected**	40922
Unit cell dimensions [Å]	a = 9.219(2)	**Unique Reflections**	5114
	b = 13.320(2)	R_{int}	0.0354
	c = 20.320(3)	**Restraints / Parameters**	1023 / 411
	β = 94.74(2)	$R1$ ($I>2\sigma(I)$)	0.0463
Volume [Å^3]	2486.7(8)	w$R2$ **(all data)**	0.1045
Crystal size [mm]	0.270 x 0.110 x 0.100	**max. diff. peak / hole [eÅ^{-3}]**	0.526 and −0.325

6.15.1.3 Crystal structure of NG_MZ_36: $C_{30}H_{47}AlN_4$

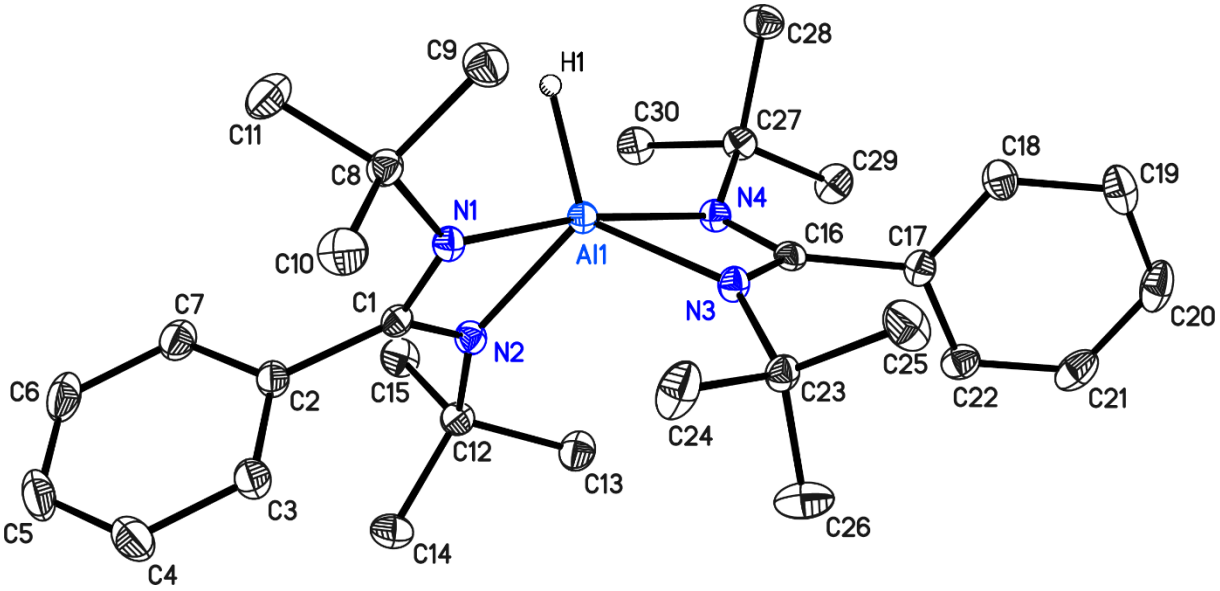

Figure 6-17: Asymmetric unit of NG_MZ_36. The anisotropic displacement parameters are depicted at the 50% probability level. The hydrogen atoms are omitted for clarity.

The metal bound hydrogen atom (H1) was refined freely.

Structure code	NG_SB_MZ_36	**CCDC Number**	1898151
Empirical Formula	$C_{30}H_{47}AlN_4$	**Crystal colour and shape**	colourless blocks
Formula weight [g·mol^{-1}]	490.69	**Z**	2
Sample temperature [K]	100(2)	**μ [mm^{-1}]**	0.094
Wavelength [Å]	0.71073	**F(000)**	536
Crystal System	Triclinic	**Θ range [°]**	1.753 to 27.476
Space group	$P\bar{1}$	**Reflections collected**	81427
Unit cell dimensions [Å]	a = 11.027(2)	**Unique Reflections**	6659
	b = 12.575(2)	**R_{int}**	0.0313
	c = 10.12.850(3)	**Restraints / Parameters**	0 / 332
	α = 65.28(2)	**$R1$ ($I>2\sigma(I)$)**	0.0339
	β = 74.87(3)	**w$R2$ (all data)**	0.0883
	γ = 64.27(4)	**max. diff. peak / hole [eÅ^{-3}]**	0.350 and −0.249
Volume [Å^3]	1451.2(6)		
Crystal size [mm]	0.326 x 0.324 x 0.134		

6.15.1.4 Crystal structure of NG_MZ_27: $C_{30}H_{46}CoN_4$

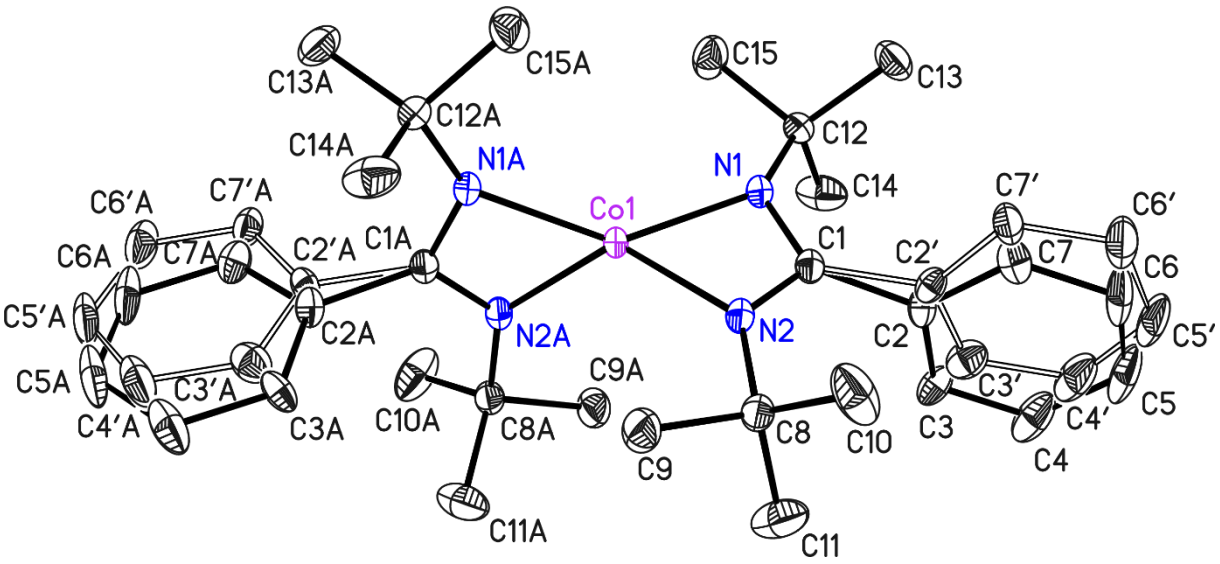

Figure 6-18: Molecular structure of NG_MZ_27. The asymmetric unit contains only half of the molecule. The anisotropic displacement parameters are depicted at the 50% probability level. The hydrogen atoms are omitted for clarity.

The phenyl ring (C2-C7) was disordered over two positions. The occupancy of the minor position refined to 0.4570(77). The disorder was refined with distance restraints and restraints for the anisotropic displacement parameters.

Structure code	NG_MZ_27	**CCDC Number**	2121393
Empirical Formula	$C_{30}H_{46}CoN_4$	**Crystal colour and shape**	purple blocks
Formula weight [g·mol^{-1}]	521.64	Z	4
Sample temperature [K]	100(2)	μ [mm^{-1}]	0.605
Wavelength [Å]	0.71073	F(000)	1124
Crystal System	Monoclinic	Θ **range [°]**	2.134 to 26.443
Space group	C2/c	**Reflections collected**	50565
Unit cell dimensions [Å]	a = 24.580(3)	**Unique Reflections**	3044
	b = 8.452(2)	R_{int}	0.0218
	c = 18.280(3)	**Restraints / Parameters**	429 / 220
	β = 129.06(2)	$R1$ ($I>2\sigma(I)$)	0.0245
Volume [Å^3]	2948.8(11)	w$R2$ **(all data)**	0.0647
Crystal size [mm]	0.239 x 0.233 x 0.218	**max. diff. peak / hole [eÅ^{-3}]**	0.483 and −0.338

6.15.1.5 Crystal structure of NG_MZ_60: $C_{40}H_{65}AlN_2$

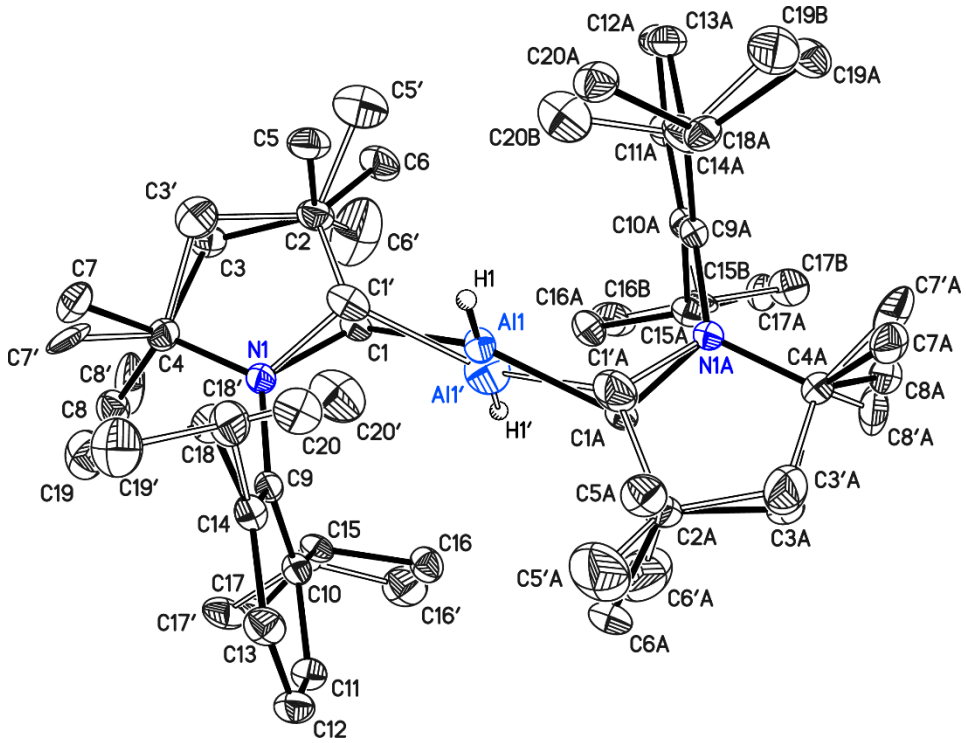

Figure 6-19: Molecular structure of NG_MZ_60. The asymmetric unit contains only half of the molecule. The anisotropic displacement parameters are depicted at the 50% probability level. The hydrogen atoms are omitted for clarity.

The isopropyl groups (C15-C17, C18-C20) and the carbene-metal fragment were each disordered over two positions. The occupancies of the minor positions refined to 0.193(22), 0.202(17) and 0.1516(25) respectively. All disordered groups were refined with distance restraints and restraints for the anisotropic displacement parameters. The metal bound hydrogen atom (H1) was refined freely.

Structure code	NG_MZ_60	**CCDC Number**	2121394
Empirical Formula	$C_{40}H_{65}AlN_2$	**Crystal colour and shape**	colourless blocks
Formula weight [g·mol^{-1}]	600.92	Z	4
Sample temperature [K]	100(2)	μ [mm^{-1}]	0.084
Wavelength [Å]	0.71073	F(000)	1328
Crystal System	Orthorhombic	Θ **range [°]**	1.744 to 27.889
Space group	*Pbcn*	**Reflections collected**	86052
Unit cell dimensions [Å]	a = 12.561(2)	**Unique Reflections**	4353
	b = 12.415(2)	R_{int}	0.0416
	c = 23.347(3)	**Restraints / Parameters**	493 / 314
		$R1$ ($I>2\sigma(I)$)	0.0457
Volume [Å^3]	3640.8(9)	w$R2$ **(all data)**	0.1384
Crystal size [mm]	0.331 x 0.192 x 0.169	**max. diff. peak / hole [eÅ^{-3}]**	0.412 and −0.577

6.15.1.6 Crystal structure of NG_MZ_97: $C_{24}H_{40}NOP$

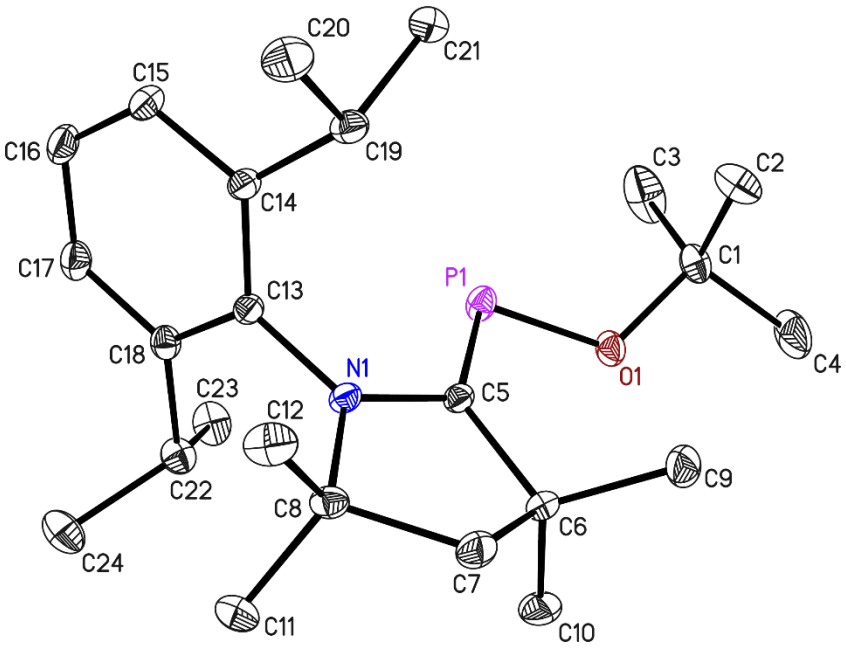

Figure 6-20: Asymmetric unit of NG_MZ_97. The anisotropic displacement parameters are depicted at the 50% probability level. The hydrogen atoms are omitted for clarity.

Structure code	NG_MZ_97	**CCDC Number**	2121395
Empirical Formula	$C_{24}H_{40}NOP$	**Crystal colour and shape**	colourless blocks
Formula weight [g·mol^{-1}]	389.54	Z	4
Sample temperature [K]	100(2)	μ [mm^{-1}]	0.131
Wavelength [Å]	0.71073	F(000)	856
Crystal System	Monoclinic	Θ **range [°]**	1.183 to 36.399
Space group	$P2_1/c$	**Reflections collected**	77226
Unit cell dimensions [Å]	a = 17.861(3)	**Unique Reflections**	11354
	b = 9.167(2)	R_{int}	0.0432
	c = 14.783(2)	**Restraints / Parameters**	0 / 255
	β = 105.56(2)	$R1$ ($I>2\sigma(I)$)	0.0429
Volume [Å^3]	2331.7(7)	w$R2$ **(all data)**	0.1168
Crystal size [mm]	0.254 x 0.177 x 0.128	**max. diff. peak / hole [eÅ^{-3}]**	0.618 and −0.341

6.15.1.7 Crystal structure of NG_MZ_138: $C_{30}H_{47}IN_4Si$

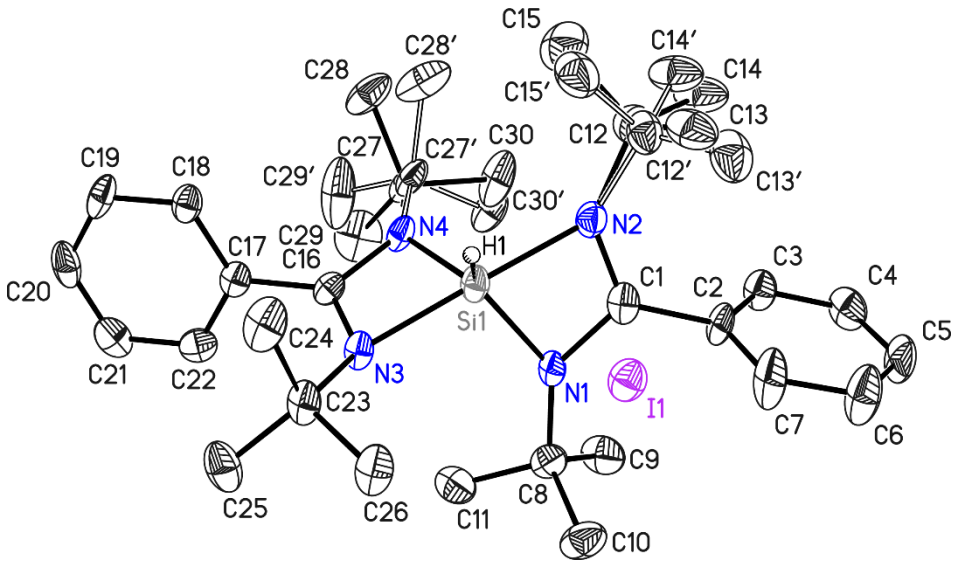

Figure 6-21: Asymmetric unit of NG_MZ_138. The anisotropic displacement parameters are depicted at the 50% probability level. The hydrogen atoms are omitted for clarity.

Two ^{t}Bu groups were disordered over two positions. The disorder was refined with distance restraints and restraints for the anisotropic displacement parameters. The occupancy of the minor components refined to 0.290(18) (C12-C15) and 0.407(26) (C27-C30). The anisotropic displacement parameters of C14 and C14‘ were constrained to be identical. The silicon bound hydrogen atom (H1) was refined freely.

Structure code	NG_MZ_138	**CCDC Number**	2121396
Empirical Formula	$C_{30}H_{47}IN_4Si$	**Crystal colour and shape**	yellow plates
Formula weight [g·mol^{-1}]	618.70	Z	4
Sample temperature [K]	100(2)	μ [mm^{-1}]	1.067
Wavelength [Å]	0.71073	F(000)	1288
Crystal System	Monoclinic	Θ **range [°]**	2.153 to 27.001
Space group	Cc	**Reflections collected**	33359
Unit cell dimensions [Å]	a = 15.120(2)	**Unique Reflections**	5843
	b = 12.793(2)	R_{int}	0.0949
	c = 18.567(3)	**Restraints / Parameters**	488 / 403
	β = 117.53(2)	$R1$ ($I>2\sigma(I)$)	0.0363
Volume [Å^3]	3184.8(10)	w$R2$ **(all data)**	0.0692
Crystal size [mm]	0.114 x 0.060 x 0.048	**max. diff. peak / hole [eÅ^{-3}]**	0.343 and −0.401

6.15.2 Service Dr. Sudipta Roy and Dr. Kartik Chandra Mondal

6.15.2.1 Crystal structure of NG_SR_SbCl: $C_{30}H_{46}Br_{0.17}Cl_{0.83}Sb$

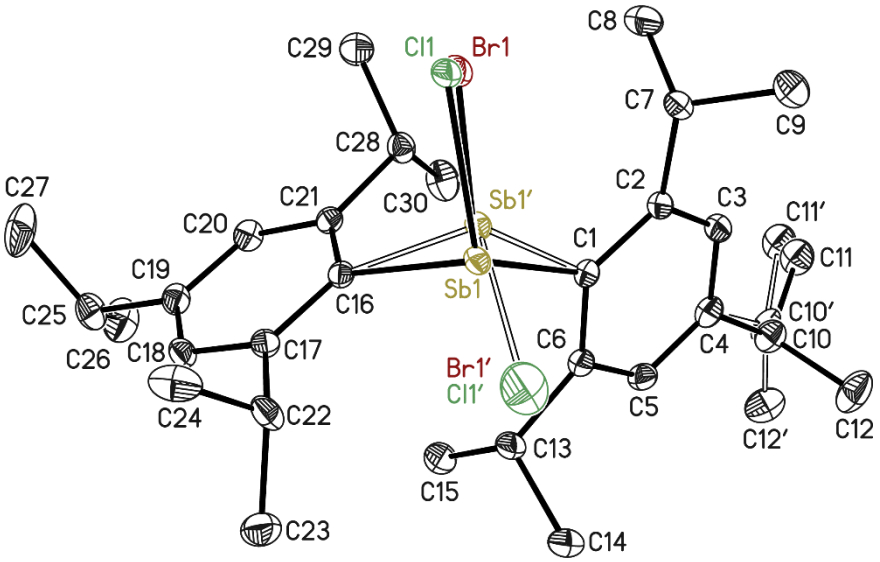

Figure 6-22: Asymmetric unit of NG_SR_SbCl. The anisotropic displacement parameters are depicted at the 50% probability level. The hydrogen atoms are omitted for clarity.

The antimony and halogen atoms were disordered over two positions. They were refined with distance restraints and constraints for the anisotropic displacement parameters. The occupancy of the minor position of antimony refined to 0.0574(10) (Sb1'), the occupancies of chlorine refined to 0.802(2) (Cl1) and 0.026(2) (Cl1') and those of bromine to 0.1409(14) (Br1) and 0.0312(15) (Br1'). A further disorder was found at one ^{i}Pr group. The group was refined with distance restraints and restraints for the anisotropic displacement parameters. The occupancy of the minor position refined to 0.070(4) (C10'-C12').

Structure code	NG_SR_SbCl	**CCDC Number**	2078143
Empirical Formula	$C_{30}H_{46}Br_{0.17}Cl_{0.83}Sb$	**Crystal colour and shape**	colourless blocks
Formula weight [g·mol^{-1}]	571.52	Z	4
Sample temperature [K]	100(2)	μ [mm^{-1}]	1.259
Wavelength [Å]	0.71073	F(000)	1188
Crystal System	Monoclinic	Θ **range [°]**	1.856 to 26.643
Space group	$P2_1/n$	**Reflections collected**	85505
Unit cell dimensions [Å]	a = 13.211(2)	**Unique Reflections**	6120
	b = 9.615(2)	R_{int}	0.0429
	c = 23.311(3)	**Restraints / Parameters**	523 / 351
	β = 95.76(2)	$R1$ ($I>2\sigma(I)$)	0.0194
Volume [Å^3]	2946.1(9)	w$R2$ **(all data)**	0.0461
Crystal size [mm]	0.207 x 0.131 x 0.112	**max. diff. peak / hole [eÅ^{-3}]**	0.520 and −0.268

6.15.2.2 Crystal structure of NG_SR_17_8: $C_{48}H_{96}Br_{3.42}Cl_{10.58}Mg_4O_{12}Sb_2$

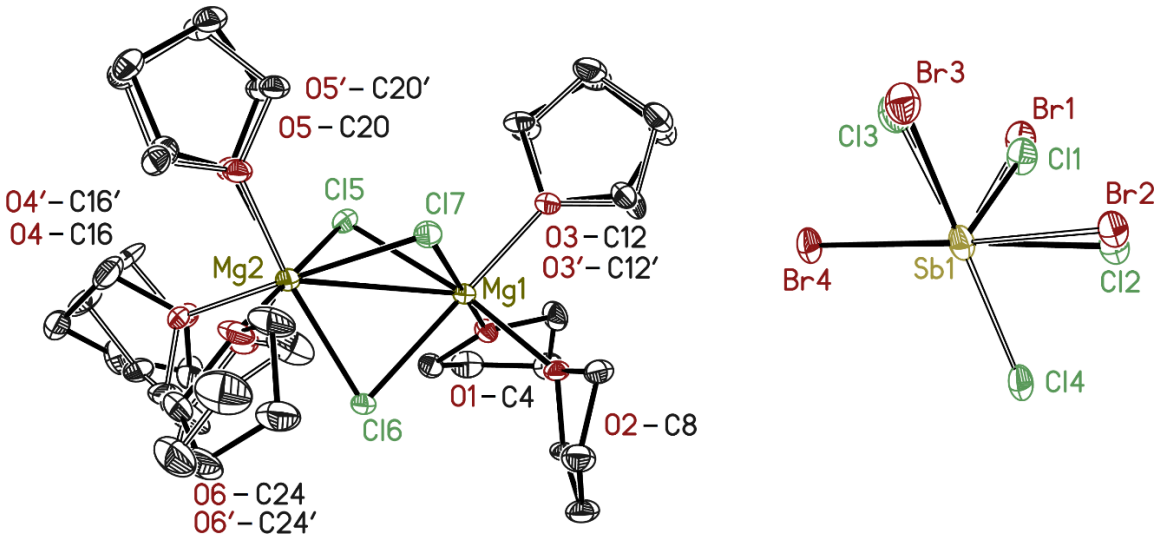

Figure 6-23: Asymmetric unit of NG_SR_17_8. The anisotropic displacement parameters are depicted at the 50% probability level. The hydrogen atoms are omitted for clarity.

Four of the thf molecules were disordered over two positions. The occupancies of the minor positions refined to 0.204(12) (O3'-C12'), 0.336(10) (O4'-C16'), 0.150(11) (O5'-C20'), 0.314(13) (O6-C24). The occupancy of the bromine atoms refined to 0.672(2) (Br3), 0.769(2) (Br4), 0.109(2) (Br1) and 0.158(2) (Br2). All disordered groups were refined with distance restraints and restraints for the anisotropic displacement parameters.

Structure code	NG_SR_17_8	**CCDC Number**	2078144
Empirical Formula	$C_{48}H_{96}Br_{3.42}Cl_{10.58}Mg_4O_{12}Sb_2$	**Crystal colour and shape**	yellow blocks
Formula weight [g·mol^{-1}]	1854.25	Z	1
Sample temperature [K]	100(2)	μ [mm^{-1}]	1.623
Wavelength [Å]	0.71073	F(000)	930
Crystal System	Triclinic	Θ **range [°]**	1.291 to 20.589
Space group	$P\bar{1}$	**Reflections collected**	68068
Unit cell dimensions [Å]	a = 11.492(2)	**Unique Reflections**	7593
	b = 12.810(2)	R_{int}	0.0506
	c = 13.501(3)	**Restraints / Parameters**	1741 / 561
	a = 97.01(2)	$R1$ ($I>2\sigma(I)$)	0.0261
	β = 107.72(2)	w$R2$ (all data)	0.0633
	γ = 98.91(2)	**max. diff. peak / hole [eÅ^{-3}]**	0.834 and −0.699
Volume [Å^3]	1839.9(6)		
Crystal size [mm]	0.261 x 0.172 x 0.123		

6.15.2.3 Crystal structure of NG_SR_17_23: $C_{66}H_{106}Sb_2$

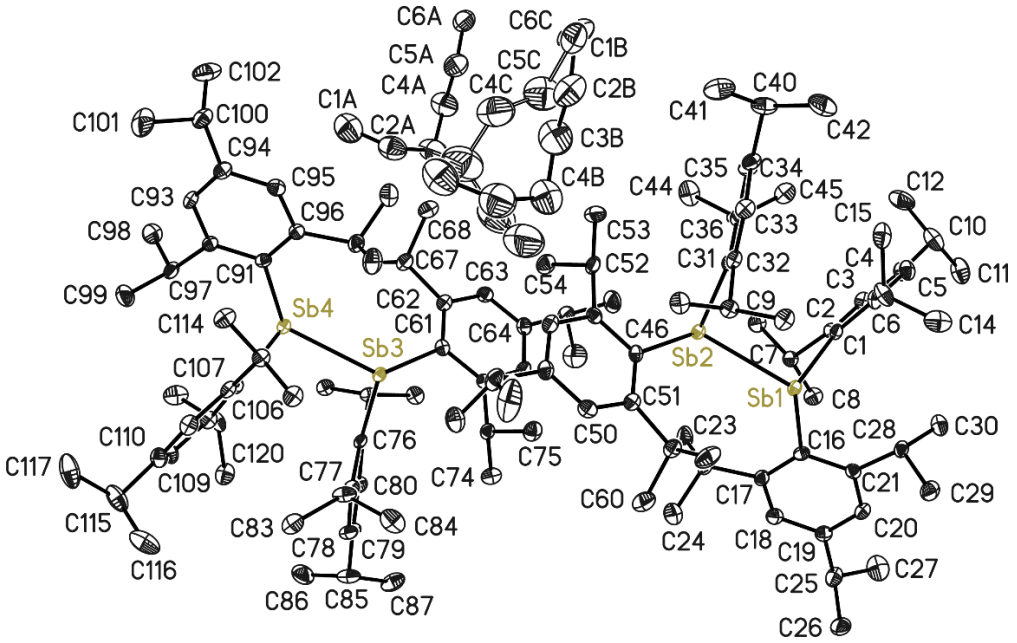

Figure 6-24: Asymmetric unit of NG_SR_17_23. The anisotropic displacement parameters are depicted at the 50% probability level. The hydrogen atoms are omitted for clarity.

A solvent hexane molecule was disordered over two positions. It was refined with distance restraints and restraints for the anisotropic displacement parameters. The occupancy of the minor position refined to 0.475(7) (C1B-C6B). The structure can also be solved in a smaller unit cell (a = 13.255(2), b = 13.428(2), c = 18.330(3), α = 72.28(2), β = 88.14(2), γ = 87.32(2)). Then the asymmetric unit contains only one molecule of $(Tip)_4Sb_2$, which suffers from severe disorder.

Structure code	NG_SR_17_23	**CCDC Number**	2078145
Empirical Formula	$C_{66}H_{106}Sb_2$	**Crystal colour and shape**	yellow blocks
Formula weight [g·mol^{-1}]	1143.00	Z	4
Sample temperature [K]	100(2)	μ [mm^{-1}]	0.906
Wavelength [Å]	0.71073	F(000)	2416
Crystal System	Triclinic	Θ **range [°]**	0.832 to 25.357
Space group	$P\bar{1}$	**Reflections collected**	238565
Unit cell dimensions [Å]	a = 13.255(2)	**Unique Reflections**	22677
	b = 19.142(3)	R_{int}	0.0466
	c = 25.810(4)	**Restraints / Parameters**	267 / 1334
	α = 108.36(3)	$R1$ ($I>2\sigma(I)$)	0.0363
	β = 92.72(2)	w$R2$ **(all data)**	0.0803
	γ = 90.10(2)	**max. diff. peak / hole [eÅ^{-3}]**	0.966 and −0.997
Volume [Å^3]	6207(2)		
Crystal size [mm]	0.213 x 0.186 x 0.157		

6.15.2.4 Crystal structure of NG_SR_17_19: $C_{119}H_{199}K_3O_5Sb_3$

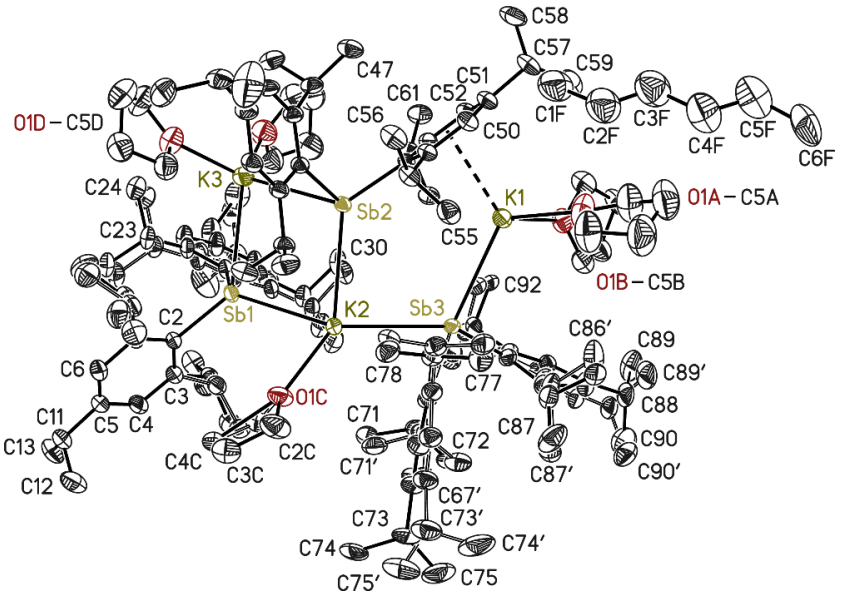

Figure 6-25: Asymmetric unit of NG_SR_17_19. The anisotropic displacement parameters are depicted at the 50% probability level. The hydrogen atoms as well as disordered positions in all of the coordinating thf and hexane molecules are omitted for clarity.

Each of the thf molecules was disordered over two positions. The occupancies of the minor positions refined to 0.312(5) (O1A'-C5A'), 0.242(7) (O1B'-C5B'), 0.446(4) (O1C'-C5C'), 0.189(4) (O1D'-C5D'), 0.284(8) (O1E'-C5E'). The hexane molecule was disordered over 7 positions. The sum of occupancies was fixed to 1.5. The occupancies for the individual positions were initially refined and then fixed. Three of the Tip substituents were disordered over two positions, in one substituent the disorder was only treated on the isopropyl groups. The occupancies of the minor positions refined to 0.435(8) (C8'-10'), 0.45(2) (C14-C16), 0.477(4) (C17'-C31'), 0.364(5) (C64'-C78'), 0.208(7) (C79-C93). All disordered groups were refined with distance restraints and restraints for the anisotropic displacement parameters.

Structure code	NG_SR_17_19	**CCDC Number**	2078146
Empirical Formula	$C_{119}H_{199}K_3O_5Sb_3$	**Crystal colour and shape**	red plates
Formula weight [g·mol^{-1}]	2192.32	Z	4
Sample temperature [K]	100(2)	μ [mm^{-1}]	0.801
Wavelength [Å]	0.71073	F(000)	4652
Crystal System	Monoclinic	Θ **range [°]**	1.053 to 26.384
Space group	$P2_1/c$	**Reflections collected**	357097
Unit cell dimensions [Å]	a = 14.898(2)	**Unique Reflections**	25205
	b = 36.172(3)	R_{int}	0.0648
	c = 23.327(3)	**Restraints / Parameters**	10755 / 2162
	β = 101.37(2)	$R1$ ($I>2\sigma(I)$)	0.0312
Volume [Å^3]	12324(3)	w$R2$ **(all data)**	0.0731
Crystal size [mm]	0.302 x 0.248 x 0.122	**max. diff. peak / hole [eÅ^{-3}]**	0.556 and −0.482

6.15.2.5 Crystal structure of NG_SUDIPTA368: $C_{38}H_{62}LiO_2Sb_2$

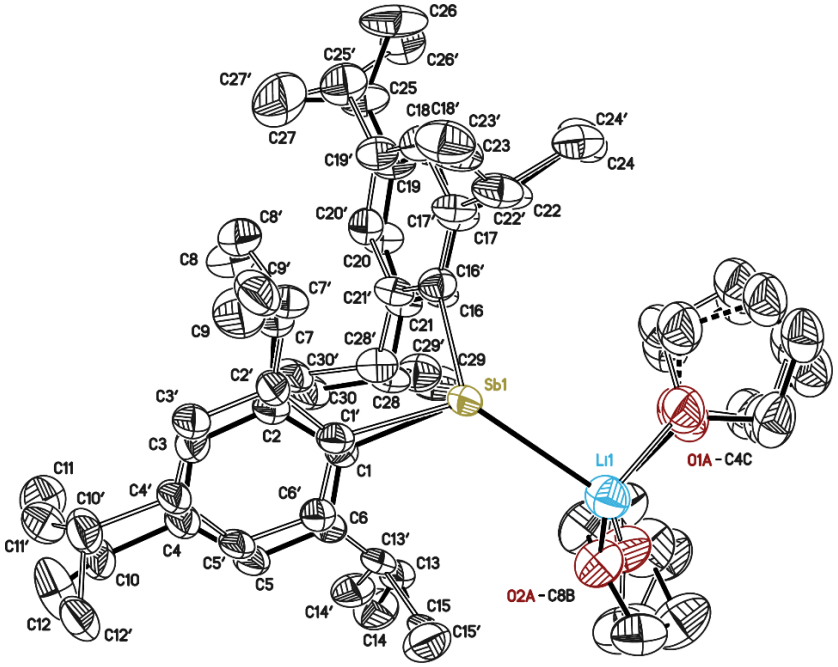

Figure 6-26: Asymmetric unit of NG_SUDIPTA368. The anisotropic displacement parameters are depicted at the 50% probability level. The hydrogen atoms are omitted for clarity.

Both aryl substituents and one thf molecule were disordered over two positions. The occupancies of the minor positions refined to 0.085(4) (C1'-15'), 0.188(7) (C16'-C30') and 0.280(8) (O2B-C8B). The second thf molecule is disordered over 3 positions. The sum of the occupancies of all three positions was restrained to be one. The occupancies refined to 0.532(3), 0.346(3) and 0.122(3). All disorder was refined with distance restraints and restraints for the anisotropic displacement parameters.

Structure code	NG_SUDIPTA368	**CCDC Number**	2078147
Empirical Formula	$C_{38}H_{62}LiO_2Sb_2$	**Crystal colour and shape**	black blocks
Formula weight [g·mol^{-1}]	679.56	Z	2
Sample temperature [K]	200(2)	μ [mm^{-1}]	0.745
Wavelength [Å]	0.71073	F(000)	720
Crystal System	Triclinic	Θ **range [°]**	2.447 to 26.407
Space group	$P\bar{1}$	**Reflections collected**	80094
Unit cell dimensions [Å]	a = 11.723(2)	**Unique Reflections**	7840
	b = 12.824(2)	R_{int}	0.0270
	c = 13.869(4)	**Restraints / Parameters**	3761 / 790
	α = 81.53(2)	$R1$ ($I>2\sigma(I)$)	0.0210
	β = 89.90(2)	w$R2$ (all data)	0.0562
	γ = 69.05(2)	**max. diff. peak / hole [eÅ^{-3}]**	0.804 and −0.376
Volume [Å^3]	1923.0(7)		
Crystal size [mm]	0.250 x 0.230 x 0.200		

6.15.2.6 Crystal structure of NG_SUDIPTAEN361: $C_{48}H_{70}NaOSb_2$

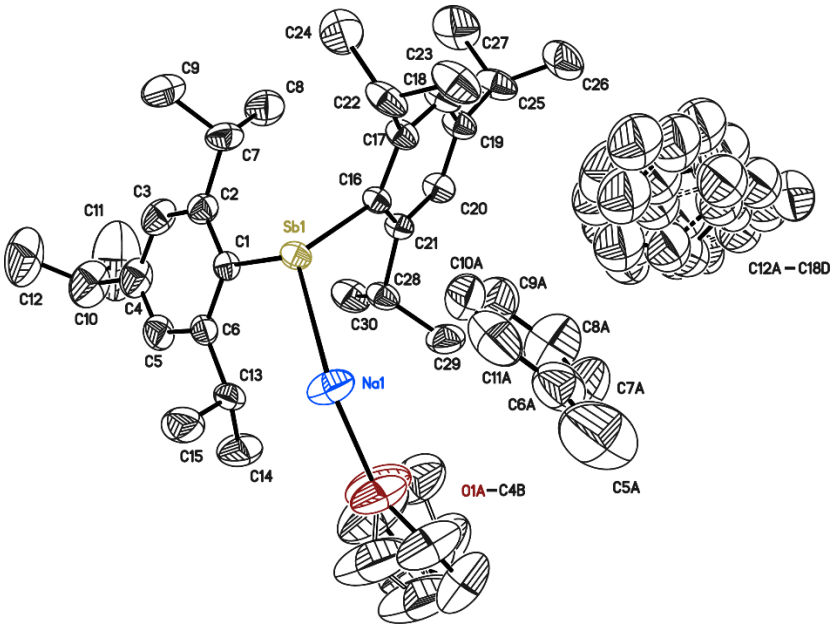

Figure 6-27: Asymmetric unit of NG_SUDIPTAEN361. The anisotropic displacement parameters are depicted at the 50% probability level. The hydrogen atoms are omitted for clarity.

The thf molecule was disordered over two positions. It was refined with distance restraints and constraints for the anisotropic displacement parameters. The occupancy of the minor position (O1B-C4B) refined to 0.408(12.) One toluene molecule was disordered about 4 positions. It was refined with distance restraints and restraints for the anisotropic displacement parameters. The sum of the occupancies of all three positions was restrained to be one. The occupancies refined to 0.367(3), 0.234(3), 0.220(3) and 0.179(3).

Structure code	NG_SUDIPTAEN361	**CCDC Number**	2078148
Empirical Formula	$C_{48}H_{70}NaOSb$	**Crystal colour and shape**	orange blocks
Formula weight [g·mol^{-1}]	807.78	Z	2
Sample temperature [K]	200(2)	μ [mm^{-1}]	0.631
Wavelength [Å]	0.71073	F(000)	856
Crystal System	Triclinic	Θ **range [°]**	2.966 to 26.363
Space group	$P\bar{1}$	**Reflections collected**	109940
Unit cell dimensions [Å]	a = 14.024(3)	**Unique Reflections**	9515
	b = 14.249(3)	R_{int}	0.0534
	c = 14.446(2)	**Restraints / Parameters**	2338 / 711
	a = 66.86(2)	$R1$ ($I>2\sigma(I)$)	0.0337
	β = 61.49(2)	w$R2$ **(all data)**	0.0816
	γ = 78.69(2)	**max. diff. peak / hole [eÅ^{-3}]**	2.258 and −0.606
Volume [Å^3]	2332.4(9)		
Crystal size [mm]	0.200 x 0.180 x 0.150		

6.15.2.7 Crystal structure of NG_SR_Pd: $C_{33}H_{28}NO_3PPd$

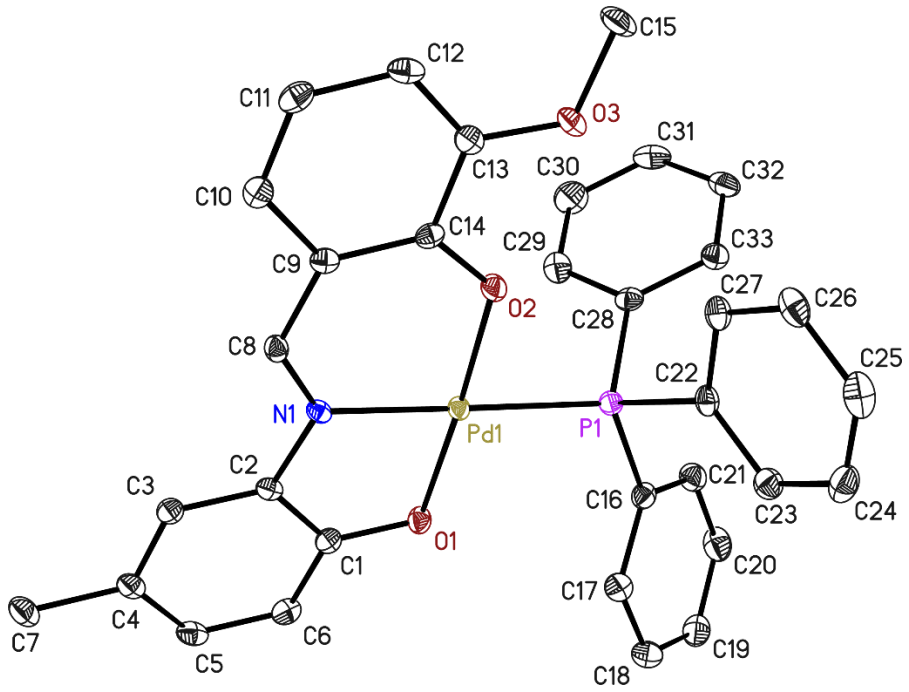

Figure 6-28: Asymmetric unit of NG_SR_Pd. The anisotropic displacement parameters are depicted at the 50% probability level. The hydrogen atoms are omitted for clarity.

Structure code	NG_SR_Pd	**CCDC Number**	2126046
Empirical Formula	$C_{33}H_{28}NO_3PPd$	**Crystal colour and shape**	orange plates
Formula weight [g·mol^{-1}]	623.93	Z	4
Sample temperature [K]	100(2)	μ [mm^{-1}]	0.416
Wavelength [Å]	0.56086	$F(000)$	1272
Crystal System	Monoclinic	Θ **range [°]**	1.780 to 20.572
Space group	$P2_1/n$	**Reflections collected**	103696
Unit cell dimensions [Å]	a = 9.623(2)	**Unique Reflections**	5592
	b = 27.061(3)	R_{int}	0.0576
	c = 10.526(2)	**Restraints / Parameters**	0 / 354
	β = 95.51(2)	$R1$ ($I>2\sigma(I)$)	0.0239
Volume [Å^3]	2728.4(8)	w$R2$ (all data)	0.0518
Crystal size [mm]	0.247 x 0.189 x 0.068	**max. diff. peak / hole [eÅ^{-3}]**	0.376 and −0.445

6.15.2.8 Crystal structure of NG_KM_387G: $C_{23}H_{35}IN_2$

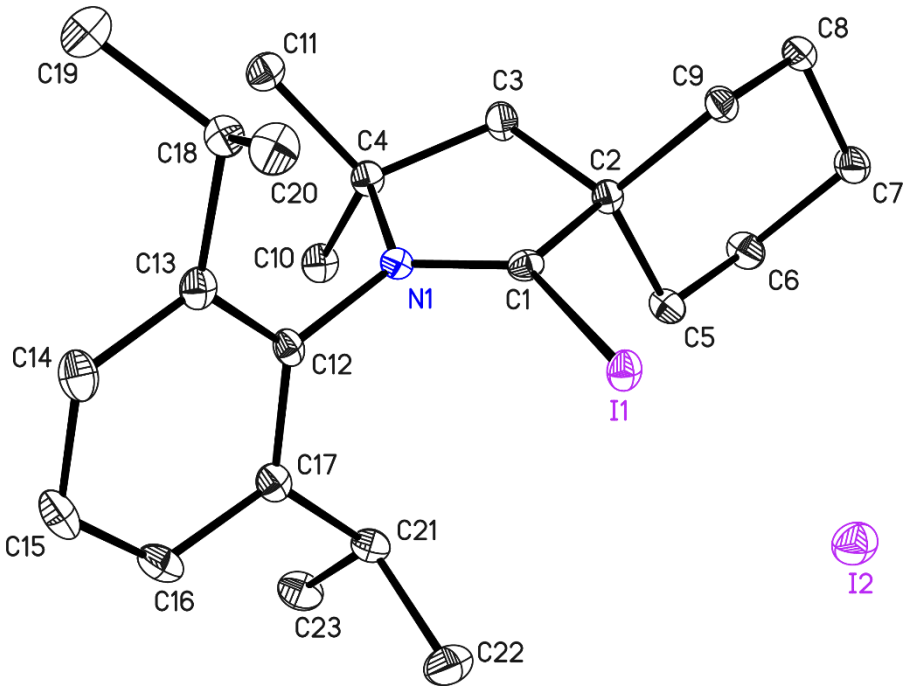

Figure 6-29: Asymmetric unit of NG_KM_387G. The anisotropic displacement parameters are depicted at the 50% probability level. The hydrogen atoms are omitted for clarity.

Structure code	NG_KM_387G	**CCDC Number**	2126071
Empirical Formula	$C_{23}H_{35}IN_2$	**Crystal colour and shape**	green blocks
Formula weight [g·mol^{-1}]	579.32	Z	4
Sample temperature [K]	100(2)	μ [mm^{-1}]	2.696
Wavelength [Å]	0.56086	F(000)	1144
Crystal System	Monoclinic	Θ **range [°]**	2.068 to 26.397
Space group	$P2_1/n$	**Reflections collected**	71156
Unit cell dimensions [Å]	a = 11.227(2)	**Unique Reflections**	4779
	b = 17.469(3)	R_{int}	0.0238
	c = 11.945(2)	**Restraints / Parameters**	0 / 241
	β = 93.15(2)	$R1$ ($I>2\sigma(I)$)	0.0117
Volume [Å^3]	2339.2(7)	w$R2$ **(all data)**	0.0289
Crystal size [mm]	0.164 x 0.161 x 0.160	**max. diff. peak / hole [eÅ^{-3}]**	0.375 and −0.218

6.15.3 Service Dr. Samja Banerjee

6.15.3.1 Crystal structure of NG_SB_GaCl: $C_{35}H_{54}GaClN_3 \cdot ½ (C_7H_8)$

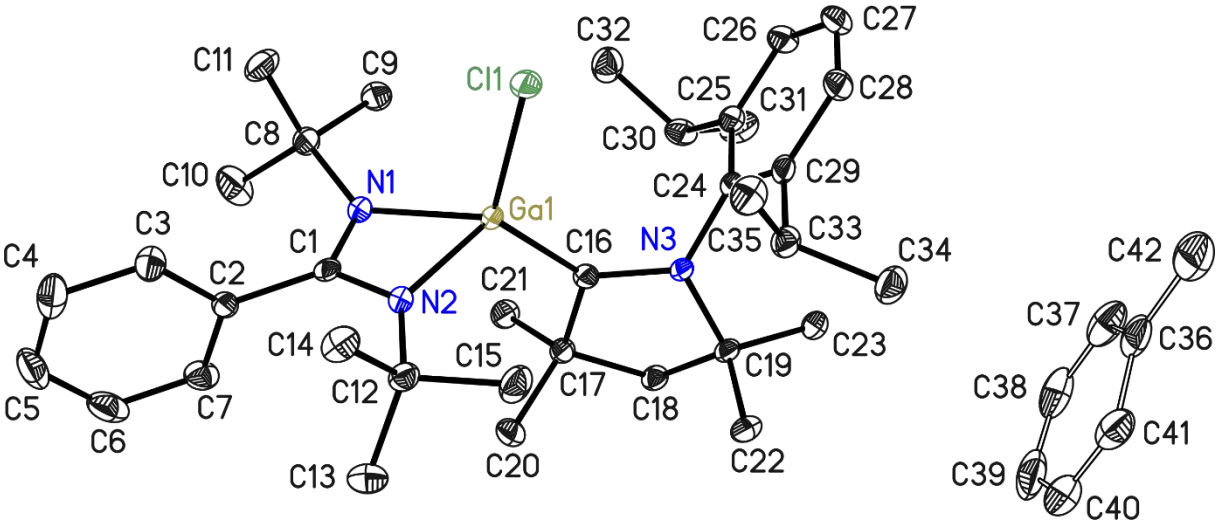

Figure 6-30: Asymmetric unit of NG_SB_GaCl. Anisotropic displacement parameters are depicted at the 50% probability level. Hydrogen atoms are omitted for clarity.

The toluene molecule was disordered about an inversion centre. It was refined with distance restraints and restraints for the anisotropic displacement parameters.

Structure code	NG_SB_GaCl	**CCDC Number**	2010645
Empirical Formula	$C_{35}H_{54}GaClN_3 \cdot ½ (C_7H_8)$	**Crystal colour and shape**	red blocks
Formula weight [g·mol^{-1}]	668.05	Z	4
Sample temperature [K]	100(2)	μ [mm^{-1}]	0.841
Wavelength [Å]	0.71073	F(000)	1432
Crystal System	Monoclinic	Θ **range [°]**	1.217 to 27.493
Space group	$P2_1/n$	**Reflections collected**	79447
Unit cell dimensions [Å]	a = 10.087(2)	**Unique Reflections**	8519
	b = 11.009(2)	R_{int}	0.0600
	c = 33.526(4)	**Restraints / Parameters**	93 / 439
	β = 93.64(2)	$R1$ ($I>2\sigma(I)$)	0.0344
Volume [Å^3]	3715.5(11)	w$R2$ **(all data)**	0.0791
Crystal size [mm]	0.270 x 0.246 x 0.152	**max. diff. peak / hole [eÅ^{-3}]**	0.542 and −0.458

6.15.3.2 Crystal structure of NG_SB_In2: $C_{30}H_{46}BrInN_4$

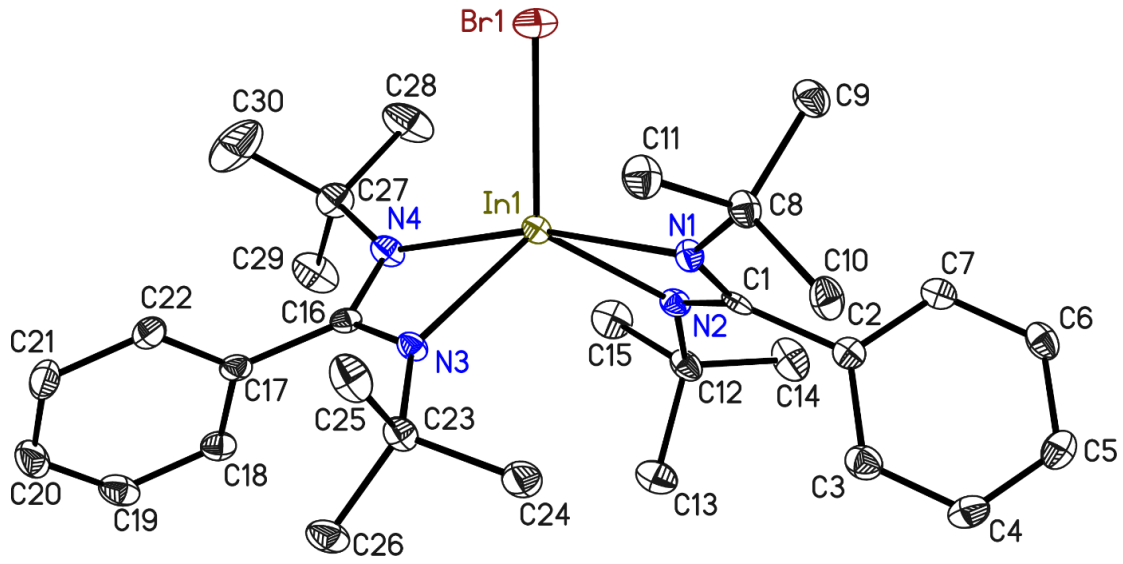

Figure 6-31: Asymmetric unit of NG_SB_In2. The anisotropic displacement parameters are depicted at the 50% probability level. The hydrogen atoms are omitted for clarity.

Structure code	NG_SB_In2	**CCDC Number**	2027411
Empirical Formula	$C_{30}H_{46}BrInN_4$	**Crystal colour and shape**	colourless blocks
Formula weight [g·mol^{-1}]	657.44	Z	4
Sample temperature [K]	100(2)	μ [mm^{-1}]	1.116
Wavelength [Å]	0.56086	F(000)	1352
Crystal System	Monoclinic	Θ **range [°]**	1.867 to 20.545
Space group	$P2_1/c$	**Reflections collected**	58248
Unit cell dimensions [Å]	a = 10.025(2)	**Unique Reflections**	6337
	b = 11.767(2)	R_{int}	0.0662
	c = 26.548(3)	**Restraints / Parameters**	0 / 338
	β = 99.56(2)	$R1$ ($I>2\sigma(I)$)	0.0257
Volume [Å^3]	3088.2(9)	w$R2$ (all data)	0.0517
Crystal size [mm]	0.173 x 0.149 x 0.094	**max. diff. peak / hole [eÅ^{-3}]**	0.393 and −0.355

6.15.3.3 Crystal structure of NG_SB_In_Tol: $C_{30}H_{46}BrInN_4 \cdot ½ (C_7H_8)$

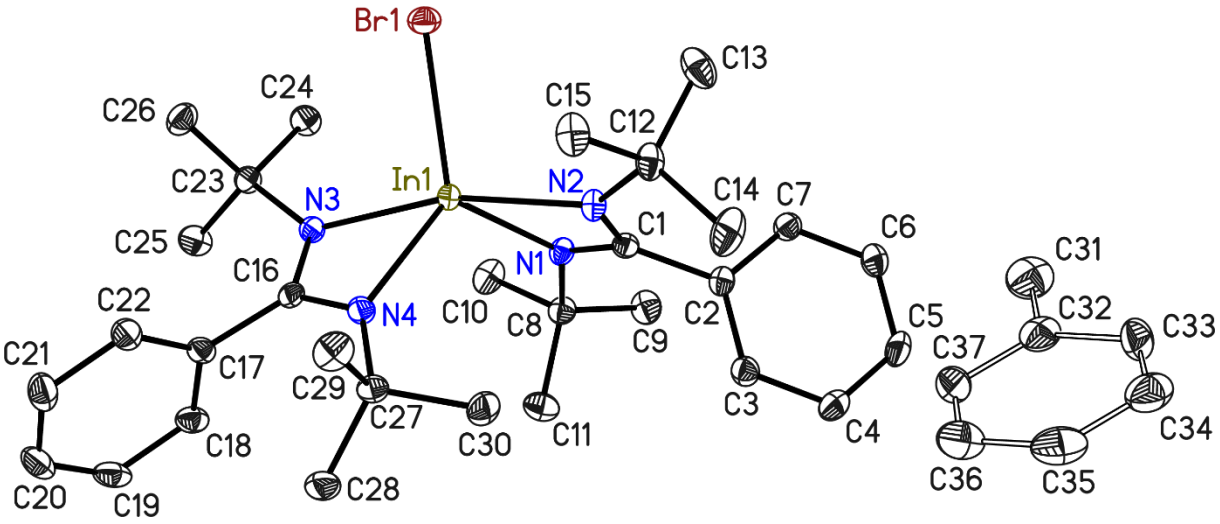

Figure 6-32: Asymmetric unit of NG_SB_In_Tol. The anisotropic displacement parameters are depicted at the 50% probability level. The hydrogen atoms are omitted for clarity.

The toluene molecule was disordered about an inversion centre. It was refined with distance restraints and restraints for the anisotropic displacement parameters.

Structure code	NG_SB_In_Tol	**CCDC Number**	2027412
Empirical Formula	$C_{35}H_{46}BrInN_4 \cdot ½ (C_7H_8)$	**Crystal colour and shape**	colourless blocks
Formula weight [g·mol^{-1}]	703.50	Z	4
Sample temperature [K]	100(2)	μ [mm^{-1}]	1.912
Wavelength [Å]	0.71073	F(000)	1452
Crystal System	Monoclinic	Θ range [°]	1.593 to 27.497
Space group	$P2_1/n$	**Reflections collected**	74445
Unit cell dimensions [Å]	a = 9.763(2)	**Unique Reflections**	7762
	b = 21.991(3)	R_{int}	0.0308
	c = 15.761(2)	**Restraints / Parameters**	118 / 401
	β = 94.32(2)	$R1$ ($I>2\sigma(I)$)	0.0172
Volume [Å^3]	3374.2(9)	w$R2$ (all data)	0.0415
Crystal size [mm]	0.374 x 0.239 x 0.128	**max. diff. peak / hole [eÅ^{-3}]**	0.372 and −0.191

6.15.3.4 Crystal structure of NG_SB_In_I: $C_{35}H_{46}IInN_4$

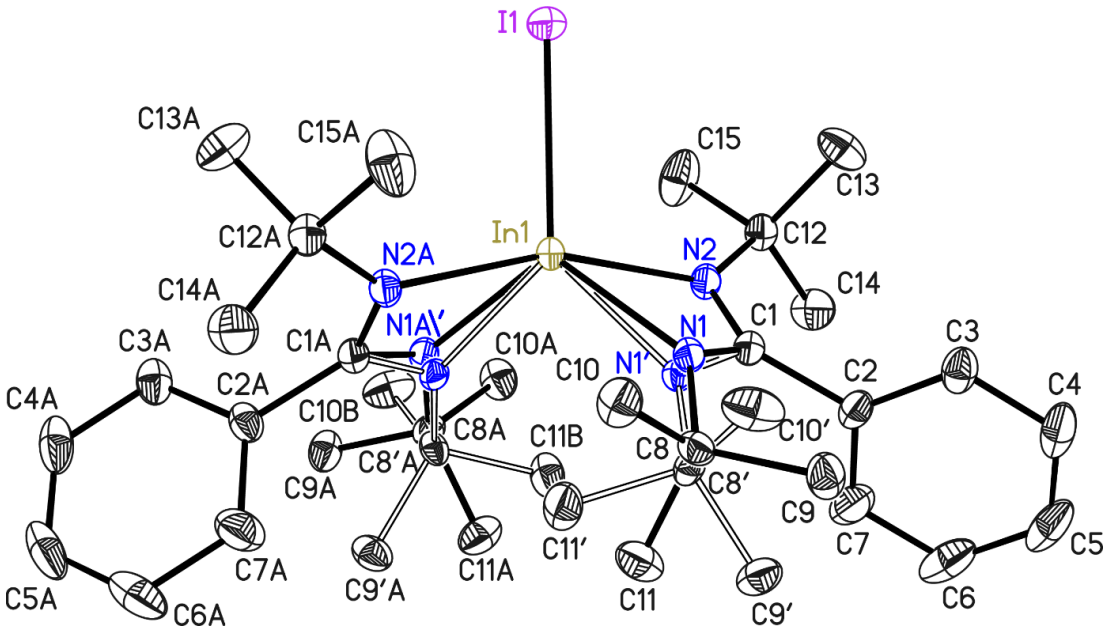

Figure 6-33: Molecular structure of NG_SB_In_I. The asymmetric unit contains only half of the molecule. The anisotropic displacement parameters are depicted at the 50% probability level. The hydrogen atoms are omitted for clarity.

Parts of the molecule (N1, C8-C11) were disordered over two positions. The occupancy of the minor position refined to 0.268(3). All disordered parts were refined with distance restraints and restraints for the anisotropic displacement parameters.

Structure code	NG_SB_In_I	**CCDC Number**	2027413
Empirical Formula	$C_{35}H_{46}IInN_4$	**Crystal colour and shape**	colourless blocks
Formula weight [g·mol^{-1}]	704.43	Z	4
Sample temperature [K]	100(2)	μ [mm^{-1}]	1.733
Wavelength [Å]	0.71073	F(000)	1424
Crystal System	Monoclinic	Θ **range [°]**	2.032 to 28.334
Space group	C2/c	**Reflections collected**	54423
Unit cell dimensions [Å]	a = 20.114(3)	**Unique Reflections**	3971
	b = 9.710(2)	R_{int}	0.0240
	c = 16.382(2)	**Restraints / Parameters**	318 / 219
	β = 94.76(2)	$R1$ ($I>2\sigma(I)$)	0.0146
Volume [Å^3]	3188.5(9)	w$R2$ **(all data)**	0.0369
Crystal size [mm]	0.347 x 0.228 x 0.170	**max. diff. peak / hole [eÅ^{-3}]**	0.751 and −0.766

6.15.3.5 Crystal structure of NG_SB_InBr_Molly: $C_{46}H_{58}Br_2In_2N_4$

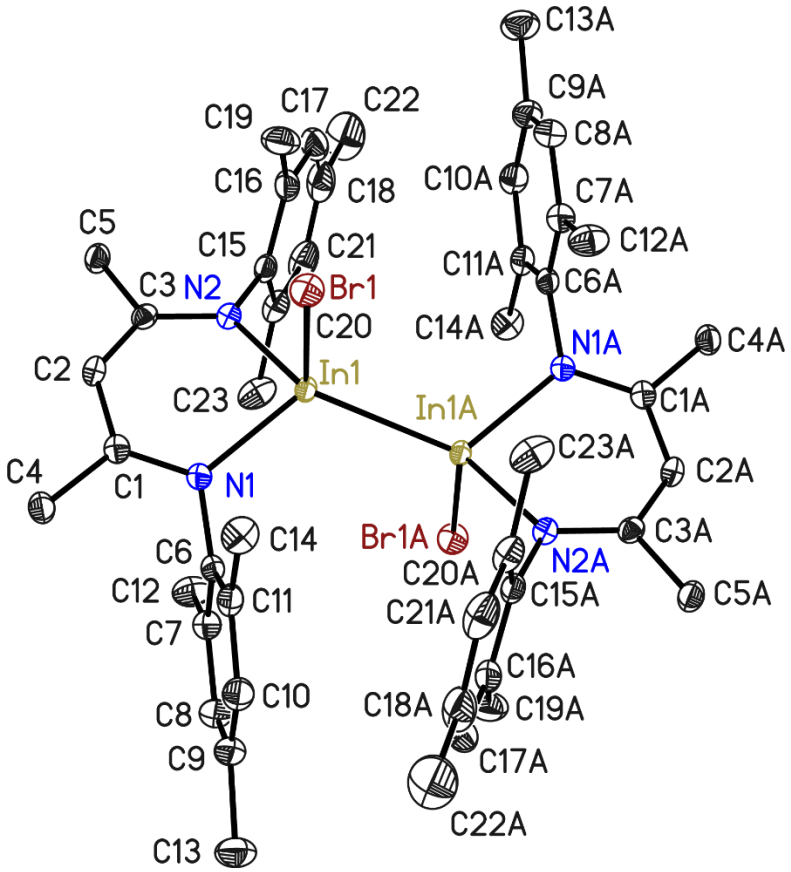

Figure 6-34: Molecular structure of NG_SB_InBr_Molly. The asymmetric unit contains only half of the molecule. The anisotropic displacement parameters are depicted at the 50% probability level. The hydrogen atoms are omitted for clarity.

Structure code	NG_SB_InBr_Molly	**CCDC Number**	2027414
Empirical Formula	$C_{46}H_{58}Br_2In_2N_4$	**Crystal colour and shape**	colourless blocks
Formula weight [g·mol^{-1}]	1056.42	Z	2
Sample temperature [K]	100(2)	μ [mm^{-1}]	2.841
Wavelength [Å]	0.71073	F(000)	1060
Crystal System	Monoclinic	Θ **range [°]**	2.221 to 27.502
Space group	$P2_1/c$	**Reflections collected**	24146
Unit cell dimensions [Å]	a = 12.090(2)	**Unique Reflections**	5144
	b = 10.962(2)	R_{int}	0.0243
	c = 17.663(2)	**Restraints / Parameters**	0 / 252
	β = 104.50(2)	$R1$ ($I>2\sigma(I)$)	0.0173
Volume [Å^3]	2245.7(7)	w$R2$ (all data)	0.0454
Crystal size [mm]	0.576 x 0.303 x 0.246	**max. diff. peak / hole [eÅ^{-3}]**	0.448 and −0.280

6.15.3.6 Crystal structure of NG_SB_AlB: $C_{15}H_{23}AlCl_2N_2$

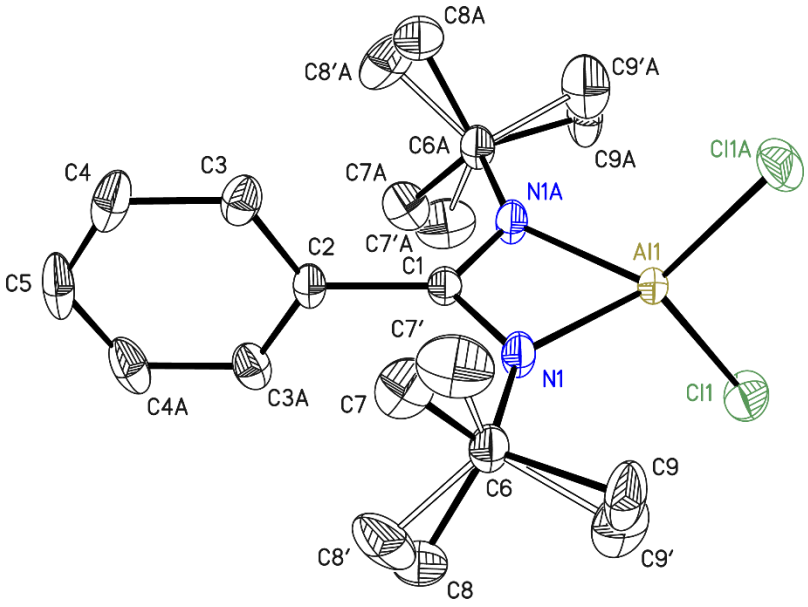

Figure 6-35: Molecular structure of NG_SB_AlB. The asymmetric unit contains only half of the molecule. The anisotropic displacement parameters are depicted at the 50% probability level. Hydrogen atoms are omitted for clarity.

The ^{t}Bu group (C7-C9) was disordered over two positions. It was refined with distance restraints and restraints for the anisotropic displacement parameters. The occupancy of the minor component refined to 0.265(14).

Structure code	NG_SB_AlB	**CCDC Number**	2063440
Empirical Formula	$C_{15}H_{23}AlCl_2N_2$	**Crystal colour and shape**	colourless blocks
Formula weight [g·mol^{-1}]	329.23	Z	4
Sample temperature [K]	100(2)	μ [mm^{-1}]	0.401
Wavelength [Å]	0.71073	F(000)	696
Crystal System	Monoclinic	Θ range [°]	2.415 to 27.546
Space group	C2/c	**Reflections collected**	42384
Unit cell dimensions [Å]	a = 14.536(3)	**Unique Reflections**	2074
	b = 11.272(2)	R_{int}	0.0310
	c = 12.613(2)	**Restraints / Parameters**	135 / 127
	β = 119.07(2)	$R1$ ($I>2\sigma(I)$)	0.0261
Volume [Å^3]	1806.3(6)	w$R2$ (all data)	0.0720
Crystal size [mm]	0.283 x 0.246 x 0.183	**max. diff. peak / hole [eÅ^{-3}]**	0.338 and −0.210

6.15.3.7 Crystal structure of NG_SB_AlEtCl: $C_{17}H_{28}AlClN_2$

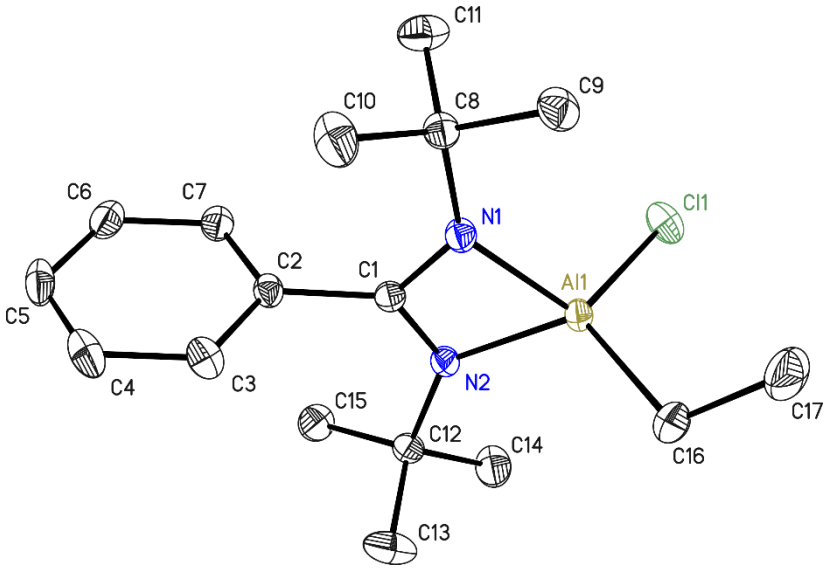

Figure 6-36: Asymmetric unit of NG_SB_AlEtCl. The anisotropic displacement parameters are depicted at the 50% probability level. Hydrogen atoms are omitted for clarity.

Structure code	NG_SB_AlEtCl	**CCDC Number**	2063442
Empirical Formula	$C_{17}H_{28}AlClN_2$	**Crystal colour and shape**	colourless blocks
Formula weight [g·mol^{-1}]	322.84	Z	8
Sample temperature [K]	100(2)	μ [mm^{-1}]	0.245
Wavelength [Å]	0.71073	F(000)	1392
Crystal System	Orthorhombic	Θ **range [°]**	1.751 to 27.540
Space group	*Pbca*	**Reflections collected**	105377
Unit cell dimensions [Å]	a = 8.855(2)	**Unique Reflections**	4348
	b = 18.353(2)	R_{int}	0.0420
	c = 23.262(3)	**Restraints / Parameters**	0 / 197
Volume [Å^3]	3780.4(11)	$R1$ ($I>2\sigma(I)$)	0.0310
Crystal size [mm]	0.321 x 0.293 x 0.201	w$R2$ **(all data)**	0.0868
		max. diff. peak / hole [eÅ^{-3}]	0.364 and −0.237

6.15.3.8 Crystal structure of NG_SB_AlClF: $C_{34}H_{56}Al_2F_2N_4$

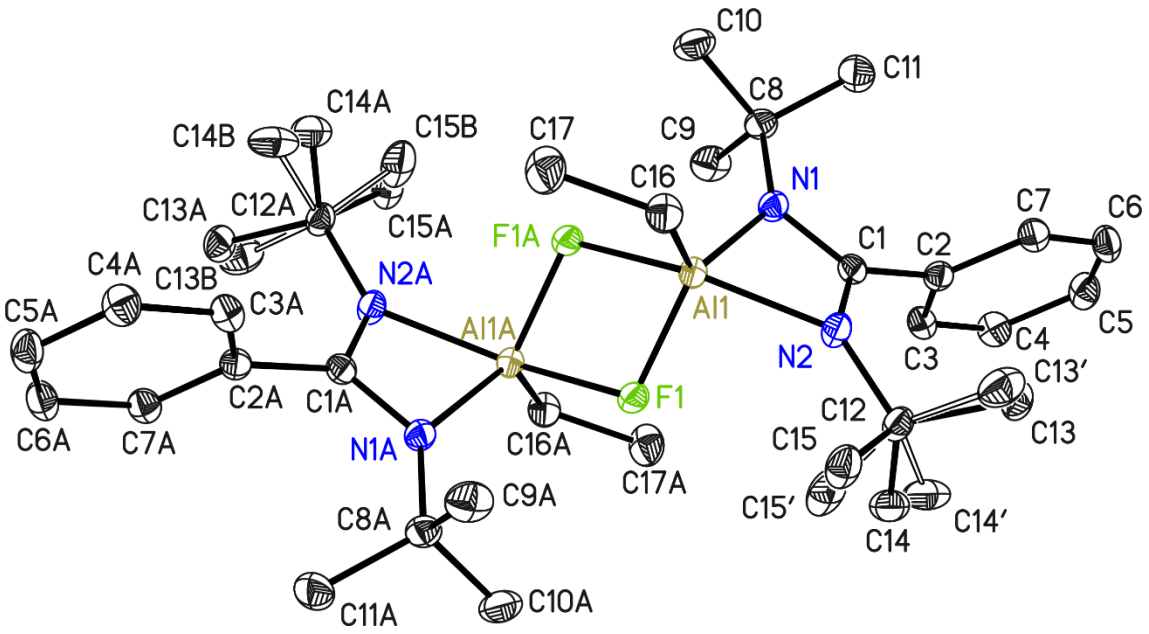

Figure 6-37: Molecular structure of NG_SB_AlClF. The asymmetric unit contains only half of the molecule. The anisotropic displacement parameters are depicted at the 50% probability level. Hydrogen atoms are omitted for clarity.

One ^{t}Bu group was disordered over two positions. The disorder was refined with distance restraints and restraints for the anisotropic displacement parameters. The occupancy of the minor component refined to 0.348(13).

Structure code	NG_SB_AlClF	**CCDC Number**	2063443
Empirical Formula	$C_{34}H_{56}Al_2F_2N_4$	**Crystal colour and shape**	colourless blocks
Formula weight [g·mol^{-1}]	612.78	Z	1
Sample temperature [K]	100(2)	μ [mm^{-1}]	0.122
Wavelength [Å]	0.71073	F(000)	332
Crystal System	Triclinic	Θ **range [°]**	1.919 to 26.447
Space group	$P\bar{1}$	**Reflections collected**	27907
Unit cell dimensions [Å]	a = 8.606(2)	**Unique Reflections**	3575
	b = 10.033(2)	R_{int}	0.0287
	c = 10.782(3)	**Restraints / Parameters**	99 / 228
	α = 97.12(2)	$R1$ ($I>2\sigma(I)$)	0.0304
	β = 94.75(2)	w$R2$ (all data)	0.0825
	γ = 107.96(4)	**max. diff. peak / hole [eÅ^{-3}]**	0.304 and −0.201
Volume [Å^3]	871.5(4)		
Crystal size [mm]	0.385 x 0.226 x 0.194		

6.15.3.9 Crystal structure of NG_SB_AlClEt: $C_{34}H_{56}Al_2Cl_2N_4O_2$

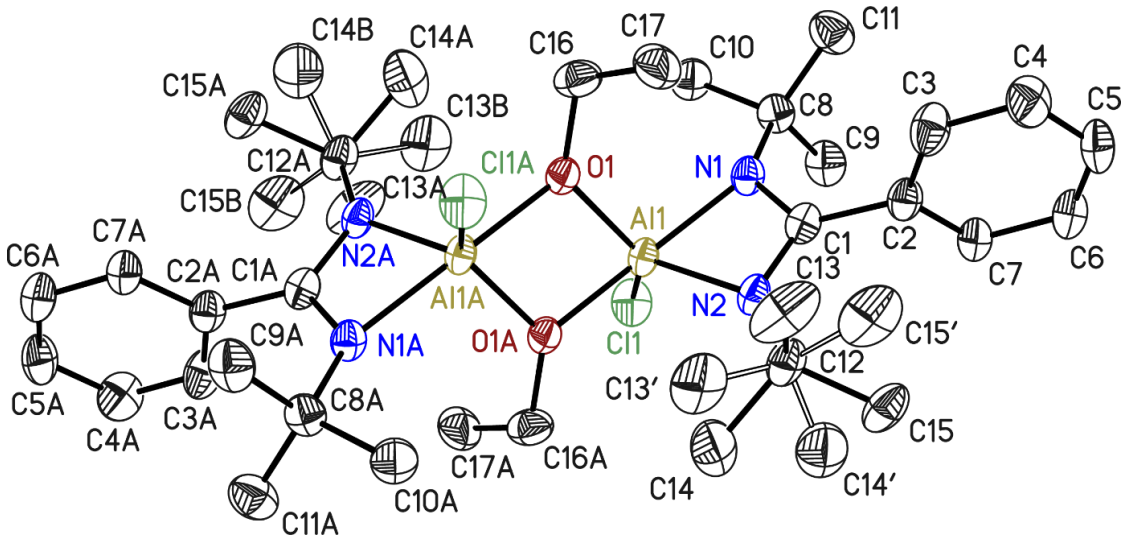

Figure 6-38: Molecular structure of NG_SB_AlClEt. The asymmetric unit contains only half of the molecule. The anisotropic displacement parameters are depicted at the 50% probability level. Hydrogen atoms are omitted for clarity.

The data were collected on a non-merohedral twin. The twin law was 1 0 0.2 0 −1 0 0 0 −1. The fractional contribution of the minor twin domain refined to 0.4745(16). One ^{t}Bu group was disordered over two positions. The disorder was refined with distance restraints and restraints for the anisotropic displacement parameters. The occupancy of the minor component refined to 0.168(6).

Structure code	NG_SB_AlClEt	**CCDC Number**	2063444
Empirical Formula	$C_{34}H_{56}Al_2Cl_2N_4O_2$	**Crystal colour and shape**	colourless needles
Formula weight [g·mol^{-1}]	677.68	Z	2
Sample temperature [K]	100(2)	μ [mm^{-1}]	0.259
Wavelength [Å]	0.71073	F(000)	728
Crystal System	Monoclinic	Θ **range [°]**	1.880 to 25.721
Space group	$P2_1/c$	**Reflections collected**	29431
Unit cell dimensions [Å]	a = 10.996(2)	**Unique Reflections**	3501
	b = 9.237(3)	R_{int}	0.0889
	c = 18.370(2)	**Restraints / Parameters**	117 / 232
	β = 99.85(2)	$R1$ ($I>2\sigma(I)$)	0.0536
Volume [Å^3]	1838.3(6)	w$R2$ **(all data)**	0.1272
Crystal size [mm]	0.200 x 0.129 x 0.068	**max. diff. peak / hole [eÅ^{-3}]**	0.518 and −0.324

6.15.3.10 Crystal structure of NG_SB_AlEt: $2(C_{37}H_{59}AlN_3) \cdot (C_7H_8)$

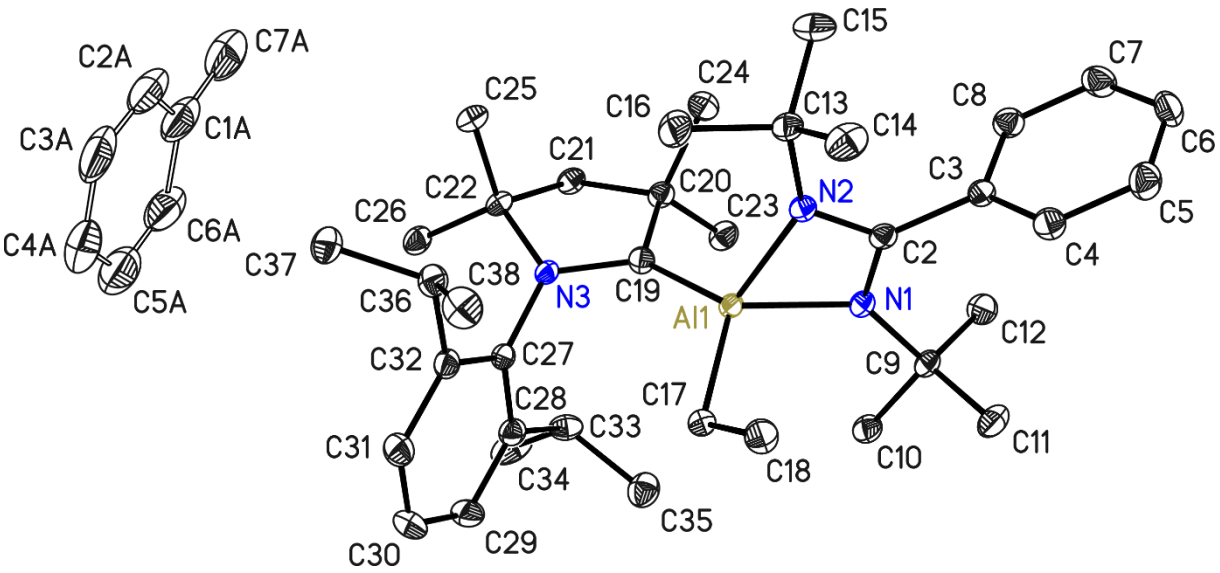

Figure 6-39: Asymmetric unit of NG_SB_AlEt. The anisotropic displacement parameters are depicted at the 50% probability level. Hydrogen atoms are omitted for clarity.

The toluene molecule was disordered about an inversion centre and was refined with distance restraints and restraints for the anisotropic displacement parameters.

Structure code	NG_SB_AlEt	**CCDC Number**	2063445
Empirical Formula	$2(C_{37}H_{59}AlN_3) \cdot (C_7H_8)$	**Crystal colour and shape**	red blocks
Formula weight [g·mol^{-1}]	1237.83	Z	2
Sample temperature [K]	100(2)	μ [mm^{-1}]	0.083
Wavelength [Å]	0.71073	F(000)	1360
Crystal System	Monoclinic	Θ **range [°]**	1.230 to 26.418
Space group	$P2_1/n$	**Reflections collected**	158850
Unit cell dimensions [Å]	a = 10.653(2)	**Unique Reflections**	7809
	b = 10.796(3)	R_{int}	0.0353
	c = 33.282(3)	**Restraints / Parameters**	118 / 449
	β = 95.72(2)	$R1$ ($I>2\sigma(I)$)	0.0352
Volume [Å^3]	3808.7(11)	w$R2$ **(all data)**	0.0916
Crystal size [mm]	0.467 x 0.332 x 0.252	**max. diff. peak / hole [eÅ^{-3}]**	0.375 and −0.258

6.15.3.11 Crystal structure of NG_SB_Sb_amidinate: $C_{124}H_{194}F_2Li_{10}N_{16}O$

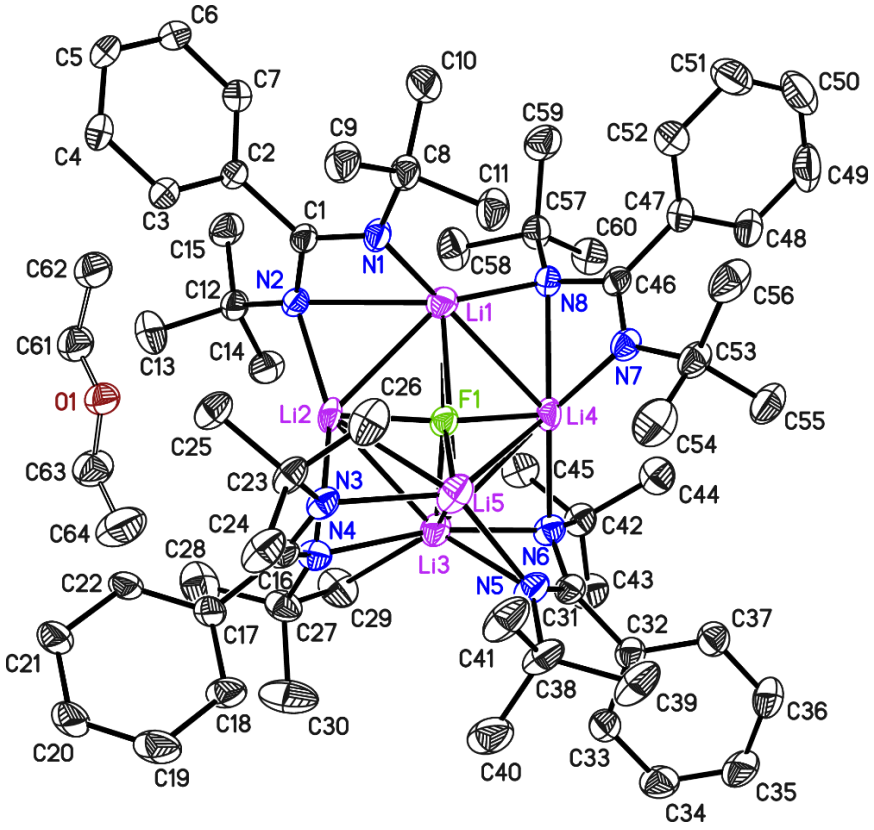

Figure 6-40: Asymmetric unit of NG_SB_Sb_amidinate. The anisotropic displacement parameters are depicted at the 50% probability level. Hydrogen atoms are omitted for clarity.

The diethyl ether molecule was disordered about an inversion centre and was refined with restraints for the anisotropic displacement parameters.

Structure code	NG_SB_Sb_amidinate	**CCDC Number**	2126126
Empirical Formula	$C_{124}H_{194}F_2Li_{10}N_{16}O$	**Crystal colour and shape**	colourless blocks
Formula weight [g·mol^{-1}]	2032.34	Z	1
Sample temperature [K]	100(2)	μ [mm^{-1}]	0.065
Wavelength [Å]	0.71073	F(000)	1106
Crystal System	Triclinic	Θ **range [°]**	1.161 to 25.052
Space group	$P\bar{1}$	**Reflections collected**	66895
Unit cell dimensions [Å]	a = 13.054(2)	**Unique Reflections**	10930
	b = 13.488(2)	R_{int}	0.0523
	c = 18.966(3)	**Restraints / Parameters**	442 / 793
	a = 76.79(2)	$R1$ ($I>2\sigma(I)$)	0.0464
	β = 72.12(2)	w$R2$ (all data)	0.1179
	γ = 89.23(4)	**max. diff. peak / hole [eÅ^{-3}]**	0.485 and −0.176
Volume [Å^3]	3088.2(9)		
Crystal size [mm]	0.339 x 0.138 x 0.119		

6.15.3.12 Crystal structure of NG_SB_Ga_cat: $C_{15}H_{23}Cl_2GaN_2$

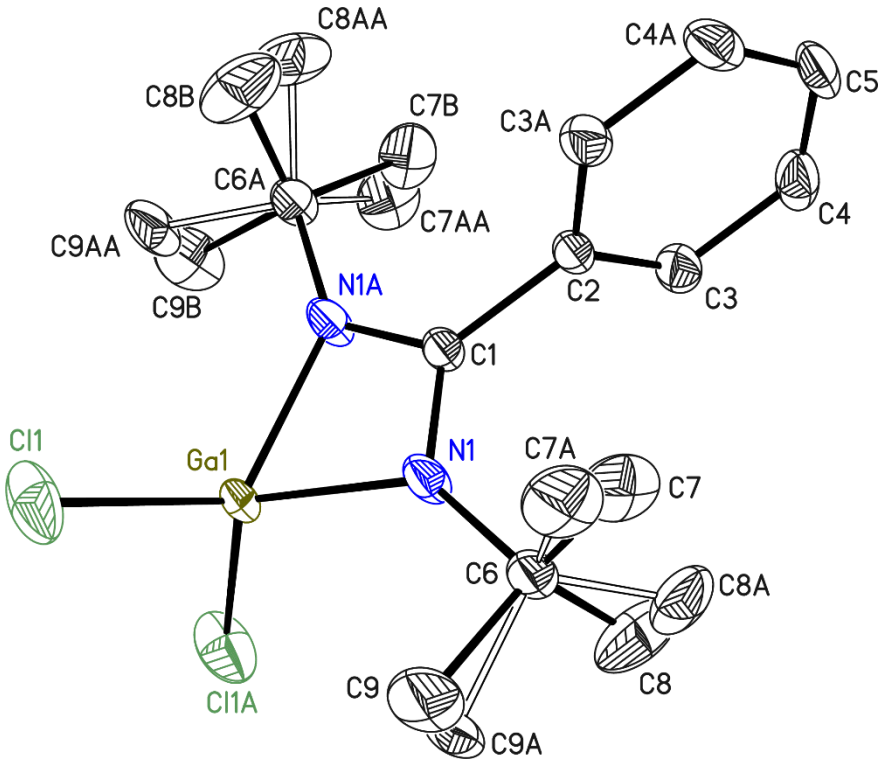

Figure 6-41: Asymmetric unit of NG_SB_Ga_cat. The anisotropic displacement parameters are depicted at the 50% probability level. Hydrogen atoms are omitted for clarity.

The data were collected on a merohedral twin. The twin law is a two fold rotation along (1 0 −1). The fractional contribution of the minor twin domain refined to 0.1416(16). The ᵗBu group (C7-C9) was disordered over two positions. It was refined with distance restraints and restraints for the anisotropic displacement parameters. The occupancy of the minor component refined to 0.429(18).

Structure code	NG_SB_Ga_cat	**CCDC Number**	2144444
Empirical Formula	$C_{15}H_{23}Cl_2GaN_2$	**Crystal colour and shape**	colourless plates
Formula weight [g·mol^{-1}]	371.97	Z	4
Sample temperature [K]	100(2)	μ [mm^{-1}]	1.804
Wavelength [Å]	0.71073	F(000)	768
Crystal System	Monoclinic	Θ **range [°]**	2.407 to 26.408
Space group	$C2/c$	**Reflections collected**	15526
Unit cell dimensions [Å]	a = 14.553(3)	**Unique Reflections**	1871
	b = 11.340(2)	R_{int}	0.0267
	c = 12.589(2)	**Restraints / Parameters**	135 / 128
	β = 119.16(2)	$R1$ ($I>2\sigma(I)$)	0.0208
Volume [Å^3]	1814.3(6)	w$R2$ **(all data)**	0.0538
Crystal size [mm]	0.462 x 0.306 x 0.060	**max. diff. peak / hole [eÅ^{-3}]**	0.390 and −0.345

6.15.3.13 Crystal structure of NG_SB_Ga_cat3: $C_{15}H_{25}Cl_4GaN_2$

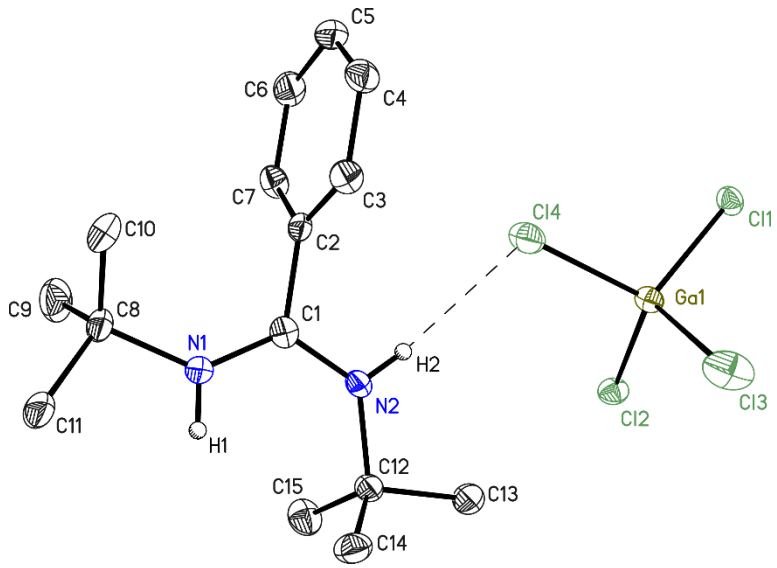

Figure 6-42: Asymmetric unit of NG_SB_Ga_cat3. The anisotropic displacement parameters are depicted at the 50% probability level. Hydrogen atoms except for H1 and H2 are omitted for clarity.

Hydrogen atoms H1 and H2 were refined freely.

Structure code	NG_SB_Ga_cat3	**CCDC Number**	2144445
Empirical Formula	$C_{15}H_{25}Cl_4GaN_2$	**Crystal colour and shape**	colourless blocks
Formula weight [g·mol^{-1}]	444.89	Z	4
Sample temperature [K]	100(2)	μ [mm^{-1}]	1.799
Wavelength [Å]	0.71073	F(000)	912
Crystal System	Orthorhombic	Θ **range [°]**	1.814 to 26.355
Space group	$P2_12_12_1$	**Reflections collected**	17672
Unit cell dimensions [Å]	a = 8.412(2)	**Unique Reflections**	4334
	b = 15.856(3)	R_{int}	0.0223
	c = 15.903(3)	**Restraints / Parameters**	1 / 213
Volume [Å^3]	2121.2(8)	$R1$ ($I>2\sigma(I)$)	0.0175
Crystal size [mm]	0.387 x 0.245 x 0.238	w$R2$ **(all data)**	0.0430
Absolute structure parameter[415]	0.007(3)	**max. diff. peak / hole [eÅ^{-3}]**	0.482 and −0.322

6.15.3.14 Crystal structure of NG_SB_Ga2: $C_{30}H_{46}Cl_2Ga_2N_4$

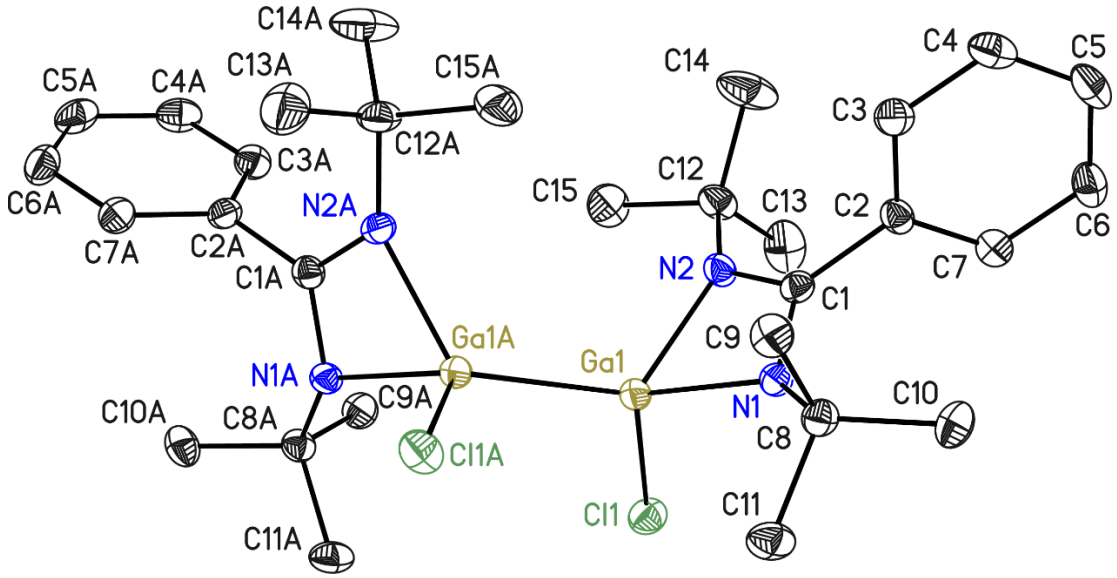

Figure 6-43: Asymmetric unit of NG_SB_SiF_2. The anisotropic displacement parameters are depicted at the 50% probability level. Hydrogen atoms are omitted for clarity.

Data were collected on a split crystal with three components. The final refinement was done on untwinned merged data from all domains.

Structure code	NG_SB_Ga2	**CCDC Number**	2144446
Empirical Formula	$C_{30}H_{46}Cl_2Ga_2N_4$	**Crystal colour and shape**	colourless blocks
Formula weight [g·mol^{-1}]	673.05	Z	4
Sample temperature [K]	100(2)	μ [mm^{-1}]	1.821
Wavelength [Å]	0.71073	F(000)	1400
Crystal System	Monoclinic	Θ **range [°]**	1.938 to 26.475
Space group	C2/c	**Reflections collected**	146235
Unit cell dimensions [Å]	a = 23.069(3)	**Unique Reflections**	3406
	b = 8.896(2)	R_{int}	0.0776
	c = 17.634(2)	**Restraints / Parameters**	0 / 178
	β = 114.36(2)	$R1$ ($I>2\sigma(I)$)	0.0337
Volume [Å^3]	3296.7(10)	w$R2$ **(all data)**	0.0797
Crystal size [mm]	0.376 x 0.171 x 0.163	**max. diff. peak / hole [eÅ^{-3}]**	0.505 and −0.350

6.15.3.15 Crystal structure of NG_SB_SiF$_2$: $C_{26}H_{36}F_3NSi$

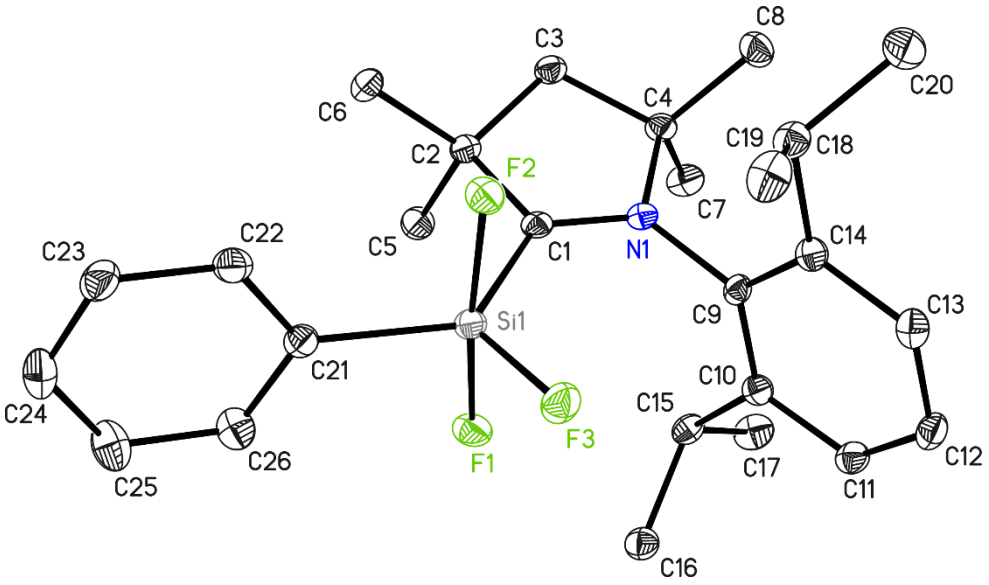

Figure 6-44: Asymmetric unit of NG_SB_Ga2. The anisotropic displacement parameters are depicted at the 50% probability level. Hydrogen atoms are omitted for clarity.

Structure code	NG_SB_SiF$_2$	**CCDC Number**	2149531
Empirical Formula	$C_{26}H_{36}F_3NSi$	**Crystal colour and shape**	colourless blocks
Formula weight [g·mol^{-1}]	447.65	Z	2
Sample temperature [K]	100(2)	μ [mm^{-1}]	0.136
Wavelength [Å]	0.71073	F(000)	480
Crystal System	Triclinic	Θ **range [°]**	1746 to 27.488
Space group	$P\bar{1}$	**Reflections collected**	26187
Unit cell dimensions [Å]	a = 9.028(2)	**Unique Reflections**	5400
	b = 11.223(2)	R_{int}	0.0302
	c = 12.911(3)	**Restraints / Parameters**	0 / 288
	α = 104.88(2)	$R1$ ($I>2\sigma(I)$)	0.0337
	β = 109.46(2)	w$R2$ **(all data)**	0.0887
	γ = 92.20(2)	**max. diff. peak / hole [eÅ^{-3}]**	0.467 and −0.290
Volume [Å^3]	1181.0(5)		
Crystal size [mm]	0.355 x 0.145 x 0.108		

6.15.4 Service Dr. Arun Kumar

6.15.4.1 Crystal structure of NG_AK_AlI2: $C_{14}H_{17}AlN_2Cl_{1.78}I_{0.22}$

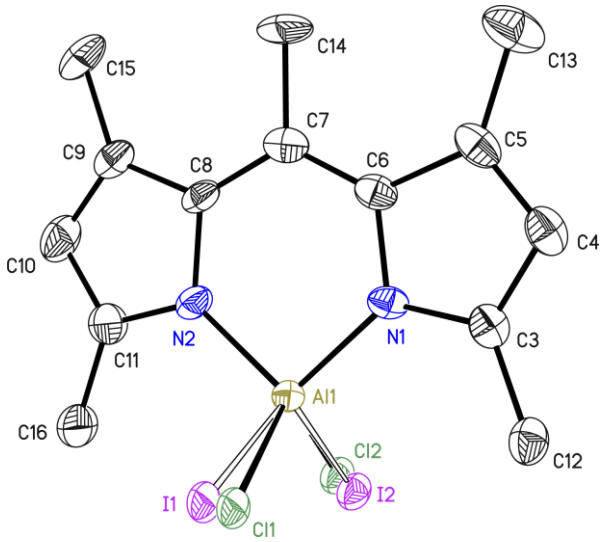

Figure 6-45: Asymmetric unit of NG_AK_AlI2. The anisotropic displacement parameters are depicted at the 50% probability level. Hydrogen atoms are omitted for clarity.

The data were collected on a non-merohedral twin. The twin law was −1 0 0 0 −1 0 0 0 1. The fractional contribution of the minor twin domain refined to 0.335(3). Both halides suffered from substitutional disorder. The disorder was refined with restraints for the anisotropic displacement parameters. The occupancy of the minor components refined to 0.138(2) (I1) and to 0.077(2) (I2).

Structure code	NG_AK_AlI2	**CCDC Number**	–
Empirical Formula	$C_{14}H_{17}AlN_2Cl_{1.78}I_{0.22}$	**Crystal colour and shape**	orange blocks
Formula weight [g·mol^{-1}]	330.84	Z	4
Sample temperature [K]	100(2)	μ [mm^{-1}]	0.855
Wavelength [Å]	0.71073	F(000)	679
Crystal System	Monoclinic	Θ **range [°]**	1.078 to 25.557
Space group	$P2_1/n$	**Reflections collected**	33762
Unit cell dimensions [Å]	a = 7.270(2)	**Unique Reflections**	2893
	b = 11.286(3)	R_{int}	0.0419
	c = 18.894(2)	**Restraints / Parameters**	14 / 186
	β = 90.09(2)	$R1$ ($I>2\sigma(I)$)	0.0488
Volume [Å^3]	1550.2(6)	w$R2$ **(all data)**	0.0996
Crystal size [mm]	0.240 x 0.122 x 0.122	**max. diff. peak / hole [eÅ^{-3}]**	0.318 and −0.376

6.15.4.2 Crystal structure of NG_AK_DippAl: $C_{31}H_{39}AlN_2I_2$

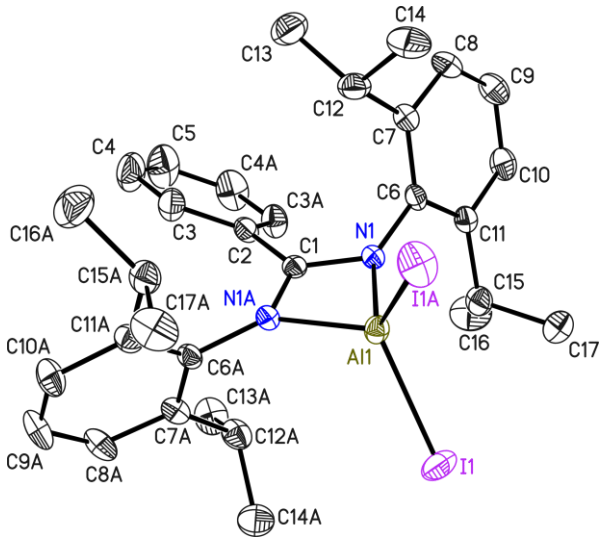

Figure 6-46: Asymmetric unit of NG_AK_DippAl. The anisotropic displacement parameters are depicted at the 50% probability level. Hydrogen atoms are omitted for clarity.

Structure code	NG_AK_DippAl	**CCDC Number**	2144443
Empirical Formula	$C_{31}H_{39}AlN_2I_2$	**Crystal colour and shape**	colourless blocks
Formula weight [g·mol^{-1}]	720.42	Z	3
Sample temperature [K]	100(2)	μ [mm^{-1}]	0.1.963
Wavelength [Å]	0.71073	F(000)	1074
Crystal System	Trigonal	Θ **range [°]**	1.539 to 26.425
Space group	$P3_121$	**Reflections collected**	29077
Unit cell dimensions [Å]	a = 15.276(3)	**Unique Reflections**	3387
	c = 112.183(2)	R_{int}	0.0273
		Restraints / Parameters	0 / 169
		$R1$ ($I>2\sigma(I)$)	0.0157
Volume [Å^3]	2462.1(10)	w$R2$ (all data)	0.0369
Crystal size [mm]	0.251 x 0.213 x 0.190	**max. diff. peak / hole [eÅ^{-3}]**	0.389 and −0.220

6.15.4.3 Crystal structure of NG_AK_Al2: $C_{69}H_{86}Al_2N_4I_2 \cdot C_7H_8$

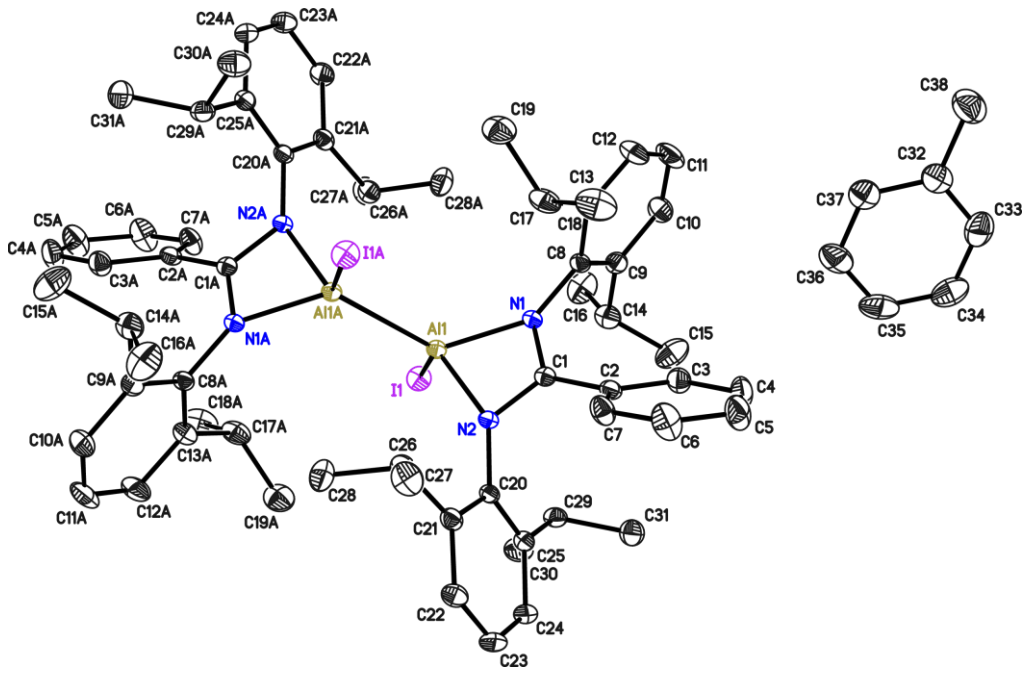

Figure 6-47: Asymmetric unit of NG_AK_Al2. The anisotropic displacement parameters are depicted at the 50% probability level. Hydrogen atoms are omitted for clarity.

Structure code	NG_AK_Al2	**CCDC Number**	2144447
Empirical Formula	$C_{69}H_{86}Al_2N_4I_2 \cdot C_7H_8$	**Crystal colour and shape**	colourless blocks
Formula weight [g·mol^{-1}]	1371.31	Z	2
Sample temperature [K]	100(2)	μ [mm^{-1}]	0.964
Wavelength [Å]	0.71073	F(000)	1420
Crystal System	Monoclinic	Θ **range [°]**	1.376 to 26.377
Space group	$P2_1/c$	**Reflections collected**	46646
Unit cell dimensions [Å]	a = 14.823(2)	**Unique Reflections**	7180
	b = 10.705(2)	R_{int}	0.0248
	c = 22.172(3)	**Restraints / Parameters**	0 / 388
	β = 93.55(2)	$R1$ ($I>2\sigma(I)$)	0.0225
Volume [Å^3]	3511.5(9)	w$R2$ (all data)	0.0598
Crystal size [mm]	0.721 x 0.714 x 0.216	**max. diff. peak / hole [eÅ^{-3}]**	0.756 and −0.383

6.15.4.4 Crystal structure of NG_AK_DipAl2: $C_{69}H_{86}Al_2N_4 \cdot C_6H_{14}$

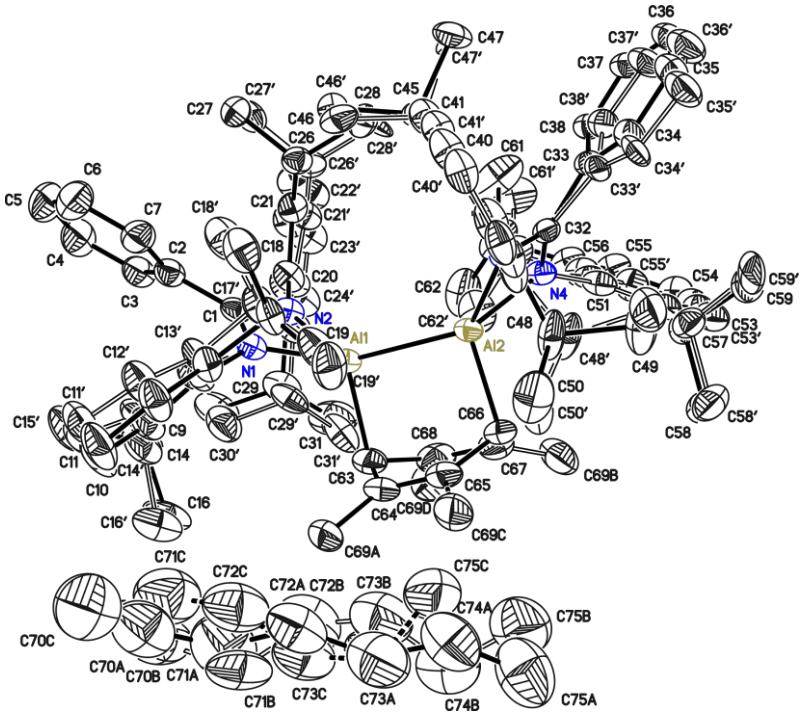

Figure 6-48: Asymmetric unit of NG_AK_DipAl2. The anisotropic displacement parameters are depicted at the 50% probability level. Hydrogen atoms are omitted for clarity.

The hexane molecule was disordered over three positions. The disorder was refined with distance restraints and restraints for the anisotropic displacement parameters. The occupancies refined to 0.702(3) (C70A-C75A), 0.174(3) (C70B-C75B) and 0.129(2) (C70C-C75C). Major parts of the ligand were disordered over two positions. The disorder was refined with restraints for the anisotropic displacement parameters. The occupancy of the minor components refined to 0.248(9) (C20'-C31', C51'-C62'), 0.281(12) (C39'-C50'), 0.204(11) (C33'-C38') and 0.285(17) (C8'-C19').

Structure code	NG_AK_DipAl2	**CCDC Number**	–
Empirical Formula	$C_{69}H_{86}Al_2N_4 \cdot C_6H_{14}$	**Crystal colour and shape**	red blocks
Formula weight [g·mol^{-1}]	1111.54	Z	8
Sample temperature [K]	100(2)	μ [mm^{-1}]	0.085
Wavelength [Å]	0.71073	F(000)	4832
Crystal System	Monoclinic	Θ **range [°]**	0.813 to 25.073
Space group	$C2/c$	**Reflections collected**	352358
Unit cell dimensions [Å]	a = 51.318(8)	**Unique Reflections**	12110
	b = 16.903(3)	R_{int}	0.0503
	c = 16.156(3)	**Restraints / Parameters**	5266 / 1371
	β = 102.58(2)	$R1$ ($I>2\sigma(I)$)	0.0418
Volume [Å^3]	13678(4)	w$R2$ **(all data)**	0.1195
Crystal size [mm]	0.333 x 0.278 x 0.168	**max. diff. peak / hole [eÅ^{-3}]**	0.343 and −0.267

6.15.5 Service Dr. Mohd Nazish

6.15.5.1 Crystal structure of NG_NS_040: $C_{32}H_{52}BIN_3Si$

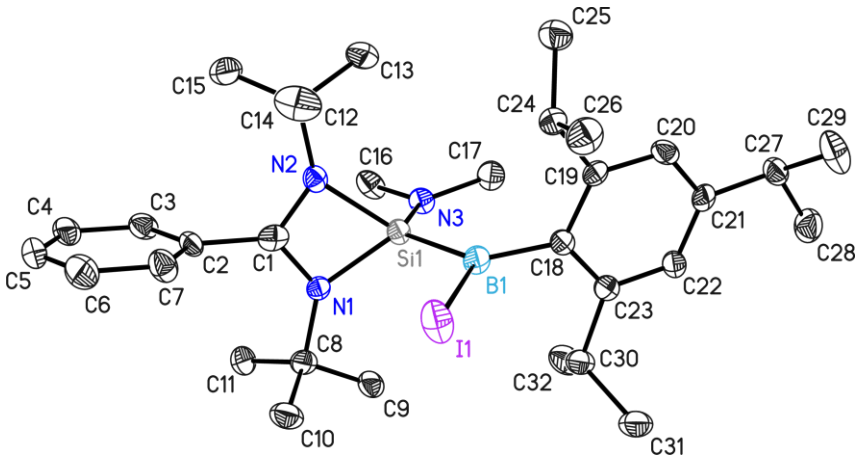

Figure 6-49: Asymmetric unit of NG_NS_040. The anisotropic displacement parameters are depicted at the 50% probability level. Hydrogen atoms are omitted for clarity.

The data were collected on a non-merohedral twin. The twin law was −1 0 0 0 −1 0 0 0 1. The fractional contribution of the minor twin domain refined to 0.2999(17).

Structure code	NG_NS_040	**CCDC Number**	2113991
Empirical Formula	$C_{32}H_{52}BIN_3Si$	**Crystal colour and shape**	orange plates
Formula weight [g·mol^{-1}]	644.56	Z	4
Sample temperature [K]	100(2)	μ [mm^{-1}]	1.003
Wavelength [Å]	0.71073	F(000)	1348
Crystal System	Monoclinic	Θ **range [°]**	1.095 to 25.171
Space group	$P2_1/n$	**Reflections collected**	126965
Unit cell dimensions [Å]	a = 12.626(2)	**Unique Reflections**	6038
	b = 18.594(3)	R_{int}	0.0597
	c = 14.454(2)	**Restraints / Parameters**	0 / 358
	β = 90.75(2)	$R1$ ($I>2\sigma(I)$)	0.0447
Volume [Å^3]	3393.0(9)	w$R2$ **(all data)**	0.0938
Crystal size [mm]	0.426 x 0.224 x 0.122	**max. diff. peak / hole [eÅ^{-3}]**	0.656 and −1.317

6.15.5.2 Crystal structure of NG_NS_0130: $C_{204}H_{287}N_8Sb_4Si_4 \cdot 6\ (C_4H_{10}O)$

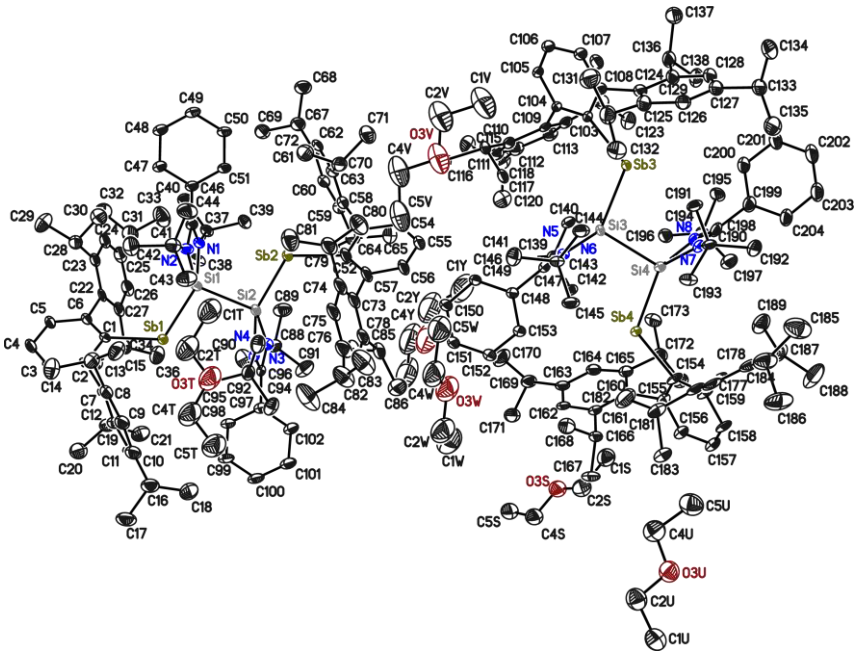

Figure 6-50: Asymmetric unit of NG_NS_0130. The anisotropic displacement parameters are depicted at the 50% probability level. Hydrogen atoms are omitted for clarity.

The structure was refined as pseudo-merohedral and inversion twin. The fractional contributions refined to 0.30(2) (twin law 1 0 0 0 1 0 0 0 −1), 0.18(2) (twin law −1 0 0 0 −1 0 0 0 −1), and 0.19(2) (twin law −1 0 0 0 −1 0 0 0 1). The data additionally show signs of modulation. Therefore, the level of residual density is relatively high. The structure was refined with distance restraints to restrain equivalent bonds and angles in the two independent molecules and also with restraints for the anisotropic displacement parameters.

Structure code	NG_NS_0130	**CCDC Number**	2172971
Empirical Formula	$C_{204}H_{287}N_8Sb_4Si_4 \cdot 6\ (C_4H_{10}O)$	**Crystal colour and shape**	violet blocks
Formula weight [g·mol^{-1}]	3895.48	Z	2
Sample temperature [K]	100(2)	μ [mm^{-1}]	0.570
Wavelength [Å]	0.71073	F(000)	4158
Crystal System	Monoclinic	Θ **range [°]**	0.771 to 25.649
Space group	$P2_1$	**Reflections collected**	105488
Unit cell dimensions [Å]	a = 17.396(2)	**Unique Reflections**	39942
	b = 23.625 (3)	R_{int}	0.0694
	c = 26.403(3)	**Restraints / Parameters**	7311 / 2254
	β = 90.02(2)	$R1$ ($I>2\sigma(I)$)	0.0728
Volume [Å^3]	10851(2)	w$R2$ (all data)	0.1902
Crystal size [mm]	0.323 x 0.278 x 0.263	**max. diff. peak / hole [eÅ^{-3}]**	4.096 and −1.657

6.15.5.3 Crystal structure of NG_NS_262: $C_{34}H_{56}N_5SiCl_{0.87}Br_{0.13}$

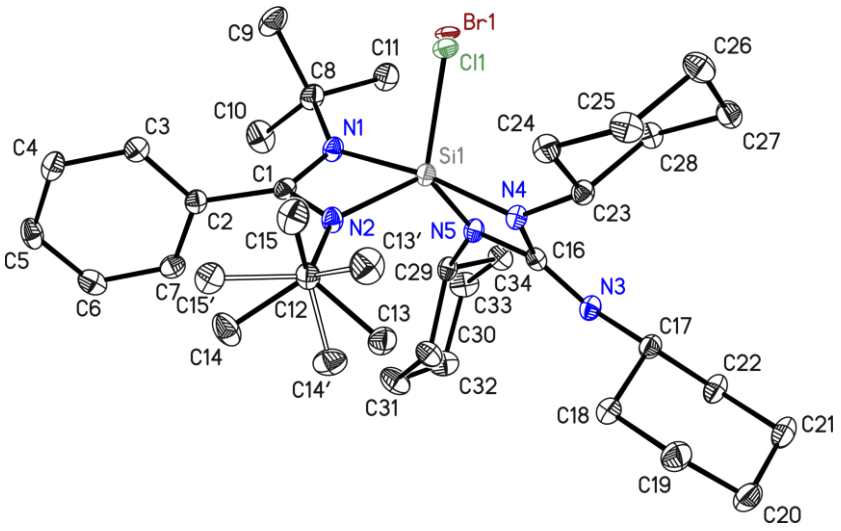

Figure 6-51: Asymmetric unit of NG_NS_262. The anisotropic displacement parameters are depicted at the 50% probability level. Hydrogen atoms are omitted for clarity.

One ^{t}Bu group (C13-C15) was disordered over two positions. It was refined with distance restraints and restraints for the anisotropic displacement parameters. The occupancy of the minor component refined to 0.0349(19). The halide suffered from substitutional disorder. The occupancy of the minor component refined to 0.1274(15) (Br1).

Structure code	NG_NS_262	**CCDC Number**	2212301
Empirical Formula	$C_{34}H_{56}N_5SiCl_{0.87}Br_{0.13}$	**Crystal colour and shape**	colourless blocks
Formula weight [g·mol^{-1}]	604.04	Z	4
Sample temperature [K]	100(2)	μ [mm^{-1}]	0.327
Wavelength [Å]	0.71073	F(000)	1313
Crystal System	Monoclinic	Θ **range [°]**	1.608 to 26.499
Space group	$P2_1/c$	**Reflections collected**	89810
Unit cell dimensions [Å]	a = 10.267(2)	**Unique Reflections**	6817
	b = 17.452(3)	R_{int}	0.0467
	c = 18.764(3)	**Restraints / Parameters**	138 / 411
	β = 101.19(2)	$R1$ ($I>2\sigma(I)$)	0.0294
Volume [Å^3]	3298.2(9)	w$R2$ (all data)	0.0751
Crystal size [mm]	0.202 x 0.143 x 0.137	**max. diff. peak / hole [eÅ^{-3}]**	0.324 and −289

7 References

[1] W. C. Röntgen, *Sitzungsberichte der Würzburger physik.-med. Gesellschaft* **1895**, *137*, 132–141.

[2] W. C. Röntgen, *Sitzungsberichte der Königlich Preussischen Akademie der Wissenschaften zu Berlin* **1897**, 576–592.

[3] W. C. Röntgen, *Sitzungsberichte der Würzburger physik.-med. Gesellschaft* **1896**, 11–19.

[4] H. Otremba, *Wilhelm Conrad Röntgen. Ein Leben im Dienst der Wissenschaft*, Fränkische Gesellschaftsdruckerei, Würzburg, **1970**.

[5] A. Forchel, M. Holtz, M. Mansky, D. Meschede, F. Schock, S. Zimmermann, *125 Jahre neue Einsichten - Entdeckung der Strahlen durch Wilhelm Conrad Röntgen, Würzburg 1895*, Julius-Maximilians-Universität Würzburg, Würzburg, **2020**.

[6] W. C. Röntgen, *Nature* **1896**, *53*, 274–276.

[7] W. C. Röntgen, *Ann. Phys.* **1898**, *300*, 1–11.

[8] W. C. Röntgen, *Ann. Phys.* **1898**, *300*, 12–17.

[9] W. C. Röntgen, *Ann. Phys.* **1898**, *300*, 18–37.

[10] W. Crookes, *Phil. Trans. R. Soc.* **1879**, *170*, 135–164.

[11] E. Wiechert, *Schriften d. phys.-ökon. Gesell. zu Königsberg in Pr.* **1897**, *1*, 3–16.

[12] E. A. Davis, I. J. Falconer, *J.J. Thomson and the discovery of the electron*, CRC Press Taylor & Francis Group, Boca Raton, London, New York, **1997**.

[13] J. Plücker, *Ann. Phys.* **1858**, *179*, 88–106.

[14] G. F. Knoll, *Radiation detection and measurement*, Wiley, New York, NY, **2000**.

[15] W. D. Coolidge, United States Patent US 1,203,495, **1916**.

[16] W. D. Coolidge, *Journal of the Franklin Institute* **1925**, *199*, 619–648.

[17] F. Guthrie, *Proc. R. Soc. Lond.* **1873**, *21*, 168–169.

[18] F. Guthrie, *The London, Edinburgh, and Dublin Philosophical Magazine and Journal of Science* **1873**, *46*, 257–266.

[19] G. W. C. Kaye, *Journal of the Röntgen Society* **1922**, *18*, 15–26.

[20] P. T. Weeks, *Phys. Rev.* **1917**, *10*, 564–574.

[21] R. Kegerreis, *Phys. Rev.* **1927**, *29*, 775–781.

[22] B. K. Agarwal, *X-Ray Spectroscopy*, Springer, New York, **1991**.

[23] A. Müller, *Proc. R. Soc. Lond. A* **1927**, *117*, 30–42.

[24] A. Müller, *Proc. R. Soc. Lond. A* **1929**, *125*, 507–516.

[25] A. Müller, *Nature* **1929**, *124*, 128.

[26] A. Müller, *Proc. R. Soc. Lond. A* **1931**, *132*, 646–649.

[27] W. R. Gray, *BJR* **1930**, *3*, 171–177.

[28] R E Clay, *Proc. Phys. Soc.* **1934**, *46*, 703–712.

[29] Z. J. Atlee, J. T. Wilson, J. C. Filmer, *J. Appl. Phys.* **1940**, *11*, 611–615.

[30] W. T. Astbury, R. D. Preston, *Nature* **1934**, *133*, 460–461.

[31] H. P. Klug, *Rev. Sci. Instrum.* **1941**, *12*, 155–156.

[32] A. Hadding, *Z. Physik* **1920**, *3*, 369–371.

[33] J. Becker, *Zeits. f. Elektrochem. Angew. Physik. Chem.* **1927**, *33*, 181–182.

[34] H. Brackney, Z. J. Atlee, *Rev. Sci. Instrum.* **1943**, *14*, 59–63.

[35] F. Hertlein, A. Oehr, C. Hoffmann, C. Michaelsen, J. Wiesmann, *Part. Part. Syst. Charact.* **2005**, *22*, 378–383.

[36] H. Wolter, *Ann. Phys.* **1952**, *445*, 94–114.

[37] H. Wolter, *Ann. Phys.* **1952**, *445*, 286–295.
[38] K. Schwarzschild, *Astronomische Mittheilungen von der Koeniglichen Sternwarte zu Goettingen* **1905**, *10*, 4–28.
[39] M. Montel in *X-ray Microscopy and Microradiography* (Eds.: V. E. Cosslett, A. Engstrom, H. H. Pattee, Jr.), Academic Press, New York, **1957**, 177–185.
[40] P. Kirkpatrick, A. V. Baez, *J. Opt. Soc. Am.* **1948**, *38*, 766–774.
[41] M. Schuster, H. Göbel, *Adv. x-ray anal.* **1995**, *39*, 57–71.
[42] M. R. Schuster, H. Goebel, L. Bruegemann, D. Bahr, F. Burgaezy, C. Michaelsen, M. Stoermer, P. Ricardo, R. Dietsch, T. Holz, H. Mai in *SPIE Proceedings* (Eds.: C. A. MacDonald, K. A. Goldberg, J. R. Maldonado, H. H. Chen-Mayer, S. P. Vernon), SPIE, **1999**, 183–198.
[43] M. Bargheer, N. Zhavoronkov, R. Bruch, H. Legall, H. Stiel, M. Woerner, T. Elsaesser, *Appl. Phys. B* **2005**, *80*, 715–719.
[44] T. Schulz, K. Meindl, D. Leusser, D. Stern, J. Graf, C. Michaelsen, M. Ruf, G. M. Sheldrick, D. Stalke, *J. Appl. Cryst.* **2009**, *42*, 885–891.
[45] U. W. Arndt, *J. Appl. Cryst.* **1990**, *23*, 161–168.
[46] O. Hemberg, M. Otendal, H. M. Hertz, *Appl. Phys. Lett.* **2003**, *83*, 1483–1485.
[47] O. Hemberg, *Opt. Eng.* **2004**, *43*, 1682.
[48] T. Tuohimaa, M. Otendal, H. M. Hertz in *SPIE Proceedings* (Eds.: G. A. Kyrala, J.-C. J. Gauthier, C. A. MacDonald, A. M. Khounsary), SPIE, **2005**, 59180U.
[49] M. Otendal, T. Tuohimaa, H. M. Hertz, *J. Appl. Phys.* **2007**, *101*, 26102.
[50] T. Tuohimaa, M. Otendal, H. M. Hertz, *Appl. Phys. Lett.* **2007**, *91*, 74104.
[51] M. Otendal, T. Tuohimaa, U. Vogt, H. M. Hertz, *Rev. Sci. Instrum.* **2008**, *79*, 16102.
[52] R. D. Deslattes, E. G. Kessler, Jr., P. Indelicato, L. de Billy, E. Lindroth, J. Anton, J. S. Coursey, D. J. Schwab, C. Chang, R. Sukumar, K. Olsen, R. A. Dragoset, *X-ray Transition Energies (version 1.2), NIST Standard Reference Database 128*, National Institute of Standards and Technology, Gaithersburg, MD, **2005**.
[53] T. Tuohimaa, J. Ewald, M. Schlie, J. M. Fernández-Varea, H. M. Hertz, U. Vogt, *Appl. Phys. Lett.* **2008**, *92*, 233509.
[54] D. H. Larsson, P. A. C. Takman, U. Lundström, A. Burvall, H. M. Hertz, *Rev. Sci. Instrum.* **2011**, *82*, 123701.
[55] J. M. Lafferty, *J. Appl. Phys.* **1951**, *22*, 299–309.
[56] A. N. Broers, *J. Appl. Phys.* **1967**, *38*, 1991–1992.
[57] A. N. Broers, *Rev. Sci. Instrum.* **1969**, *40*, 1040–1045.
[58] M. Wansleben, C. Zech, C. Streeck, J. Weser, C. Genzel, B. Beckhoff, R. Mainz, *J. Anal. At. Spectrom.* **2019**, *34*, 1497–1502.
[59] M. B. Diop, L. Diop, T. Maris, *Acta Crystallogr. E, Cryst. Commun.* **2016**, *72*, 482–485.
[60] I. Elkin, T. Maris, P. Hildgen, *Acta Crystallogr. E, Cryst. Commun.* **2017**, *73*, 1044–1047.
[61] I. Elkin, T. Maris, P. Hildgen, C. J. Barrett, *Acta Crystallogr. E, Cryst. Commun.* **2018**, *74*, 1486–1490.
[62] I. Elkin, T. Maris, A. Melkoumov, P. Hildgen, X. Banquy, G. Leclair, C. Barrett, *Acta Crystallogr. E, Cryst. Commun.* **2018**, *74*, 458–460.
[63] Y. Gautier, T. Maris, W. G. Skene, *Acta Crystallogr. E, Cryst. Commun.* **2019**, *75*, 589–592.

[64] G. A. Seck, A. Sene, L. Diop, T. Maris, *Acta Crystallogr. E, Cryst. Commun.* **2016**, *72*, 273–275.
[65] A. Mehr, F. Henneberg, A. Chari, D. Görlich, T. Huyton, *Acta Crystallogr. D, Struct. Biol.* **2020**, *76*, 1222–1232.
[66] A. Pan, W. G. Saw, M. S. Subramanian Manimekalai, A. Grüber, S. Joon, T. Matsui, T. M. Weiss, G. Grüber, *Acta Crystallogr. D, Struct. Biol.* **2017**, *73*, 402–419.
[67] W. G. Saw, G. Tria, A. Grüber, M. S. Subramanian Manimekalai, Y. Zhao, A. Chandramohan, G. Srinivasan Anand, T. Matsui, T. M. Weiss, S. G. Vasudevan, G. Grüber, *Acta Crystallogr. D, Struct. Biol.* **2015**, *71*, 2309–2327.
[68] M. S. Subramanian Manimekalai, W. G. Saw, A. Pan, A. Grüber, G. Grüber, *Acta Crystallogr. D, Struct. Biol.* **2016**, *72*, 795–807.
[69] Z. Lai, S. Zhang, N. Zheng, S. Yu, M. Ageishi, H. Jinnai, Y. Cao, *J. Appl. Cryst.* **2020**, *53*, 27–33.
[70] Z. Liang, N. Zheng, B. Ni, Z. Lai, H. Niu, S. Zhang, Y. Cao, *IUCrJ* **2021**, *8*, 215–224.
[71] Y. M. Klein, A. Prescimone, M. Neuburger, E. C. Constable, C. E. Housecroft, *CrystEngComm* **2017**, *19*, 2894–2902.
[72] M. B. Diop, L. Diop, L. Plasseraud, T. Maris, *Acta Crystallogr. E, Cryst. Commun.* **2015**, *71*, 520–522.
[73] M. B. Diop, L. Diop, L. Plasseraud, T. Maris, *Acta Crystallogr. E, Cryst. Commun.* **2016**, *72*, 355–357.
[74] A. Addala, Z. Setifi, Y. Morimoto, B. Artetxe, T. Matsumoto, J. M. Gutiérrez-Zorrilla, C. Glidewell, *Acta Crystallogr. E, Cryst. Commun.* **2018**, *74*, 1717–1726.
[75] A. K.-W. Chan, M. Ng, K.-H. Low, V. W.-W. Yam, *J. Am. Chem. Soc.* **2018**, *140*, 8321–8329.
[76] M. B. Diop, L. Diop, T. Maris, *Acta Crystallogr. E, Cryst. Commun.* **2015**, *71*, 1064–1066.
[77] M. Ndiaye, A. Samb, L. Diop, T. Maris, *Acta Crystallogr. E, Cryst. Commun.* **2015**, *71*, 947–949.
[78] M. Ndiaye, A. Samb, L. Diop, T. Maris, *Acta Crystallogr. E, Cryst. Commun.* **2016**, *72*, 1047–1049.
[79] M. Ndiaye, A. Samb, L. Diop, T. Maris, *Acta Crystallogr. E, Cryst. Commun.* **2016**, *72*, 1–3.
[80] Z. Setifi, H. C. Kwong, E. R. T. Tiekink, T. Maris, F. Setifi, *Acta Crystallogr. E, Cryst. Commun.* **2020**, *76*, 835–840.
[81] N. Bélanger-Desmarais, C. Reber, *Molbank* **2017**, *2017*, M937.
[82] J. H. Hubbell, S. M. Seltzer, *Tables of X-Ray Mass Attenuation Coefficients and Mass Energy-Absorption Coefficients, NIST Standard Reference Database 126*, National Institute of Standards and Technology, Gaithersburg, MD, **2004**.
[83] Bruker AXS Inc., *SAINT v8.30C*, Bruker AXS Inst Inc., Wi, USA, Madison, **2013**.
[84] M. Sevvana, M. Ruf, I. Usón, G. M. Sheldrick, R. Herbst-Irmer, *Acta Crystallogr. D, Struct. Biol.* **2019**, *75*, 1040–1050.
[85] N. K. Hansen, P. Coppens, *Acta Crystallogr. A, Found. Adv.* **1978**, *34*, 909–921.
[86] H. A. Kramers, *The London, Edinburgh, and Dublin Philosophical Magazine and Journal of Science* **1923**, *46*, 836–871.
[87] L. Krause, R. Herbst-Irmer, G. M. Sheldrick, D. Stalke, *J. Appl. Cryst.* **2015**, *48*, 3–10.
[88] G. M. Sheldrick, *Acta Crystallogr. C, Struct. Chem.* **2015**, *71*, 3–8.

[89] G. M. Sheldrick, *XPREP*, Georg-August-Universität Göttingen, Germany, **2015**.
[90] K. Diederichs, P. A. Karplus, *Nature Struct. Biol.* **1997**, *4*, 269–275.
[91] M. S. Weiss, *J. Appl. Cryst.* **2001**, *34*, 130–135.
[92] Bruker AXS Inc., "SC-XRD Detectors", can be found under https://www.bruker.com/en/products-and-solutions/diffractometers-and-scattering-systems/single-crystal-x-ray-diffractometers/sc-xrd-components/detectors.html, accessed 03.04.2022.
[93] G. M. Sheldrick, *Acta Crystallogr. A, Found. Adv.* **2015**, *71*, 3–8.
[94] C. B. Hübschle, G. M. Sheldrick, B. Dittrich, *J. Appl. Cryst.* **2011**, *44*, 1281–1284.
[95] J. Wai, D. Lubinski, C. P. Benbow, *J. Educ. Psychol.* **2009**, *101*, 817–835.
[96] L. Glasser, *J. Chem. Educ.* **1967**, *44*, 502.
[97] H. H. Jaffé, *Symmetry in Chemistry*, Dover Publications, **2013**.
[98] S. E. McKay, S. R. Boone, *J. Chem. Educ.* **2001**, *78*, 1487.
[99] M. M. Orchin, H. H. Jaffe, *J. Chem. Educ.* **1970**, *47*, 372.
[100] M. Zeldin, *J. Chem. Educ.* **1966**, *43*, 17.
[101] P. Brown, *J. Chem. Educ.* **1971**, *48*, 535.
[102] M. C. Caserio, *J. Chem. Educ.* **1980**, *57*, A347.
[103] J. L. Carlos, *J. Chem. Educ.* **1968**, *45*, 248.
[104] D. C. Harris, M. D. Bertolucci, *Symmetry and spectroscopy. An introduction to vibrational and electronic spectroscopy*, Dover, New York, NY, **2014**.
[105] M. L. Myrick, P. E. Colavita, A. E. Greer, B. Long, D. Andreatta, *J. Chem. Educ.* **2004**, *81*, 379.
[106] C. P. Brock, T. Hahn, H. Wondratschek, U. Müller, U. Shmueli, E. Prince, A. Authier, V. Kopský, D. B. Litvin, E. Arnold, D. M. Himmel, M. G. Rossmann, S. Hall, B. McMahon, M. I. Aroyo, *International Tables for Crystallography*, International Union of Crystallography, Chester, England, **2016**.
[107] H.-K. Wu, P. Shah, *Sci. Ed.* **2004**, *88*, 465–492.
[108] M. G. Jones, J. Minogue, T. R. Tretter, A. Negishi, R. Taylor, *Sci. Ed.* **2006**, *90*, 111–123.
[109] T. Herman, J. Morris, S. Colton, A. Batiza, M. Patrick, M. Franzen, D. S. Goodsell, *Biochem. Mol. Biol. Educ.* **2006**, *34*, 247–254.
[110] G. E. Höst, C. Larsson, A. Olson, L. A. E. Tibell, *LSE* **2013**, *12*, 471–482.
[111] P. Moeck, J. Stone-Sundberg, T. J. Snyder, W. Kaminsky, *J. Mater. Educ.* **2014**, *36*, 77–96.
[112] J. P. Brannon, I. Ramirez, D. Williams, G. A. Barding, Y. Liu, K. M. McCulloch, P. Chandrasekaran, S. C. E. Stieber, *J. Chem. Educ.* **2020**, *97*, 2273–2279.
[113] L. Casas, *J. Appl. Cryst.* **2020**, *53*, 1583–1592.
[114] M. L. Brown, D. Hartling, H. N. Tailor, K. van Wieren, G. B. Houghton, I. G. McGregor, C. D. Hansen, N. Merbouh, *CrystEngComm* **2019**, *21*, 5757–5766.
[115] L. Casas, E. Estop, *J. Chem. Educ.* **2015**, *92*, 1338–1343.
[116] P. P. Rodenbough, W. B. Vanti, S.-W. Chan, *J. Chem. Educ.* **2015**, *92*, 1960–1962.
[117] A. J. Olson, Y. H. E. Hu, E. Keinan, *Proc. Natl. Acad. Sci.* **2007**, *104*, 20731–20736.
[118] W. Kaminsky, T. Snyder, P. Moeck, *Acta Crystallogr. A, Found. Adv.* **2014**, *70*, C1278-C1278.

[119] P. Moeck, J. Stone-Sundberg, T. J. Snyder, W. Kaminsky, *MRS Proc.* **2014**, *1716*.
[120] G. N. Lewis, *J. Am. Chem. Soc.* **1916**, *38*, 762–785.
[121] I. Kaufmann, K. M. Hamza, C.-J. Rundgren, L. Eriksson, *Int. J. Sci. Educ.* **2017**, *39*, 1601–1624.
[122] W.-Y. Ahmad, S. Omar, *J. Chem. Educ.* **1992**, *69*, 791.
[123] W.-Y. Ahmad, M. B. Zakaria, *J. Chem. Educ.* **2000**, *77*, 329.
[124] B. B. Miburo, *J. Chem. Educ.* **1998**, *75*, 317.
[125] P. Nassiff, W. A. Czerwinski, *J. Chem. Educ.* **2015**, *92*, 1409–1411.
[126] J. A. Brady, J. N. Milbury-Steen, J. L. Burmeister, *J. Chem. Educ.* **1990**, *67*, 491.
[127] M. M. Cooper, N. Grove, S. M. Underwood, M. W. Klymkowsky, *J. Chem. Educ.* **2010**, *87*, 869–874.
[128] G. Nicoll, *J. Chem. Educ.* **2003**, *80*, 205.
[129] J. Q. Pardo, *J. Chem. Educ.* **1989**, *66*, 456.
[130] G. V. Shultz, A. R. Gere, *J. Chem. Educ.* **2015**, *92*, 1325–1329.
[131] L. Pauling, *J. Chem. Soc.* **1948**, *17*, 1461–1467.
[132] L. Pauling, *The nature of the chemical bond*, Cornell University Press, New York, **1939**.
[133] P. G. Mezey, E. -C. Haas, *J. Chem. Phys.* **1982**, *77*, 870–876.
[134] D. Cruickshank, *J. Mol. Struct.* **1985**, *130*, 177–191.
[135] D. Cruickshank, M. Eisenstein, *J. Mol. Struct.* **1985**, *130*, 143–156.
[136] I. Mayer, *J. Mol. Struct. Theochem.* **1987**, *149*, 81–89.
[137] W. Yu, L. W. Guo, H. C. Lin, C. T. Kao, C. J. Tsai, J. W. Bats, *Inorg. Chem.* **1988**, *27*, 520–523.
[138] A. E. Reed, P. v. R. Schleyer, *J. Am. Chem. Soc.* **1990**, *112*, 1434–1445.
[139] J. Cioslowski, P. R. Surján, *J. Mol. Struct. Theochem.* **1992**, *255*, 9–33.
[140] J. Cioslowski, S. T. Mixon, *Inorg. Chem.* **1993**, *32*, 3209–3216.
[141] J. A. Dobado, H. Martínez-García, Molina, M. R. Sundberg, *J. Am. Chem. Soc.* **1998**, *120*, 8461–8471.
[142] T. Stefan, R. Janoschek, *J. Mol. Model.* **2000**, *6*, 282–288.
[143] I. Love, *The journal of physical chemistry. A* **2009**, *113*, 2640–2646.
[144] W. Kutzelnigg, *Angew. Chem.* **1984**, *96*, 262–286; *Angew. Chem. Int. Ed.* **1984**, *23*, 272–295.
[145] M. S. Schmøkel, S. Cenedese, J. Overgaard, M. R. V. Jørgensen, Y.-S. Chen, C. Gatti, D. Stalke, B. B. Iversen, *Inorg. Chem.* **2012**, *51*, 8607–8616.
[146] F. A. Cotton, G. Wilkinson, C. A. Murillo, M. Bochmann, *Advanced inorganic chemistry*, Wiley, New York, Weinheim, **1999**.
[147] L. G. Wade, *Organic chemistry*, Pearson Prentice Hall, Upper Saddle River, NJ, **2006**.
[148] C. Bruhn, D. Steinborn, "Schwefelsäure - Chemgapedia", can be found under http://www.chemgapedia.de/vsengine/vlu/vsc/de/ch/6/ac/bibliothek/_vlu/schwefelsaeure.vlu.html, accessed 12.11.2021.
[149] S. Alvarez, *Angew. Chem.* **2012**, *124*, 610–621; *Angew. Chem. Int. Ed.* **2012**, *51*, 590–600.
[150] J. Brecher, *Pure and Applied Chemistry* **2008**, *80*, 277–410.
[151] A. Nandi, S. Kozuch, *Chemistry* **2020**, *26*, 759–772.

[152] G. Frenking, *Angew. Chem.* **2014**, *126*, 6152–6158; *Angew. Chem. Int. Ed.* **2014**, *53*, 6040–6046.
[153] D. Himmel, I. Krossing, A. Schnepf, *Angew. Chem.* **2014**, *126*, 6159–6160; *Angew. Chem. Int. Ed.* **2014**, *53*, 6047–6048.
[154] D. Himmel, I. Krossing, A. Schnepf, *Angew. Chem.* **2014**, *126*, 378–382; *Angew. Chem. Int. Ed.* **2014**, *53*, 370–374.
[155] E. Fischer, *Ber. Dtsch. Chem. Ges.* **1891**, *24*, 1836–1845.
[156] E. Fischer, *Ber. Dtsch. Chem. Ges.* **1891**, *24*, 2683–2687.
[157] M. S. Newman, *J. Chem. Educ.* **1955**, *32*, 344.
[158] V. Gold, *The IUPAC Compendium of Chemical Terminology*, International Union of Pure and Applied Chemistry (IUPAC), Research Triangle Park, NC, **2019**.
[159] G. Snatzke, *Nachr. Chem. Tech.* **1960**, *8*, 110–111.
[160] H.-B. Bürgi, S. C. Capelli, A. E. Goeta, J. A. K. Howard, M. A. Spackman, D. S. Yufit, *Chem. Eur. J.* **2002**, *8*, 3512.
[161] B. F. Decker, J. S. Kasper, *Acta Cryst.* **1959**, *12*, 503–506.
[162] D. Geist, R. Kloss, H. Follner, *Acta Crystallogr. B, Struct. Sci.* **1970**, *26*, 1800–1802.
[163] R. E. Hughes, C. H. L. Kennard, D. B. Sullenger, H. A. Weakliem, D. E. Sands, J. L. Hoard, *J. Am. Chem. Soc.* **1963**, *85*, 361–362.
[164] C. E. Housecroft, E. C. Constable, *Chemistry. An introduction to organic, inorganic and physical chemistry*, Pearson Prentice Hall, Harlow, Munich, **2010**.
[165] R. J. Gillespie, R. S. Nyholm, *Q. Rev., Chem. Soc.* **1957**, *11*, 339.
[166] R. J. Gillespie, E. A. Robinson, *Angew. Chem.* **1996**, *108*, 539–560; *Angew. Chem. Int. Ed.* **1996**, *35*, 495–514.
[167] K. Wade, *J. Chem. Soc. D* **1971**, 792.
[168] K. Wade, *Adv. Inorg. Chem. Radiochem.* **1976**, *18*, 1–66.
[169] M. Juhasz, S. Hoffmann, E. Stoyanov, K.-C. Kim, C. A. Reed, *Angew. Chem.* **2004**, *116*, 5466–5469; *Angew. Chem. Int. Ed.* **2004**, *43*, 5352–5355.
[170] M. J. Lage, G. J. Platt, M. Treglia, *J. Econ. Educ.* **2000**, *31*, 30–43.
[171] Otterbein University, "Symmetry Resources at Otterbein University", can be found under https://symotter.org, accessed 02.11.2021.
[172] J. K. Cockcroft, H. Driessen, "Screw Symmetry: Helical Screw Axes", can be found under http://pd.chem.ucl.ac.uk/pdnn/symm1/screw3.htm, accessed 14.02.2022.
[173] B. Grenier, R. Ballou, *EPJ Web of Conferences* **2012**, *22*, 6.
[174] J. P. Birk, J. Foster, *J. Chem. Educ.* **1989**, *66*, 1015.
[175] E. B. Flint, *J. Chem. Educ.* **2011**, *88*, 907–909.
[176] K. Fuchigami, M. Schrandt, G. L. Miessler, *J. Chem. Educ.* **2016**, *93*, 1081–1084.
[177] V. F. Scalfani, T. P. Vaid, *J. Chem. Educ.* **2014**, *91*, 1174–1180.
[178] L. T. Sein, *J. Chem. Educ.* **2010**, *87*, 827–828.
[179] S. G. Cady, *J. Chem. Educ.* **1997**, *74*, 794.
[180] C. Elsworth, B. T. Y. Li, A. Ten, *J. Chem. Educ.* **2017**, *94*, 827–828.
[181] K. M. Seymour, *J. Chem. Educ.* **1938**, *15*, 192.
[182] A. Scattergood, *J. Chem. Educ.* **1937**, *14*, 140.
[183] S. Lenzer, B. Smarsly, N. Graulich, *J. Chem. Educ.* **2019**, *96*, 1630–1639.
[184] Y. Komuro, K. Sone, *J. Chem. Educ.* **1961**, *38*, 580.

[185] D. P. Sunderland, *J. Chem. Educ.* **2014**, *91*, 432–436.
[186] J. H. Westbrook, R. C. DeVries, *J. Chem. Educ.* **1957**, *34*, 220.
[187] Y.-Z. Ma, Z.-L. Yang, Y. Wang, H.-H. Wang, S. J. Tian, *J. Chem. Educ.* **2020**, *97*, 4063–4068.
[188] B. Mattson, *J. Chem. Educ.* **2000**, *77*, 622.
[189] N. K. Kildahl, L. Berka, G. M. Bodner, *J. Chem. Educ.* **1986**, *63*, 62.
[190] M. Laing, *J. Chem. Educ.* **1997**, *74*, 795.
[191] A. W. Mann, *J. Chem. Educ.* **1973**, *50*, 652.
[192] R. C. Olsen, *J. Chem. Educ.* **1967**, *44*, 728.
[193] L. T. Sein, S. E. Sein, *J. Chem. Educ.* **2015**, *92*, 1419–1421.
[194] T. Li, J. H. Worrell, *J. Chem. Educ.* **1989**, *66*, 73.
[195] T. H. Bindel, *J. Chem. Educ.* **2002**, *79*, 468.
[196] C. H. L. Kennard, *J. Chem. Educ.* **1979**, *56*, 238.
[197] Z. Dauter, M. Jaskolski, *J. Appl. Cryst.* **2010**, *43*, 1150–1171.
[198] U. Müller, S. Ivlev, S. Schulz, C. Wölper, *Angew. Chem.* **2021**, *133*, 17592–17594; *Angew. Chem. Int. Ed.* **2021**, *60*, 17452–17454.
[199] S. L. Ackermann, D. J. Wolstenholme, C. Frazee, G. Deslongchamps, S. H. M. Riley, A. Decken, G. S. McGrady, *Angew. Chem.* **2015**, *127*, 166–170; *Angew. Chem. Int. Ed.* **2015**, *54*, 164–168.
[200] S. L. Ackermann, D. J. Wolstenholme, C. Frazee, G. Deslongchamps, S. H. M. Riley, A. Decken, G. S. McGrady, *Angew. Chem.* **2015**, *127*, 7578; *Angew. Chem. Int. Ed.* **2015**, *54*, 7470.
[201] R. Lingnau, J. Strähle, *Angew. Chem.* **1988**, *100*, 409–410; *Angew. Chem. Int. Ed. Engl.* **1988**, *27*, 436.
[202] A. Haaland, K. Rypdal, H. P. Verne, W. Scherer, W. R. Thiel, *Angew. Chem.* **1994**, *106*, 2515–2517; *Angew. Chem. Int. Ed.* **1995**, *33*, 2443–2445.
[203] S. K. Dey, S. Shit, S. P. Dey, S. Mitra, K. M. A. Malik, *Chem. Lett.* **2011**, *40*, 810–812.
[204] E. Amemiya, A. Loo, D. G. Shlian, G. Parkin, *Chem. Sci.* **2020**, *11*, 11763–11776.
[205] E. Irmer, *Restraints in der Kristallstrukturverfeinerung und systematische Überprüfung von Datenbankenstrukturen auf höhere Symmetrie*; Dissertation, Göttingen, **1990**.
[206] G. Bergerhoff, I. D. Brown in *Crystallographic Databases* (Eds.: F. H. Allen, G. Bergerhoff, R. Sievers), International Union of Crystallography, Chester, England, **1987**, 77–95.
[207] A. N. Desnoyer, A. Nicolay, M. S. Ziegler, K. V. Lakshmi, T. R. Cundari, T. D. Tilley, *J. Am. Chem. Soc.* **2021**, *143*, 7135–7143.
[208] C. R. Groom, I. J. Bruno, M. P. Lightfoot, S. C. Ward, *Acta Crystallogr. B, Struct. Sci.* **2016**, *72*, 171–179.
[209] A. L. Spek, *Acta Crystallogr. E, Cryst. Commun.* **2020**, *76*, 1–11.
[210] A. L. Spek, *J. Appl. Cryst.* **2003**, *36*, 7–13.
[211] L. A. Paul, N. C. Röttcher, J. Zimara, J.-H. Borter, J.-P. Du, D. Schwarzer, R. A. Mata, I. Siewert, *Organometallics* **2020**, *39*, 2405–2414.
[212] A. L. Spek, *Acta Crystallogr. C, Struct. Chem.* **2015**, *71*, 9–18.
[213] T. Y. Tou, S. W. Ng, *Acta Crystallogr. C, Struct. Chem.* **2021**, *77*, 586–590.
[214] J. Zyss, J. L. Oudar, *Phys. Rev. A* **1982**, *26*, 2028–2048.

[215] H. H. Lee, H. J. Kim, *Appl. Phys. Express* **2012**, *5*, 51401.
[216] A. Coda, F. Pandarese, *J. Appl. Cryst.* **1976**, *9*, 193–198.
[217] J. P. Dougherty, S. K. Kurtz, *J. Appl. Cryst.* **1976**, *9*, 145–158.
[218] S. Sivaraman, C. Balakrishnan, A. A. Prasad, R. M. Sokalingam, S. P. Meenakshisundaram, R. Markkandan, *Molecular Crystals and Liquid Crystals* **2017**, *656*, 153–168.
[219] B. R. Srinivasan, N. U. Parsekar, R. A. Apreyan, A. M. Petrosyan, *Molecular Crystals and Liquid Crystals* **2019**, *680*, 75–84.
[220] C. P. Brock, E. C. Lingafelter, *J. Chem. Educ.* **1980**, *57*, 552.
[221] CCDC, "CSD Space Group Statistics – Space Group Frequency Ordering", can be found under https://www.ccdc.cam.ac.uk/support-and-resources/ccdcresources/84242e1ccbe540f8b816e1f6fee4eedb.pdf, accessed 21.02.2022.
[222] "Tinkercad", can be found under https://www.tinkercad.com, accessed 13.12.2021.
[223] N. Graw, D. Stalke, *J. Appl. Cryst.* **2022**, *55*, 144–148.
[224] N. Graw, D. Stalke, *Acta Crystallogr. A, Found. Adv.* **2021**, 77, C765-C765.
[225] H.-W. Wanzlick, E. Schikora, *Angew. Chem.* **1960**, *72*, 494.
[226] H.-W. Wanzlick, H.-J. Kleiner, *Angew. Chem.* **1961**, *73*, 493.
[227] H.-W. Wanzlick, B. Lachmann, E. Schikora, *Chem. Ber.* **1965**, *98*, 3170–3177.
[228] H.-W. Wanzlick, H.-J. Schönherr, *Angew. Chem.* **1968**, *80*, 154; *Angew. Chem. Int. Ed.* **1968**, *7*, 141–142.
[229] K. Öfele, *J. Organomet. Chem.* **1968**, *12*, P42-P43.
[230] A. J. Arduengo, R. L. Harlow, M. Kline, *J. Am. Chem. Soc.* **1991**, *113*, 361–363.
[231] F. E. Hahn, M. C. Jahnke, *Angew. Chem.* **2008**, *120*, 3166–3216; *Angew. Chem. Int. Ed.* **2008**, *47*, 3122–3172.
[232] M. N. Hopkinson, C. Richter, M. Schedler, F. Glorius, *Nature* **2014**, *510*, 485–496.
[233] V. Nesterov, D. Reiter, P. Bag, P. Frisch, R. Holzner, A. Porzelt, S. Inoue, *Chem. Rev.* **2018**, *118*, 9678–9842.
[234] D. Enders, O. Niemeier, A. Henseler, *Chem. Rev.* **2007**, *107*, 5606–5655.
[235] J. Baumgartner, C. Marschner, *Rev. Inorg. Chem.* **2014**, *34*, 119–152.
[236] S. Díez-González, N. Marion, S. P. Nolan, *Chem. Rev.* **2009**, *109*, 3612–3676.
[237] P. Schwab, M. B. France, J. W. Ziller, R. H. Grubbs, *Angew. Chem.* **1995**, *107*, 2179–2181; *Angew. Chem. Int. Ed.* **1995**, *34*, 2039–2041.
[238] M. Scholl, S. Ding, C. W. Lee, R. H. Grubbs, *Org. Lett.* **1999**, *1*, 953–956.
[239] R. H. Grubbs, *Angew. Chem.* **2006**, *118*, 3845–3850; *Angew. Chem. Int. Ed.* **2006**, *45*, 3760–3765.
[240] A. Sekiguchi, V. Y. Lee, *Organometallic compounds of low-coordinate si, ge, sn and pb. From phantom species to stable compounds*, Wiley, Hoboken, N.J., **2013**.
[241] M. Asay, C. Jones, M. Driess, *Chem. Rev.* **2011**, *111*, 354–396.
[242] Y. Ding, H. W. Roesky, M. Noltemeyer, H.-G. Schmidt, P. P. Power, *Organometallics* **2001**, *20*, 1190–1194.
[243] A. E. Ayers, T. M. Klapötke, H. V. R. Dias, *Inorg. Chem.* **2001**, *40*, 1000–1005.
[244] A. Akkari, J. J. Byrne, I. Saur, G. Rima, H. Gornitzka, J. Barrau, *J. Organomet. Chem.* **2001**, *622*, 190–198.
[245] H. V. R. Dias, Z. Wang, *J. Am. Chem. Soc.* **1997**, *119*, 4650–4655.

[246] I. Saur, S. Garcia Alonso, H. Gornitzka, V. Lemierre, A. Chrostowska, J. Barrau, *Organometallics* **2005**, *24*, 2988–2996.
[247] M. Stender, A. D. Phillips, P. P. Power, *Inorg. Chem.* **2001**, *40*, 5314–5315.
[248] Y. Yang, N. Zhao, Y. Wu, H. Zhu, H. W. Roesky, *Inorg. Chem.* **2012**, *51*, 2425–2431.
[249] E. Ballestero-Martínez, J. Klosin, B. D. Fahlman, L. W. Pineda, *Eur. J. Inorg. Chem.* **2014**, *2014*, 5233–5239.
[250] S. Yao, M. Brym, K. Merz, M. Driess, *Organometallics* **2008**, *27*, 3601–3607.
[251] E. C. Y. Tam, N. A. Maynard, D. C. Apperley, J. D. Smith, M. P. Coles, J. R. Fulton, *Inorg. Chem.* **2012**, *51*, 9403–9415.
[252] L. Ferro, P. B. Hitchcock, M. P. Coles, J. R. Fulton, *Inorg. Chem.* **2012**, *51*, 1544–1551.
[253] Y. Ding, Q. Ma, H. W. Roesky, R. Herbst-Irmer, I. Usón, M. Noltemeyer, H.-G. Schmidt, *Organometallics* **2002**, *21*, 5216–5220.
[254] A. Jana, G. Schwab, H. W. Roesky, D. Stalke, *Inorg. Chim. Acta* **2010**, *363*, 4408–4410.
[255] Y. Ding, H. Hao, H. W. Roesky, M. Noltemeyer, H.-G. Schmidt, *Organometallics* **2001**, *20*, 4806–4811.
[256] S. L. Choong, W. D. Woodul, C. Schenk, A. Stasch, A. F. Richards, C. Jones, *Organometallics* **2011**, *30*, 5543–5550.
[257] A. Jana, D. Ghoshal, H. W. Roesky, I. Objartel, G. Schwab, D. Stalke, *J. Am. Chem. Soc.* **2009**, *131*, 1288–1293.
[258] L. W. Pineda, V. Jancik, K. Starke, R. B. Oswald, H. W. Roesky, *Angew. Chem.* **2006**, *118*, 2664–2667; *Angew. Chem. Int. Ed.* **2006**, *45*, 2602–2605.
[259] I. Saur, G. Rima, K. Miqueu, H. Gornitzka, J. Barrau, *J. Organomet. Chem.* **2003**, *672*, 77–85.
[260] A. Jana, P. P. Samuel, H. W. Roesky, C. Schulzke, *J. Fluor. Chem.* **2010**, *131*, 1096–1099.
[261] P. B. Hitchcock, M. F. Lappert, P. L. Pye, *J. Chem. Soc., Dalton Trans.* **1977**, 2160–2172.
[262] H. Arii, F. Nakadate, K. Mochida, *Organometallics* **2009**, *28*, 4909–4911.
[263] I. Saur, G. Rima, H. Gornitzka, K. Miqueu, J. Barrau, *Organometallics* **2003**, *22*, 1106–1109.
[264] Y. Ding, Q. Ma, I. Usón, H. W. Roesky, M. Noltemeyer, H.-G. Schmidt, *J. Am. Chem. Soc.* **2002**, *124*, 8542–8543.
[265] L. W. Pineda, V. Jancik, R. B. Oswald, H. W. Roesky, *Organometallics* **2006**, *25*, 2384–2387.
[266] L. W. Pineda, V. Jancik, H. W. Roesky, D. Neculai, A. M. Neculai, *Angew. Chem.* **2004**, *116*, 1443–1445; *Angew. Chem. Int. Ed.* **2004**, *43*, 1419–1421.
[267] A. Jana, B. Nekoueishahraki, H. W. Roesky, C. Schulzke, *Organometallics* **2009**, *28*, 3763–3766.
[268] L. W. Pineda, V. Jancik, H. W. Roesky, R. Herbst-Irmer, *Angew. Chem.* **2004**, *116*, 5650–5652; *Angew. Chem. Int. Ed.* **2004**, *43*, 5534–5536.
[269] L. W. Pineda, V. Jancik, H. W. Roesky, R. Herbst-Irmer, *Inorg. Chem.* **2005**, *44*, 3537–3540.
[270] Y. Yang, H. W. Roesky, P. G. Jones, C.-W. So, Z. Zhang, R. Herbst-Irmer, H. Ye, *Inorg. Chem.* **2007**, *46*, 10860–10863.

[271] C. Copéret, M. Chabanas, R. Petroff Saint-Arroman, J.-M. Basset, *Angew. Chem.* **2003**, *115*, 164–191; *Angew. Chem. Int. Ed.* **2003**, *42*, 156–181.
[272] H. W. Roesky, I. Haiduc, N. S. Hosmane, *Chem. Rev.* **2003**, *103*, 2579–2595.
[273] T. J. Hadlington, M. Driess, C. Jones, *Chem. Soc. Rev.* **2018**, *47*, 4176–4197.
[274] R. J. Corriu, J. J. Moreau, *J. Organomet. Chem.* **1972**, *40*, 97–105.
[275] A. Jana, H. W. Roesky, C. Schulzke, *Dalton Trans.* **2010**, *39*, 132–138.
[276] A. Jana, S. S. Sen, H. W. Roesky, C. Schulzke, S. Dutta, S. K. Pati, *Angew. Chem.* **2009**, *121*, 4310–4312; *Angew. Chem. Int. Ed.* **2009**, *48*, 4246–4248.
[277] A. Jana, G. Tavčar, H. W. Roesky, M. John, *Dalton Trans.* **2010**, *39*, 9487–9489.
[278] G. Tan, W. Wang, B. Blom, M. Driess, *Dalton Trans.* **2014**, *43*, 6006–6011.
[279] N. Blaquiere, S. Diallo-Garcia, S. I. Gorelsky, D. A. Black, K. Fagnou, *J. Am. Chem. Soc.* **2008**, *130*, 14034–14035.
[280] H. Wu, W. Zhou, T. Yildirim, *J. Am. Chem. Soc.* **2008**, *130*, 14834–14839.
[281] P. Bazinet, G. P. Yap, D. S. Richeson, *J. Am. Chem. Soc.* **2001**, *123*, 11162–11167.
[282] H. Arii, F. Nakadate, K. Mochida, T. Kawashima, *Organometallics* **2011**, *30*, 4471–4474.
[283] C. K. Jha, S. Karwasara, S. Nagendran, *Chem. Eur. J.* **2014**, *20*, 10240–10244.
[284] P. Mahawar, M. K. Wasson, M. K. Sharma, C. K. Jha, G. Mukherjee, P. Vivekanandan, S. Nagendran, *Angew. Chem.* **2020**, *132*, 21561–21565; *Angew. Chem. Int. Ed.* **2020**, *59*, 21377–21381.
[285] D. J. Doyle, P. B. Hitchcock, M. F. Lappert, G. Li, *J. Organomet. Chem.* **2009**, *694*, 2611–2617.
[286] A. Jana, H. W. Roesky, C. Schulzke, A. Döring, T. Beck, A. Pal, R. Herbst-Irmer, *Inorg. Chem.* **2009**, *48*, 193–197.
[287] M. J. Taylor, A. J. Saunders, M. P. Coles, J. R. Fulton, *Organometallics* **2011**, *30*, 1334–1339.
[288] A. P. Dove, V. C. Gibson, E. L. Marshall, A. J. P. White, D. J. Williams, *Chem. Commun.* **2001**, 283–284.
[289] A. P. Dove, V. C. Gibson, E. L. Marshall, H. S. Rzepa, A. J. P. White, D. J. Williams, *J. Am. Chem. Soc.* **2006**, *128*, 9834–9843.
[290] M. Zhong, Y. Ding, D. Jin, X. Ma, Y. Liu, B. Yan, Y. Yang, J. Peng, Z. Yang, *Inorg. Chim. Acta* **2019**, *486*, 669–674.
[291] L. A.-M. Harris, M. P. Coles, J. R. Fulton, *Inorg. Chim. Acta* **2011**, *369*, 97–102.
[292] D. W. N. Wilson, S. J. Urwin, E. S. Yang, J. M. Goicoechea, *J. Am. Chem. Soc.* **2021**, *143*, 10367–10373.
[293] A. Jana, H. W. Roesky, C. Schulzke, P. P. Samuel, *Inorg. Chem.* **2010**, *49*, 3461–3464.
[294] W. Wang, S. Inoue, S. Yao, M. Driess, *Chem. Commun.* **2009**, 2661–2663.
[295] A. Jana, S. P. Sarish, H. W. Roesky, C. Schulzke, P. P. Samuel, *Chem. Commun.* **2010**, *46*, 707–709.
[296] A. Jana, R. Azhakar, H. W. Roesky, I. Objartel, D. Stalke, *Z. Anorg. Allg. Chem.* **2011**, *637*, 1795–1799.
[297] S. Inoue, M. Driess, *Organometallics* **2009**, *28*, 5032–5035.
[298] E. C. Y. Tam, D. C. Apperley, J. D. Smith, M. P. Coles, J. R. Fulton, *Inorg. Chem.* **2017**, *56*, 14831–14841.

[299] A. Jana, I. Objartel, H. W. Roesky, D. Stalke, *Dalton Trans.* **2010**, *39*, 4647–4650.
[300] L. A.-M. Harris, E. C. Y. Tam, M. P. Coles, J. R. Fulton, *Dalton Trans.* **2014**, *43*, 13803–13814.
[301] L. Ferro, P. B. Hitchcock, M. P. Coles, H. Cox, J. R. Fulton, *Inorg. Chem.* **2011**, *50*, 1879–1888.
[302] A. Jana, H. W. Roesky, C. Schulzke, A. Döring, *Angew. Chem.* **2009**, *121*, 1126–1129; *Angew. Chem. Int. Ed.* **2009**, *48*, 1106–1109.
[303] A. Jana, H. W. Roesky, C. Schulzke, *Inorg. Chem.* **2009**, *48*, 9543–9548.
[304] M. Beller, J. Seayad, A. Tillack, H. Jiao, *Angew. Chem.* **2004**, *116*, 3448–3479; *Angew. Chem. Int. Ed.* **2004**, *43*, 3368–3398.
[305] A. Jana, H. W. Roesky, C. Schulzke, P. P. Samuel, *Organometallics* **2010**, *29*, 4837–4841.
[306] P. Bazinet, G. P. A. Yap, G. A. DiLabio, D. S. Richeson, *Inorg. Chem.* **2005**, *44*, 4616–4621.
[307] V. M. Jiménez-Pérez, B. M. Muñoz-Flores, H. W. Roesky, T. Schulz, A. Pal, T. Beck, Z. Yang, D. Stalke, R. Santillan, M. Witt, *Eur. J. Inorg. Chem.* **2008**, *2008*, 2238–2243.
[308] S. M. Mansell, C. A. Russell, D. F. Wass, *Inorg. Chem.* **2008**, *47*, 11367–11375.
[309] H. Arii, M. Matsuo, F. Nakadate, K. Mochida, T. Kawashima, *Dalton Trans.* **2012**, *41*, 11195–11200.
[310] J. Kobayashi, T. Kushida, T. Kawashima, *J. Am. Chem. Soc.* **2009**, *131*, 10836–10837.
[311] A. G. Avent, C. Drost, B. Gehrhus, P. B. Hitchcock, M. F. Lappert, *Z. Anorg. Allg. Chem.* **2004**, *630*, 2090–2096.
[312] C. Drost, P. B. Hitchcock, M. F. Lappert, *Angew. Chem. Int. Ed.* **1999**, *38*, 1113–1116; *Angew. Chem.* **1999**, *111*, 1185–1187.
[313] M. Chen, J. R. Fulton, P. B. Hitchcock, N. C. Johnstone, M. F. Lappert, A. V. Protchenko, *Dalton Trans.* **2007**, 2770–2778.
[314] L. W. Pineda, V. Jancik, S. Nembenna, H. W. Roesky, *Z. Anorg. Allg. Chem.* **2007**, *633*, 2205–2209.
[315] M. J. Taylor, E. J. Coakley, M. P. Coles, H. Cox, J. R. Fulton, *Organometallics* **2015**, *34*, 2515–2521.
[316] A. Jana, S. P. Sarish, H. W. Roesky, C. Schulzke, A. Döring, M. John, *Organometallics* **2009**, *28*, 2563–2567.
[317] E. C. Tam, M. P. Coles, J. D. Smith, J. R. Fulton, *Polyhedron* **2015**, *85*, 284–294.
[318] A. Jana, H. W. Roesky, C. Schulzke, P. P. Samuel, A. Döring, *Inorg. Chem.* **2010**, *49*, 5554–5559.
[319] E. C. Y. Tam, N. C. Johnstone, L. Ferro, P. B. Hitchcock, J. R. Fulton, *Inorg. Chem.* **2009**, *48*, 8971–8976.
[320] J. R. Fulton, P. B. Hitchcock, N. C. Johnstone, E. C. Y. Tam, *Dalton Trans.* **2007**, 3360–3362.
[321] S. Yao, S. Block, M. Brym, M. Driess, *Chem. Commun.* **2007**, 3844–3846.
[322] N. Villegas-Escobar, D. E. Ortega, D. Cortés-Arriagada, R. Durán, D. Yepes, S. Gutiérrez-Oliva, A. Toro-Labbé, *J. Phys. Chem. C* **2017**, *121*, 12127–12135.
[323] A. Jana, S. P. Sarish, H. W. Roesky, D. Leusser, I. Objartel, D. Stalke, *Chem. Commun.* **2011**, *47*, 5434–5436.

[324] J. P. H. Charmant, M. F. Haddow, F. E. Hahn, D. Heitmann, R. Fröhlich, S. M. Mansell, C. A. Russell, D. F. Wass, *Dalton Trans.* **2008**, 6055–6059.
[325] L. Bourget-Merle, M. F. Lappert, J. R. Severn, *Chem. Rev.* **2002**, *102*, 3031–3066.
[326] M. S. Hill, D. J. Liptrot, C. Weetman, *Chem. Soc. Rev.* **2016**, *45*, 972–988.
[327] R. L. Webster, *Dalton Trans.* **2017**, *46*, 4483–4498.
[328] C. Chen, S. M. Bellows, P. L. Holland, *Dalton Trans.* **2015**, *44*, 16654–16670.
[329] S. Hohloch, B. M. Kriegel, R. G. Bergman, J. Arnold, *Dalton Trans.* **2016**, *45*, 15725–15745.
[330] A. D. Phillips, *Organomet. Chem.* **2014**, *39*, 72–147.
[331] Y.-C. Tsai, *Coord. Chem. Rev.* **2012**, *256*, 722–758.
[332] C. Cui, H. W. Roesky, H.-G. Schmidt, M. Noltemeyer, H. Hao, F. Cimpoesu, *Angew. Chem. Int. Ed.* **2000**, *39*, 4274–4276; *Angew. Chem.* **2000**, *112*, 4444–4446.
[333] N. J. Hardman, B. E. Eichler, P. P. Power, *Chem. Commun.* **2000**, 1991–1992.
[334] M. S. Hill, P. B. Hitchcock, *Chem. Commun.* **2004**, 1818–1819.
[335] M. S. Hill, P. B. Hitchcock, R. Pongtavornpinyo, *Dalton Trans.* **2005**, 273–277.
[336] A. Stasch, C. Jones, *Dalton Trans.* **2011**, *40*, 5659–5672.
[337] C. Jones, *Nat. Rev. Chem.* **2017**, *1*, 877.
[338] F. Baier, Z. Fei, H. Gornitzka, A. Murso, S. Neufeld, M. Pfeiffer, I. Rüdenauer, A. Steiner, T. Stey, D. Stalke, *J. Organomet. Chem.* **2002**, *661*, 111–127.
[339] H. Gornitzka, D. Stalke, *Organometallics* **1994**, *13*, 4398–4405.
[340] C.-H. Chen, M.-L. Tsai, M.-D. Su, *Organometallics* **2006**, *25*, 2766–2773.
[341] W. W. Schoeller, *Inorg. Chem.* **2011**, *50*, 2629–2633.
[342] M. N. Sudheendra Rao, H. W. Roesky, G. Anantharaman, *J. Organomet. Chem.* **2002**, *646*, 4–14.
[343] Y. Mizuhata, T. Sasamori, N. Tokitoh, *Chem. Rev.* **2009**, *109*, 3479–3511.
[344] D.-R. Dauer, *Studies of group 13 metal complexes bearing nacnac-mimetic bisheterocyclo methanides and amides*; Dissertation, Cuvillier Verlag, Göttingen, **2016**.
[345] V. M. Zubarovskii, *Zhurnal Obshchei Khimii* **1951**, *21*, 2199–2205.
[346] W. Ried, J. Patschorke, *Justus Liebigs Ann. Chem.* **1956**, *599*, 44–50.
[347] E. S. Lane, *J. Chem. Soc.* **1953**, 2238.
[348] D. E. Ryan, B. K. Afghan, *Analytica Chimica Acta* **1969**, *44*, 115–122.
[349] F. Ragaini, M. Pizzotti, S. Cenini, A. Abbotto, G. A. Pagani, F. Demartin, *J. Organomet. Chem.* **1995**, *489*, 107–112.
[350] A. Abbotto, V. Alanzo, S. Bradamante, G. A. Pagani, C. Rizzoli, G. Calestani, *Gazetta Chimica Italiana* **1991**, *121*, 365–368.
[351] A. Abbotto, S. Bruni, F. Cariati, G. A. Pagani, *Spectrochimica Acta Part A* **2000**, *56*, 1543–1552.
[352] M. A. Pujar, T. D. Bharamgoudar, D. N. Sathyanarayana, *Transition Met. Chem.* **1988**, *13*, 423–425.
[353] I. Koehne, *Novel Bulky Bis(benzoxazol-2-yl)methan Ligands in s-Block Metal Coordination*; Dissertation, Göttingen, **2018**.
[354] J. Kretsch, *Chelate Ligands for the Stabilisation of Low-Valent Main Group Compounds*; Dissertation, Göttingen, **2021**.

[355] J. Kretsch, I. Koehne, M. Lõkov, I. Leito, D. Stalke, *Eur. J. Inorg. Chem.* **2019**, *2019*, 3258–3264.
[356] D.-R. Dauer, I. Koehne, R. Herbst-Irmer, D. Stalke, *Eur. J. Inorg. Chem.* **2017**, *2017*, 1966–1978.
[357] D.-R. Dauer, D. Stalke, *Dalton Trans.* **2014**, *43*, 14432–14439.
[358] D.-R. Dauer, M. Flügge, R. Herbst-Irmer, D. Stalke, *Dalton Trans.* **2016**, *45*, 6136–6148.
[359] T. Stey, M. Pfeiffer, J. Henn, S. K. Pandey, D. Stalke, *Chem. Eur. J.* **2007**, *13*, 3636–3642.
[360] J. Hey, D. Leusser, D. Kratzert, H. Fliegl, J. M. Dieterich, R. A. Mata, D. Stalke, *Phys. Chem. Chem. Phys.* **2013**, *15*, 20600–20610.
[361] T. Stey, J. Henn, D. Stalke, *Chem. Commun.* **2007**, 413–415.
[362] C. Kling, D. Leusser, T. Stey, D. Stalke, *Organometallics* **2011**, *30*, 2461–2463.
[363] T. Stey, D. Stalke in *The Chemistry of Organolithium Compounds*, John Wiley & Sons, Hoboken, NJ, USA, **2004**, 47–120.
[364] D.-R. Dauer, M. Flügge, R. Herbst-Irmer, D. Stalke, *Dalton Trans.* **2016**, *45*, 6149–6158.
[365] I. Koehne, N. Graw, T. Teuteberg, R. Herbst-Irmer, D. Stalke, *Inorg. Chem.* **2017**, *56*, 14968–14978.
[366] I. Koehne, S. Bachmann, T. Niklas, R. Herbst-Irmer, D. Stalke, *Chem. Eur. J.* **2017**, *23*, 13141–13149.
[367] J. Kretsch, A.-K. Kreyenschmidt, T. Schillmöller, M. Lõkov, R. Herbst-Irmer, I. Leito, D. Stalke, *Chem. Eur. J.* **2021**, *27*, 9858–9865.
[368] J. Kretsch, A. Kreyenschmidt, R. Herbst-Irmer, D. Stalke, *Dalton Trans.* **2018**, *47*, 12606–12612.
[369] I. Koehne, S. Bachmann, R. Herbst-Irmer, D. Stalke, *Angew. Chem.* **2017**, *129*, 15337–15342; *Angew. Chem. Int. Ed.* **2017**, *56*, 15141–15145.
[370] I. Koehne, R. Herbst-Irmer, D. Stalke, *Eur. J. Inorg. Chem.* **2017**, *2017*, 3322–3326.
[371] J. Kretsch, R. Herbst-Irmer, D. Stalke, *Z. Anorg. Allg. Chem.* **2018**, *644*, 657–660.
[372] C. M. Legendre, D. Lüert, R. Herbst-Irmer, D. Stalke, *Dalton Trans.* **2021**, *50*, 16810–16818.
[373] D. Lüert, R. Herbst-Irmer, D. Stalke, *Eur. J. Inorg. Chem.* **2021**, *2021*, 5085–5090.
[374] D. Lüert, A.-K. Kreyenschmidt, C. M. Legendre, R. Herbst-Irmer, D. Stalke, *Inorg. Chem.* **2022**, *61*, 5234–5244.
[375] J. Kretsch, A. Kreyenschmidt, T. Schillmöller, R. Herbst-Irmer, D. Stalke, *Inorg. Chem.* **2020**, *59*, 13690–13699.
[376] J. Kretsch, A. Kreyenschmidt, T. Schillmöller, C. Sindlinger, R. Herbst-Irmer, D. Stalke, *Inorg. Chem.* **2021**, *60*, 7389–7398.
[377] H. Ben Ammar, J. Le Nôtre, M. Salem, M. T. Kaddachi, P. H. Dixneuf, *J. Organomet. Chem.* **2002**, *662*, 63–69.
[378] K. V. Arsenyeva, M. G. Chegerev, A. V. Cherkasov, K. I. Pashanova, I. V. Ershova, O. Y. Trofimova, A. V. Piskunov, *Mendeleev Commun.* **2021**, *31*, 330–333.
[379] R. K. Siwatch, D. Yadav, G. Mukherjee, G. Rajaraman, S. Nagendran, *Inorg. Chem.* **2013**, *52*, 13384–13391.

[380] S.-H. Zhang, C.-W. So, *Organometallics* **2011**, *30*, 2059–2062.
[381] E. O. Fischer, H. Grubert, *Z. Anorg. Allg. Chem.* **1956**, *286*, 237–242.
[382] D. R. Armstrong, M. J. Duer, M. G. Davidson, D. Moncrieff, C. A. Russell, C. Stourton, A. Steiner, D. Stalke, D. S. Wright, *Organometallics* **1997**, *16*, 3340–3351.
[383] A. F. Reid, P. C. Wailes, *Aust. J. Chem.* **1966**, *19*, 309.
[384] M. J. S. Gynane, D. H. Harris, M. F. Lappert, P. P. Power, P. Rivière, M. Rivière-Baudet, *J. Chem. Soc., Dalton Trans.* **1977**, 2004–2009.
[385] A. Bondi, *J. Phys. Chem.* **1964**, *68*, 441–451.
[386] A. W. Addison, T. N. Rao, J. Reedijk, J. van Rijn, G. C. Verschoor, *J. Chem. Soc., Dalton Trans.* **1984**, 1349–1356.
[387] T. Ochiai, T. Szilvási, D. Franz, E. Irran, S. Inoue, *Angew. Chem.* **2016**, *128*, 11791–11796; *Angew. Chem. Int. Ed.* **2016**, *55*, 11619–11624.
[388] S. Sinhababu, R. K. Siwatch, G. Mukherjee, G. Rajaraman, S. Nagendran, *Inorg. Chem.* **2012**, *51*, 9240–9248.
[389] T. T. Dang, F. Boeck, L. Hintermann, *J. Org. Chem.* **2011**, *76*, 9353–9361.
[390] J. S. Hrkach, K. Matyjaszewski, *Macromolecules* **1990**, *23*, 4042–4046.
[391] E. L. Myers, C. P. Butts, V. K. Aggarwal, *Chem. Commun.* **2006**, 4434–4436.
[392] I. W. Stolz, G. R. Dobson, R. K. Sheline, *Inorg. Chem.* **1963**, *2*, 323–326.
[393] C. Christiansen, *Ann. Phys.* **1884**, *23*, 298–306.
[394] W. C. Price, K. S. Tetlow, *J. Chem. Phys.* **1948**, *16*, 1157–1162.
[395] C. V. Raman, *Proc. Indian Acad. Sci. (Math. Sci.)* **1949**, *29*, 381–390.
[396] R. K. Sheline, *J. Am. Chem. Soc.* **1950**, *72*, 5761–5762.
[397] M. Mantina, A. C. Chamberlin, R. Valero, C. J. Cramer, D. G. Truhlar, *J. Phys. Chem. A* **2009**, *113*, 5806–5812.
[398] *Match! - Phase Analysis using Powder Diffraction*, Crystal Impact - Dr. H. Putz & Dr. K. Brandenburg GbR, Kreuzherrenstr. 102, 53227 Bonn, Germany.
[399] A. Vaitkus, A. Merkys, S. Gražulis, *J. Appl. Cryst.* **2021**, *54*, 661–672.
[400] P. B. Hitchcock, M. F. Lappert, G. Li, M. P. Coles, *Dalton transactions (Cambridge, England : 2003)* **2009**, 7820–7826.
[401] L. A. Lesikar, A. F. Richards, *Journal of Organometallic Chemistry* **2006**, *691*, 4250–4256.
[402] R. Dovesi, A. Erba, R. Orlando, C. M. Zicovich-Wilson, B. Civalleri, L. Maschio, M. Rérat, S. Casassa, J. Baima, S. Salustro, B. Kirtman, *WIREs Comput. Mol. Sci.* **2018**, *8*, 171.
[403] D. Vilela Oliveira, J. Laun, M. F. Peintinger, T. Bredow, *J. Comput. Chem.* **2019**, *40*, 2364–2376.
[404] S. Grimme, J. Antony, S. Ehrlich, H. Krieg, *J. Chem. Phys.* **2010**, *132*, 154104.
[405] R. F. W. Bader, *Atoms in molecules. A quantum theory*, Clarendon Press, Oxford, **2003**.
[406] C. Gatti, S. Casassa, *TOPOND14 User Manual*, CNR ISTM of Milan, Milan, Spain, **2017**.
[407] Y. A. Abramov, A. Volkov, G. Wu, P. Coppens, *Acta Crystallogr. A, Found. Adv.* **2000**, *56*, 585–591.
[408] T. A. Keith, *AIMAll (Version 19.10.12)*, TK Gristmill Software, Overland Park KS, USA, **2019**.
[409] R. Bianchi, G. Gervasio, D. Marabello, *Inorg. Chem.* **2000**, *39*, 2360–2366.
[410] T. Kottke, D. Stalke, *J. Appl. Cryst.* **1993**, *26*, 615–619.

[411] D. Stalke, *Chem. Soc. Rev.* **1998**, *27*, 171.
[412] L. Krause, R. Herbst-Irmer, D. Stalke, *J. Appl. Cryst.* **2015**, *48*, 1907–1913.
[413] G. M. Sheldrick, "Alphabetical list of SHELXL instructions", can be found under https://shelx.uni-goettingen.de/shelxl_html.php#ISOR, accessed 17.02.2022.
[414] S. Becker, P. Müller, *Chem. Eur. J.* **2017**, *23*, 7081–7086.
[415] S. Parsons, H. D. Flack, T. Wagner, *Acta Crystallogr. B, Struct. Sci.* **2013**, *69*, 249–259.

8 Acknowledgements

A PhD is in many ways very similar to going on journey. Even if you have prepared the best route map before embarking, you never know what life has up its sleeves. Dead ends, detours and pitfalls may lurk for you, and surely you could struggle through all of that on your own. But more important than anything else to keep your spirits up and to get back on track are your fellows – whether you are carrying jewellery to Mount Doom or navigating on your quest to obtain a PhD. So it is only right to thank those who have accompanied me on my journey.

Foremost I would like to acknowledge my advisor, Prof. Dr. Dietmar Stalke, who welcomed me in his research group. He always had an open ear – and no less important – his office an open door. He (almost) never said no, had my back when necessary and placed his trust in me. And all the serious science aside, I am especially grateful for the opportunity he gave me to dive into the joy of demonstration experiments and Christmas lectures. There are people who just tell you what to do and there are people who stand by you even if you wear a dress and a wig. I'm glad I worked with the latter.

I am highly grateful to Jun.-Prof. Dr. Anna Krawczuk, who willingly stepped in to become my second supervisor despite my aversion of potatoes.

I would also like to thank Prof. Dr. Manuel Alcarazo for his willingness to be my third supervisor and especially for helpful discussions regarding the synthetic part of this thesis.

I want to thank Anna, Helena, Paula, Xiaobai and Sebastian for reading the first drafts of this thesis and providing valuable feedback.

A big shout-out to my lab mate Christina. I think we had an awesome time sharing the lab and she deserves honours for not only accepting but actually liking my weird music. Although she somewhat destroyed the order that I had painstakingly built up in the lab when she moved in with her smelly sulphur chemistry, I am not mad about it, because that was a small price to pay for getting to know her, enjoying her enthusiastic, quirky attitude and becoming good friends.

I would like to thank Annika, Christian, Helena and Niklas, the guys working in the “ED Büro” aka the meme office, for very helpful discussions about crystallography in general and all the tips and tricks you showed me for the cases when the path from crystal to structure was not quite straightforward. I will not forget our successful launch of the “MC3 Support Helpdesk – Teaching crystallography since 1911.” And of course I have to thank Regine, who conjured up a bit of

crystallography magic every time I got stuck and saved data, I could not even get a structure solution of, from the trash can.

I am especially grateful to Annika for guiding my very first steps in crystallography. I do remember well how I even failed to correctly start the most basics programmes in the beginning. Considering that in the end a good portion of my work is crystallography related, Annika for sure did a good job introducing me to it. In the same vein Helena deserves credit for training me to become a "Maschienenschrauber". She shared all the secret tricks with me for maintaining diffractometers and I admire her for her ability to spend hours on beam alignment without losing patience, yelling at equipment or giving in to the urge to scrap the whole diffractometer.

I would like to thank Tobi and Laura not only for keeping me supplied with all the stuff that one needs in a lab but also for the fun times we had preparing experiments and demonstrations for (Christmas) lectures.

To Niklas and the people at Bruker AXS, Incoatec and Excillum AB I am thankful for the cooperation on the MetalJet project.

I am grateful to Xiaobai for his assistance in taking photographs of the models I created. The pictures turned out really nice la! Also the video team of the University did a great job recording the space group models in action.

I want to thank Anne and Franziska for bearing with my questions about (and demand for) heteronuclear NMR experiments and in general everything NMR related that cannot be done with an automatic sampler.

Many thanks to Paula, whose knowledge on powder X-ray diffraction sparked new hope to a project that I would otherwise have considered a dead end.

Simon, Merit and Flemming, who joined me in the lab as students, traded their work force for the chance to learn something (I guess). I hope that deal worked out for them, because it did for me. I am very thankful for the contributions they made to my synthetic work.

Of course I have to thank all the members of the Stalke group – past and present. As initially said the value of a great work environment cannot be overestimated. I am immensely thankful for this group being supportive and collaborative and more than just a group of co-workers. Discussing the state of the nation during hour long lunch breaks, WoDuR escalation, laser tag, Kegeln, group trips (including conferences), last minute PhD hat crafting, pub crawls, parties for all sorts of reasons; there were so many occasions that it is hard to remember all of them, but they all certainly proved that we are a functioning group of crazy people – in the best sense of that word, of course.

Acknowledgement is also due to the administrative and technical staff at the Faculty of Chemistry. I am particularly indebted to Dr. Claudia Stückl, Heike and the troop of facility managers for help with various organisational obstacles, as well as to the workshop staff, who never failed to turn ideas born on paper into reality - even if it meant to fill rubber ducks with construction foam and cutting them in half on a band saw.

The Lower Saxony Ministry of Science and Culture is acknowledged for partial funding of this work within the framework of the *Innovation plus* funding programme.

On a more personal note, I would like to thank Anna, Dan and Sebastian for making sure I do not forget that there is life outside of university. I have been spoiled with food and drinks to a degree that should be embarrassing.

Lastly, I have to thank my mother and brother who have been supportive throughout my life and Sebastian for becoming a part of it.